

Université catholique de Louvain
Faculté d'Ingénierie Biologique, Agronomique et Environnementale

Full-wave inversion of near-field ground penetrating radar data for hydrogeophysical characterization of soil

ANH PHUONG TRAN

FEBRUARY 2014

Thèse présentée en vue de l'obtention
du grade de Docteur en Sciences Agronomiques
et Ingénierie Biologique

Jury members:

President:	Prof. M. Vanclooster (UCL, Belgium)
Supervisor:	Prof. S. Lambot (UCL, Belgium)
Readers:	Dr. F. André (UCL, Belgium)
	Prof. C. Craeye (UCL, Belgium)
	Prof. I. Huynen (UCL, Belgium)
	Prof. E. C. Slob (Delft University of Technology, The Netherlands)

To know, is to know that you know nothing. That is the meaning of true knowledge.

Socrates

Acknowledgements

This thesis was carried out at the Environmental sciences, Earth and life Institute, Université catholique de Louvain (UCL, Belgium), from April 2010 to January 2014 under the financial support of the FSR-UCL scholarship, UCL-ARC project and DROPS project funded by the European Commission under the 7th Framework Programme for Research and Technological Development.

Foremost, I would like to express my deepest appreciation to my supervisor Prof. Sébasitien Lambot for his valuable idea, motivation, enthusiasm and continuous support. His guidance helped me in all the time of research and writing of this thesis. I have been learnt from him a lot things, not only his tremendous academic knowledge but also his kind personality. I would have not expect to have a such good supervisor for my PhD study like him.

I am indebted to Dr. Frédéric André for his worthful advice on GPR and EMI forward and inverse modeling problem, Prof. Christophe Crayey and his research group for their antenna design and enthusiastic support in solving electromagnetic problems, and Prof. Marnik Vanclooster for his explanation about soil hydrological model. Dr. Milija Zupanski deserves my heartfelt gratitude for his valuable ideas and answers to my questions concerning data assimilation problems.

Many of results in this thesis were came from laboratory experiments, which were performed with the helps of Frédéric Laurent and Sébastien François. I would like to thank them for their support of experimental installation and field campaign measurements.

I profoundly acknowledge my jury members Frédéric André, Isabelle Huynen, Marnik Vanclooster, Christophe Crayey and Evert Slob for their advices during my research, reading this thesis and providing valuable comments and suggestions.

I want to express my gratitude to the Environmental science–Earth and Life Science Institute (UCL) for accepting me to pursue the PhD program and providing me necessary facilities to do the research work.

I cordially express my thankfulness to all my colleagues from Environmental Science, Earth and Life Science Institute of UCL as well as my Vietnam friends in Louvain-la-neuve and Leuven for their friendship during my PhD time. Particularly, I would like to thank to my GPR colleagues (Julien, Jadoon, Siavash, Nicolas, Laurence, Alberic) and officemate François for their sharing and discussion on topics of GPR and hydrological studies, which much help me to get new ideas for my research and enjoyable non-research time.

Last but not least, I would like to express my special thank to my parents and younger brother for their unconditional love and support throughout my degree. My wife who is always beside me with her love and accompaniment during this journey. One word "thanks" is never enough for her. Finally, I would like to devote this work to my little son with whom I have more motivation to continue my research.

Contents

1 Introduction **1**
1.1 Research topic . . . 1
1.2 Statement of problem . . . 5
1.3 Thesis objectives . . . 6
1.4 Thesis outline . . . 7

2 Numerical evaluation of a full-wave antenna model for near-field applications **11**
2.1 Introduction . . . 12
2.2 Near-field, full-wave GPR model . . . 13
2.3 Numerical experiments using data from a FDTD antenna model . . . 15
2.4 Determination of transmission and reflection transfer functions . . . 17
2.5 Reconstruction of layered media by near-field antenna model . . . 20
2.6 Response surface analysis . . . 26
2.7 Conclusions . . . 27

3 Antenna height threshold for near-field or far-field modeling **31**
3.1 Introduction . . . 32
3.2 Theory . . . 33
3.2.1 Green's function . . . 33
3.2.2 Partial derivative of Green's function . . . 34
3.2.3 Near-field and far-field antenna models . . . 35
3.3 Results and discussion . . . 36
3.3.1 Antenna threshold for far-field antenna modeling . . . 36
3.4 Validation of the antenna height threshold . . . 37
3.4.1 Numerical experiments . . . 37
3.4.2 Laboratory validation . . . 39
3.5 Antenna height threshold versus number of source/field points . . . 44
3.6 Conclusion . . . 45

4 Intrinsic modeling of antenna array in near-field conditions **49**
4.1 Introduction . . . 50
4.2 Intrinsic array model . . . 51
4.3 Determination of antenna characteristic transfer functions . . . 52
4.3.1 Far-field model calibration . . . 52
4.3.2 Simplified antenna array model calibration . . . 54
4.3.3 Full antenna array model calibration . . . 55
4.4 Antenna array system . . . 56
4.5 Results and discussion . . . 57
4.6 Conclusion . . . 62

5 Coupling of mixing models with GPR inversion 65
5.1 Introduction . . . 66
5.2 Theory . . . 67
5.2.1 Forward modeling . . . 67
5.2.2 Mixing models . . . 67
5.2.3 Parameter estimation . . . 69
5.3 Experimental results . . . 72
5.3.1 Experimental setup . . . 72
5.3.2 Accuracy of water content estimation . . . 73
5.3.3 Frequency dependence of electric properties . . . 78
5.4 Uncertainty analysis . . . 80
5.5 Discussion . . . 81
5.6 Conclusion . . . 83

6 Validation of near-field GPR modeling for soil moisture estimation 85
6.1 Introduction . . . 86
6.2 Methodology . . . 87
6.2.1 The forward model . . . 87
6.2.2 Inverse modeling . . . 87
6.3 GPR systems and antenna calibration . . . 88
6.3.1 GPR systems . . . 88
6.3.2 Antenna calibration . . . 89
6.4 Validation . . . 92
6.4.1 Experimental description . . . 92
6.4.2 Accuracy of GPR data . . . 94
6.4.3 Estimation of water content . . . 97
6.5 Soil moisture profile estimation . . . 98
6.6 Summary and conclusion . . . 103

7 Soil moisture profile reconstruction from ground penetrating radar data 105
7.1 Introduction . . . 106
7.2 Materials and methods . . . 108
7.2.1 Data assimilation procedure . . . 108
7.2.2 The hydrodynamic model . . . 108
7.2.3 The observation operator . . . 109
7.2.4 The maximum likelihood ensemble filter . . . 111
7.2.5 Numerical simulation . . . 113
7.3 Results and discussion . . . 119
7.3.1 Assimilation results . . . 119
7.3.2 Effect of the update interval . . . 121
7.4 Conclusion . . . 123

8 Joint estimation of soil moisture profile and hydraulic parameters 125
8.1 Introduction . . . 126
8.2 Theory . . . 128
8.2.1 The petrophysical relationship . . . 128
8.2.2 The state augmentation method . . . 129
8.3 Experimental setup . . . 131
8.3.1 Numerical experiment . . . 131
8.4 Results and discussion . . . 134
8.4.1 Soil moisture profile estimation . . . 134
8.4.2 Parameter estimation . . . 138

8.5 Conclusion 138

9 Conclusion and Perspectives **141**
9.1 Conclusion 141
9.2 Perspectives 145

References **149**

List of publications **171**

International Conferences **172**

About the author **174**

Chapter 1

Introduction

1.1 Research topic

Although shallow soil water occupies only a tiny portion of global water on the earth (0.05% of total liquid freshwater [Dingman, 1994]), its importance has long been acknowledged for hydrology, meteorology, agriculture and ecological diversity [Hubbard and Rubin, 2005; Vereecken et al., 2008]. In hydrology, the availability of soil moisture is the main factor that governs the separation of rainfall into runoff and infiltration. Disregarding the spatial pattern of antecedent soil moisture may cause significant errors on flood prediction [e.g., Merz and Bardossy, 1998; Brocca et al., 2010; Minet et al., 2010a; Nied et al., 2013]. Soil moisture is also a crucial factor that controls the partitioning of radiation energy into latent and sensible heat fluxes, and consequently, near-surface temperature and precipitation [Seneviratne et al., 2010]. As a result, inclusion of surface soil moisture in numerical weather models is necessary to improve the accuracy of weather forecast [Drusch, 2007; Mahfouf, 2010]. In agriculture, soil moisture plays a key role for plant growth in the sense that it is not only itself a nutrient but also serves as a solvent and carrier to transport other biochemical nutrients for plants. Too little or too much water both impact on the health of plant and crop yield. For ecosystems, soil moisture conditions are closely linked to the form, functioning and organization of vegetation, and therefore, largely influence on ecological diversity [Rodriguez-Iturbe, 2000].

Yet, the contaminants from inadequately treated sewage, poor agriculture practices and control of wastewater discharge from industrial plants as well as ill-considered placement of landfills have resulted in the pollution of soil and water and degradation of our ecosystem. The changes of hydrological cycle and water distribution under the impacts of global warming have made the problems become more severe. Sustainable management of land and water resources, therefore, is of crucial importance. In that sense, timely and accurate quantification of soil moisture conditions ranging from point to regional scale, which provides information for hydro-meteorological forecast, agriculture management practices and environmental protection, is an urgent demand [Hubbard and Rubin, 2005]. Soil moisture also exhibits high variability in time and space, and nonlinearly depends on its controlling factors (e.g.,

rainfall, evaporation, topography, soil type and vegetation) [Famiglietti et al., 1998; Western et al., 2000]. Hence, for a clear understanding on soil moisture dynamics, it is necessary to characterize soil moisture with a high spatiotemporal resolution.

Given the importance of soil moisture, there are numerous techniques developed for characterizing this variable. Excellent review on these techniques were presented in Rubin and Hubbard [2005]. Robinson et al. [2008b] and Vereecken et al. [2008] classified these techniques into three categories, namely, contact-based, geophysical and remote sensing instrumentations. The contact-based sensing instruments indirectly estimate soil moisture via the neutron thermalization (neutron moisture meter [Bell et al., 1987; Evett, 2003]), electric permittivity (capacitance probes [Paltineanu and Starr, 1997; David and Renato, 2009], time domain reflectivity [Hupet and Vanclooster, 2002; Robinson et al., 2003; Topp et al., 2003]), electrical resistivity (electrical resistivity tomography [Daily et al., 1992; Michot et al., 2003]) or thermal properties (heat pulse sensors [Heitman et al., 2003; Valente et al., 2006; Pedro et al., 2013]). These techniques enable to provide relatively accurate soil moisture with a high temporal resolution at the point scale. However, their small supporting volume makes them time-consuming and labor-intensive to estimate soil moisture at the catchment scale because many measurements are needed to perform. In conditions like hard or stony soils, measurements using these techniques are even impossible [Robinson et al., 2012]. Recently, wireless networks of sensors were introduced to improve the spatial coverage of contacted-based soil moisture data measurements [Bogena et al., 2007; Kerkez et al., 2012].

The second category is remote sensing techniques, namely, synthetic aperture radar (SAR) [Kornelsen and Coulibaly, 2013], soil moisture and ocean salinity mission (SMOS) [Kerr, 2007], advanced scatterometer (ASCAT) [Bartalis et al., 2007]. These techniques estimate soil moisture based on the relationship between its electric permittivity and backscattered reflection from the soil surface [Jackson, 1993; Schmugge, 1998; Walker et al., 2004; Alvarez-Mozos et al., 2006]. They are able to provide soil moisture data with a large extent but their spatiotemporal resolution is too coarse for catchment characterization. In addition, their characterized depth is limited to only upmost soil layer (0-5 cm) and the measurements are influenced by the vegetation and surface roughness [Wagner et al., 2007; Verhoest et al., 2008].

Clearly, there is a scale gap between the contact-based and remote sensing techniques. In that respect, geophysical techniques (ground-penetrating radar (GPR) and electromagnetic induction (EMI)) are ideal to retrieve soil moisture at the field scale. EMI is a promising technique for soil moisture estimation. However, due to the fact that, EMI is not only sensitive to soil moisture but also other soil properties including clay content, salinity, organic matters and tem-

perature, the accuracy of soil moisture estimation also depends on the accurate determination of these properties [Sudduth et al., 2003; Rodríguez-Pérez et al., 2011; André et al., 2012].

Over the last two decades, GPR has become an advanced non-destructive technique that has been intensively used to characterize media with high spatial resolution in many disciplines. GPR was applied for detection of archaeological anomalies [Vaughan, 1986; Conyers, 2006; Papadopoulos et al., 2009] and landmines [Gader et al., 2001; Sato et al., 2004; Lopera et al., 2007a; Soldovieri et al., 2011], evaluation of bridge decks and roads [Spagnolini and Rampa, 1999; Scott et al., 2000; Abudayyeh et al., 2008], crack inspection in cement-based materials [Benedetto et al., 2005; Nadakuduti et al., 2006; Dérobert et al., 2008; Patriarca et al., 2011], locating buried pipe systems [Windsor et al., 2005; Pettinelli et al., 2009] and coal mines [Cook, 1977], fracture mapping [Grasmueck, 1996], forensics investigation [Owsley, 1995], determination of the volume and structural aspects of ice and snow [Bailey et al., 1964; Brown et al., 2011], stratigraphy and sedimentology [Davis and Annan, 1989; Neal, 2004], and planetary exploration on Mars and the moon [Simmons, 1972]. The theoretical foundation underpinning the applications of GPR is a combination of Maxwell's equations and constitutive relationships. While Maxwell's equations describe the propagation of electromagnetic waves in a medium, the constitutive relationships quantify the response of electromagnetic fields to medium electromagnetic properties (i.e., magnetic permeability (μ), electric conductivity (σ) and electric permittivity (ε)). Consequently, given the electromagnetic properties of materials, the media can be characterized by analyzing GPR data. An excellent review on the theory and history of the GPR is provided by Annan [2002]. Applications and recent advancements of GPR are founded in Jol [2009] and Slob et al. [2010].

In hydrogeophysics, GPR has been used for soil stratigraphy imaging [Davis and Annan, 1989; Grandjean et al., 2006], aquifer characterization [Annan et al., 1991; Tronicke et al., 2004; Mahmoudzadeh et al., 2012], contamination detection and mapping [Nigel, 2007], soil moisture estimation [Serbin and Or, 2004; Rucker and Ferre, 2005; Minet et al., 2011; Steelman and Endres, 2012], water infiltration monitoring [Bano, 2006; Looms et al., 2008; Saintenoy et al., 2008], and soil hydraulic characterization [Kowalsky et al., 2005; Lambot et al., 2009; Doetsch et al., 2010; Jadoon et al., 2012], and thawing zones detecting in permafrost areas [Olhoeft, 1980; Hinkel et al., 2001; Westermann et al., 2010]. Due to the fact that the electric permittivity of water is prominently greater than those of the other components (air and soil particles), there is a strong correlation between GPR data and soil moisture. Several methods to estimate soil moisture from GPR data were proposed using the electromagnetic wave travel time or amplitude information. For instance, Huisman et al. [2001]; Grote et al. [2003]

and Galagedara et al. [2005a] derived the soil electric permittivity from Common Mid Point (CMP) or Wide Angle Reflection and Refraction (WARR) measurements using the travel time of the direct ground wave. Soil moisture was also estimated from first arrival travel time data collected with zero- [Rucker and Ferre, 2005], and multi-offset borehole GPR measurements [Hubbard et al., 1997]. Redman et al. [2002]; Serbin and Or [2004] used soil surface reflection amplitude obtained from off-ground GPR measurements to estimate the soil surface electric permittivity. These methods worked well in some applications. However, as these methods rely on relatively strong simplifications with respect to electromagnetic wave propagation phenomena and only use a part of information contained in the GPR data, their accuracy and applicability are limited.

With the recent advances in computational technology, there have been an increasing number of studies following the full-wave inverse modeling approaches, which mobilize all information of GPR data to characterize the dielectric medium. One approach is to numerically solve Maxwell's equations by using the finite difference time domain (FDTD) [Ernst et al., 2007; Warren and Giannopoulos, 2011; Atteia and Hussein, 2010; Buchner et al., 2012] or finite element time domain (FETD) [Chen and Huang, 1998; Davit, 2007; Durand and Slodic, 2011] methods. Another approach is the integration technique that uses the electric field integral equations (EFIE) to characterize the antenna and method of moments (MoM) to approximate this integral equation by a linear system of basis functions and their associated expansion coefficients [Craeye et al., 2004; Fernández-Pantoja et al., 2009; Gonzalez-Ovejero and Craeye, 2011]. Yet, modeling simultaneously the antenna and the medium domains has remained a challenge for the numerical approaches due to different requirements in terms of spatial resolution of each domain. Due to their long computation time, it is also impractical to apply these approaches in an inversion framework for which computation time is an important aspect as the electromagnetic model has to be run a large number of times, and the accuracy of radar data is a prerequisite in inverse modeling.

In order to avoid the excessive computation time of the numerical approaches, several authors simplified Maxwell's equations so that they can be analytically solved under specific assumptions. Gentili and Spagnolini [2000] modeled a GPR horn antenna at some distance over a three-dimensional (3-D) layered medium using an array of frequency independent source dipoles and a feeding line characteristic impedance. However, the interactions between antenna and medium were not accounted for in this model. Lambot et al. [2004c] developed a far-field frequency-domain antenna model to characterize planar layered media. The model takes into account the antenna effects through transmission and reflection transfer functions, and the wave propagation in the media is simulated by 3-D Green's functions. The model proved

its efficiency and accuracy for estimating the properties of different materials in both laboratory [Lambot et al., 2004c; Minet et al., 2010b], and field experiments [Jadoon et al., 2008; Minet et al., 2011]. The approach also allows for rapid data acquisition by mounting the GPR system on mobile platforms.

1.2 Statement of problem

Although the far-field GPR model developed by Lambot et al. [2004c] provides a relatively good estimation of soil moisture, to satisfy the far-field assumption of this model, the antenna has to be situated far enough from the soil surface [Tran et al., 2013a]. To overcome this limitation, Lambot and André [2013] generalized the far-field GPR model so that it can be also applied to near-field conditions while still resorting to an analytical, closed-form solution of Maxwell's equations. Using this model, the antenna can be operated near the medium surface, which increases the information content in GPR data, and therefore, increases the accuracy of the inverse solution and reconstruction possibilities. Moreover, the smaller foot print of the antenna in the near-field region makes the assumption of local homogeneity within the antenna foot print to be more valid and the spatial resolution of soil moisture data is higher. However, in order to use the near-field antenna model for digital soil mapping, model evaluation using both synthetic and realistic experiments under different conditions and different antenna types are necessary. Another important question is whether, for a given antenna height, we should use the near- or far-field GPR model. Although the near-field GPR model provides more accurate estimation, the far-field one is more effective in terms of computing resources. As a result, it is necessary to quantify the antenna height threshold at which the far-field model holds.

Conventional single channel GPR performs measurements in two typical configurations, namely single-offset and multi-offset. While the single-offset configuration can rapidly perform measurements, its information is insufficient to reconstruct the multi-layered medium, especially in the case lacking a clear reflector. The multi-offset configuration (e.g., CMP or WARR) can provide more layer information, but it is time-consuming for data acquisition. Recently, efforts have been made to design array GPR systems, which are composed of multiple element antennas [Sato et al., 2004; Yarovoy et al., 2007b; Gerhards et al., 2008; Pan et al., 2012]. The use of GPR array permits to simultaneously record several GPR datasets at different offsets in one measurement, and therefore, increases information content of the subsurface in GPR data. However, in these studies, GPR array data were still processed using simple methods, which use only a part of GPR information (e.g., electromagnetic travel time).

In order to increase the accuracy of soil moisture estimation, besides GPR modeling, another factor should be considered is the petrophysical relationship, that links soil moisture with electromagnetic properties. Common approaches usually employed the empirical equations (e.g., Topp et al. [1980]) to obtain soil moisture from electric permittivity. Although these empirical equations are widely used in geoscience, they are limited to the calibrated probe (e.g., TDR) and specific collected samples. The frequency dependence of the electric conductivity and electric permittivity was not accounted for [Wagner et al., 2011]. Therefore, a semi-theoretical approach, which can be applied globally, should be integrated into full-wave GPR inversion for more accurate soil moisture estimation.

The final issue mentioned in this thesis is coupling of the GPR model and hydrological model. In many hydrological studies and applications (e.g., groundwater recharge estimation, root water uptake or land-atmosphere interactions), surface soil moisture data are insufficient. Although the penetrating depth of GPR is larger than that of remote sensing techniques, it is still far away from the requirements of these studies. Moreover, in the full-wave GPR inverse problem, using 1-layer soil model suffers from large errors even in a controlled condition due to the vertical heterogeneity of soil moisture because of the hydraulic gradient effect. On the other hand, using multi-layered soil model can improve the soil moisture estimation but it encounters the ill-posedness of the inverse modeling due to too many unknown parameters and correlation between these parameters in the inverse problem. It is also not practical to frequently implement GPR measurements to obtain soil moisture data with a high temporal resolution. Consequently, it is necessary to improve the accuracy of soil moisture estimation for the deeper soil layers with a high spatiotemporal resolution. This problem can be effectively solved by coupling the GPR model with a soil hydrodynamic model in a data assimilation framework in which the hydrodynamic and the electromagnetic model regularize each other. Whenever GPR data are available, they are directly assimilated to correct the soil moisture prediction from the hydrodynamic model. Vice versa, the hydrodynamic model keeps the soil moisture derived from GPR inverse modeling at a physically reasonable value.

1.3 Thesis objectives

This thesis was implemented in the frameworks of three projects: (1) FSR-UCL: "*Development and integration of advanced ground penetrating radar and electromagnetic induction for soil hydrogeophysical characterization and monitoring to support sustainable and optimal management of soil and water resources*", (2) EU-FP7 "*DROPS: Drought-tolerant yielding plants*", and

(3) ARC-UCL, which aims at "*increasing our understanding of soil organic matter dynamics in complex landscapes and use this to improve predictions of regional scale soil carbon balances*". Within these frameworks, the objectives of the thesis are calibrating and validating the new near-field GPR model developed by Lambot and André [2013] for soil moisture characterization, and integrating the GPR model into the hydrodynamic model to estimate soil hydraulic properties and characterize soil moisture profile dynamics. To implement these general objectives, the following issues have been addressed:

1. To numerically evaluate the near-field antenna model for the reconstruction of planar layered media.
2. To determine the antenna height threshold under which the near-field model is necessary (or above which the far-field model holds).
3. To take into account the frequency dependence of the electric permittivity and apparent conductivity of soil in the full-wave GPR inverse modeling to increase the accuracy of soil moisture estimation.
4. To validate the near-field antenna model and estimate the soil moisture of a sandy soil layer in laboratory conditions.
5. To develop a novel calibration algorithm for the full-wave GPR array characterization.
6. To directly assimilate GPR data into a hydrological model to estimate the soil hydraulic parameters and improve the soil moisture profile prediction.

1.4 Thesis outline

To present the results that implement the objectives mentioned in the previous section, the thesis was structured into 9 chapters and linked together as outlined in Figure 1.1. Linkages between the chapters are represented by the arrows in which the black ones represent the links established in this study and the red denotes the works that will be implemented in the future. Chapter 1 introduces the general context, research topic and problem statement of the thesis, while conclusion remarks and perspectives of the future research are presented in Chapter 9. Main contents of the thesis are detailed in chapters from 2 to 8 as follows:

1. Chapter 2 describes the new near-field antenna model and the numerical evaluation results of this model using a FDTD antenna model

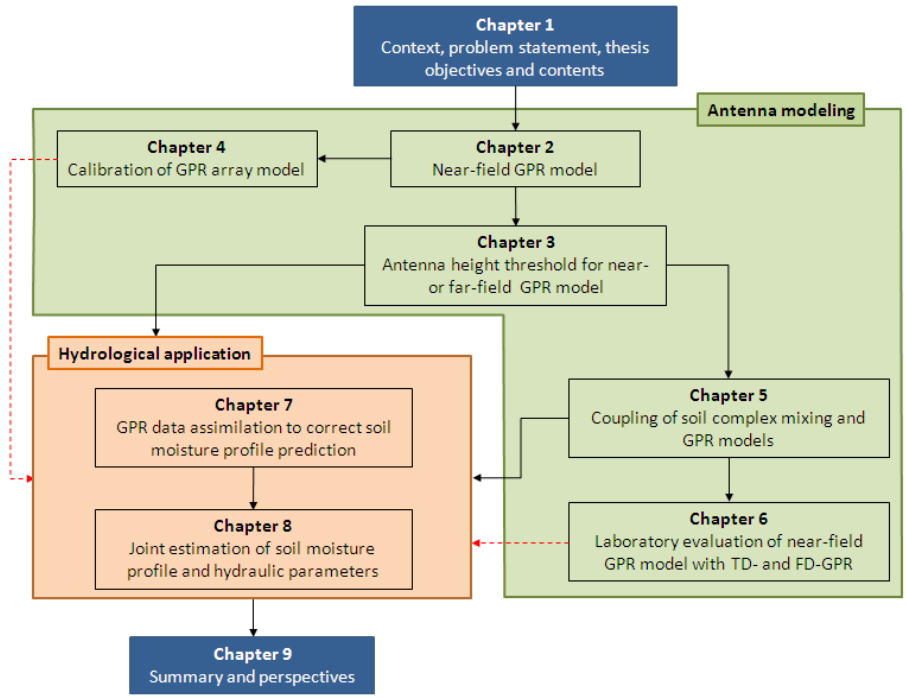

Figure 1.1. Flowchart for PhD thesis. The black arrows represent the links between chapters established in this study, and the red ones denote the works in the future.

(GprMax3D). The near-field GPR model is calibrated using numerical GPR data generated by GprMax3D model [Giannopoulos, 2005] above a synthetic perfect electric conductor (PEC). After that, the GrpMax-3D model was employed to create numerical GPR data above an artificial layered medium with different scenarios of antenna height, layering, thickness and electromagnetic properties. The calibrated near-field antenna model is evaluated by full-wave inversion of these GPR data to reproduce the electromagnetic properties of the medium. The near-field antenna model presented in this chapter is used in Chapters 3, 5 and 6.

2. Chapter 3 answers the following question: what is the antenna height threshold for the near- or far-field GPR model. This threshold is determined by analyzing the variation of the spatial derivatives of the Green's function over the antenna aperture as a function of the antenna height. A brief description of the electromagnetic wave propagation in planar layered media using Green's functions, analytical solution of Maxwell's equations, is also presented in this chapter. The outcome of this chapter is the basis for the selection of the near- or far-field antenna model based

on the antenna height in the other chapters.

3. Chapter 4 presents a novel optimization approach to calibrate the GPR array full-wave model. The arrays are considered as a combination of several couples of transmitting-receiving antennas with different offsets in which each couple is modeled by the near-field antenna model in Chapter 2. The calibration approach is based on the progressively-completing model approach in which the results obtained from the simplified GPR array model are used as initial guesses for the complicated one for a good initial values. Linear and nonlinear optimization algorithms are also combined to reduce the number of unknown parameters for the model calibration. The approach is preliminary tested by calibrating the model of a two-element antenna array with different offsets.

4. Chapter 5 couples the soil dielectric mixing model with the full-wave GPR inverse modeling. The approach allows to account for the frequency dependence of the electric permittivity and apparent electric conductivity via the water component, whose electromagnetic properties are linked to the frequency by Debye's equation. We validate the approach by laboratory experiments with sand. The approach is applied for the research in Chapters 6 and 8. The far-field antenna model in the chapter is also used in Chapters 7 and 8.

5. Chapter 6 shows the validation results of the near-field antenna model for estimating the electromagnetic properties and correlated moisture of a sand using both frequency and time domain radars. The characteristic transfer functions of antennas were determined using measurements with the antenna at different distances, from near- to far-field conditions, from a copper plane. The model and its calibrated transfer functions were validated by inverting GPR data to predict the moisture of a sand layer subject to different levels of saturation. The effect of the hydraulic gradient on the vertical heterogeneity of soil is also shown. This effect is accounted for by applying the multi-layered soil model which is based on the retention curve function of van Genuchten [1980]. A more effective approach to solve this problem is proposed in Chapters 7 and 8.

6. Chapter 7 introduces a closed-loop data assimilation procedure based on the maximum likelihood ensemble filter algorithm (MLEF) to update the vertical soil moisture profile from time-lapse GPR data. A hydrodynamic model is used to propagate the system state in time and the antenna model and petrophysical relationships to link the state variable with the observation data, which enables us to directly assimilate the

GPR data. Instead of using the surface soil moisture only, the approach allows one to use the information of the whole soil moisture profile for the assimilation to take advantage of deeper intrusion depth of GPR than the remote sensing techniques. The data assimilation framework developed in this chapter is expanded in chapter 8 for simultaneously estimating soil moisture and hydraulic parameters.

7. Chapter 8 explores the possibility of the GPR data assimilation to solve the case where both initial moisture conditions and model parameters are unknown. The assimilation framework in Chapter 7 is modified by combining the MLEF algorithm and the state augment approach to simultaneously estimate the model state and parameters, instead of only soil moisture like in Chapter 7. The advantage of the direct GPR data assimilation is also proved by comparing it with the surface soil moisture data assimilation. Future research will use data obtained from the near-field GPR and/or array to provide more information about soil moisture profile for the data assimilation.

Chapter 2

Numerical evaluation of a full-wave antenna model for near-field applications *

Abstract In this study, we numerically evaluated a full-wave antenna model for near-field conditions using a Finite-Difference Time-Domain (FDTD) antenna model. The antenna is effectively characterized by a series of source and field points and reflection/transmission transfer functions which, by using analytical solutions of Maxwell's equations, enable us to significantly reduce computation times compared to numerical approaches. The full-wave GPR model was calibrated by a series of radar data from numerical measurements performed above an infinite perfect electric conductor (PEC). The calibration results provided a very good agreement with data from the FDTD antenna model giving a correlation coefficient of 0.9995. The model was subsequently verified by using it to invert responses from the FDTD antenna model to reconstruct the electric properties of an artificial medium subject to 8 scenarios of layering, thickness and electric properties. Full-wave inverse modeling enabled us to very well reproduce the GPR data both in time and frequency domains, resulting in accurate estimations of the electric permittivity. The relative errors of the permittivity estimation were less than 5% for all medium scenarios and antenna heights. Inversion also provided very good estimations of the electric conductivity when this parameter was relatively high, but poor results were obtained for low conductivities. Response surface analysis showed that the model was more sensitive to permittivity than conductivity, and more sensitive to high than low conductivities. Our modeling approach shows great potential to apply full-wave inversion for retrieving the electric properties of the subsurface from near- and far-field radar measurements.

*Adapted from A. P. Tran, C. Warren, F. André, A. Giannopoulos, and S. Lambot, Numerical Evaluation of a Full-wave Antenna Model for Near-field Applications, *Near Surface Geophysics*, 11(2), 155-165, doi: 10.3997/1873-0604.2012052, 2013.

2.1 Introduction

Over the past 20 years, Ground-Penetrating Radar (GPR) has been constantly developed to become one of the most popular noninvasive techniques to apply for environmental and geotechnical engineering, sedimentology, glaciology and archaeology. However, the accuracy of the GPR application for the characterization of a medium is usually limited due to difficulties in modeling the GPR-medium system which contains two sub-systems of different size: the antenna and medium [Farnoosh et al., 2008]. While it is still impossible to analytically solve Maxwell's equations for this complex system, many efforts have been made to find an approximate solution. In general, they can be classified as into three approaches: differential equations, integral equations, and simplified analytical solutions. The first approach discretizes the volume of the computational space into grids to find approximate numerical solutions of Maxwell's equations using Finite-Element Time Domain (FETD) [Chen and Huang, 1998; Davit, 2007; Durand and Slodic, 2011] or Finite-Difference Time Domain (FDTD) models [Giannopoulos, 2005; Ghasemi and Abrishamian, 2007; Atteia and Hussein, 2010; Warren and Giannopoulos, 2011]. However, these models have not been able to properly describe the actual radar data due to inherent discrepancies between the real and conceptualized antenna model configurations. Another drawback of these methods are that they require excessive computing time, which causes many difficulties for inverse modeling using commonly available computing resources to estimate the electric properties of a medium.

Integration techniques use the electric field integral equation (EFIE) to characterize the antenna [Craeye et al., 2004; Chen et al., 2010]. Method of moments (MoM) is then employed to approximate the integral equation problem by a linear system of basic functions and their associated expansion coefficients. Once the expansion coefficients are known, the current distribution and radiation characteristics of the antenna can be determined. In order to account for the effects of the reflected electric field from the lossy half-spaces, the EFIE was modified by adding the reflected wave component [Fernández-Pantoja et al., 2009]. In comparison with the differential approach, the integral equation approach is more effective in characterizing the antenna system, but a limitation of this approach is its inability to consider the multiple reflections between antenna and medium. Recently, in order to take advantages as well as overcome the drawbacks of integration and numerical approaches in modeling different parts of the problem, several authors have used a hybrid technique that combines the MoM to describe the antenna, with a differential equation approach to model the medium [Huang et al., 1999; Farnoosh et al., 2008].

A third approach has been followed based on the idea that as media are

situated in the far-field region of the antenna, Maxwell's equations can be simplified and solved analytically. Gentili and Spagnolini [2000] modeled a GPR horn antenna at some distance over a three-dimensional (3-D) layered medium using an array of frequency independent source dipoles and a feeding line characteristic impedance. The multiple reflections between the antenna terminal section and the target were neglected. Lambot et al. [2004c] assumed that in the far-field conditions, a horn antenna can be modeled by one point source-receiver for wave propagation in planar layered media. The authors used reflection and transmission transfer functions to characterize the antenna, and a Green's function–exact analytical solutions of Maxwell's equations to simulate wave propagation in planar layered media. Nevertheless, due to the far-field assumption, the GPR energy transmitted into the medium is relatively small, which limits the application of the method only for materials with low absorption properties or shallow reflections [Holger, 2008]. In addition, the relative large antenna footprint when the medium is in the far-field region of the antenna may cause the assumption of the planar homogeneity to be violated. Consequently, for increasing backscattered GPR signals and decreasing antenna footprint for a higher spatial resolution, it is necessary to develop an antenna model that can properly work in near-field conditions.

Lambot and André [2013] generalized the far-field antenna model so that it can work in both near- and far-field conditions. Because it was based on the analytical solutions of Maxwell's equations, compared to numerical models, the computation time of this model was considerably reduced. The authors verified the model in laboratory conditions with water from near- to far-field and observed that the model provided unprecedented accuracy for describing experimental data.

In this study, we further evaluate the near-field, full-wave antenna model of Lambot and André [2013] by inverting GPR data generated from a FDTD antenna model to retrieve the electric properties of an artificial medium with several thicknesses and antenna heights. Accordingly, we assumed that the actual radar configuration is exactly described by the FDTD antenna model, and this model is used to perform numerical experiments above artificial media with known electric properties. The near-field, full-wave antenna model uses these signals to calibrate the antenna and predict the electric properties of the medium.

2.2 Near-field, full-wave GPR model

As the medium is located in the near-field region of the antenna, the assumption of a local plane wave over the antenna aperture does not hold any more [Lambot et al., 2004c; Lopera et al., 2007b]. The scattered field distribution

depends on the antenna distance and medium properties. An effective approach for capturing the scattered field distribution is to consider an equivalent set of infinitesimal electric dipoles ($J_{x,n}$, $n = 1 \cdots N$) for the source and a set of points ($E_{x,m}$, $m = 1 \cdots N$) where the field is calculated for the receiver. With this approximation, the antenna waves in the near-field region can be decomposed into planar waves, allowing to describe the antenna using a limited number of characteristic reflection and transmission transfer functions using the superposition principle. Similar to the far-field model [Lambot et al., 2004c], the wave propagation between source or field points and the reference plane of the radar transmission line is characterized by transmission and reflections transfer functions, which in particular permits to account for the antenna-medium coupling. However, unlike the far-field model, where the antenna is modeled by only one source/field point, the interactions among the multiple source and field points make the near-field model much more complicated. When a wave is transmitted from a point source to the medium, the reflected wave from the medium can come to all field points. In turn, the wave at the field points partly is transmitted to the antenna reference plane and the remaining is reflected back to the medium, forming damped infinite transmission-reflection loops between the medium and field points. The above interactions between the radar reference plane and the source-medium-field points can be formulated in the frequency domain as follows [Lambot and André, 2013]:

$$S = \frac{b}{a} = T_0 + T_s(\mathbf{I_N} - \mathbf{G_0}\mathbf{R_s})^{-1}\mathbf{G}T_i \tag{2.1}$$

with

$$T_s = \begin{bmatrix} T_{s,1} & T_{s,2} & \cdots & T_{s,N} \end{bmatrix} \tag{2.2}$$

$$\mathbf{R_s} = \begin{bmatrix} R_{s,1} & 0 & \cdots & 0 \\ 0 & R_{s,2} & \cdots & 0 \\ \vdots & \vdots & & \vdots \\ 0 & 0 & \cdots & R_{s,N} \end{bmatrix} \tag{2.3}$$

$$T_i = \begin{bmatrix} T_{i,1} & T_{i,2} & \cdots & T_{i,N} \end{bmatrix}^T \tag{2.4}$$

$$\mathbf{G_0} = \begin{bmatrix} G^0_{11} & G^0_{12} & \cdots & G^0_{1N} \\ G^0_{21} & G^0_{22} & \cdots & G^0_{2N} \\ \vdots & \vdots & & \vdots \\ G^0_{N1} & G^0_{N2} & \cdots & G^0_{NN} \end{bmatrix} \tag{2.5}$$

and

$$\mathbf{G} = \begin{bmatrix} G_{11} & G_{12} & \cdots & G_{1N} \\ G_{21} & G_{22} & \cdots & G_{2N} \\ \vdots & \vdots & & \vdots \\ G_{N1} & G_{N2} & \cdots & G_{NN} \end{bmatrix} \tag{2.6}$$

where $S(\omega)$ denotes the ratio between the backscattered field $b(\omega)$ and incident field $a(\omega)$; $T_0(\omega)$ is the transmission or reflection transfer functions of antenna in free space for source-receiver. This function quantifies the return loss within the antenna and does not depend on the backscattered electric field from a medium. $T_{i,k}(\omega)$ is the transmission transfer function for field incident from the radar reference plane onto the point source k^{th} and describes the frequency dependent antenna gain and phase delay between the measured point (radar reference plane) and the point sources. $T_{s,k}(\omega)$ denotes the transmission transfer function for field incident from the field point k^{th} onto the radar reference plane, describing the antenna gain and phase delay between the field points and measured point; and $R_{s,k}(\omega)$ is the reflection transfer function for the field incident from the layered medium onto the field point k^{th}, thereby inherently accounting for multiple wave reflections between the antenna and medium. Subscripts k ($k = 1, ...N$) denote the index of point sources or field points that are used to model the antennas. N is the total number of point sources or field points. $G_{ij}(\omega)$ and $G^0_{ij}(\omega)$ are the layered Green's functions for fields incident from field point i^{th} to source point j^{th}, and field points i^{th} to field point j^{th}, respectively. They are defined as the backscattered x-directed component of electric field for a unit-strength x-directed electric current source [Lambot et al., 2004c] and calculated by using a recursive scheme to compute the reflection transfer functions of the layered medium in the spectral domain [Chew, 1990; Michalski and Mosig, 1997; Slob and Fokkema, 2002].

2.3 Numerical experiments using data from a FDTD antenna model

GprMax3D is part of a suite of electromagnetic simulation software, developed by Giannopoulos [2005] originally in 1996, which is particularly suited to modeling GPR. GprMax3D is based on the FDTD method and approximates Maxwell's equations to simulate the propagation of electromagnetic waves in different media. The software has been widely used for various applications [Galagedara et al., 2005b; Warren and Giannopoulos, 2011]. In this study we used an antenna model developed using GprMax3D to perform numerical experiments above a layer. The antenna model was developed based on the 1.5 GHz bowtie antenna from GPR manufacturer Geophysical Survey Systems, Inc. (GSSI, Salem, Massachusetts, USA). Figure 2.1a shows a mesh of the FDTD antenna model, highlighting all of the modeled components and figure 2.1b shows the time domain representation of the excitation pulse and the power spectral density in dB. The excitation pulse has a Gaussian shape with a center frequency of 1.71GHz, and a pulse width of 0.5845 ns. A cell size of 1 mm was used for the model with a time step of 1.926 ps, and a time window

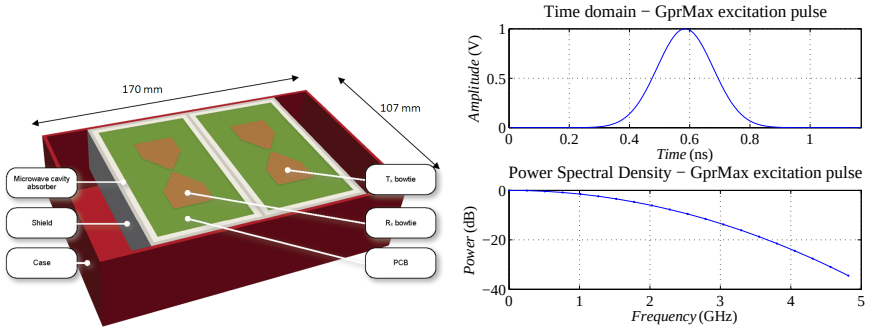

(a) (b)

Figure 2.1. (a) FDTD mesh of GSSI 1.5 GHz antenna model (modified from Warren and Giannopoulos [2011]); (b) Time domain excitation pulse and power spectral density used in FDTD simulation.

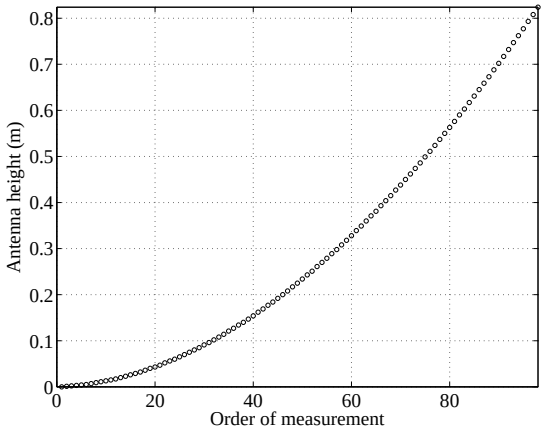

Figure 2.2. Antenna height for the calibration as a function of the measurement order.

of 50 ns. A full description of the process and results from the development of the antenna model can be found in Warren and Giannopoulos [2011].

For calibrating the near-field antenna model, 98 numerical measurements corresponding to antenna heights from 0 to 0.824 m above an infinite PEC were generated from the FDTD antenna model. This configuration was chosen for its simplicity, and the fact that the scattered fields are exactly known. Figure 2.2 shows the exponential distribution of the 98 antenna height measurements that were made. The antenna was raised with small height steps in the near-field region to increase the density of measurements and with larger height steps in the far-field region.

For verification of the near-field antenna model, 8 scenarios of layering, thickness, and electric properties were chosen to represent reality. Table 2.1

Table 2.1. Information on synthesis experimental setup.

Experiment	Number of layers	Layer thickness	electric properties
Scenario 1	1 layer	h_1=5 cm	ε_r=4.5; σ=0.0015 S/m
Scenario 2	1 layer	h_1=5 cm	ε_r=11.2; σ=0.095 S/m
Scenario 3	1 layer	h_1=15 cm	ε_r=4.5; σ=0.0015 S/m
Scenario 4	1 layer	h_1=15 cm	ε_r=11.2; σ=0.095 S/m
Scenario 5	2 layer	h_1=5 cm	ε_{1r}=4.5; σ_1=0.0015 S/m
		h_2=5 cm	ε_{2r}=11.2; σ_2=0.095 S/m
Scenario 6	2 layer	h_1=15 cm	ε_{1r}=11.2; σ_1=0.095 S/m
		h_2=15 cm	ε_{2r}=4.5; σ_2=0.0015 S/m
Scenario 7	2 layer	h_1=5 cm	ε_{1r}=4.5; σ_1=0.0015 S/m
		h_2=15 cm	ε_{2r}=11.2; σ_2=0.095 S/m
Scenario 8	2 layer	h_1=5 cm	ε_{1r}=11.2; σ_1=0.095 S/m
		h_2=15 cm	ε_{2r}=4.5; σ_2=0.0015 S/m

outlines the parameters that were used for each scenario. Based on these parameters, we obtained numerical GPR responses from the FDTD antenna model, which were subsequently used by the near-field model to reconstruct the medium. In all scenarios, the lower boundary was controlled by a PEC. For the 1-layered scenarios, we tested our model with two configurations of the electric properties: low permittivity and conductivity (scenarios 1 and 3), and high permittivity and conductivity (scenarios 2 and 4). The layers had thicknesses of 5 cm (scenarios 1, 2) and 15 cm (scenarios 3, 4), respectively. Highly contrasting electric properties were chosen for the 2-layer scenarios. In total 64 numerical experiments were conducted, and in all cases the antenna was situated at heights of 2, 2.5, 3, 3.5, 4, 5, 8, and 10 cm, respectively.

2.4 Determination of transmission and reflection transfer functions

In order to apply Equation (2.1) for inverse modeling to estimate the electric properties of a medium, the antenna transfer functions ($T.$, $Ts.$, $Rs.$) must be known. This can be done by inversely solving Equation (2.1) for a known layered medium for which the Green's functions $G_{..}$ and $G^0_{..}$ can be calculated and S(ω) can be performed. Determination of the antenna transfer functions is a non-linear inverse problem. As there are too many unknown calibration parameters, it is not easy to acquire the optimal values for these parameters with common optimization strategies. The specific strategy that was applied to this inverse problem is described in Lambot and André [2013]. Firstly, based on the far-field data, the optimization approach for the linear inverse problem as presented in Lambot et al. [2006a] to estimate the transmission and reflection

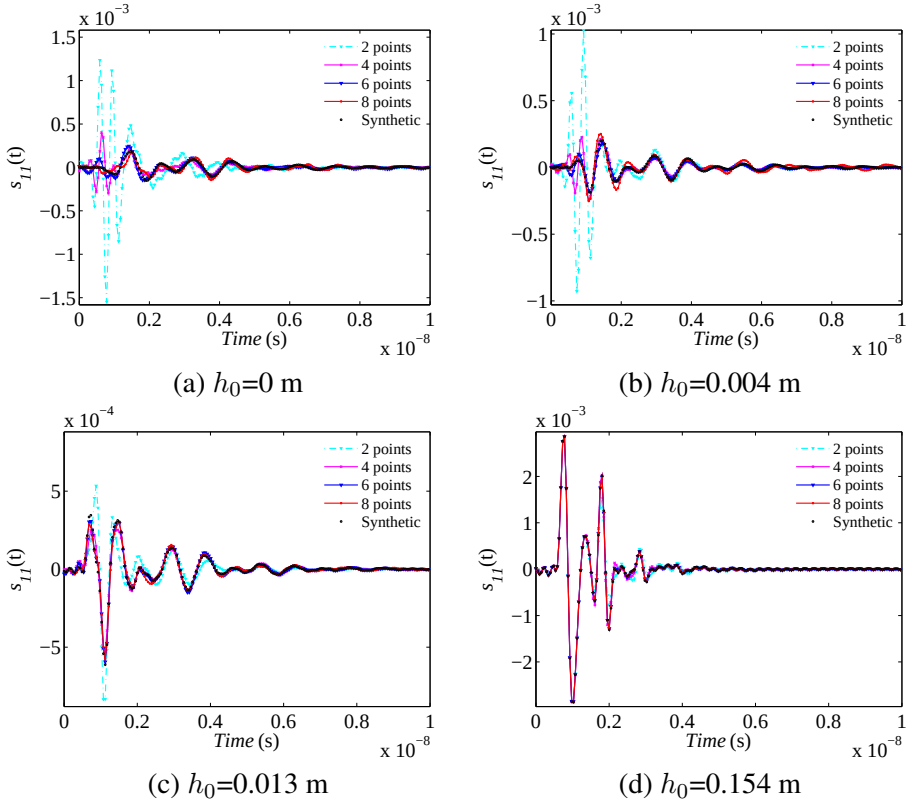

Figure 2.3. Comparison of calibrated GPR data with different number of points to characterize the antennas and measured GPR data at several antenna heights.

transfer functions in the far-field conditions is used. These functions are then used to constrain the near-field calibration problem. Once the optimal transfer functions are found for the first frequency, they are used as initial guesses for estimating the functions for the next frequency using a local optimization algorithm.

We used the synthetic data obtained from the FDTD antenna model above the PEC to calibrate the transfer functions. In these experiments, the medium was modeled as two layers by the near-field antenna model, in which the upper layer (air) had a electric permittivity of 1 and conductivity of 0 S/m, and the lower layer was assumed as a PEC. The thickness of the air layer varied with the antenna height. In order to select a suitable number of sources/receivers, we modeled the antennas by 2-, 4-, 6- and 8-point configurations, and then calibrated the antenna Equation (2.1) for each configuration. Figure 2.3 compares the performance of the GPR model with these configurations in comparison with synthetic GPR data at antenna heights of 0, 0.004, 0.013 and 0.154 m. The figure shows that at antenna heights of 0 and 0.004 m, the calibrated GPR

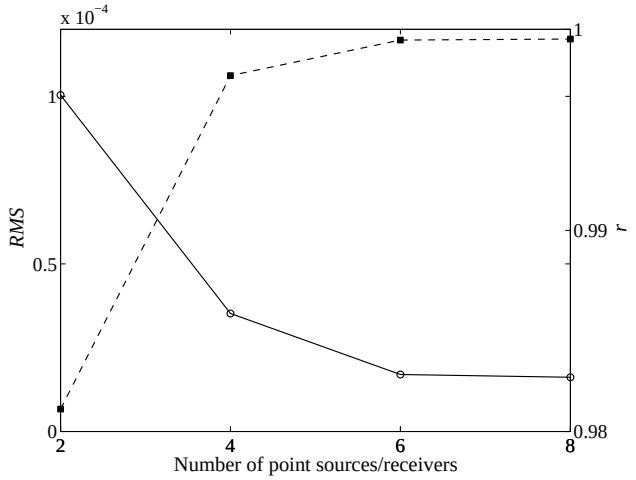

Figure 2.4. The dependence of the r and RMS between modeled and optimized data on numbers of point sources/receivers. The calculation was performed for 98 data points at different antenna heights.

data of the 6- and 8-point are much better than those of the 2- and 4-point antenna. When the antenna height increases to 0.013 m, although the performance of the 6- and 8-point antenna is still better, the differences between these 2 configurations with the 4-point configuration are invisible. The performance of 2-point antenna is also much improved at an antenna of 0.013 m. When the antenna height is 0.154 m, all of the antenna configurations agree very well with each other and with synthetic GPR data.

Figure 2.4 plots the cross correlation coefficient (r) and root mean square error (RMS) between modeled and optimized GPR data as a function of number of sources/receivers. It shows that as the number of sources/receivers characterizing the antennas increases from 2 to 4 points, the correlation between modeled and optimized signals increases rapidly. However, this increase is reduced considerably when the number of sources/receivers increases from 4 to 6 points, and there is negligible improvement in the correlation coefficients obtained from the 6- and 8-point configurations (r increases from 0.99946 to 0.99951). As the number of source/receivers increases from 2 to 6 points, the RMS decreases quickly from 0.1×10^{-3} to 0.017×10^{-3}. However, this criterion shows a minor change as the antennas are characterized by 6 and 8 sources/receivers (RMS =0.017×10^{-3} and 0.0162×10^{-3}, respectively). In brief, the agreement between measured and modeled is very good as the number of sources/receivers is equal to 6 points and there is no noticeable improvement when the antennas are described by more than 6 points (in this specific case). On the other hand, when the number of sources/receivers rises, the

number of transmission and reflection transfer functions of the antenna model quickly increases. This makes the antenna calibration to be much more difficult and increases the computational time of inversion. Consequently, in this study, we used the configuration with 6 point sources/receivers and its transmission/reflection transfer functions to describe the antenna behaviors.

Figure 2.6 presents the GPR data generated by the FDTD antenna model and those obtained from calibrating the near-field full-wave model with the antenna above a PEC at different levels. The constant horizontal lines in Figure 2.6a and 2.6b represent the direct coupling between the transmitter and the receiver. Below the direct signals are the first order reflected signals whose travel time increase with increasing antenna height. The other signals under the first order reflections are multiple reflections between the antenna and the PEC. It should be noted that when the antenna height is less than 1 cm, the reflected signals from the PEC surface and the direct signals arrive at almost the same time, and therefore cannot be easily separately distinguished. Figure 2.6b shows that the near-field model has been calibrated to account for these effects. Figure 2.6c shows that most of the errors appear at the PEC reflection and multiple reflection between the antenna and PEC, indicating that the transfer functions $R_{s,\cdot}$ might not well determined.

2.5 Reconstruction of layered media by near-field antenna model

Based on the data obtained from the FDTD antenna model, we applied near-field full-wave inverse modeling to reproduce the GPR signals and predict the electric permittivity and conductivity of the 1- and 2-layered scenarios at different antenna heights. Figure 2.5 illustrates the setup of the numerical experiments. We used 3 layers (air, dielectric layer and PEC) to model the 1-layered dielectric medium scenarios and 4 layers (air, dielectric layer 1, dielectric layer 2 and PEC) for the 2-layered medium scenarios, in which the electric permittivity and conductivity of air and PEC were known. To control the number of parameters, we also assumed that the thickness of the dielectric layer was already known. Accordingly, there were 3 unknown parameters (the antenna height (h_0), electric permittivity (ε_r) and conductivity (σ) for the 1-layered scenarios, and 5 parameters (h_0, ε_{1r} σ_1, ε_{2r}, σ_2) for the 2-layered scenarios. The unknown parameters were found by using the global multilevel coordinate search (GMCS) optimization algorithm [Huyer and Neumaier, 1999] combined with the Nelder-Mead Simplex algorithm in the frequency domain [Lambot et al., 2002]. By minimizing the difference between the FDTD antenna model data and the near-field model data, the parameters could be obtained. The parameter space for the global searching was set from 50% to

150% of the true values.

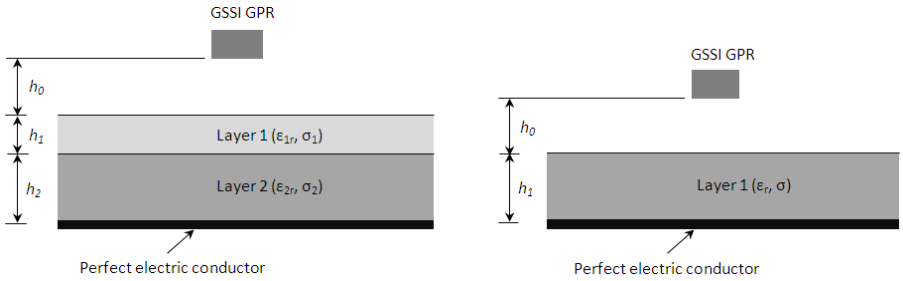

Figure 2.5. Illustration of the numerical experiment setup which includes the artificial GSSI GPR (centre frequency of 1.5 GHz), the perfect electric conductor and the 1-layered (right) and 2-layered (left) dielectric medium.

Due to the fact that the FDTD antenna model data is in the time domain and near-field model is solved in the frequency domain, the FDTD data was transformed into the frequency domain by the Discrete Fourier transform. The frequency range for inversion was selected to satisfy the conditions, namely, 1) the difference between the original time domain signals and those converted back from the frequency to time domain was negligible; and 2) the frequency range was as short as possible to minimize the computation time. According to these conditions, we used a frequency range of 200-4000 MHz with a step of 20 MHz.

Figure 2.7 shows the modeled and optimized GPR data in both time and frequency domains for the scenarios 2 (1-layered medium) and 5 (2-layered medium) at antenna heights of 2.5 and 8 cm. The results indicate that the near-field full-wave GPR model can reproduce very well the GPR signals synthetically generated by the FDTD antenna model in both time and frequency domains at two antenna heights. In the time domain, the full-wave model is able to accurately predict the main reflections both in arrival time and amplitude. We can see that the antenna couplings are visible at around 0.75–1 ns in all figures, indicating the constant transmitting velocity of the direct couplings and distance between two antennas. The upper layer reflections are difficult to detect at both antenna heights as they couple with the antenna couplings. The reflections from the PEC appear respectively at 2.1 and 2.4 ns when the antenna is situated at 2.5 cm and 8 cm for the 1-layer scenario, and at 2.8 ns and 3.1 ns for the 2-layered scenario. For the 2-layered scenario, we also observed the reflections from the upper–lower layer boundary at 1.7 and 2 ns for antenna heights of 2.5 and 8 cm, respectively. The figure also shows that the amplitudes of the reflections from the PEC and upper–lower boundary (for the 2-layered scenario) are reduced as the antenna height increases, due to the fact that less electromagnetic energy is able to penetrate into the layered media.

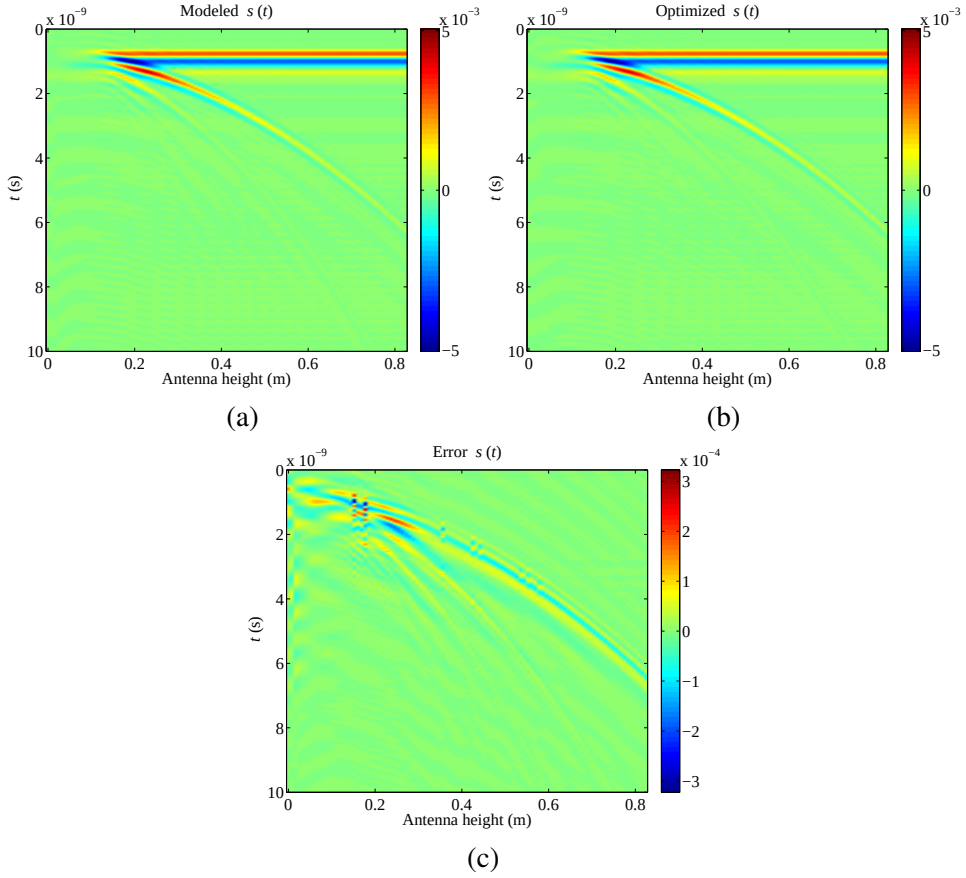

Figure 2.6. Modeled (a), optimized (b) data and the difference between them (c) in the time domain for calibration stage with antenna located at different heights above a PEC. Modeled data were generated from the FDTD antenna model.

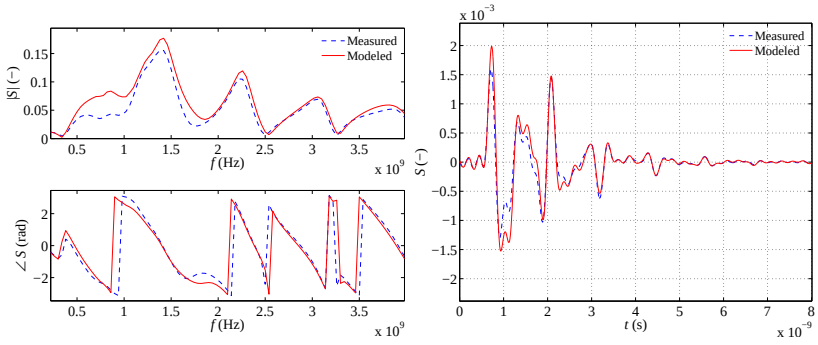

(a) h_0=2.5 cm; h_1=5 cm; ε_r=11.2; σ=0.095 S/m

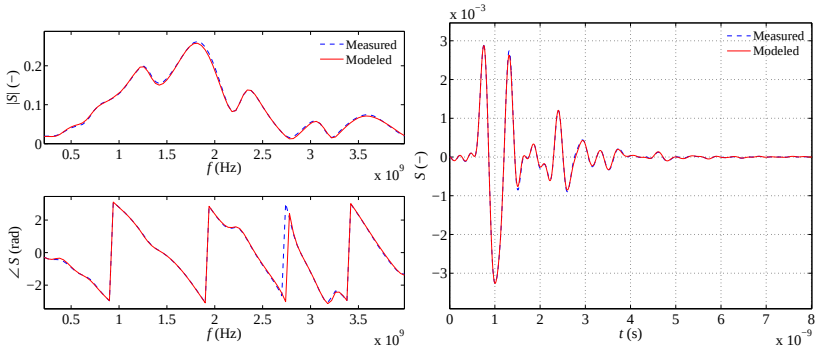

(b) h_0=8 cm; h_1=5 cm; ε_r=11.2; σ=0.095 S/m

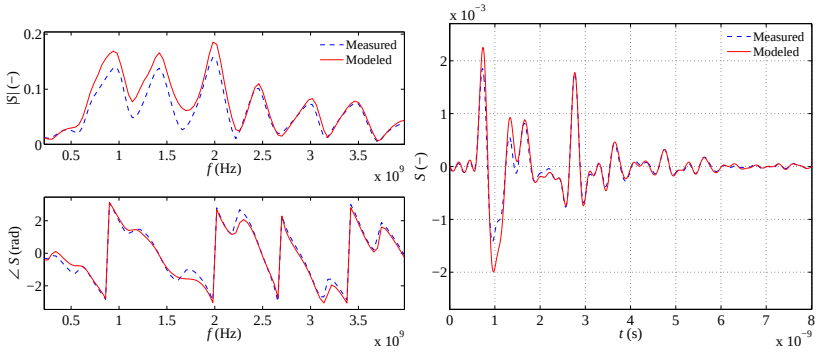

(c) h_0=2.5 cm; h_1=5 cm; ε_1=4.5; σ_1=0.0015 S/m; h_2=5 cm; ε_2=11.2; σ_2=0.095 S/m

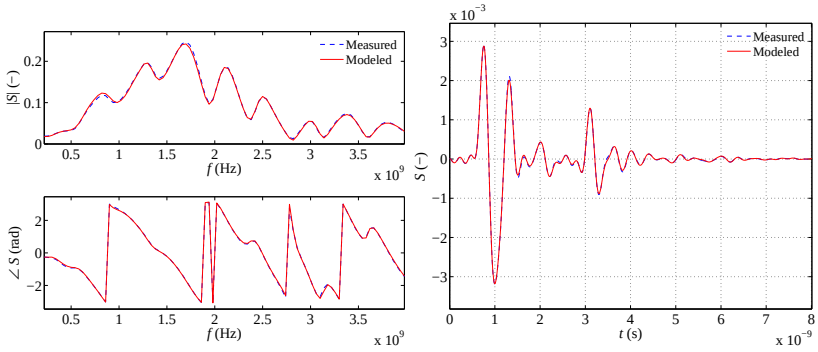

(d) h_0=8 cm; h_1=5 cm; ε_1=4.5; σ_1=0.0015 S/m; h_2=5 cm; ε_2=11.2; σ_2=0.095 S/m

Figure 2.7. Modeled and optimized GPR signals S(ω) at antenna heights of 2.5 (a, c) and 8 cm (b, d) in both the frequency and time domains for scenario 2 (h_1 = 5 cm; ε_r = 11.2; σ = 0.095 S/m) (a, b) and scenario 5 (h_1 = 5 cm; ε_{1r} = 4.5; σ_1 = 0.0015 S/m; h_2 = 5 cm; ε_{2r} = 11.2; σ_2 = 0.095 S/m) (c, d).

Compared to the data obtained at the antenna height of 2.5 cm, our model performs better at the antenna height of 8 cm. At the antenna height of 2.5 cm, there are some gaps between the magnitudes of the model and optimization for both scenarios in the frequency range of 0.5-1.8 GHz in the frequency domain. However, at the antenna height of 8 cm, the optimized and modeled signals match perfectly. In the time domain, while discrepancies with respect to the amplitude between modeled and optimized GPR data are visible around 1–2 ns at the antenna height of 2.5 cm, we cannot observe any differences between them at the antenna height of 8 cm. This might be explained from the fact that as the antenna is near the medium, characterization of the antennas by 6 point sources/receivers is inadequate to approximate the radar wave as a combination of planar waves, and that the performance of such antenna calibration is reduced as the antenna approaches the medium surface (see Figure 2.3). It is worth noting that both calibration and inversion rely on the outcomes of FDTD model, thus the errors of FDTD model might also contribute to less accuracy of our model at the smaller antenna height.

Figure 2.8 presents the relative errors of the optimized permittivities and conductivities as a function of the antenna height. We can observe that the optimized permittivities are in excellent agreement with the modeled values. The relative errors between modeled and optimized permittivities in all scenarios are less than 5%. Regarding the conductivity, it is clear that there are two groups of relative errors depending on the value of the conductivity. With the higher conductivities (0.095 S/m), the gaps between the modeled and optimized values are quite small with most of the relative errors less than 10%. However, the errors are much larger for the lower conductivity (0.0015 S/m), many greater than 30% and some tending to go to the upper and lower limits of the selected range (50 - 150% true value). The reason for this can be attributed to the sensitivity of the Green's function to conductivity (especially low values) for this antenna configuration. Low conductivity is also a reason for high relative errors, although absolute errors are small.

Figure 2.8 also shows that, in general, the relative errors increase as the antenna approaches the medium surface. This stems from the fact that the discrepancy between the FDTD antenna model and the near-field antenna model increases with the decreasing antenna height. The FDTD antenna model used the FDTD scheme to model the antennas and media, and describes the wave propagation in the media as well as medium - antenna interactions by numerically solving the Maxwell's equations. The near-field antenna model generalizes the analytical solution of the Maxwell's equations for the far-field condition by using a number of sources and field points to characterize the antennas. Wave propagation in the media is simulated by the Green's function and the interactions between the media and antennas are described by the system of equations (Equation (2.1)) with the transmission and reflection transfer func-

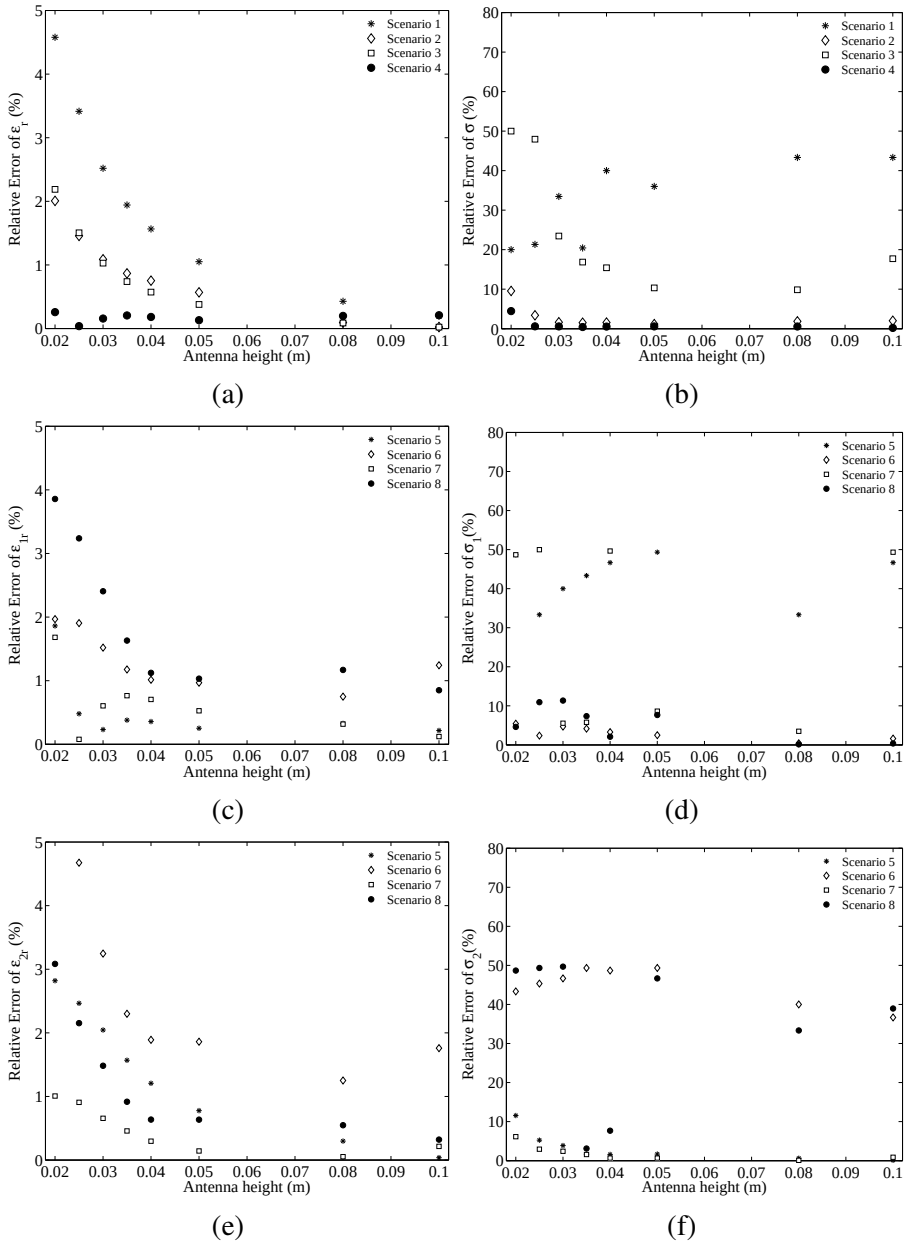

Figure 2.8. Relative errors of the optimized electric properties in relationship with the antenna height for the 1-layered scenarios (a, b), upper (c, d) and lower layer (e, f) of the 2-layered scenarios.

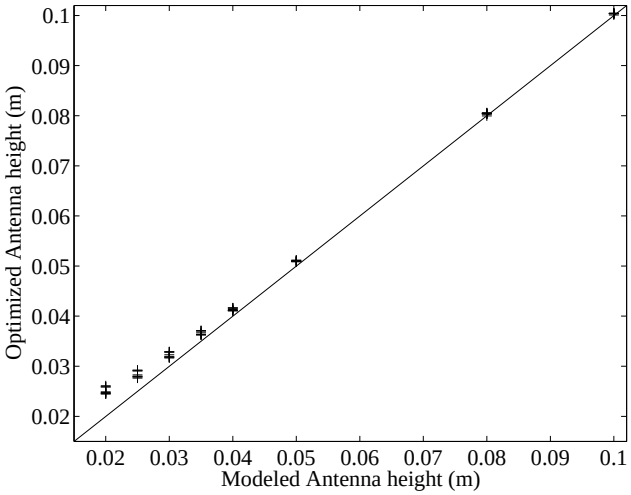

Figure 2.9. Comparison of the modeled antenna heights and those derived from near-field full-wave inversion.

tions. Thus, as the antenna height reduces, 6 point sources and receivers are not sufficient to characterize the antenna, causing less accuracy of the estimated electric properties.

Figure 2.9 compares the antenna heights used by the FDTD antenna model with those derived from GPR signal inversion. It shows that for each of the antenna heights the optimized antenna heights are slightly overestimated but approximately identical in all scenarios. Similar to the optimized electric permittivity and conductivity, the difference between model and optimization lessens with increasing antenna height. As shown in Figure 2.9, the largest difference is found at the height of 2 cm with errors around 4-6 mm for all of the scenarios. However, when the antenna is at a height of 5 cm, the error reduces rapidly to 0.9-1.2 mm, and when the antenna is at heights of 8 and 10 cm, the difference between model and optimization is negligible.

2.6 Response surface analysis

The response surface analysis of the objective function is a necessary part of the inversion procedure because it provides an insight into the dependence of a model on its parameters. Through the response surface analysis, we can also qualitatively evaluate the parameter sensitivity as well as the uniqueness of the inversion. By perturbing pairs of the parameters in the range from 50% to 150% of the true values while holding the other parameters constant, the variations of the objective function in relationship to the parameters can be estimated. Acknowledging that the objective function responds similarly to

all antenna heights, in this chapter, we present our analysis for an antenna height of 4 cm. We demonstrate the analysis on the topography of the objective function in relation to the electric permittivity and conductivity for 1-layered scenarios (1-4), and the electric permittivities of the upper and lower layers for 2-layered scenarios (5-8).

Figure 2.10a-d shows, in a 2-D σ–ε_r plane, the variations of the objective functions for 1-layered scenarios. In general, it can be seen that the objective function reduces rapidly as the electric permittivities approach the true values, which is explained by the high sensitivity of the Green's function to the electric permittivity. Thus, very accurate electric permittivities are obtained by inverting GPR data. In contrast, the objective function does not change very much when the conductivity varies in the selected parameter range (50 - 150% of true value). Especially, as the permittivities are in the neighboring region of their true values, it is difficult to observe the variation of the objective function with respect to the conductivity. This implies that the Green's function is not very sensitive to the conductivity and the contribution of the permittivity to the electromagnetic model is much higher than the conductivity in these scenarios. As a result, the optimized conductivities are less accurate than the permitivities. The figures also show that the Green's function is more sensitive to the high conductivity (0.095 S/m) than low conductivity (0.0015 S/m), which makes the estimation of the high conductivity more accurate.

In the ε_{1r}–ε_{2r} plane (Figure 2.10e-h) which depicts the response surface to the variation of the upper and lower electric permittivities, the topography of the objective function is more complicated with more local minima compared with the ε–σ plane. This can be attributed to the configuration of the 2-layered scenarios with contrasting electric properties, which makes the shape of the obtained Green's function more complex. However, very good approximations are obtained, indicating that the global optimization algorithm can successfully obtain the correct parameters. The response surface is relatively sensitive with the permittivity of both upper and lower layers. Figure 2.10 also shows the effect of the layer thickness on the response surface topography. All scenarios show that there are more local minima in the topography of the objective function with the thicker layer, making the optimization more difficult. Again, the Green's function, which becomes more complex with increasing layer thickness, is the reason for this fact.

2.7 Conclusions

In this chapter, we evaluated the recently developed full-wave GPR model, which can be applied for both near- and far-field scenarios by using it to reproduce GPR data generated from a FDTD antenna model and reconstruct the

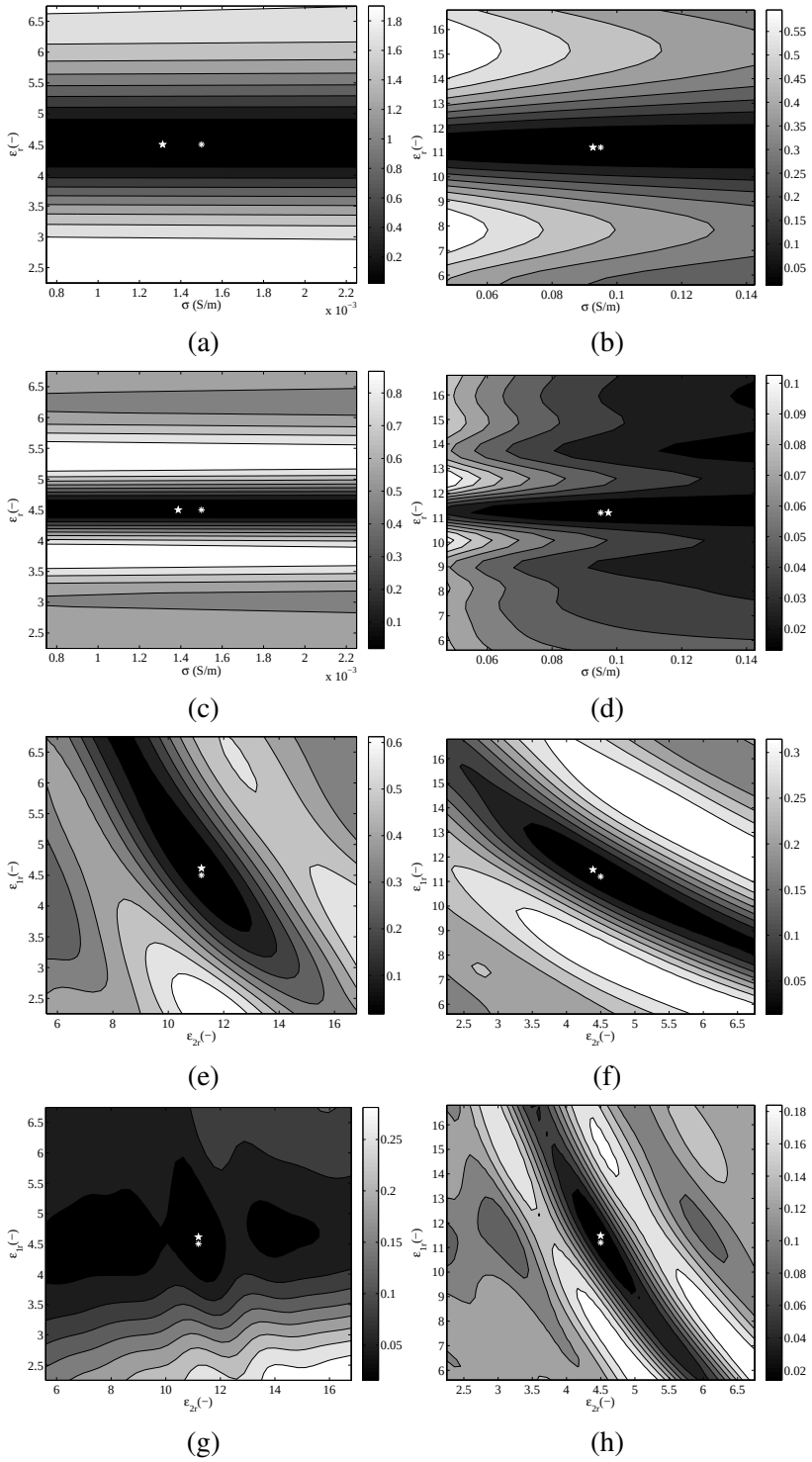

Figure 2.10. Response surface of the objective functions with pairs of parameters in 8 scenarios. White asterisk and star markers represent the locations of the optimized and true values, respectively. The objective function is depicted in the σ–ε_r coordinates (a, b, c, d) for the 1-layered scenarios (1-4), and in ε_{1r}–ε_{2r} coordinates (e, f, g, h) for the 2-layered scenarios (5-8). Calculations were based on an antenna height of 4 cm.

electric properties of layered media. The calibration results above an artificial PEC show that the two models match well with the correlation coefficient of approximately 1. We then employed the calibrated model to estimate the electric properties of a synthetic medium subject to 8 scenarios of layering, thickness and electric properties to represent most of the realistic cases. Very good agreements with the modeled values were obtained for the electric permittivity (less than 5%) and high conductivity (less than 10%) in all scenarios. However, for the low conductivity, the inversion could not provide reliable results. Response surface analysis of the objective function pointed out that the insensitivity of the Green's function to the low conductivity is the reason for this problem. It is worth noting that as the antenna approaches the medium surface, agreements between the FDTD antenna model and the full-wave GPR model, as well as between modeled and optimized parameters reduce. This is due to the fact that the use of 6 point sources/receivers to describe the antenna behavior is insufficient for such distances.

By using the Green's function to simulate wave propagation in layered media, our near-field model is more effective in terms of computing time than the numerical models to quantitatively investigate the electric properties of the medium by full-wave inverse modeling. Furthermore, the obtained results also imply that the model can reproduce well the GPR signals and accurately estimate the parameters of the layers with different scenarios. This indicates that the model is suitable for real world applications. Future research will focus on finding more effective strategies for calibrating transfer functions as well as implementing our model for field conditions to investigate hydro-geophysical properties of soil in a digital soil mapping context. In addition, the proposed radar method appears to be a very promising solution for non-destructive testing of materials in general.

Chapter 3

Near-field or far-field full-wave ground-penetrating radar modeling as a function of the antenna height above a planar layered medium *

Abstract The selection of a near-field or far-field ground-penetrating radar (GPR) model is an important question for an accurate but computationally effective characterization of medium electric properties using full-wave inverse modeling. We determined an antenna height threshold for the near-field and far-field full-wave GPR models by analyzing the variation of the spatial derivatives of the Green's function over the antenna aperture. The obtained results showed that the ratio of this threshold to the maximum dimension of the antenna aperture is approximately equal to 1.2. Subsequently, we validated the finding threshold through numerical and laboratory experiments using a homemade 1–3 GHz Vivaldi antenna with an aperture of 24 cm. For the numerical experiments, we compared the synthetic GPR data generated from several scenarios of layered medium using both near-field and far-field antenna models. The results indicated that above the antenna height threshold, the near-field and far-field GPR data perfectly agreed. For the laboratory experiments, we conducted GPR measurements at different antenna heights above a water layer. The near-field model performed better for antenna heights smaller than the threshold value ($\approx$ 29 cm), while both models had similar results for larger heights. Next, we expanded the problem by determining the antenna height threshold as a function of the number of source/field points that characterizes the antenna. This study provides valuable insights to specify the antenna height threshold above which the far-field model can be used for a given antenna.

*Adapted from A. P. Tran, F. André, C. Craeye, and S. Lambot, Near-field or far-field full-wave ground penetrating radar modeling as a function of the antenna height above a planar layered medium, *Progress in Electromagnetic Research* , 141, 415-430, 2013.

3.1 Introduction

Over the last two decades, ground-penetrating radar (GPR) has become an advanced non-destructive technique that is widely used in geoscience [Steelman and Endres, 2012], archeology [Papadopoulos et al., 2009] and civil engineering [Pettinelli et al., 2009; Crocco et al., 2010]. However, most of the existing techniques rely on strong simplifications concerning the wave propagation and antenna mutual coupling, which inherently limits the GPR effectiveness. Recently, with developments in computational technology, efforts have been made to model the antenna by numerical methods, e.g., finite difference time domain (FDTD) [Ernst et al., 2007; Atteia and Hussein, 2010], or method of moments (MoM) [Fernández-Pantoja et al., 2009]. Yet, simultaneous modeling of the antennas and medium is still a challenge for these methods due to the different spatial resolution requirements of the two domains. It is also difficult to apply these methods in inverse modeling frameworks for the fact that they require a significant computation time.

For significant decreasing computation time, Lambot et al. [2004c] developed a far-field antenna model to characterize planar layered media, which accounts for the antenna effects through transmission/reflection transfer functions. The wave propagation in planar layered media is simulated using 3-D Green's function. Nevertheless, the model requires the antenna to be situated far enough from the medium to satisfy the far-field assumption. Lambot and André [2013] generalized the far-field model so that it also applies to near-field conditions while still resorting to an analytical, closed-form solution of Maxwell's equations. The model was successfully validated in laboratory conditions. Comparison between this model and a FDTD-based model (GprMax, Giannopoulos [2005]) was recently evaluated by Tran et al. [2013c].

Although the near-field GPR model provides more accurate estimations, the far-field one is more effective in terms of computation time. However, it is not clear to which extent of the antenna height, the far-field GPR model holds. As a result, it is necessary to find an antenna height threshold for the selection of the GPR model depending on the antenna location. In this study, we theoretically estimate the antenna height threshold by analyzing the partial derivatives of the Green's function over the antenna aperture. Then, this threshold is validated by comparing the near- and far-field GPR models using both numerical and laboratory experiments. Finally, we expand the problem by investigating the relationship between the antenna height threshold and the number of source/field points that characterizes the antenna.

3.2 Theory

3.2.1 Green's function

The propagation of electromagnetic waves in planar layered media can be simulated by the Green's functions, which are solutions of Maxwell's equations. In our case, the Green's functions are defined as the scattered x-directed electric field at the field point for a unit-strength x-directed electric source [Slob and Fokkema, 2002; Lambot et al., 2004c]. In the spectral domain, the Green's function at the source point is written as below:

$$\tilde{G}_{..} = \left[\cos^2(k_\theta)\left(\frac{\Gamma_0 R_0^{TM}}{2\eta_0} + \frac{\zeta_0 R_0^{TE}}{2\Gamma_0}\right) - \frac{\zeta_0 R_0^{TE}}{2\Gamma_0}\right]\exp(-2\Gamma_0 h_0) \quad (3.1)$$

in which $G_{..}$ is the Green's function with dots (..) referring the field and the source points, respectively; k_θ is the spectral-domain angular coordinate in the polar coordinate system; R_0^{TM} and R_0^{TE} are the transverse magnetic (TM) and electric (TE) global reflection coefficients at the free-space interface accounting for all reflections from the N-layered medium. These coefficients are determined by using an upward recursive scheme as below:

$$R_n^{TE} = \frac{r_n^{TE} + R_{n+1}^{TE}\exp(-2\Gamma_2 h_{n+1})}{1 + r_n^{TE} R_{n+1}^{TE}\exp(-2\Gamma_{n+1} h_{n+1})} \quad (3.2)$$

$$R_n^{TM} = \frac{r_n^{TM} + R_{n+1}^{TM}\exp(-2\Gamma_{n+1} h_{n+1})}{1 + r_n^{TM} R_{n+1}^{TM}\exp(-2\Gamma_{n+1} h_{n+1})} \quad (3.3)$$

$$r_n^{TE} = \frac{\mu_{n+1}\Gamma_n - \mu_n\Gamma_{n+1}}{\mu_{n+1}\Gamma_1 + \mu_1\Gamma_{n+1}} \quad (3.4)$$

$$r_n^{TM} = \frac{\eta_{n+1}\Gamma_n - \eta_n\Gamma_{n+1}}{\eta_{n+1}\Gamma_n + \eta_n\Gamma_{n+1}} \quad (3.5)$$

where subscript n ($n = 0, \cdots, N-1$) denotes the index of the nth interface increasing from the top to bottom layer, in which $n = 0$ represents the upper half-space (free-space) interface; r_n^{TM} and r_n^{TE} are the TM- and TE- mode local reflection coefficients of the nth interface; h_n is the layer thickness with h_0 indicating the distance between the source/receiver points and the first medium interface; Γ_n is the vertical wavenumber defined as $\Gamma_n = \sqrt{k_\rho^2 + \zeta_n\eta_n}$, whilst $\zeta_n = j\omega\mu_n$ and $\eta_n = \sigma_n + j\omega\varepsilon_n$ with μ_n, ε_n and σ_n are the electric permittivity, magnetic permeability and electric conductivity, respectively. For the upper half-space, we have $\Gamma_0 = \sqrt{k_\rho^2 - \left(\frac{\omega}{c}\right)^2}$ with c being the free-space wave velocity; k_ρ is the spectral-domain radial coordinate in the polar coordinate system.

The upward recursive scheme begins to calculate the TM and TE global reflection coefficients at the interface $(N-1)^{th}$ with $R_{N-1}^{TM} = r_{N-1}^{TM}$ and $R_{N-1}^{TE} = r_{N-1}^{TE}$ for the fact that there is no reflection from the lower half-space.

The spatial-domain Green's functions are obtained from their spectral-domain counterpart using the inverse Fourier transform:

$$G_{..} = \left(\frac{1}{2\pi}\right)^2 \int_0^{+\infty} \int_0^{2\pi} \exp[-j\rho\cos(\theta)k_\rho\cos(k_\theta) + \rho\sin(\theta)k_\rho\sin(k_\theta)]\tilde{G}_{..}k_\rho dk_\rho dk_\theta \quad (3.6)$$

By introducing the first kind Bessel functions $J_m(k_\rho\rho)$:

$$J_m(k_\rho\rho) = \frac{(-j)^{-m}}{2\pi}\int_0^{2\pi}\exp(-jk_\rho\rho cos(\varphi))cos(m\varphi)d\varphi \quad (3.7)$$

the 2-dimensional integral (3.6) can be reduced to a 1-dimensional one as below:

$$G_{..} = \frac{1}{8\pi}\int_0^{+\infty}\left[J_0(k_\rho\rho)\tilde{g}_1 - J_2(k_\rho\rho)\cos(2\theta)\tilde{g}_2\right]\exp\left(-2\Gamma_0 h_0\right)k_\rho dk_\rho \quad (3.8)$$

where

$$\tilde{g}_1 = \frac{\Gamma_0 R_0^{TM}}{\eta_0} - \frac{\zeta_0 R_0^{TE}}{\Gamma_0} \quad (3.9)$$

and

$$\tilde{g}_2 = \frac{\Gamma_0 R_0^{TM}}{\eta_0} + \frac{\zeta_0 R_0^{TE}}{\Gamma_0} \quad (3.10)$$

in which m denotes the order of the Bessel functions. $\rho = \sqrt{(\triangle x)^2 + (\triangle y)^2}$ and $\theta = \arctan(\frac{\triangle y}{\triangle x})$ with $\triangle x = x_{field} - x_{source}$ and $\triangle y = y_{field} - y_{source}$ are, respectively, the distance and angle between the source and field point in the polar coordinate system.

3.2.2 Partial derivative of Green's function

The relationship between the far-field threshold and the antenna aperture size was investigated by analyzing the variations of the backscattered field over the antenna aperture. Accordingly, we evaluated the partial derivatives of the Green's function with respect to the antenna spatial variables, namely, ρ and θ. If these derivatives are equal to zero, the Green's function is supposed to be constant everywhere in the region delineated by the antenna aperture and, therefore, the far-field assumption will be satisfied. From Equation (3.8), the derivatives are derived as:

$$\begin{aligned}\frac{\partial G_{..}}{\partial\rho} &= \frac{1}{8\pi}\frac{\partial}{\partial\rho}\int_0^{+\infty}\left[J_0(k_\rho\rho)\tilde{g}_1 - J_2(k_\rho\rho)\cos(2\theta)\tilde{g}_2\right]\exp\left(-2\Gamma_0 h_0\right)k_\rho dk_\rho \\ &= \frac{1}{8\pi}\int_0^{+\infty}\left[\frac{\partial J_0(k_\rho\rho)}{\partial\rho}\tilde{g}_1 - \frac{\partial J_2(k_\rho\rho)}{\partial\rho}\cos(2\theta)\tilde{g}_2\right]\exp\left(-2\Gamma_0 h_0\right)k_\rho dk_\rho\end{aligned} \quad (3.11)$$

$$\frac{\partial G_{..}}{\partial \theta} = \frac{1}{8\pi}\frac{\partial}{\partial \theta}\int_0^{+\infty} [J_0(k_\rho \rho)\tilde{g}_1 - J_2(k_\rho \rho)\cos(2\theta)\tilde{g}_2]\exp\left(-2\Gamma_0 h_0\right) k_\rho dk_\rho \quad (3.12)$$

It is worth noting that, in formula (3.11), only the Bessel functions J_0 and J_2 depend on ρ, and in formula (3.12), only the component $\cos(2\theta)$ depends on θ. After doing some rearrangements, we obtain:

$$\frac{\partial G_{..}}{\partial \rho} = \frac{1}{8\pi}\int_0^{+\infty} \{-J_1(k_\rho \rho)\tilde{g}_1 - \frac{1}{2}\tilde{g}_2\cos(2\theta)[J_1(k_\rho \rho) + J_3(k_\rho \rho)]\}\exp\left(-2\Gamma_0 h_0\right) k_\rho^2 dk_\rho \quad (3.13)$$

$$\frac{\partial G_{..}}{\partial \theta} = \frac{1}{4\pi}\int_0^{+\infty} J_2(k_\rho \rho)\tilde{g}_2\sin(2\theta)\exp\left(-2\Gamma_0 h_0\right) k_\rho dk_\rho \quad (3.14)$$

Formulas (3.13) and (3.14) indicate that the antenna height-dependent derivatives $\frac{\partial G_{..}}{\partial \rho}$ and $\frac{\partial G_{..}}{\partial \theta}$ are equal to zero only when the antenna height approaches the infinite, $h_0 \rightarrow +\infty$. This implies that the far-field condition cannot be perfectly satisfied with an finite value of h_0. Consequently, we attempted to find an antenna height at which both of the above derivatives are relatively small as a practical threshold for the far-field modeling.

3.2.3 Near-field and far-field antenna models

For validating the antenna height threshold, we compared the near- and far-field antenna models at different heights. The numerical and laboratory validations proved that the near-field antenna model works well in both near- and far-field conditions [Tran et al., 2013c; Lambot and André, 2013]. Consequently, the antenna height threshold for the far-field modeling can be verified if the behaviors of the near- and far-field antenna models are approximately identical at that threshold. The paragraphs below briefly present the two models:

Near-field antenna model: The near-field antenna model was proposed by Lambot and André [2013] to capture the scattered field distribution in both near- and far-field conditions. This model is presented in Chapter 2.

Far-field antenna model: When the far-field condition is satisfied, the scattered fields can be approximated by a plane wave. Hence, the antenna can be effectively characterized by an infinitesimal source/field point and transmission/reflection transfer functions T_0, T_1 and $R_{s,1}$ which simplifies Equation (2.1) to the far-field model of Lambot et al. [2004c]:

$$S(\omega) = T_0 + \frac{T_1 G_{11}^0}{1 - G_{11}^0 R_{s,1}} \quad (3.15)$$

It is apparent that the far-field model is much effective in terms of computation time than the near-field one for the fact that it has a more simple radar equation and less Green's function evaluation. Indeed, we only need to calculate the Green's function G^0_{11} in the far-field model, while all $G^0_{..}$ and $G_{..}$ need to be evaluated in the near-field model. The larger the number of source/field points, the longer computation time we need. Therefore, the far-field model should be applied when the far-field condition is satisfied.

3.3 Results and discussion

3.3.1 Antenna threshold for far-field antenna modeling

Figure 3.1 shows the amplitude of the spatial complex derivatives of the Green's function versus the antenna height and frequency. Our evaluation was performed for a synthetic 2-layered medium. The upper and lower electric properties of the medium were fixed to ε_{r1}=4, σ_1=0.0063 S/m and ε_{r2}=9, σ_2=0.0296 S/m, and their thicknesses were h_1=12 cm and h_2=15 cm, respectively.

We considered three antenna types: A homemade Vivaldi antenna, a linear polarized double-ridged horn antenna (BBHA 9120-F, Schwarzbeck Mess-Elektronik, Schönau, Germany) and a commercial bowtie antenna (400-MHz GSSI, Geophysical Survey Systems, Inc., *www.geophysical.com*). The Vivaldi antenna has an aperture of 24 cm and a height of 20 cm [Bhattacharya et al., 2010; Sarkis and Craeye, 2010]. It was operated in the frequency range 1-3.0 GHz with a frequency step of 8 MHz. The BBHA 9120-F antenna was operated in the frequency range 200-2000 MHz with a step of 6 MHz. Its aperture area is 68$\times$95 cm^2. The model 5103-400 MHz GSSI antenna works in the time domain with a center frequency f_c=400 MHz. The dipole spacing between the transmitter and receiver bowtie antennas is 16 cm and distance from the dipole to the edge of antenna housing is 6 cm. We selected the frequency range for this antenna from $f_c/2$ to $2f_c$ with a step 20 MHz. It is worth noting that the angular variable θ vanishes in the cases of the Vivaldi and BBHA 9120-F antennas as these two antennas act simultaneously as both transmitter and receiver.

In Figure 3.1, instead of using the antenna height, we used the ratio of the antenna height to the maximum dimension of the antenna aperture (h_0/D) to account for the dependence of the far-field antenna height threshold on the antenna aperture dimension. This ratio varies from 0 to 5 with a step of 0.1. The figure shows that, for all antenna types, the amplitudes of the partial derivatives of the Green's functions are negatively proportional to the antenna height. For selecting the near- or far-field antenna height threshold, we subjectively relied

on two criteria:

$$\begin{aligned}\sum_f \frac{\partial G(f, h_0^i/D)}{\partial \rho} \Big/ \frac{\partial G(f, h_0^{i+1}/D)}{\partial \rho} \leq 1.1 \\ \sum_f \frac{\partial G(f, h_0^i/D)}{\partial \theta} \Big/ \frac{\partial G(f, h_0^{i+1}/D)}{\partial \theta} \leq 1.1\end{aligned} \tag{3.16}$$

and

$$\begin{aligned}\sum_f \frac{\partial G(f, h_0^i/D)}{\partial \rho} \Big/ \frac{\partial G(f, h_0^1/D)}{\partial \rho} \leq 0.17 \\ \sum_f \frac{\partial G(f, h_0^i/D)}{\partial \theta} \Big/ \frac{\partial G(f, h_0^1/D)}{\partial \theta} \leq 0.17\end{aligned} \tag{3.17}$$

where the superscript i represents the derivatives of the Green's functions at the antenna height i^{th} and f is the frequency. The first criterion indicates that beyond the antenna height threshold, the Green's functions derivatives slowly decrease and the second one indicates that these derivatives are relatively small compared to those at 0 cm height. Based on these two criteria, the antenna height threshold are determined at $h_0 = 1.2D$. Figure 3.1 shows that the Green's functions derivatives quickly reduce when the antenna height increases from 0 to around $1.2D$. After that, they slowly approach zero when the antenna height continues increasing. Figure 3.1 also shows that the amplitudes of the derivatives is higher for the higher frequency, implying that the Green's functions fluctuate more with increasing frequency. Yet, the effect of frequency on the derivatives is especially pronounced for the small antenna heights, while it appears to be insignificant when the antenna height is larger than about $1.2D$. Similar results were also obtained for the other scenarios of the medium. As a result, we may consider the antenna height $h_0 = 1.2D$ as a threshold for the near-field and far-field full-wave GPR models.

3.4 Validation of the antenna height threshold

3.4.1 Numerical experiments

In this section, we validated the antenna height threshold determined in the previous section by comparing the near- and far-field models using numerical experiments. We constructed a synthetic medium with 1 and 2 layers on an infinite perfect electric conductor (PEC). For the 1-layered medium, the layer thickness is 15 cm and its relative electric permittivity and conductivity are, respectively, $\varepsilon_r = 9$ and $\sigma = 0.0296$ S/m. In the case of the 2-layered medium, we used a layer thickness of 12 cm for the first layer and 15 cm for the second

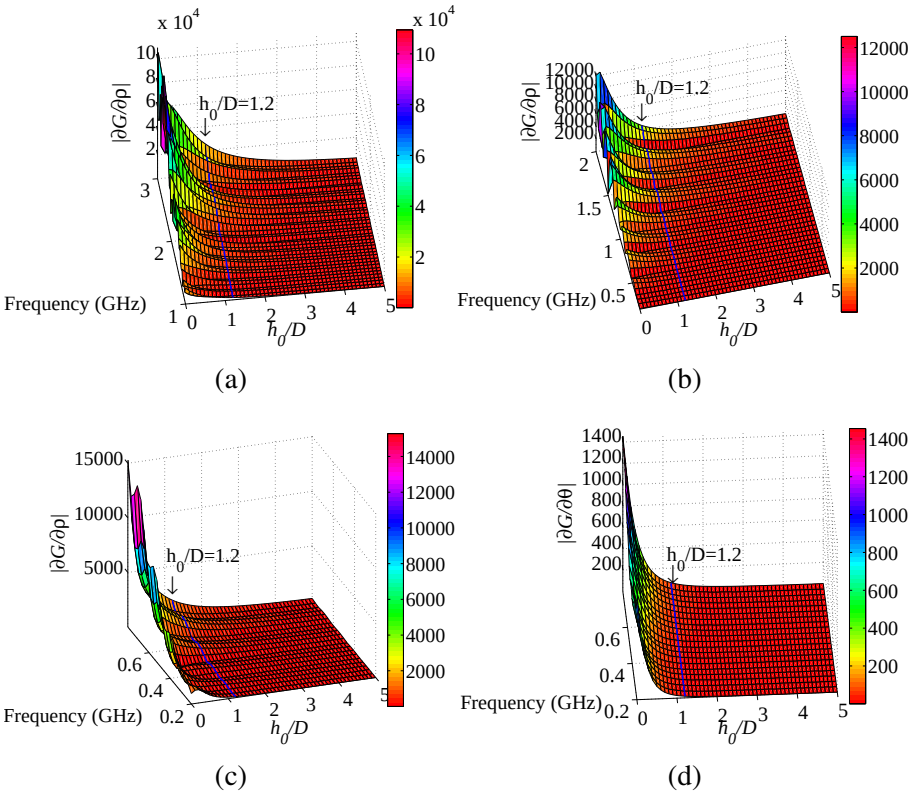

Figure 3.1. Derivatives of the Green's function with respect to the variables ρ (a, b, c) and θ (d) versus ratio of the antenna height to the maximum dimension of the antenna aperture (D) and frequency for the Vivaldi (a), BBHA 9120-F (b) and 400-MHz GSSI antennas (c,d). The analysis used the 2-layered medium with ε_{r1}=4, σ_1=0.0063 S/m, ε_{r2}=9, σ_2=0.0296 S/m, h_1=12 cm and h_2=15 cm.

layer. With respect to the electric properties of the medium, we considered two scenarios: scenario 1: $\varepsilon_{r1} = 4$, $\sigma_1 = 0.0063$ S/m, $\varepsilon_{r2} = 9$, $\sigma_2 = 0.0296$ S/m, and scenario 2: $\varepsilon_{r1} = 9$, $\sigma_1 = 0.0296$ S/m, $\varepsilon_{r2} = 4$, $\sigma_2 = 0.0063$ S/m.

We considered the Vivaldi antenna with the maximum aperture $D = 24$ cm, operating in a frequency range of 1–3.0 GHz and step of 8 MHz. In the near-field antenna model, the antenna is characterized by 6 source/field points and their associated transimission/reflection transfer functions. The transfer functions were obtained via the model calibration as presented in Chapter 6. Numerical comparison between the two models was performed at different antenna heights ranging from 0.1 to $2D$. Figure 3.2 presents the GPR data generated by these models for the 1- and 2-layered medium scenarios. On the left panel, the magnitude and phase of the near- and far-field GPR data at the antenna height threshold ($h_0 = 1.2D$) are shown. The figure indicates that for all scenarios, the phases of the far-field antenna GPR data perfectly agree with the near-field ones. In terms of the magnitude values, there are negligible differences between the two models, which is attributed to the errors of the transmission/reflection transfer functions. The quantitative comparison between their synthetic GPR data was evaluated by the sum of squared residuals (SSR):

$$SSR = |S_{11}^{FF} - S_{11}^{NF}|^T |S_{11}^{FF} - S_{11}^{NF}| \tag{3.18}$$

in which S_{11}^{NF} and S_{11}^{FF} are the complex near- and far-field GPR data vectors. The relationship between SSR and the antenna height is presented on the right panel of Figure 3.2. As expected, the discrepancy between the far- and near-field antenna models quickly decreases when the antenna height increases from $0.1D$ to $1.2D$. When the antenna height is larger $1.2D$, the difference is constant at around 0. This proves that the antenna height threshold $h_0 = 1.2D$ is suitable for the far-field modeling.

3.4.2 Laboratory validation

For more realistic comparison of the near- and far-field models in terms of both GPR signals and parameter estimation, we carried out GPR measurements above a water layer with a thickness of 4.9 cm on a copper plane as shown in Figure 3.3. The GPR system works in the frequency domain and consists of a stepped-frequency continuous-wave vector network analyzer (VNA, ZVRE, Rohde Schwarz, Munich, Germany) and a homemade single Vivaldi antenna. The VNA and Vivaldi antenna were connected to each other by a 50 Ω coaxial cable.

Measurements were conducted at 16 different antenna heights ranging from 0 cm to 70 cm. Temperature and electric conductivity of water were 17.2°C and 0.0806 S/m, respectively. The frequency dependence of the water complex permittivity was described by the Debye model [Debye, 1929]. The

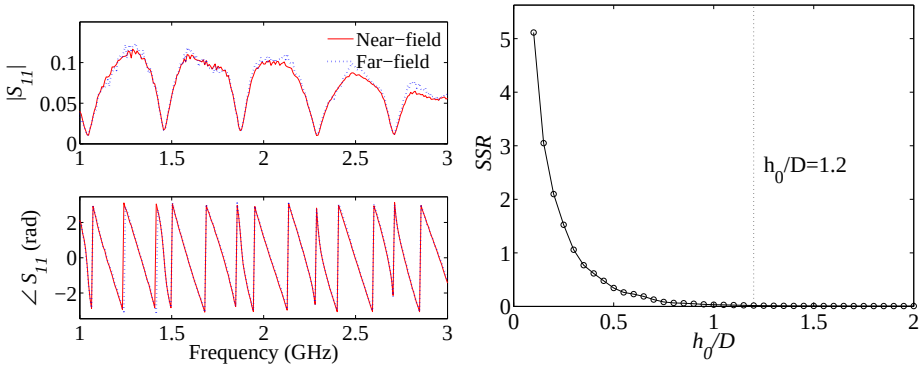

(a) 1-layered medium: $\varepsilon_r = 9$, $\sigma = 0.0296$ S/m

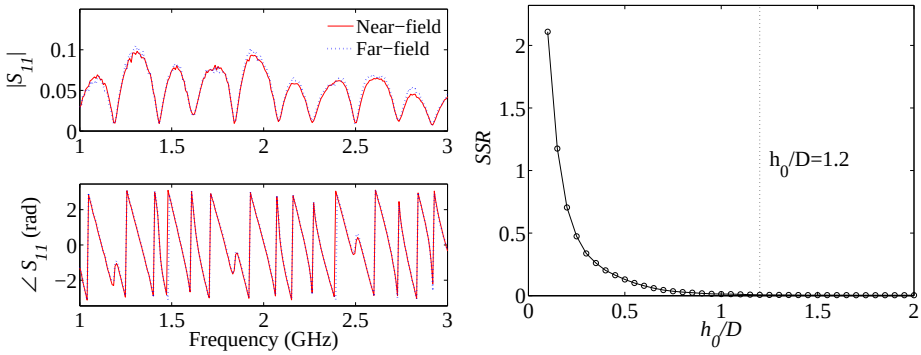

(b) 2-layered medium: $\varepsilon_{r1} = 4$, $\sigma_1 = 0.0063$ S/m, $\varepsilon_{r2} = 9$, $\sigma_2 = 0.0296$ S/m

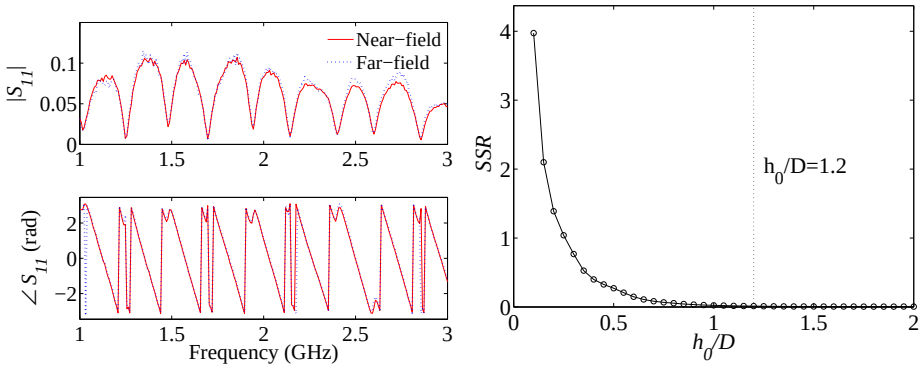

(c) 2-layered medium: $\varepsilon_{r1} = 9$, $\sigma_1 = 0.0296$ S/m, $\varepsilon_{r2} = 4$, $\sigma_2 = 0.0063$ S/m

Figure 3.2. Comparison of the GPR data (S_{11}) generated by the near- and far-field antenna models under different scenario of medium. The left panel shows the magnitude and phase of the near- and far-field GPR data at the antenna height threshold for the far-field modeling ($h_0 = 1.2D$ with D being the maximum dimension of the antenna aperture). The right panel presents the sum of squared residuals (SSR) between near- and far-field GPR data as a function of the antenna height.

relationship between the water temperature and the relaxation time was formulated by the Klein and Swift [Klein and Swift, 1977] equation, and between the temperature and the static permittivity by Stogryn's equation [Stogryn, 1970].

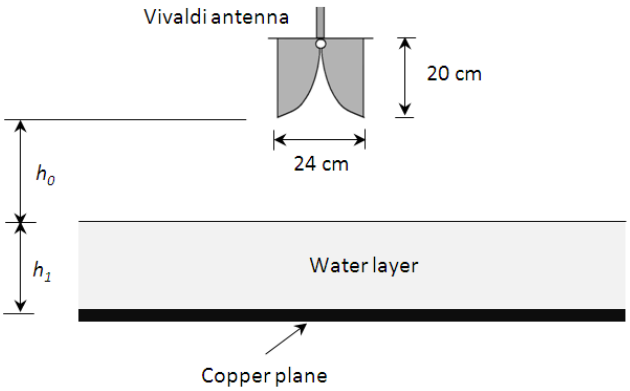

Figure 3.3. Laboratory experimental setup including the water layer, the Vivaldi antenna, and the copper plane working as a perfect electric conductor. The thickness of water layer was 4.9 cm, and the antenna was situated at heights from 0 cm to 70 cm.

The antenna height and water thickness were considered as unknowns in this experiment. These variables were estimated at each antenna height by inverse modeling of GPR data using both near- and far-field models. The parameter space for the water thickness was [2.5,7.5] cm and extended from 50% to 150% of the measured values for the antenna height.

Figure 3.4 compares frequency-domain modeled GPR data obtained by the two models with measured ones at several heights from 0 to 29 cm. The near-field model reproduces very well the measured GPR data for all antenna heights. There are only small discrepancies in the range 1.7–2.2 GHz for an antenna height of 0 cm. In contrast, the agreement between far-field modeled and measured GPR data is not good as that observed for the near-field one. However, the difference between them considerably reduces as the antenna height increases. For antenna heights of 0 and 5 cm, the measurements are not well reproduced by the far-field model. For antenna heights of 10 and 15 cm, although there are still some small gaps between far-field modeled and measured data, their difference significantly decreases. At 20 cm, the differences are negligible and at 29 cm ($1.2D$), we cannot differentiate the far-field GPR data from the near-field and measured ones.

Figure 3.5 shows the variation of the SSR for the near- and far-field GPR models versus the antenna height. The figure excludes the SSR values corresponding with the antenna height equal to 0 cm because it is very large for the far-field model. When the antenna increases from 5 to 29 cm, while the SSR for the near-field model is constantly very small, that of the far-field model sig-

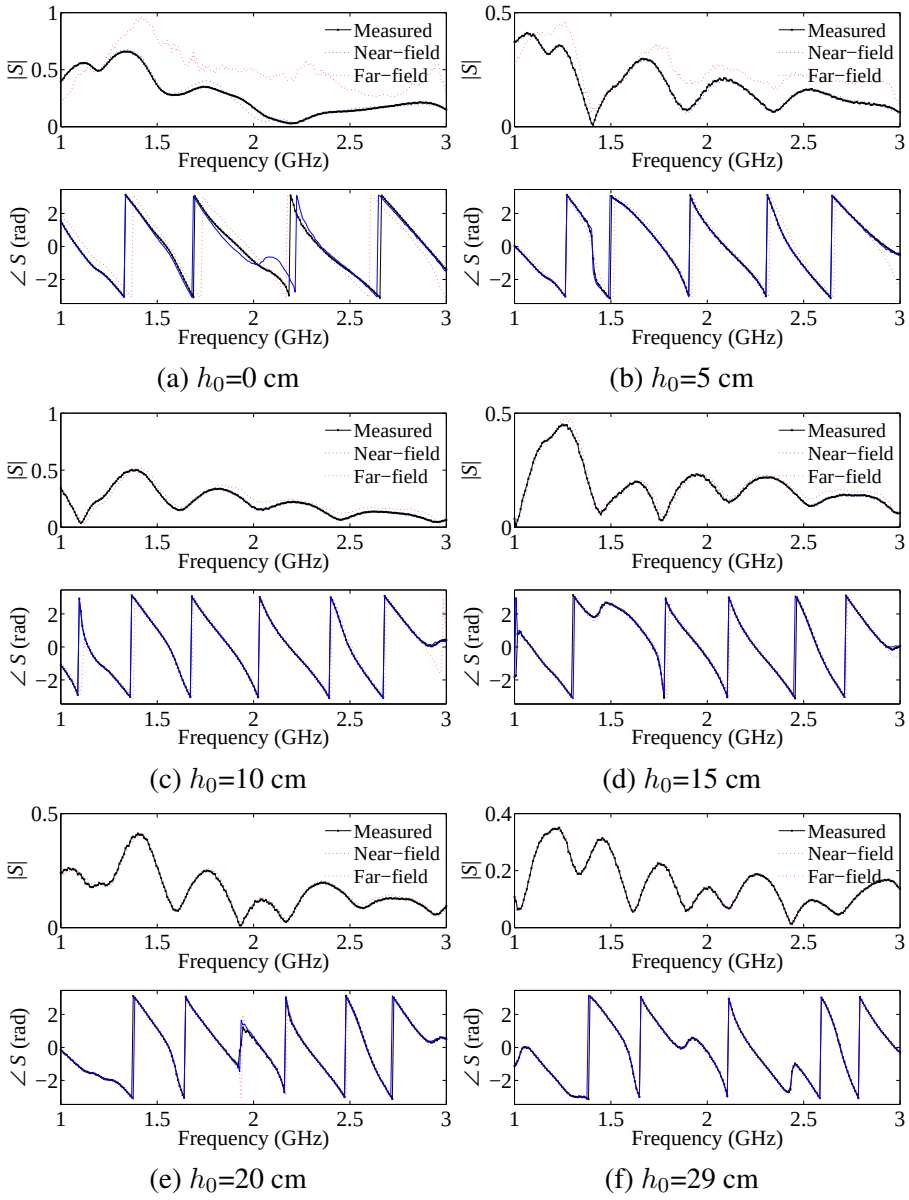

Figure 3.4. Comparison of the magnitude and phase of the near-field and far-field modeled GPR data with measured ones in the frequency domain domain at antenna heights of 0, 5, 10, 15, 20 and 29 cm.

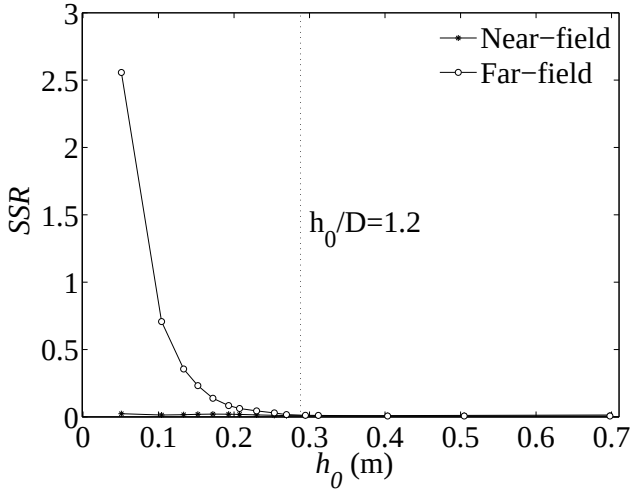

Figure 3.5. The SSR corresponding with the near- and far-field GPR models at different antenna heights.

nificantly decreases. When the antenna height is greater than 29 cm, the SSR of both models is identical and nearly equal to 0. This strengthens our findings that the antenna height $h_0 = 1.2D$ is a suitable threshold for the far-field modeling.

Figure 3.6 compares the antenna height and water thickness estimated by the two models and their measured counterparts. The figure shows that the near-field model perfectly reproduces the antenna height and water thickness at all antenna heights. The high accuracy of the estimated parameters and very close agreement of modeled and measured GPR data prove the correctness of the near-field model and proper determination of its transmission/reflection functions. Therefore, this model can be used for characterization of the medium properties in both near- and far-field conditions. As for the far-field model, accurate results are also obtained for antenna heights greater than or equal to 5 cm. However, when the antenna contacts with the water surface, the estimated antenna height and water thickness are no longer reasonable. It is worth noting that although the SSR of the far-field model increases significantly when the antenna moves from 29 cm down to 5 cm, the parameter estimation is still accurate. This might be explained by the small number of unknown parameters and high sensitivity of GPR data to these parameters.

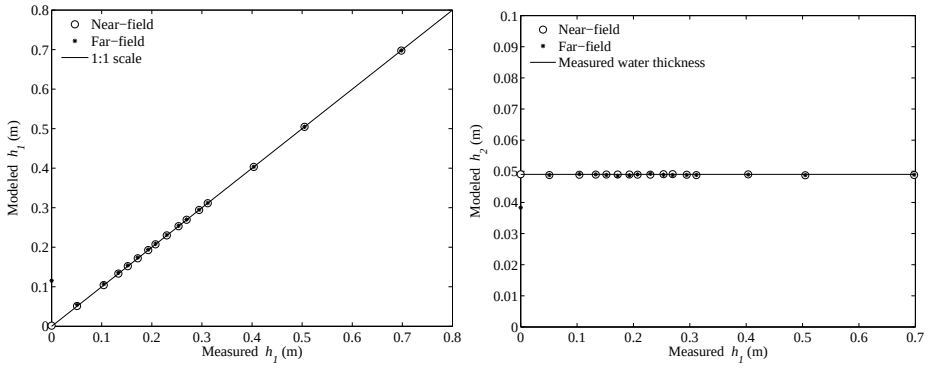

Figure 3.6. Comparison of measured and modeled antenna height (a) and water thickness (b). The circle and asterisk markers describe the values estimated by near-field and far-field model, respectively.

3.5 Antenna height threshold versus number of source/field points

Due to the fact that when the antenna approaches the medium, the backscattered field becomes more complicated and, therefore, the number of source/field points which characterizes the antenna needs to be increased. In this section, we present the relationship between the number of source/field points and the antenna height threshold above which these source/field points and their associated transmission/reflection transfer functions are considered to be sufficient to model the antenna. Our analysis was applied for the Vivaldi antenna in which the antenna was characterized by 1, 4, 6 and 8 points. Data for the analysis were obtained from 100 measurements corresponding with 100 distances from 0 to 72 cm from a copper plane as presented in Chapter 6. We used these data to determine the antenna transmission/reflection functions corresponding with each set of source/field points, and estimate the antenna height threshold above which these transfer functions well characterize the antenna. The algorithm is based on the idea of the bisection method that numerically finds a root of an equation. Accordingly, the antenna height threshold is obtained by narrowing down the interval which contains that threshold as presented in Figure 3.7. We assumed that the threshold is found when the interval is less than 0.2 cm. The origin interval is from 0 to $1.2D$. We also assumed that the antenna is well characterized when the correlation coefficient (r) between modeled and measured data is equal to or greater than 0.999 and the root mean square error (RMS) lower than 3×10^{-5}. The algorithm to calibrate the near-field GPR model and to estimate the antenna characteristic

transmission/reflection transfer functions were presented in Lambot and André [2013].

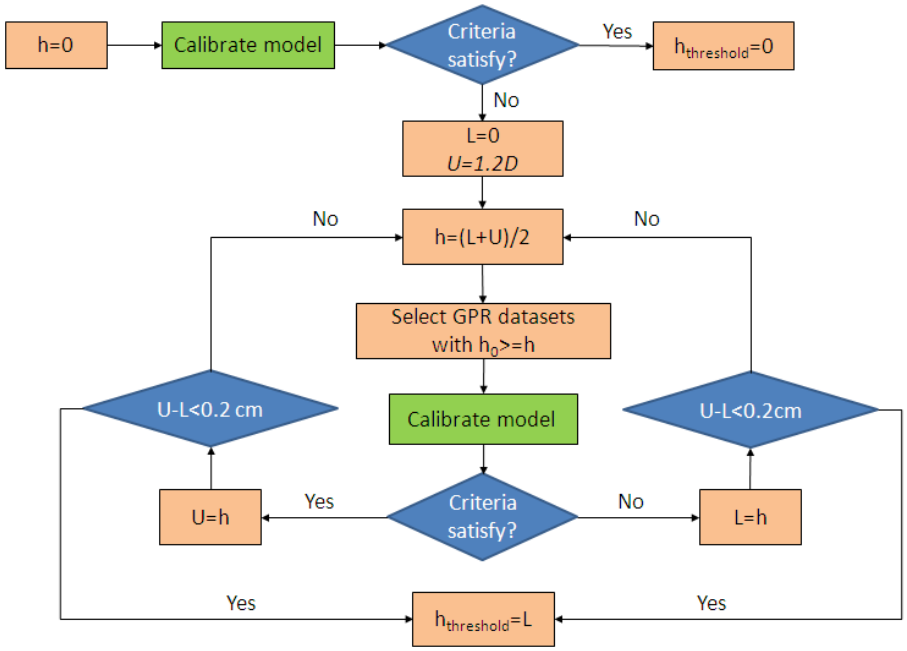

Figure 3.7. Procedure to determine the antenna height threshold for a given number of source/field points.

Figure 3.8 shows the relationship between the number of source/field points and the antenna height threshold. The threshold for the 1 source/field point is at the near- and far-field threshold ($1.2D$). For the 6- and 8-point configurations, the modeled and measured GPR data well agree with all values of antenna heights (r=0.9993, 0.9999, and RMS=0.9×10^{-5}, 1.9×10^{-5} for 6 and 8 points, respectively). As a result, the thresholds for these two configurations are 0 cm. With 4 source/field points, the threshold is 2 cm with r=0.999 and RMS=2.7×10^{-5}.

3.6 Conclusion

We specified the antenna height threshold above which the far-field model can be effectively applied by evaluating the spatial variation of the Green's function over the antenna aperture. Accordingly, we calculated the partial derivatives of the Green's function with respect to the spatial polar coordinates (ρ, θ), and analyzed their variations with different antenna heights and frequencies. Assuming that the Green's functions are approximately constant everywhere over

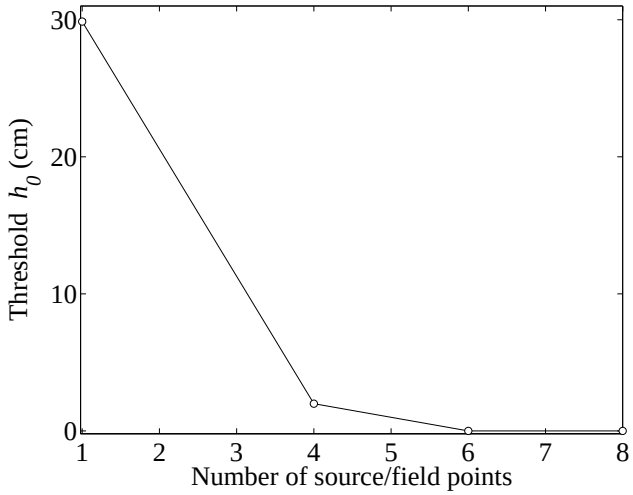

Figure 3.8. Number of source/field points versus the antenna height threshold above which this number of source/field points is sufficient to characterize the antenna.

the antenna aperture, and, therefore, equaling the amplitude of their spatial derivatives to zero, the antenna height threshold was found to be $h = 1.2D$ for all kinds of antennas.

We validated the above threshold both by numerical and laboratory experiments using a homemade 1–3 GHz Vivaldi antenna. For the numerical evaluation, we compared the synthetic GPR data generated by both of the near- and far-field antenna models above 1- and 2-layered scenarios with antenna heights ranging from 0.1 to $2D$. The obtained results indicate that above the antenna height threshold, the performance of the near- and far-field antenna models is similar, both in magnitude and phase.

For laboratory experiments, we compared the two models by conducting GPR measurements from 0 to 70 cm above a water layer. The optimized results showed that the near-field GPR model perfectly estimated the antenna height and water thickness at all antenna heights with very small difference between modeled and measured GPR data. The far-field model predicted well the unknown parameters for antenna heights beyond 5 cm ($\approx 0.2D$). Regarding the GPR data, the difference between far-field modeled and measured data increased rapidly as the antenna moved from 29 ($\approx 1.2D$) down to 0 cm. However, at antenna heights larger or equal to 29 cm, the far-field model data showed very good agreement with the near-field modeled and measured data.

Finally, the relationship between the number of source/field points and the antenna height above which these source/field points and their associated transmission/reflection transfer functions are sufficient to model the Vivaldi antenna was also considered in this study. The obtained results showed that when the

number of points was equal to or higher than 6, the antenna was well modeled at all antenna heights. The antenna was well characterized with the 4-point configuration when the antenna height was equal to or greater than 2 cm.

Chapter 4

Intrinsic modeling of antenna array in near-field conditions *

Abstract Antenna arrays have been increasingly used in many civil engineering and geoscience applications as they allow collecting multi-offset measurements simultaneously, thereby providing additional information for subsurface imaging and characterization. In this study, we extended a new near-field intrinsic antenna modeling approach to antenna arrays. The array is considered as a combination of couples of transmitting-receiving antennas with different offsets. Each couple of antennas is characterized using an equivalent set of infinitesimal source/field points and reflection/transmission transfer functions. We propose an iterative approach to calibrate the model through which the antenna model is progressively completed. To reduce the number of simultaneous unknown parameters, linear and nonlinear optimization algorithms are combined together. We also applied the time gain for both modeled and measured array data to compensate for the antenna attenuation, which is expected to improve the accuracy of the calibration. We validate the proposed calibration approach to an antenna array with a two-Vivaldi antenna elements operating in the frequency range 0.8-3 GHz. The offset between the antennas varied from 10-40 cm. Calibration data consisted of 100 measurements corresponding with the antenna array at 100 different heights above a copper plane. The calibrated and measured antenna array data closely agree with correlation coefficients larger than 0.9979 and root mean square error less than 2.3×10^{-5}. These results open a new development avenue to apply the antenna array for digital soil mapping and non-destructive testing of materials using full-wave inverse modeling.

*Adapted from A. P. Tran, A. D. Coster, and S. Lambot, Intrinsic modeling of antenna array in near-field conditions, *IEEE Geoscience and Remote Sensing Letters*, In preparation

4.1 Introduction

The use of nondestructive testing techniques (NDT) for highly-resolved imaging and characterization of materials has been extensively researched in recent years. Among existing NDT techniques, ground-penetrating radar (GPR) is one of the most popular ones, which has proved its valuableness in many applications in civil engineering [Nadakuduti et al., 2006; Pettinelli et al., 2009; Crocco et al., 2010; Patriarca et al., 2011], archeology [Papadopoulos et al., 2009] and geosciences [Kowalsky et al., 2005; Lambot et al., 2009; Mahmoudzadeh et al., 2012]. In most applications, array data were collected by the conventional single channel GPR in two typical configurations, namely single-offset and multi-offset. While the single-offset configuration can rapidly perform measurements, its information is insufficient to reconstruct multiple layers, especially in the case where clear reflectors are missing. By contrast, the multi-offset configuration (e.g., common-midpoint (CMP) or Wide Angle Reflection and Refraction (WARR)) can provide more information about the medium, but it is very time-consuming for data acquisition. To solve this problem, many efforts have been made to design antenna array systems, which are composed of multiple antenna elements to simultaneously record a large amount of data in a single measurement. The data obtained from the antenna array are also more accurate than the multi-offset configuration as the offset between the antennas are fixed and well known.

Recently, several antenna array systems including both homemade and commercial ones have been developed. For the homemade systems, Sato et al. [2004] developed a stepped-frequency continuous-wave (SFCW) GPR array system (SAR-GPR) with the transmitting and receiving antennas being arranged similar to the CMP configuration. Using this GPR array, data are sequentially acquired by operating the pairs of transmitting–receiving antennas. Yarovoy et al. [2007b] designed a more compact system that comprises a single transmitter and a linear receiver array. The system more rapidly performs measurements than the CMP-like array for the fact that all receiving antennas simultaneously receive the backscattered signals which are reflected from a medium. For the commercial array, 3D-Radar (*http://www.3d-radar.com*) developed a SFCW GeoScope GPR containing up to 31 antennas. The antenna elements are arranged in a linear array where the transmitting and receiving antennas alternated with each other. Mala (MALÅ Geoscience, *http://www.malags.com*) designed the MIRA 3D array with 9 transmitting and 8 receiving antennas aligned in two overlapping rows. GSSI (*www.geophysical.com*) produced an array containing 14 pairs of transmitting/receiving dipoles, placed in three rows, with axes in 45° to the horizontal direction [Francese et al., 2009].

With respect to practical applications, the antenna array has been suc-

cessfully applied in many case studies concerning land mine detection [Yarovoy et al., 2007a; Feng et al., 2009; Tomizawa et al., 2009] and investigation of burial architectures in archeological sites [Francese et al., 2009; Trinks et al., 2009; Linford et al., 2010]. In hydrogeophysics, there are only few studies that used the antenna array to quantitatively characterize the subsurface soil moisture. Gerhards et al. [2008] and Pan et al. [2012] collected continuous multi-offset measurements using multi-channel GPR configuration. The thickness and water content of the upmost soil layer were estimated using the travel time information from all available channels at a common reflection point. The disadvantage of this approach is that only a part of information contained in GPR data (wave propagation velocity) was used, which inherently causes errors for soil moisture estimation.

In this study, we introduce a full-wave antenna array model and propose a specific optimization strategy to calibrate this model. The array is conceptualized as a set of transmitting–receiving antennas and, therefore, each couple can be simulated by the near-field antenna model developed by Lambot and André [2013]. Then, the calibration algorithm is applied for each couple. The algorithm is based on 1) the progressive completeness of the model structure to find a good initial guess for the optimization, and 2) the combination of linear and nonlinear optimization algorithms to reduce number of unknown parameters. In addition, to compensate for the antenna signal attenuation and increase the accuracy of the calibration, we applied the time gain for both modeled and measured array data. To the best of our knowledge, this study is the first effort tackling the problem of full-wave inverse modeling of antenna array data for reconstruction of multiple planar layered medium.

4.2 Intrinsic array model

The fundamental idea to model an antenna array is considering it as a combination of different couples of the transmitting–receiving antennas with different offsets in which each couple can be intrinsically simulated by the near-field antenna model (Equation (2.1)) developed by Lambot and André [2013]. The transmitting–receiving antennas are characterized by an equivalent set of infinitesimal source/field points to capture the scattered field distribution. Wave propagation between the source/field points and the radar transmission line reference plane is modeled via complex, frequency-dependent reflection and transmission transfer functions. Wave propagation in multiple planar media is calculated by Green's functions. The mutual coupling between the transmitting and receiving antennas is implicitly considered in the model thanks to the linearity of Maxwell's equations and the calibration procedure. More detailed explanation of the model is presented in Chapter 2.

4.3 Determination of antenna characteristic transfer functions

In order to use the antenna array model for the reconstruction of a layered medium, the reflection/transmission transfer functions for each couple of transmitting–receiving antennas must be determined by inverting Equation (2.1) given the Green's functions which can be calculated, and measured data S. This inverse problem is complicated because the number of unknown parameters is relatively large. With N source/receiver points, there are in total $3N + 1$ complex transmission/reflection transfer functions and, correspondingly, $6N + 2$ unknown parameters due to the fact that each complex functions consists of the real and imaginary parts. We assumed that the antenna has a bilateral symmetry, which reduces the number of unknown parameters to $3N + 2$ with N being an even number. However, this number of parameters is still relatively large, depending on the number of source/field points that are required. There is also no a priori information to constrain the unknown parameters, which causes many difficulties for the model calibration.

In this study, we propose an algorithm to effectively solve the problem using an approach that progressively completes the structure of the antenna array model. Results obtained from the simple model structure were used for the complicated one, as outlined in Figure 4.1, in order to provide good initial guesses for the optimization. When the antenna array is in far-field conditions, it can be modeled by 1-source/field point. This is the simplest model structure and the calibration of this model is a linear optimization problem. Next, the antenna array is modeled by several source/field points. However, the model is simplified by assuming that the functions $T_{s,\cdot}$ and $R_{s,\cdot}$ characterizing the receiving antenna are uniformly distributed ($T'_{s,k} = \frac{T_{s,k}}{T_{s,1}} = 1$ and $R_{s,k} = R_s$ ($k = 1 \cdots N$)). The calibration of this model uses the function $R_{s,1}$ estimated from the far-field model calibration as the initial guess. Finally, the full antenna array model uses the estimated values of $T'_{s,\cdot}$ and R_s as the initial guesses. For the calibration of the simplified and full antenna array models, we also combined linear and nonlinear optimization algorithms to reduce the number of unknown parameters, therefore, avoiding trapping into local minima. The detailed description of this approach is presented in the following paragraphs.

4.3.1 Far-field model calibration

When the antenna is in the far-field condition (antenna–medium distance is greater than 1.2 maximum dimension of the antenna aperture [Tran et al., 2013a]), the distribution of the backscattered field over the antenna aperture tends to be locally planar, and therefore, one source/receiver point and corre-

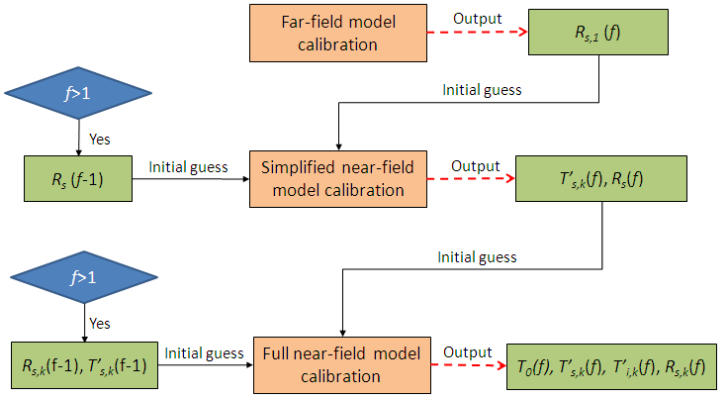

Figure 4.1. Calibration procedure for the antenna array model.

sponding antenna reflection and transmission transfer functions are sufficient to characterize the antenna. As a result, Equation (2.1) becomes:

$$S = T_0 + \frac{T_1 G_{11}^0}{1 - R_{s,1} G_{11}^0} \tag{4.1}$$

where $T_1 = T_{s,1} T_{i,1}$. To calibrate, Equation (4.1) can be rewritten as:

$$S = T_0 + S G_{11}^0 R_{s,1} + G_{11}^0 (T_1 - T_0 R_{s,1}) \tag{4.2}$$

If M far-field measurements of S are performed above a known layer for which the corresponding Green's functions can be calculated, Equation (4.2) becomes [Lambot et al., 2006a]:

$$\mathbf{b} = \mathbf{A}\mathbf{x} \tag{4.3}$$

with

$$\mathbf{b} = \begin{bmatrix} S_1 \\ S_2 \\ \vdots \\ S_M \end{bmatrix} \tag{4.4}$$

$$\mathbf{A} = \begin{bmatrix} 1 & S_1 G_{11,1}^0 & G_{11,1}^0 \\ 1 & S_2 G_{11,2}^0 & G_{11,2}^0 \\ \vdots & \vdots & \vdots \\ 1 & S_M G_{11,M}^0 & G_{11,M}^0 \end{bmatrix} \tag{4.5}$$

$$\mathbf{x} = \begin{bmatrix} T_0 \\ R_{s,1} \\ T_1 - T_0 R_{s,1} \end{bmatrix} \tag{4.6}$$

Equation (4.3) indicates that the calibration of the far-field model is a linear optimization problem. The unknown vector **x** can be computed in the least squares sense as:

$$\mathbf{x} = (\mathbf{A}^H\mathbf{A})^{-1}\mathbf{A}^H\mathbf{b} \tag{4.7}$$

Knowing **x**, the transfer functions T_0, T_1, $R_{s,1}$ can be calculated. The function $R_{s,1}$ is used as the initial guess for the next calibration stage.

4.3.2 Simplified antenna array model calibration

By dividing T_s by $T_{s,1}$ and multiplying T_i by $T_{s,1}$, Equation (2.1) is rewritten as follow:

$$S = T_0 + T_s^{'}(\mathbf{I_N} - \mathbf{G_0}\mathbf{R_s})^{-1}\mathbf{G}T_i^{'T} \tag{4.8}$$

with changing variables

$$T_i^{'} = \begin{bmatrix} T_{s,1}T_{i,1} & T_{s,1}T_{i,2} & \cdots & T_{s,1}T_{i,N} \end{bmatrix} \tag{4.9}$$

$$T_s^{'} = \begin{bmatrix} 1 & \frac{T_{s,2}}{T_{s,1}} & \cdots & \frac{T_{s,N-1}}{T_{s,1}} & \frac{T_{s,N}}{T_{s,1}} \end{bmatrix} \tag{4.10}$$

With the array equation expressed under this form, instead of functions $T_{i,.}$ and $T_{s,.}$, we determine $T_{i,.}^{'} = T_{s,1}T_{i,.}$ and $T_{s,.}^{'} = \frac{T_{s,.}}{T_{s,1}}$. The number of unknown parameters reduces to $3N$ for the fact that it is not necessary to estimate $T_{s,1}$. In order to provide a good approximation for the calibration of the full antenna array model, Equation (4.8) is simplified by assuming that the reflection ($R_{s,.}$) and transmission functions ($T_{s,.}$) characterizing the receiving antenna are uniformly distributed. As a result, the matrices $T_s^{'}$ and $\mathbf{R_s}$ become:

$$T_s^{'} = \begin{bmatrix} 1 & 1 & \cdots & 1 \end{bmatrix} \tag{4.11}$$

$$\mathbf{R_s} = R_s\mathbf{I_N} \tag{4.12}$$

and Equation (4.8) becomes:

$$S = T_0 + MT_i^{'T} \tag{4.13}$$

with

$$M = T_s^{'}(\mathbf{I_N} - \mathbf{G_0}R_s)^{-1}\mathbf{G} = \begin{bmatrix} \sum_{k=1}^{N} a_{k1} & \sum_{k=1}^{N} a_{k2} & \cdots & \sum_{k=1}^{N} a_{kN} \end{bmatrix} \tag{4.14}$$

Due to the bilateral symmetric assumption, the row matrix M and column matrix $T_i^{'T}$ are symmetric. Consequently, the Equation (4.13) reduces to:

$$S = T_0 + 2\left(T_{i,1}^{'}\sum_{k=1}^{N} a_{k1} + T_{i,2}^{'}\sum_{k=1}^{N} a_{k2} + \cdots + T_{i,N/2}^{'}\sum_{k=1}^{N} a_{kN/2}\right) \tag{4.15}$$

Equation (4.15) indicates that if the function R_s is known, the matrix M is known and, the determination of the functions T_0 and $T'_{i,\cdot}$ is a linear optimization problem as follow:

$$\begin{bmatrix} S_1 \\ S_2 \\ \vdots \\ S_M \end{bmatrix} = \begin{bmatrix} 1 & 2\sum_{k=1}^{N} a_{k1,1} & 2\sum_{k=1}^{N} a_{k2,1} & \cdots & 2\sum_{k=1}^{N} a_{kN/2,1} \\ 1 & 2\sum_{k=1}^{N} a_{k1,2} & 2\sum_{k=1}^{N} a_{k2,2} & \cdots & 2\sum_{k=1}^{N} a_{kN/2,2} \\ \vdots & \vdots & \vdots & & \vdots \\ 1 & 2\sum_{k=1}^{N} a_{k1,M} & 2\sum_{k=1}^{N} a_{k2,M} & \cdots & 2\sum_{k=1}^{N} a_{kN/2,M} \end{bmatrix} \begin{bmatrix} T_0 \\ T'_{i,1} \\ T'_{i,2} \\ \vdots \\ T'_{i,N/2} \end{bmatrix} \quad (4.16)$$

For this special structure, we propose a specific optimization strategy that combines the linear and nonlinear optimization algorithms to estimate the transmission/reflection transfer functions independently for each frequency from Equation (4.16). The real and imaginary parts of the functions R_s are optimally estimated using the Levenberg-Marquardt algorithm. For the first frequency, the initial guess of R_s for the optimization is $R_s^{ini,f} = \frac{R_{s,1}^f}{N}$ with $R_{s,1}^f$ obtained from the far-field model calibration. From the second frequency, there are two choices of initial guess: 1) $R_s^{ini,f} = \frac{R_{s,1}^f}{N}$ and 2) the estimated value of the previous frequency $R_s^{ini,f} = R_s^{f-1}$. From these two initial values, we obtain two optimized parameter sets. If these two sets are different, the one with the smallest objective function value is selected as the final functions. During the optimization process, for each trial value of R_s, the functions T_0 and $T'_{i,\cdot}$ are determined by solving the over-determined system of equations (4.16) using the Equation similar to (4.7). With this coupled linear–nonlinear optimization approach, the nonlinear least-square optimization only needs to find two parameters, and therefore, helps to easily obtain the globally optimal solution for the inverse problem (4.16). The estimated values of R_s and $T'_{s,\cdot} = \frac{T_{s,\cdot}}{T_{s,1}} = 1$ are afterwards used as initial values for the full antenna array model calibration. It is worth noting that due to the bilateral symmetry assumption ($T'_{i,N+1-k} = T'_{i,k}$, $k = 1, \cdots N/2$), only functions corresponding to the source/field points from 1 to $N/2$ need to be determined.

4.3.3 Full antenna array model calibration

For calibrating the full antenna array model, we use the formulation of Equation (4.8). Given the bilateral symmetric assumption of the antenna, this equation can be reformulated as bellow:

$$S = T_0 + 2\left(T'_{i,1}\sum_{k=1}^{N} T'_{s,k}b_{k1} + T'_{i,2}\sum_{k=1}^{N} T'_{s,k}b_{k2} + \cdots + T'_{i,N/2}\sum_{k=1}^{N} T'_{s,k}b_{kN/2}\right) \quad (4.17)$$

in which b_{ij} is the element of the matrix $(\mathbf{I_N} - \mathbf{G_0R_s})^{-1}\mathbf{G}$; $T'_{s,N+1-k} = T'_{s,k}$, $k = 1, \cdots N/2$ and $T'_{s,1} = 1$. Similar to the simplified antenna array model, the inverse problem to determine T_0, $T'_{i,\cdot}$, $T'_{s,\cdot}$, $R_{s,\cdot}$ based on Equation (4.17) also becomes a linear optimization one when the functions $R_{s,\cdot}$ and $T'_{s,\cdot}$ are known. As a result, we use the same optimization strategy as for the simplified antenna array model to calibrate the full model. Accordingly, the functions $R_{s,\cdot}$ and $T'_{s,\cdot}$ are optimized using the Levenberg-Marquardt algorithm. The initial values for $R_{s,\cdot}$ and $T'_{s,\cdot}$ are obtained from the simplified antenna array model calibration. After the first frequency, another choice of initial guess comes from the values obtained from the previous frequency. For each trial of $R_{s,\cdot}$ and $T'_{s,\cdot}$, the functions T_0 and $T'_{i,\cdot}$ can be obtained by solving the linear optimization problem. With this approach, the number of unknown parameters in the iterative nonlinear optimization problem (2.1) reduces from $3N + 2$ to $2N - 2$ and, therefore, a more accurate solution is obtained.

The above procedure is applied for each couple of transmitting–receiving antennas of the antenna array to determine their characteristic transmission/reflection transfer functions.

4.4 Antenna array system

We considered a linear array of homemade Vivaldi antennas. The antennas were aligned and connected to different ports of a SFCW vector network analyzer (VNA, ZNB8, Rohde & Schwarz, Munich, Germany) using N-type 50 Ω impedance coaxial cables (Figure 4.2). We calibrated the VNA at the connection between the antenna feed point and the coaxial cable using the standard Open-Short-Match-Through calibration kit. The ZNB8 VNA contains four ports operating in a frequency range from 9 kHz to 40 GHz and, therefore, the antenna array can include maximum four antenna elements. With this antenna array system, the reflected/transmitted fields are linked to the incident fields as below:

$$\begin{bmatrix} b_1 \\ b_2 \\ b_3 \\ b_4 \end{bmatrix} = \begin{bmatrix} S_{11} & S_{12} & S_{13} & S_{14} \\ S_{21} & S_{22} & S_{23} & S_{24} \\ S_{31} & S_{32} & S_{33} & S_{34} \\ S_{41} & S_{42} & S_{43} & S_{44} \end{bmatrix} \begin{bmatrix} a_1 \\ a_2 \\ a_3 \\ a_4 \end{bmatrix} \tag{4.18}$$

where a_i and b_i (i = 1 to 4) denote the incident and transmitted/reflected waves, respectively; S_{ij} (i, j = 1 to 4) is the transmission ($i \neq j$) or reflection transfer function ($i = j$) measured at the port i^{th} from the incident wave coming from the port j^{th}. In total, we can obtain up to 16 S-parameters in a single antenna array measurement. However, due to the reciprocity of the antenna ($S_{ij} = S_{ji}$, $i, j = 1, \cdots 4$), there are 7 meaningful measurements, namely S_{11}, S_{21}, S_{31}, S_{41}, S_{23}, S_{24} and S_{34}.

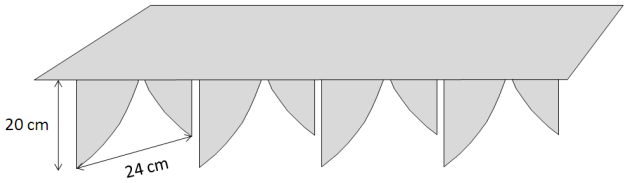

Figure 4.2. Illustration of the antenna array with 4 Vivaldi antenna elements.

Due to the fact that the objective of this study is to present the calibration strategy for the antenna array model, we used a simple array that contains only two antenna elements with different offsets. Each Vivaldi antenna element is made of aluminium and has an aperture of 24 cm which was designed by Remi Sarkis from UCL/ICTEAM [Bhattacharya et al., 2010; Sarkis and Craeye, 2010]. The measurements were performed in a frequency range of 0.8-3.0 GHz, with a step of 12 MHz, resulting in 184 frequencies.

4.5 Results and discussion

We calibrate the 2-element antenna array model with offsets $\delta = 10$, 20 and 40 cm (Figure 4.3a). For each offset, we performed 100 measurements with the array at heights (h_0) from 0 to 0.72 m above a 3×3 m^2 copper plane considered as a perfect electric conductor (PEC) (Figure 4.3b). With this configuration, the Green's functions can be easily evaluated. In the antenna array model, the transmitting and receiving antennas were, respectively, modeled by 8 equivalent set of source/field points which were evenly distributed over the antenna aperture.

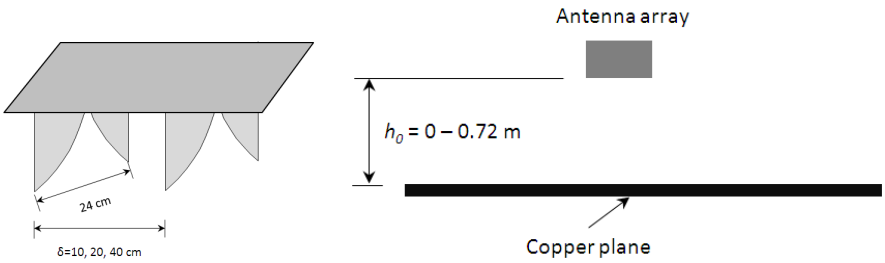

a) 2-Vivaldi element antenna array b) Laboratory experiment setup

Figure 4.3. Illustration of 2-element antenna array (a), and laboratory experimental setup to obtain calibration data (b). The experiments includes the 2-element Vivaldi antenna array and the copper plane working as a perfect electric conductor. 100 measurements corresponding with 100 heights from 0 to 0.72 m were performed. The offset between the two antennas was set at $\delta = 10$, 20 and 40 cm.

In order to compensate for the GPR signal attenuation and increase the accuracy of the antenna array model calibration, we applied the time gain for both modeled and measured array data. However, because the antenna array model calibration is carried out in the frequency domain, it is necessary to convert the time gain to the frequency one. Figure 4.4 presents the procedure performing this conversion, which is clarified as below:

1. The raw array data in the frequency-domain $[S_f(N_m \times N_f)]$ were transformed into the time-domain ones $[s_t(N_m \times N_t)]$ using the inverse discrete Fourier transform algorithm (IFFT), in which N_m represents the number of measurements, and N_f, N_t are, respectively, the number of frequencies and times in each measurement.

2. Apply the time gain $[g_t(N_m \times N_t)]$ to the time-domain array data $[s_t(N_m \times N_t)]$ to obtain the gained time-domain array data $[gs_t(N_m \times N_t])$, which then are transformed back to the frequency-domain ones $[gS_f(N_m \times N_f)]$ by the discrete Fourier transform algorithm (FFT).

3. Calculate the ratio of the gained and raw frequency-domain array data to obtain the frequency gain matrix $G_f(N_m \times N_f) = \frac{gS_f(N_m \times N_f)}{S_f(N_m \times N_f)}$

4. For each frequency f, the frequency gains of all measurements at that frequency are applied for the objective function as below:

$$OF = \sum_{i=1}^{i=N_m} |[S_f(i,f) - S_{fm}(i,f)]\, G_f(i,f)|^2 \qquad (4.19)$$

   where $S_{fm}(i,f)$ is the modeled array data corresponding with the measurement i and frequency f.

Equation (4.19) implied that for a given frequency, the objective function has stronger weights to the measurements at which this frequency contains more information of late and weak arrival signals. Based on this objective function, the transmission/reflection transfer functions for each frequency can be determined.

Figure 4.5 presents an example of array data in the time domain before and after the time gain is applied for the case with an antenna offset of 20 cm. The figure shows that the antenna coupling signal and reflection from the copper plane are clearly observed for the cases either with or without the time gain. However, while the first order multiple reflection in the origin data is relatively small, especially at the large antenna heights, it is clearly visible when the time gain is applied. Therefore, by applying the time gain, it is expected to improve the accuracy of the calibration of the antenna array model.

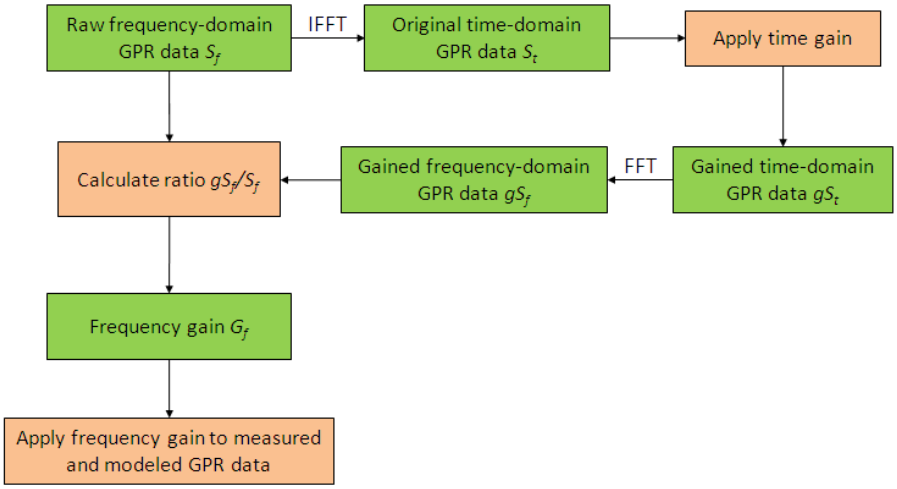

Figure 4.4. Procedure to convert the gain in the time domain to the frequency one and apply this frequency gain for modeled and measured array data for the calibration of the antenna array model.

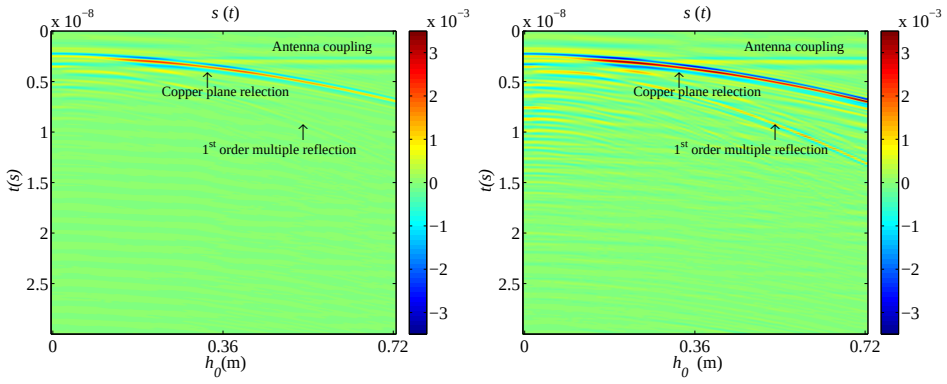

a) Raw array data b) Gained array data

Figure 4.5. Example of array data in the time domain before (a) and after (b) the time gain is applied. The antenna offset is 20 cm.

Figure 4.6 compares the time-domain measured and modeled array data S_{21} as well as the differences between them at offsets 10, 20 and 40 cm, respectively. For comparison, the results obtained from the single antenna are also presented. As can be seen from the figure, the main reflections were well reproduced by the model. For example, in Figure 4.6b (corresponding to an antenna offset of 10 cm), when the height h_0 is greater than 0.2 m, the horizontal lines at around 2.5 ns represent the antenna coupling occurring between the two antennas. The reflections from the copper plane are characterized by the lines that gradually go from 2 down to 7.5 ns. However, when the height h_0 is lower than 0.2 m, we cannot separate the antenna coupling and reflections from the copper plane because they are coupled together.

As for the relationship between the antenna offset and GPR reflection signals, we can clearly observe that the antenna coupling quickly reduces when the offset increases. With a single antenna, the antenna coupling signals are clearly observed. However, these signals are much smaller when the offset is equal to 20 cm, and they are invisible at an offset of 40 cm. This is attributed to the fact that for the single antenna case, the antenna simultaneously works as the transmitter and receiver, while for the nonzero-offset cases, the transmitting and receiving antennas are separated. As a result, the antenna coupling of the single antenna is much greater than the nonzero ones. The PEC reflections also reduce and appear later with increasing offset. It is because when the offset is larger, the propagation distance of electromagnetic wave increases. Consequently, the travel time is longer and the signal attenuation due to spherical divergence is larger.

Table 4.1 presents the quantitative evaluation of the model calibration for different offsets. We used two criteria to evaluate the performance of the calibration algorithm: the correlation coefficient (r) and root mean square error (RMS) between modeled and measured array data. The table indicates that there is a relatively good agreement between the modeled and measured array data for all antenna offsets. The RMS is lower than 2.3×10^{-5} and r is greater than 0.9979. The table also shows that the RMS decreases with increasing offset. It is because the signal amplitude is larger for a smaller offset and, therefore, the absolute differences between modeled and measured array data are larger. The r of the single antenna is slightly higher than those of the nonzero-offsets. This can be explained by the fact that when the offset is not equal to zero, measurement errors of the array heights (h_0) are higher, and the transmitting and receiving antennas are technically not perfectly identical, which inherently causes errors for the model calibration.

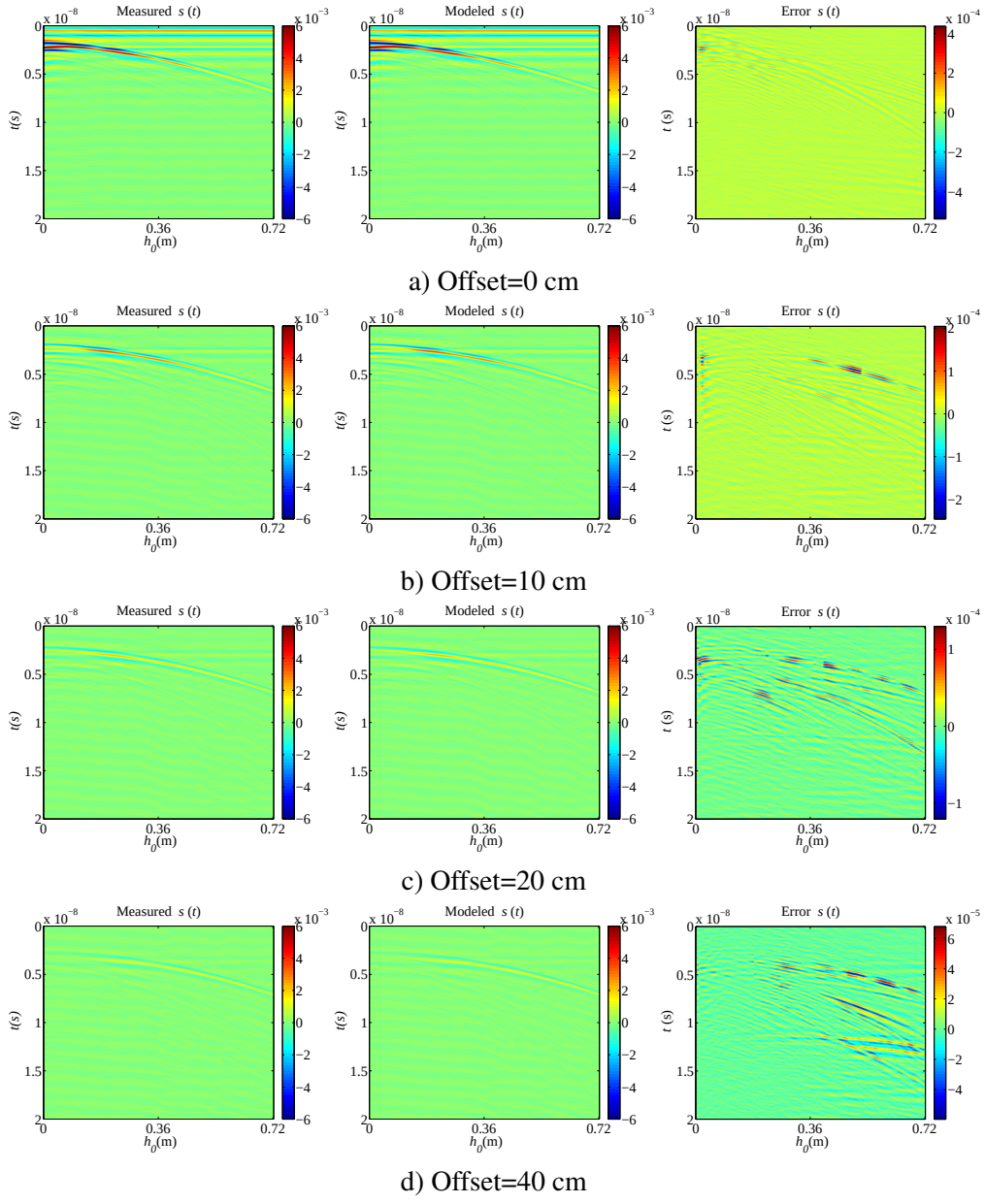

Figure 4.6. Comparison of time-domain measured (left) and modeled (middle) array data as well as the differences between them (right) at different offsets: single antenna (a), 10 cm (b), 20 cm (c) and 40 cm (d). For each antenna offset, 100 measurements were performed corresponding with 100 array heights (h_0) ranging from 0 to 0.72 m above the copper plane.

Offset (cm)	r	RMS
Single antenna	0.9994	2.29×10^{-5}
10	0.9988	1.57×10^{-5}
20	0.9979	1.41×10^{-5}
40	0.9984	0.77×10^{-5}

Table 4.1. Correlation coefficients and root mean square errors of the model calibration for a single antenna, and three 2-element GPR arrays with different offsets: 0, 10, 20 and 40 cm.

4.6 Conclusion

In this study, we proposed a new near-field calibration approach for antenna arrays and we validated the method in laboratory conditions using a two-element array of Vivaldi antennas. The array is conceptualized as several sets of transmitting-receiving antennas with different offsets. As a result, each of these antenna couples is modeled by the near-field antenna model and characterized using an equivalent set of infinitesimal source/field points and reflection/transmission transfer functions. The calibration is performed using a progressive approach through which the results from the simplified GPR model are used as initial guesses for the more complicated one. In addition, the special structure of the antenna array model allows us to combine linear and nonlinear optimization algorithms, which helps to considerably reduce the number of unknown parameters for the model calibration. Moreover, in order to compensate for the signal attenuation, we applied the time gain for both modeled and measured array data. After the time gain was applied, the multiple reflections were clearly visible, which is expected to improve the accuracy of the transmission/reflection transfer functions, especially $R_{s,\cdot}$. Relatively good agreement between modeled and measured array data for different antenna offsets was obtained. However, the calibrated array model was not validated for reconstruction of layered media. In addition, because the study only considered the 2-element antenna array, the effect of other antennas on the array data in the array was not accounted for. In future studies, a multi-element array will be used to simultaneously record several datasets with different offsets, and then calibrate the antenna array model using these datasets.

This approach opens a new development trend for applying the GPR arrays for digital soil mapping and nondestructive testing with full-wave inverse modeling. For digital soil mapping, this approach is expected to provide more accurate information about soil layer structure and soil moisture profile due to the fact that array data at different offsets are simultaneously collected in a single measurement and the full-wave inverse modeling approach is proposed to process these data. For nondestructive testing, the approach is able to reproduce the antenna coupling and backscattered signal from multi-layered media.

Consequently, by filtering these reflections from measured array data, reflections from anomalies inside the media are expected to be more visible.

Chapter 5

Coupling of dielectric mixing models with full-wave ground-penetrating radar signal inversion for sandy soil moisture estimation*

Abstract We coupled dielectric mixing models with a full-wave ground-penetrating-radar (GPR) model to estimate the soil water content by inversion. Two mixing models were taken into account in this study, namely, a power law model and the Wang and Schmugge model. With this combination, we could account for the frequency dependence of the electric permittivity and apparent conductivity in the inverse algorithm and directly estimate the soil water content. The approach was validated by a series of experiments with sandy soil in controlled laboratory conditions. The results showed that the performance of our approach is better than the common approach, which assumes a linear dependence of apparent conductivity on frequency and uses Topp's equation to transform permittivity to water content. GPR data were perfectly reproduced in the time and frequency domains, leading to very accurate water-content estimates with an average absolute error of less than 0.013 cm^3/cm^3. However, the accuracy was reduced as the water content increased. Sensitivity analysis indicated that the Green's function was most sensitive to the water content and sand-layer thickness, but much less to DC conductivity. The results also revealed that as the frequency increased, although the permittivity was nearly constant, the apparent electric conductivity and the attenuation increased remarkably, especially for wet sands due to dielectric losses. The successful validation of the proposed approach shows a promising approach to use dielectric mixing models for soil-moisture mapping from GPR measurements.

*Adapted from A. P. Tran, M. R. M. Ardekani, and S. Lambot, Coupling of Dielectric Mixing Models with Full-wave Ground-Penetrating Radar Signal Inversion for Sandy Soil Moisture Estimation, *Geophysics*, 77(3), H33-H44. doi: 10.1190/geo2011-0100.1, 2012.

5.1 Introduction

In GPR applications, the two main geophysical properties are the electric permittivity and apparent conductivity, which are frequency dependent quantities [Saarenketo, 1998; Deparis and Garambois, 2009]. As a result, in order to obtain accurate and realistic values of these properties, their frequency dependence should be taken into account in the inverse modeling scheme. However, in the GPR field there have been not many studies investigating the problem so far [West et al., 2003]. Saarenketo [1998] used a Vector Network Analyzer (VNA) to investigate the variation of the electric properties of silt and clay soils with different densities and water contents over the GPR frequency range from 30 MHz to 3 GHz. Lambot et al. [2005] assumed an independence of the permittivity and a locally linear dependence of the apparent electric conductivity on the frequency for a sandy soil in the range 1-3 GHz for the full-wave inversion of off-ground, zero-offset GPR data. This assumption worked well for the selected frequency range. However, as they mentioned, when the frequency range extends more widely and water content increases, a more appropriate model would be required.

The key step in estimating soil moisture of the subsurface from GPR signals is the transformation of the geophysical properties into water content, which typically uses petrophysical relationships. Generally, there are two main approaches to develop these relationships. The first approach uses empirical equations to relate the water content to electric permittivity based on measurements with different soil types [e.g., Topp et al., 1980]. The second approach, more advanced, predicts the water content from dielectric mixing models of soil. According to this approach, soil permittivity is expressed by the permittivities of air, water and soil particles weighted by their volume fractions. Therefore, given the permittivity and volume fraction of other components, water content can be determined [Wang and Schmugge, 1980; Dobson et al., 1985; Heimovaara, 1994]. Compared to the empirical formulas, the dielectric mixing models take into account the composition of soil materials and thus are expected to better predict the water content. However, a drawback of this approach is that it requires a priori knowledge of the porosity of the soil material and permittivities of the individual constituents [Lesmes and Friedman, 2005]. Detailed reviews on the petrophysical relationships can be found in the works of Robinson et al. [2003]; Lesmes and Friedman [2005].

In this chapter, we propose an approach that integrates different mixing models of the effective complex permittivity into the full-wave inversion of GPR signals to estimate the water content of a sandy soil. Instead of estimating the water content from the electric permittivity, we can derive directly the water content from inversion of GPR signals. The frequency dependence of the sand permittivity and apparent conductivity are accounted for via the

permittivity and conductivity of water component, which varies with the frequency by the Debye equation. By regarding soil porosity as an optimized variable, our approach also does not need to priori determine this value when the dielectric mixing models are used. Our approach is validated by controlled laboratory experiments with a sandy soil subject to various water contents. Obtained results are compared with each other and with those of Lambot et al. [2005]'s approach to select the best model for our problem. Uncertainty analysis of the electric properties and sensitivity analysis of the model signal with the optimized parameters are also presented.

5.2 Theory

5.2.1 Forward modeling

For transmitting and receiving GPR signals, we adopted a measurement system as described in the work of Lambot et al. [2004c]. The system contains a VNA and an off-ground ultra-wideband zero-offset horn antenna connected by a 50 Ω impedance coaxial cable. When the antenna height is sufficiently large (greater than 1.2 the maximum dimension of the antenna aperture), the far-field antenna model (Equation 3.15)) can be applied for this configuration. We refer to Chapter 3 for more detailed information about this model.

5.2.2 Mixing models

In order to include the frequency dependence of the permittivity and apparent conductivity, our research used the mixing models of the effective complex permittivity instead of the electric permittivity as commonly adopted approaches. Two models were taken into account in this research: a power law model and the four-component mixing model of Wang and Schmugge [1980]. The power law model is a family of equations that relates a certain power of the effective complex permittivity (ε_e) of the mixture with the same power of its components:

$$\varepsilon_e^\gamma = \theta\varepsilon_w^\gamma + (\phi - \theta)\varepsilon_a^\gamma + (1 - \phi)\varepsilon_s^\gamma \tag{5.1}$$

in which γ is the empirical coefficient of the equation, which depends on the soil structure and its orientation with respect to the electromagnetic field. Different authors used different coefficients that provided the best fit to their data [Looyenga, 1965; Dobson et al., 1985]. In this chapter, we used the most popular coefficient in soil science, γ=0.5, which was widely known as the Complex Refractive Index Model (CRIM). CRIM was also confirmed by Shutko and Reutov [1982]; Roth et al. [1990]; Gorriti [2004], as the most suitable power law model. ϕ and θ are the porosity and volumetric water content

of soil, respectively; ε_a, ε_w and ε_s are the permittivities of air, water and soil particles in which permittivity of water is a function of frequency, expressed by the Debye equation [Debye, 1929]:

$$\varepsilon_w = \varepsilon_\infty + \frac{\varepsilon_{sp} - \varepsilon_\infty}{1 + j\omega\tau} - j\frac{\sigma_{dc}}{\omega\varepsilon_0} \tag{5.2}$$

where ω is the angular frequency; σ_{dc} is the direct current (DC) conductivity (ionic conductivity) of water in the soil pores. It is worth noting that the apparent conductivity becomes the direct current conductivity as the frequency is equal to zero; ε_0 is the electric permittivity of the free space ($\varepsilon_0 = 8.8542 \times 10^{-12}$ F/m); and ε_∞ is the relative permittivity of pure water at infinite frequency, which was determined by Lane and Saxton [1952] to be 4.9. The dependence of the water permittivity on temperature ($T°C$) is accounted for via the static relative permittivity ε_{sp} [Klein and Swift, 1977]:

$$\varepsilon_{sp} = 88.045 - 0.4147T + 6.295 \times 10^{-4}T^2 + 1.075 \times 10^{-5}T^3 \tag{5.3}$$

and relaxation time τ [Stogryn, 1970]:

$$\begin{aligned}\tau = \frac{1}{2\pi}(&1.1109 \times 10^{-10} - 3.824 \times 10^{-12}T + 6.938 \times 10^{-14}T^2 \\ &- 5.096 \times 10^{-16}T^3)\end{aligned} \tag{5.4}$$

In contrast to the power law model that considers only three components of soil materials, the mixing model of Wang and Schmugge [1980] accounts for four components. In addition to the free water, soil matrix and air, the bound water component, which is tightly bound to the soil particle surface, is included in the model. Because it is nearer to the soil particle surface, the rotation of the bound water molecules is more difficult than the free water, leading to smaller electric permittivity and lowering of their relaxation frequency [West et al., 2003]. Investigating the relationship between the complex electric permittivity and soil moisture, Wang and Schmugge [1980] found that this relationship changes after the soil moisture reaches a transition point. Consequently, they assume that the transition moisture is a division between the bound and free water components. Two mixing formulas to calculate the effective complex permittivity were also developed depending on whether the soil moisture is greater or lower than the transition moisture. In addition, due to the fact that the contacting area between water and soil particles is inversely proportional to the grain size, a clay soil has a higher bound water content, and therefore, lower permittivity than a sandy soil. This dependence of the electric permittivity on the soil type was indirectly accounted for via the empirical relationships between the transition moisture and the wilting point moisture, which is a function of the sand and clay contents. The following equations present the main

ideas of Wang and Schmugge [1980]'s soil mixing model:

$$\varepsilon_e = \theta\varepsilon_x + (\phi - \theta)\varepsilon_a + (1 - \phi)\varepsilon_s,\ for\ \theta \leq \theta_t, \tag{5.5}$$

with $\varepsilon_x = \varepsilon_i + (\varepsilon_w - \varepsilon_i)\frac{\theta}{\theta_t}\zeta$,

$$\varepsilon_e = \theta_t\varepsilon_x + (\theta - \theta_t)\varepsilon_w + (\phi - \theta)\varepsilon_a + (1 - \phi)\varepsilon_s\ for\ \theta > \theta_t \tag{5.6}$$

with $\varepsilon_x = \varepsilon_i + (\varepsilon_w - \varepsilon_i)\zeta$, where ε_x stands for the permittivity of the initially absorbed water; ε_i is the permittivity of the bound water. If assuming that water present around sand particles is bound in a mono-molecular layer, we can consider the electric permittivity of the bound water to be equal to that of ice (about 3.2), although their structures are not the same [Dirksen and Dasberg, 1993; Saarenketo, 1998; Hilhorst et al., 2001; Woodhead et al., 2003]. The wilting point (θ_p), transition moisture (θ_t) and free adjustable parameter (ζ) are estimated from the sand and clay contents as follows:

$$\theta_p = 0.068 - 0.00064S + 0.0048C \tag{5.7}$$

$$\theta_t = 0.49\theta_p + 0.165 \tag{5.8}$$

$$\zeta = -0.57\theta_p + 0.481 \tag{5.9}$$

where S and C, respectively, are percentages of sand and clay in the soil materials. In this study, because we worked only with the sandy soil, S and C are equal to 100% and 0%, respectively.

5.2.3 Parameter estimation

Objective function The water content of the soil medium is directly obtained by an inverse modeling procedure in the frequency domain as shown in Figure 5.1. Besides the water content, the unknown parameter vector **b** also contains the other variables including the sand porosity (ϕ), direct current conductivity of the water in the sand pore (σ_{dc}), and thickness of the sand medium above the PEC (h). The flowchart in Figure 5.1 begins with the estimation of the Green's function from the measured reflectivity $S_{11}(\omega)$ by using Equation (3.15). Next, the frequency dependent apparent conductivity and electric permittivity are calculated by using the Debye equation (5.2) and mixing models CRIM (5.1) or Wang and Schmugge [1980]'s model (Equations (5.5, 5.6)) given parameter vector **b**. In order to estimate the modeled Green's function, our experimental configuration is simulated by a 3-layered medium (the air, sand and PEC). The air layer has electric properties equal to those of the free space (ε_r=1, σ=0 S/m), and a thickness determined as the distance from the virtual source point to the soil surface. The PEC layer that is the lower half-space in our model, has infinite thickness, infinite conductivity and relative

permittivity of 1. Based on this conceptual configuration, the modeled Green's function can then be analytically estimated using the transverse electric and magnetic global reflection coefficients in the spectral domain [Lambot et al., 2004c, 2007]. The difference between the modeled and measured Green's function are described by an objective function which is formulated in the least square sense as:

$$\Phi(\mathbf{b}) = |\mathbf{G}_{\mathbf{xx}}^{\uparrow *} - \mathbf{G}_{\mathbf{xx}}^{\uparrow}|^T \mathbf{R}^{-1} |\mathbf{G}_{\mathbf{xx}}^{\uparrow *} - \mathbf{G}_{\mathbf{xx}}^{\uparrow}| \tag{5.10}$$

where $\mathbf{G}_{\mathbf{xx}}^{\uparrow *} = G_{xx}^{\uparrow *}(\omega)$ and $\mathbf{G}_{\mathbf{xx}}^{\uparrow} = G_{xx}^{\uparrow}(\mathbf{b}, \omega)$ are the measured and simulated complex Green's function vectors; superscript T represents the complex conjugate transpose operator; $\mathbf{R}$ is the measurement error covariance matrix. Parameter vector $\mathbf{b}$ is determined at the point where the objective function (5.10) reaches its global minimum. For this non-linear inverse problem, we followed the approach of Lambot et al. [2004c] which used the global multilevel coordinate search algorithm proposed by Huyer and Neumaier [1999] combined sequentially with the Nelder-Mead simplex algorithm given by Nelder and Mead [1965] to search for the optimal parameters. The optimization parameter space is ($0.025 < \theta < 0.3$ cm^3/cm^3; $0.3 < \phi < 0.5$; $10^{-4} < \sigma_{dc} < 10^{-1}$ S/m; $0.11 < h < 0.145$ m), which covers all possible solutions of the measurements. It is worth noting that the selected upper limit of the water content is equal to the lower limit of the porosity to make sure that the estimated water content is always smaller than the porosity.

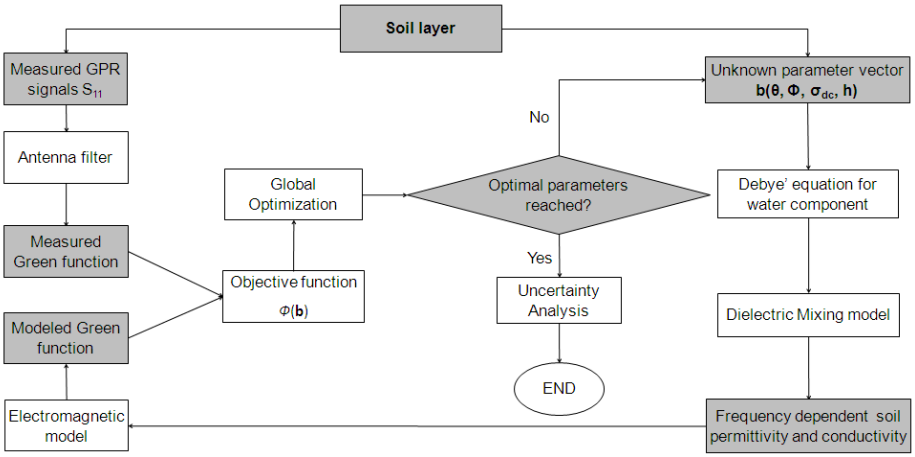

Figure 5.1. Inverse modeling flowchart to directly obtain the water content from GPR signals.

Uncertainty analysis For the nonlinear inverse problem, the uncertainty analysis can be carried out using the Monte Carlo method, which requires

to generate many realizations of the parameter sets and therefore, takes significant computing resources. In this study, we employed an approximate approach that estimates the parameter uncertainty based on the Cramer-Rao inequality [Kool and Parker, 1988; Lambot et al., 2002; Simunek and Hopmans, 2002]. For convenience, our calculation is based on the time domain data, which were transformed from those in the frequency domain by the inverse Fourier transformation. According to this approach, the parameter covariance matrix **C** can be computed as:

$$\mathbf{C} \approx \frac{\mathbf{e}^T\mathbf{e}}{n-m}\mathbf{H}^{-1} \tag{5.11}$$

where $\mathbf{e} = |\mathbf{g}_{\mathbf{xx}}^{\uparrow *} - \mathbf{g}_{\mathbf{xx}}^{\uparrow}|$ represents the difference between the modeled ($\mathbf{g}_{\mathbf{xx}}^{\uparrow *}(t)$) and measured Green's functions ($\mathbf{g}_{\mathbf{xx}}^{\uparrow *}(\mathbf{b}, t)$) in the time domain or residual vector; n and m are, respectively, the number of observations, and parameters being estimated; the elements H_{ij} of the matrix **H** are defined as:

$$H_{ij} = \frac{\partial\phi(\mathbf{b})}{\partial b_i \partial b_j} \tag{5.12}$$

The standard deviation of each optimized parameter b_i can be afterwards estimated as a root mean square of the diagonal elements of the matrix **C**:

$$s_j = \sqrt{C_{jj}} \tag{5.13}$$

Sensitivity analysis In order to evaluate the variation of the Green's function with the optimized parameters and to determine to what extent the parameters can be identified, the sensitivity analysis is a necessity. The sensitivity of a parameter is usually represented by the sensitivity coefficient, which determines the Green's function behavior around a particular point in the parameter space. In this study, we selected the region around the measured values of the porosity, water content and sand layer thickness and optimized value of the DC conductivity from 11 experiments to analyze the sensitivity. Elements S_{ij} of the sensitivity coefficient matrix **S** are given by:

$$S_{ij} = b_j J_{ij} \tag{5.14}$$

where **J**

$$J_{ij} = \frac{\partial \mathbf{G}_{\mathbf{xx}}^{\uparrow}(\mathbf{b}, t_i)}{\partial b_j} \tag{5.15}$$

is the Jacobian matrix describing the variation of the Green's function with respect to the parameter b_j at the time t_i. Due to the fact that the analytical derivative (5.15) is difficult to obtain, it is estimated using the forward finite

Table 5.1. Measured antenna heights, sand thicknesses and water contents for 11 experiments.

Experiment	Antenna height (m)	Sand thickness (m)	Water content (cm^3/cm^3)	
			Mean	Standard Deviation
1	0.253	0.131	0.0441	0.0028
2	0.287	0.132	0.0584	0.0029
3	0.318	0.129	0.066	0.0031
4	0.295	0.128	0.0701	0.0091
5	0.310	0.123	0.0787	0.0029
6	0.298	0.131	0.0982	0.0085
7	0.296	0.129	0.107	0.0087
8	0.323	0.136	0.110	0.0062
9	0.321	0.131	0.122	0.0060
10	0.282	0.129	0.148	0.0048
11	0.275	0.130	0.219	0.0036

difference approximation with a step of parameter, $\Delta b_j = 1\% b_j$. In order to compare the sensitivities of the different parameters, the average sensitivities corresponding to each parameter over the selected time frame (0–10 ns) were calculated as:

$$\xi_j = \frac{1}{n} \sum_{i=1}^{n} S_{ij} \tag{5.16}$$

It is worth noting that the sensitivity coefficients S_{ij} of the parameters b_j are normalized by b_j so that we can compare the sensitivity of the Green's function to each parameter. The parameter with the higher sensitivity coefficient have an higher chance to be identified.

5.3 Experimental results

5.3.1 Experimental setup

The experiments were conducted in controlled laboratory conditions. The size of the experiment tank was 2m x 2m plan area filled by sand with a porosity of 37.7%. The sand layer was around 13 cm thick and the relative permittivity of the dry sand is 2.64. Tap water with a DC conductivity of 0.079 S/m was used to put into the sand. For making the soil homogeneous, a concrete mixer was employed to mix the sand sample. After that, the sand surface was leveled to be flat and eliminate the impacts of surface roughness. In order to avoid the vertical heterogeneity of the water content, the GPR measurements were carried out immediately after the soil was mixed and soil surface was made flat.

The frequency-dependent complex value $S_{11}(\omega)$ was measured sequentially over the range 1–4.5 GHz with a frequency step of 2 MHz. The antenna has a length of 22 cm and an aperture dimension of 14cm x 24cm. The virtual

source point is 7 cm far away from the antenna aperture inside the antenna [Lambot et al., 2005]. We calibrated the VNA at the connection between the antenna feed point and the cable using an Open-Short-Match calibration kit.

Eleven measurements from the dry to wet states corresponding to 11 water contents were performed. For each measurement, 3 sand samples were collected at 3 locations in the region of the antenna footprint by 250 cm^3 laboratory-made metallic rings with a height of 5 cm and dried in an oven at 105^0C for at least 24 hours to determine the weight of water in the soil sample. The gravimetric water content of each sample was estimated as a ratio of the mass of water and that of the dry sand. Then, the volumetric water content was calculated by multiplying the gravimetric one by the bulk density of the sand. Finally, the volumetric water contents were averaged to obtain the mean value for each experiment.

Table 5.1 presents the information on the antenna heights, sand layer thicknesses, and water contents for each experiment. As shown in the table, the antenna was situated at heights varying from 25.3 to 32.3 cm above the sand surface, corresponding to a virtual source point situated at 32.3-39.3 cm height. The water content increased from 0.044 to 0.22 cm^3/cm^3 with a standard deviation of 0.0028-0.0091 cm^3/cm^3. It should be noted that the contributions of the horizontal variations to the measurement error were larger than that of vertical variations due to the fact that the vertical variation were averaged over the depth of the metallic ring.

5.3.2 Accuracy of water content estimation

We selected the frequency range 1–4.5 GHz for inversion to validate our approach with CRIM and Wang and Schmugge [1980] models. Moreover, for comparison purpose, the approach of Lambot et al. [2005], which assumes a linear relationship between apparent conductivity and frequency, was also applied in this study. Figures 5.2 and 5.3, respectively, show the measured and modeled Green's functions estimated by CRIM and Wang and Schmugge [1980]'s mixing models in the frequency and time domains. The WC1 experiment represents for the dry state and WC7 the wet state of sand. In both experiments, the performance of the two models in time and frequency domains was very good. In the frequency domain, the magnitude and phase angle of the modeled Green's function agreed well with those of the measured one (Figures 5.2b, 5.2d and 5.3b, 5.3d). The lower agreement was observed at the wet sand (WC7) and high frequencies (greater than around 3.2 GHz).

In the time domain, as we can see in Figures 5.2a and 5.3a, the sand surface, PEC and first order multiple reflection signals were perfectly reproduced in the first experiment. The differences between measurement and modeling were negligible. The impacts of water on the GPR signals can be witnessed in

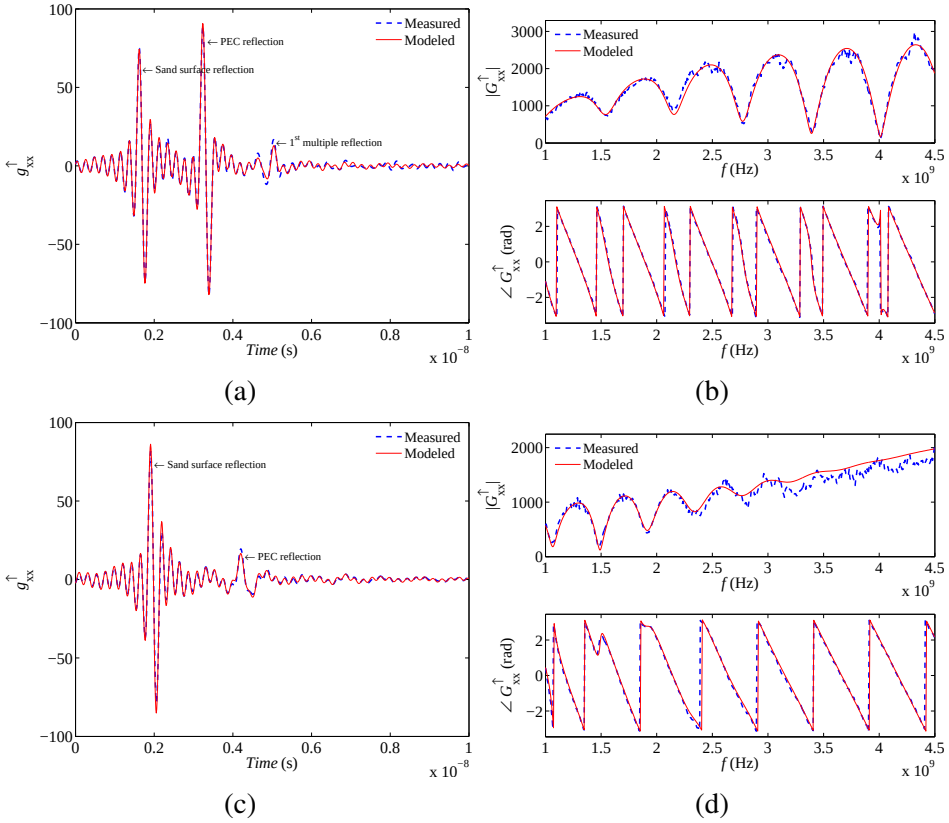

Figure 5.2. Measured and modeled Green's functions for the WC1 (θ 0.044 $cm^3.cm^{-3}$) (a and b) and the WC7 (θ=0.11 $cm^3.cm^{-3}$) (c and d) experiments. The results were obtained by coupling full-wave inversion of GPR signals with CRIM and presented in time (a and c) and frequency (b and d) domains. The time-domain Green's function ($g^{\uparrow}_{xx}$) was obtained by inverse Fourier transform from the Green's function in the frequency domain $G^{\uparrow}_{xx}$.

Figures 5.2c and 5.3c. While the amplitude of sand surface reflection signals was nearly the same as that of the WC1 experiment, the amplitude of PEC reflections reduced remarkably (82%) from 76.9 to 14 and we cannot see the multiple reflections from the sand layer in this experiment anymore. Thus, the increase of the water content caused considerable losses of GPR signals in the selected frequency range. Comparing the Green's function obtained from the two experiments, we also see that the reflection from the sand surface in the WC1 experiment arrived earlier than that from the WC7 experiment. This is because the antenna in the former experiment was located nearer the sand medium than the later one.

Figure 5.4 presents the minimum objective functions of eleven water contents achieved by inversion with the three approaches. The figure shows that,

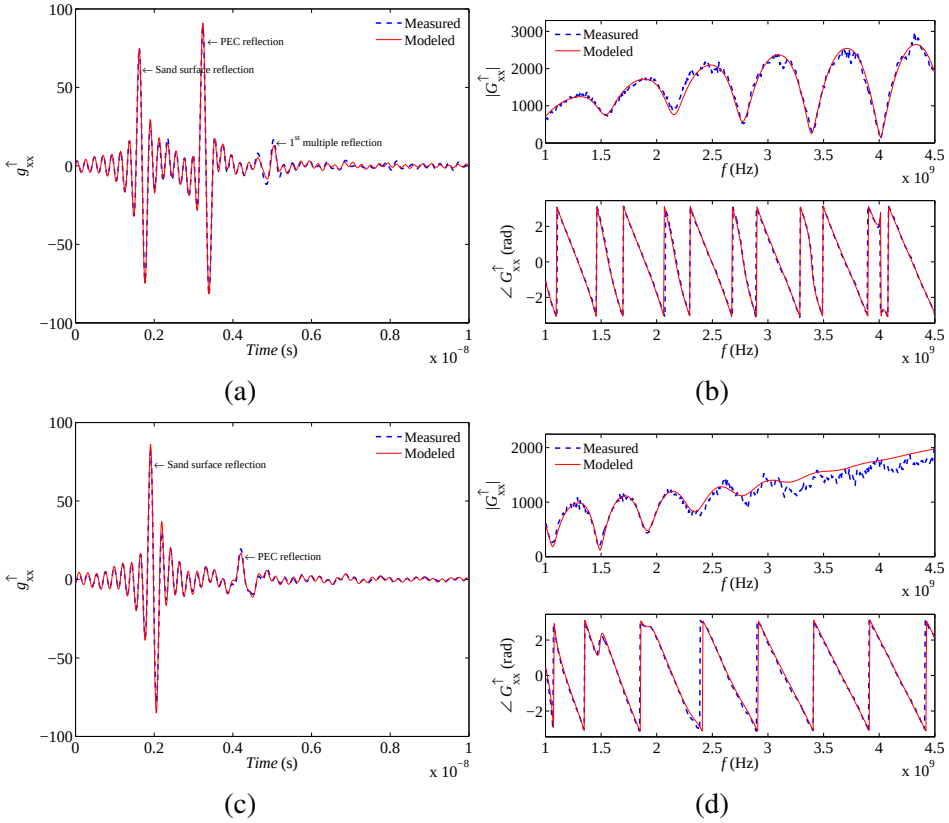

Figure 5.3. Measured and modeled Green's functions for the WC1 (θ 0.044 $cm^3.cm^{-3}$) (a, b) and the WC7 (θ=0.11 $cm^3.cm^{-3}$) (c, d) experiments. The results were obtained by coupling full-wave inversion of GPR signals with the mixing model of Wang and Schmugge [1980] and presented in time (a, c) and frequency (b, d) domains. The time-domain Green's function ($g_{xx}^{\uparrow}$) was obtained by inverse Fourier transform from the Green's function in the frequency domain $G_{xx}^{\uparrow}$.

in general, the approach of Lambot et al. [2005] provided higher errors compared to our approach and the gaps seem higher for the wetter conditions. This can be attributed to the fact that the approach of Lambot et al. [2005] assumed a linear dependence of the apparent conductivity with the frequency, while our approach accounted for the non-linear effects. In addition, it can be realized that the disagreement between measurement and model signals of all approaches increased as the water content increased. It might be explained by the more complicated interactions between water–sand and water–water in the sand mixture. Another reason may be the increase discrepancy in the hypothesis underlying the GPR model and the experimental medium related to the vertical heterogeneity of the medium with the water content. While a homogeneous layer with a unique water content value was assumed in the full-wave

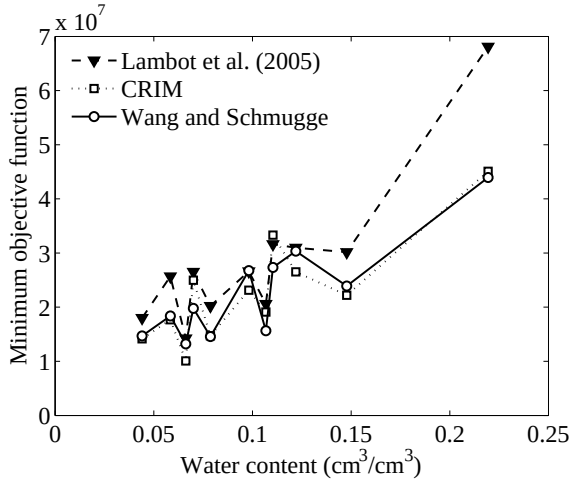

Figure 5.4. Minimum of the objective function as a function of different water contents. The results obtained by Lambot et al. [2005] approach, Wang and Schmugge [1980] model, and CRIM are compared.

GPR model, the soil is naturally wetter toward the base of the experimental tank under the effect of the hydrostatic pressure gradient. This effect is stronger as the sand water content increases, which makes the homogeneous assumption to be more violated (see Lambot et al. [2004a] for more detailed analysis on this effect). However, within the time frame to implement our experiments after the soil was mixed homogeneously, this effect is expected to be not very significant. It is worth noting as well that larger is the sand water content, larger is the reflection at the sand surface and smaller is the reflection at the bottom boundary (PEC). The permittivity (or correlated water content) information tends therefore to come from the surface reflection only with a decreasing sensitivity to permittivity for increasing permittivity, and hence, larger uncertainty. The decrease of signal/noise and lower sensitivity of the water content in the wetter condition also reduce the accuracy of the modeled water content.

The measured and optimized water contents of the approaches are compared in Figure 5.5. The approach of Lambot et al. [2005] with Topp's model underestimated the water content. For the low and medium water contents, the difference between optimized and measured values were relatively small. However, when the sand becomes wet, the disagreement between measurement and estimation using this approach was significant. Compared to Lambot et al. [2005]'s approach, CRIM and Wang and Schmugge [1980]'s mixing models presented more accurate results. The average absolute errors of water content estimation of these two models are 0.0126 and 0.0113 cm^3/cm^3, respectively, while that of Lambot et al. [2005]'s approach is 0.0156 cm^3/cm^3. The corre-

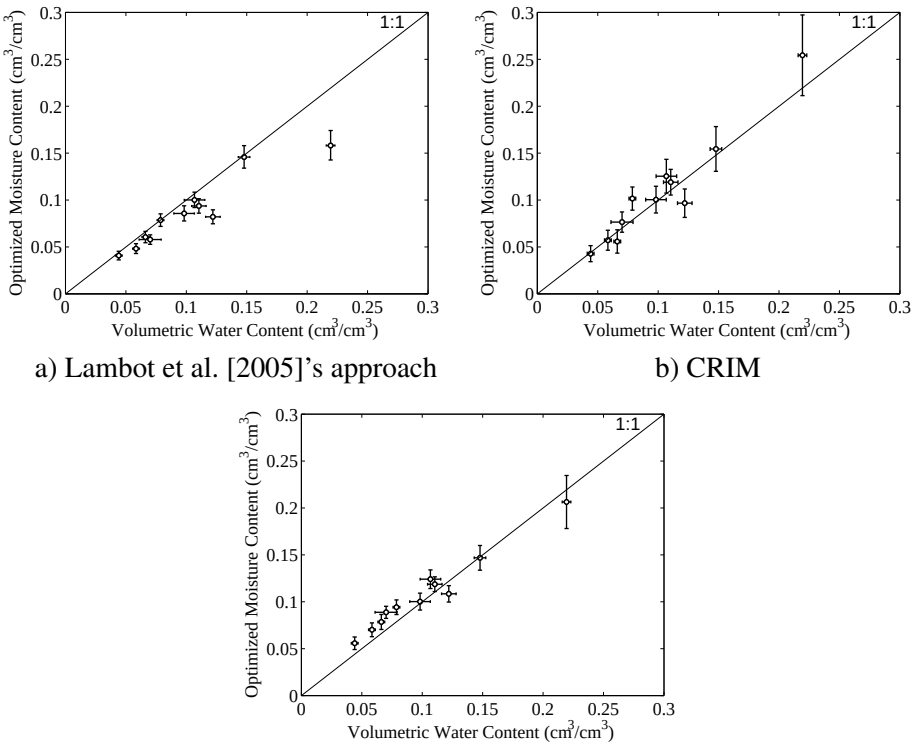

a) Lambot et al. [2005]'s approach

b) CRIM

c) Wang and Schmugge [1980]

Figure 5.5. Comparison of measured and optimized water contents. Water contents were estimated by (a) Lambot et al. [2005]'s approach, (b) CRIM, and (c) Wang and Schmugge [1980]'s model. The horizontal and vertical bars represent the confidence intervals of the measurement and inversion approximated by the standard deviations, respectively.

lation coefficients between measured and modeled water contents of our approach (0.984 for Wang and Schmugge [1980]'s model and 0.97 for CRIM) were also higher than that of Lambot et al. [2005]'s approach (0.945). There are two main reasons for this fact: 1) more complicated dependence of the permittivity and apparent conductivity are accounted for in the mixing models; and 2) by coupling the mixing models with full-wave inversion modeling, sand water content is directly estimated from GPR signals, while the approach of Lambot et al. [2005] indirectly derived this quantity via the electric permittivity. Of two mixing models, CRIM performed slightly better than Wang and Schmugge [1980]'s model for the dry sands, but for the wet sands, Wang and Schmugge [1980]'s model performance was better. Overall, Wang and Schmugge [1980]'s model predicted more accurately the water content.

Figure 5.5 also showed the confidence intervals of the measurements as

well as the inversion, which were approximated by the standard deviations. As can be seen from the figure, there is no clear trend in the measurement error. The maximum measurement error was found at the WC4 (0.0091 cm^3/cm^3) and the minimum at the WC1 (0.0028 cm^3/cm^3). This kind of error might be attributed to the heterogeneity of the sand samples at different locations and sampling errors in the horizontal plane. Comparing the confidence intervals of the inversion, we can observe that the confidence intervals of the Lambot et al. [2005] approach are more narrow than those of the mixing models. The reason for this fact is that for the approach of Lambot et al. [2005], we only considered the uncertainty of the inversion, the uncertainty of the transformation from the electric permittivity to water content by Topp's equation was not taken into account, while the mixing model approach accounted for the uncertainty of water content estimation. In addition, the uncertainty is larger when the number of parameters to estimate increases. For the two mixing models, the confidence interval of CRIM is broader than that of the Wang and Schmugge [1980]'s model for all of the measurements.

A very good agreement was also obtained for the thickness of the sand layer. The average relative error of the sand thickness for all estimations is 4.8% and the maximum error is less than 16%. As for the porosity, the optimized results were not as good as those of the water content and thickness of sand layer. The average and maximum relative errors of the estimated porosity for 11 measurements are 19.9% and 36.6%, respectively. It can be explained by the lower sensitivity of the Green's function with respect to this parameter, which is presented in the next section.

5.3.3 Frequency dependence of electric properties

In this research, the frequency dependence of the geophysical properties was considered in two different ways. Firstly, the sand water content was estimated by coupling the full-wave inversion of GPR signals with the mixing models over the entire frequency range (1-4.5 GHz). The electric permittivity and apparent conductivity of sand mixture at each frequency were afterwards obtained back from the water content by using mixing models. Secondly, the entire frequency range was divided into seven successive sub-frequency bands with steps of 400 MHz (1.0-1.4, 1.4-1.8, 1.8-2.2, 2.2-2.8, 2.8-3.2, 3.2-3.8, and 3.8-4.2 GHz). In each subband, the electric permittivity and apparent conductivity were assumed to be constant and were found by inversion of GPR signals. In this case, the optimized parameter vector was $b = [\varepsilon_r, \sigma, h]$. Figure 5.6 shows the permittivity and apparent conductivity estimated by the two approaches as a function of the frequency for eleven water contents. The mixing model used in this case was Wang and Schmugge [1980]'s model. The limited information for inversion of the short subbands sometimes caused several

unrealistic optimal values, which are not shown in the figures. Figure 5.6a implies that the permittivity slightly reduces with increasing frequency in the selected frequency range and the dry soil decreases more slowly than the wet soil. This can be explained by observing Figure 5.7a which shows the dependence of the electric permittivity of water on frequency by the Debye equation in our selected frequency range. The figure indicates that the water permittivity slowly decreases from about 80.9 at a frequency of 1 GHz to 75.4 at a frequency of 4.5 GHz.

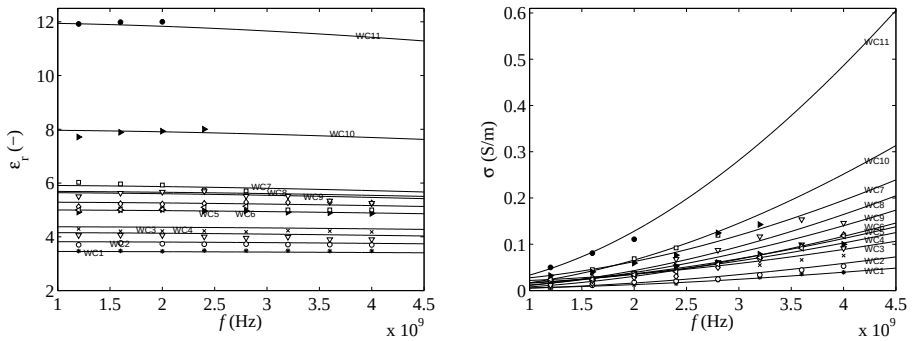

Figure 5.6. (a) The change of the sand relative permittivity and (b) apparent conductivity versus the frequency of different water contents. The solid line presents the outcomes extracted from coupling Wang and Schmugge [1980] mixing model with full-wave GPR signal inversion in the entire frequency range (1.0–4.5 GHz). Markers represent the outcomes obtained by full-wave GPR signal inversion in subsequent frequency bands (1.0–1.4, 1.4–1.8, 1.8–2.2, 2.2–2.8, 2.8–3.2, 3.2–3.8, and 3.8–4.2 GHz).

Similar to the permittivity, there was a good agreement for the apparent conductivities between the two approaches (Figure 5.6b). The gaps between them became slightly larger for the high water contents because the sand become wetter, the radar waves are more absorbed, which causes the information from reflected signals in the sub-frequency bands to be insufficient for the inversion. The figure also shows that the apparent conductivity rises significantly with the frequency, and the rising magnitude increases when the sand is wetter. These imply that the energy is lost considerably with increasing frequency and water content. The same trends were also witnessed when CRIM was adopted. Again, the dielectric losses of water component is the main factor that leads to the frequency dependence of the apparent conductivity. As shown in Figure 5.7b, the apparent conductivity of water rapidly grows from less than 0.35 S/m to greater than 5 S/m as the frequency increases from 1 GHz to 4.5 GHz.

Figure 5.8 plots the attenuation coefficient versus frequency for 11 water content measurements. The relationship between this value and the apparent

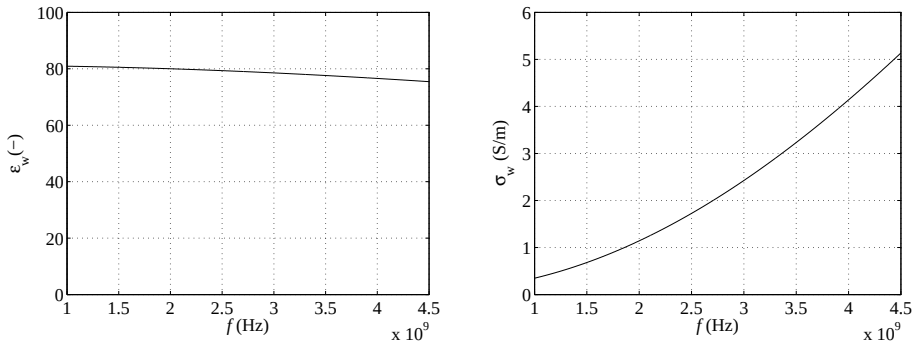

Figure 5.7. (a) Electric permittivity and (b) apparent conductivity of water computed by the Debye model at the frequency range of 1–4.5 GHz.

conductivity and permittivity is given by:

$$\alpha = \frac{1}{2}\sigma\sqrt{\frac{\mu}{\varepsilon_0\varepsilon_r}} \tag{5.17}$$

where μ is the magnetic permeability of the medium, which is assumed to be equal to that of the free space ($\mu = \mu_0 = 1.25 \times 10^{-6}$ H/m). The equation indicates that the attenuation is proportional to the apparent conductivity and inversely proportional to the permittivity. The figure shows that the variation trend of the attenuation with the frequency is similar to that of the apparent conductivity, indicating that the relationship between the attenuation and the frequency is strongly influenced by the relationship between the apparent conductivity and the frequency. However, if we observe more carefully, especially for the higher water content cases, we can see that the slope of the attenuation–frequency relation is little steeper due to the slight reduction of the permittivity with the frequency.

5.4 Uncertainty analysis

Figure 5.9 presents the sensitive coefficients of the optimized parameters for the eleven measurements. The results are calculated based on the mixing model of Wang and Schmugge [1980]. There is a consistent trend in the sensitivity of the Green's function in response to the parameters for all of the measurements. The Green's function is most sensitive with the sand thickness, especially for the dry measurements. The sensitive coefficient is up to about 126.9 and 94.3 and for the WC1 and WC2, respectively. The Green's function is also relatively sensitive with the variation of the water content. The sensitive

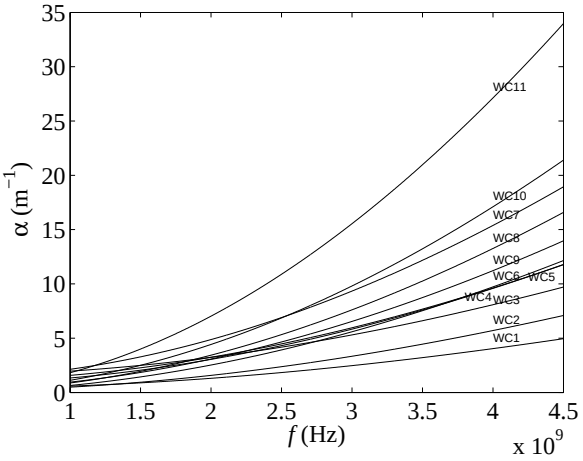

Figure 5.8. Attenuation coefficient as a function of the frequency at different states of sand moisture. The calculation is based on the mixing model of Wang and Schmugge [1980].

coefficients for the water content vary in the range 15.7–28.1, which are higher than those for the porosity (1.4–14.5). This explains for the less accurate estimated porosity compared to the sand layer thickness and water content. As for the DC conductivity (the model-derived value is less than 0.02 S/m in all experiments), the figure shows that the Green's function is insensitive with this parameter with the sensitive coefficients of all measurements lower than 0.7. Similar trends were also found in the results of the CRIM model.

5.5 Discussion

The approach was successfully validated for sandy soil. However, in reality, the soil texture is very complex. Further research will focus on the application of the integrated approach for other soil types, and in particular clay where relaxation effects are more complex due to the interactions between the soil and water molecules. Given that restricted rotation of water bound to clay minerals is a source of frequency dispersion in GPR frequency in addition to free water, the effects of the sand and clay contents on the soil electric properties are indirectly accounted for in this via the wilting point (Equation (5.7)) and transition moisture (Equation (5.8)) of Wang and Schmugge [1980]'s mixing model. By investigating the type of the soil sample, we can take into account the variation of the soil complex permittivity with the soil type. The complex electric permittivity of bound water with its own relaxation frequency should be used instead of the real one like in this study.

In real field applications, there is no perfect electric conductor (PEC) as

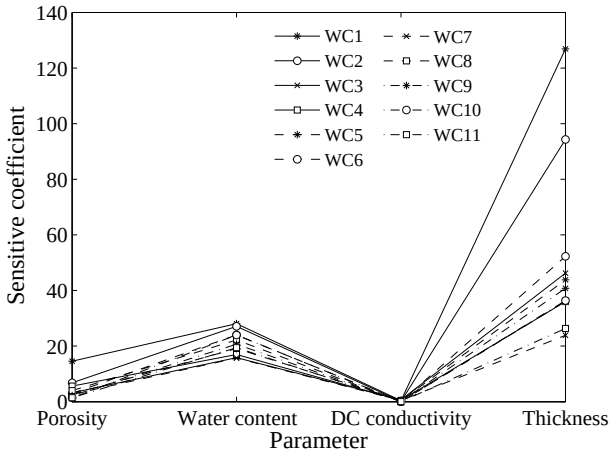

Figure 5.9. Sensitive coefficients of the porosity, water content, DC conductivity, and sand-layer thickness for 11 measurements. Our results are based on the mixing model of Wang and Schmugge [1980].

bottom boundary condition. In that case, less energy is backscattered, depending on the layer contrasts, and the information content in the radar data is therefore decreased. The technique was successfully applied in field conditions for surface soil moisture mapping Weihermüller et al. [2007]; Minet et al. [2011] and up to two layers could be reconstructed [Lambot et al., 2004b; Minet et al., 2011]. If the main interest is the very thin surface soil layer of the subsurface, the soil layer can be simulated by a homogeneous half-space below the air layer. For the case that soil moisture profile is preferred, one suggestion is to apply the water retention curve developed by van Genuchten [1980] to model the water content variation along a soil column constrained by the soil moisture at the top and the bottom of the soil column. The soil moisture values of the top and bottom layers are related to the complex permittivities by the mixing model and can be estimated by our full-wave inversion model. These implementations will increase the number of unknown parameters, which may affect the well-posedness of the inverse problems dealt with. Thus, a sensitivity analysis should be done to remove the insensitive variables. In addition, a general prior knowledge on the soil texture and structure is also important to take a reasonable constrain for the parameter space to support for the global optimization searching.

5.6 Conclusion

By coupling the dielectric mixing models of soil mixture and the full-wave inversion of zero-offset off-ground radar signals, we achieved two main improvements to enhance the accuracy of water content estimation. Firstly, the frequency dependence of the apparent permittivity and conductivity was taken into account. Secondly, unlike the currently adopted approaches, we could directly derive the water content of soil from inversion of GPR signals without the need for a specific relationship. Furthermore, in this study, we did not need to a priori specific soil porosity when the dielectric mixing models of soil were used. With these improvements together with advantages of the full-wave inversion model, our approach was successfully validated for the experimental measurements above a sandy soil layer in the laboratory conditions. The estimated Green's functions were well fitted with those of the measurements, leading to a very high accuracy of the estimated water content. The average absolute errors obtained by the approach were less than 0.013 cm^3/cm^3 and the correlation coefficients were greater than 0.97. Comparing the two mixing models, the water contents estimated by the CRIM were slightly more accurate than those of the Wang and Schmugge [1980]'s model for the dry sands, but less accurate for the wet sands. In general, performance of the Wang and Schmugge [1980]'s model is better. The accurate estimation was also obtained for the sand layer thickness with the average relative error less than 5% but less accurate for the porosity with the average relative error of about 20%. The results also pointed out that for the sandy soil, the permittivity is approximately independent of frequency and that the apparent conductivity is largely dependent on frequency. The sensitivity analysis pointed out that the Green's function is the most sensitive with the variation of the water content and sand layer thickness but insensitive with the DC conductivity. This is the reason for the very accurate estimation of the two parameters.

Chapter 6

Validation of near-field ground-penetrating radar modeling using full-wave inversion for soil moisture estimation *

Abstract We present validation results of a new ground-penetrating radar (GPR) near-field model for determining the electric properties and correlated water content of a sand using both frequency and time domain GPR systems. The antenna radiation was modeled using six source and field points, which was found to be a good compromise between high modeling accuracy and computing efficiency. We validated our model by inverting GPR data to predict the water content of a sand layer subject to 7 levels of saturation. A soil dielectric mixing model was integrated into the full-wave GPR inverse modeling to directly estimate the water content and account for the frequency dependence of the electric properties. Although the quality of the fit decreased as the antenna approached the sand surface, the results showed a close agreement between measured and modeled data, resulting in accurate estimation of the water content. The average errors of all water content estimates were 0.012 cm^3/cm^3 for the frequency domain and 0.016 cm^3/cm^3 for the time domain GPR. However, the accuracy reduced when the sand became wet. By performing numerical simulations, we found that it is due to the vertical heterogeneity of soil moisture under the effect of the hydraulic gradient. We also showed that the GPR inversion with the multi-layered soil model could account for this heterogeneity and improved the agreement between the modeled and measured GPR data as well as the accuracy of soil moisture estimation. The success of the calibration and validation in laboratory conditions demonstrates a great potential for practical applications of the radar model, notably for the digital soil mapping and non-destructive testing of materials.

*Adapted from A. P. Tran, F. André, and S. Lambot, Validation of Near-Field Ground-Penetrating Radar Modeling using Full-Wave Inversion for Soil Moisture Estimation, *IEEE Transaction on Geoscience and Remote Sensing*, Doi: 10.1109/TGRS.2013.2289952, 2014.

6.1 Introduction

Based on the rapid advancement in computing technology, many computer-based models for effectively managing land and water resources have been proposed. Yet, lack of knowledge on soil layer and its characteristics has prevented us from developing models to properly simulate the physical processes in the soil, reducing the effectiveness of the management practices [Vereecken et al., 2008]. In that respect, there is an urgent need to develop techniques allowing to characterize the soil layer in order to provide reliable data for a better management of soil and water resources.

In soil and water related studies, GPR has been employed for imaging sedimentary architecture of aquifers, mapping water table, detecting ground water contaminant, monitoring moisture dynamics and predicting spatial distribution of the physical properties controlling flow and transport (e.g., [Daniels et al., 2005; Slater and Comas, 2009]). Particularly, GPR is used to quantitatively characterize soil moisture based on the travel time or signal amplitude information. However, due to using only a part of information contained in GPR data and simplifying the wave propagation in the medium, soil moisture estimation is suffered from inherent errors. Recently, Lambot and André [2013] developed an advanced near-field GPR model for reproduction of a multilayered medium in both near- and far-field conditions. The transmitting and receiving antennas were effectively characterized by a series of source/field points and reflection/transmission transfer functions, which allows to take the maximum benefit of using analytical solutions of Maxwell' equations to noticeably reduce computation time compared to the numerical approach. This intrinsic representation of the antenna permits a complete description of wave propagation phenomena with respect to the measured signals. The authors verified the model in laboratory with water from near- to far-field conditions and observed that the model agreed very well with the experimental data. Numerical comparison between this model and the GprMax3D model [Giannopoulos, 2005] was evaluated by Tran et al. [2013c].

In this chapter, we further test the near-field radar model proposed by Lambot and André [2013] to estimate the electric properties and correlated water content of a sand subject to a series of saturation levels and using both frequency- and time-domain GPR. The transmission/reflection transfer functions were obtained by a specific optimization strategy based on the near- and far-field measurements above a copper plane. We also analyzed the relationship between the number of source/field points and the accuracy of the antenna calibration to select the configuration that best characterizes the antenna. For inversion, we integrated the dielectric mixing model of soil into the full-wave GPR inverse modeling. Finally, we proved the effect of the hydraulic gradient on the vertical heterogeneity of soil moisture by performing numerical simula-

tions, and presented the GPR inversion with a multi-layered soil profile model to account for this effect.

6.2 Methodology

6.2.1 The forward model

The forward model that relates soil moisture with GPR data contains two components. The first component is the near-field full-wave GPR model, which quantifies the relationship between the backscattered GPR data and electric properties of soil. This model is presented in Chapter 2. The second component is the petrophysical relationships, which links the electric properties with the soil water content. We followed the approach of Tran et al. [2012], which integrated a dielectric mixing model, known as the complex refractive index model (CRIM) into the full-wave GPR inverse modeling. The CRIM model assumes that the soil mixture contains three components, namely, air, water and soil particles. Therefore, its complex permittivity (ε_e) is calculated as the combination of the complex permittivity of these three components. We refer to Chapter 5 for a full description of this model.

6.2.2 Inverse modeling

The sand water content is obtained from GPR data by solving a full-wave GPR inverse problem. The main idea of the inversion is to find out the unknown parameters that provide the best agreement between modeling and measurements, which is quantitatively represented by minimizing an objective function. We formulated the objective function through the classical least-squares problem considering the measured and modeled GPR data in the frequency domain as:

$$\Phi(\mathbf{b}) = |\mathbf{S}_{11}^{*}(\omega) - \mathbf{S}_{11}(\omega, \mathbf{b})|^{T} \mathbf{C}^{-1} |\mathbf{S}_{11}^{*}(\omega) - \mathbf{S}_{11}(\omega, \mathbf{b})| \qquad (6.1)$$

where $\mathbf{C}$ is the measurement error covariance matrix; $\mathbf{S}_{11}^{*}(\omega)$ and $\mathbf{S}_{11}(\omega, \mathbf{b})$ are frequency-dependent measured and simulated GPR data vectors (arranged versus frequency). As $\mathbf{S}_{11}^{*}(\omega)$ and $\mathbf{S}_{11}(\omega, \mathbf{b})$ are complex vectors, the difference between them is expressed by the amplitude of the errors in the complex plane.

The objective function (6.1) is indirectly related to the soil properties via the unknown parameter vector $\mathbf{b} = \mathbf{b}[\theta, \sigma_{DC}, h_0]$ with h_0 being the antenna height. By minimizing objective function (6.1) using an optimization algorithm, the best-fit parameters can be obtained. The parameter space for optimization is $[0.0 < \theta < 0.4; 10^{-7} < \sigma_{DC} < 10^{-1}$ (S/m); $50\% < h_0 < 150\%$ of measured $h_0]$, which covers all possible solutions of the measurements.

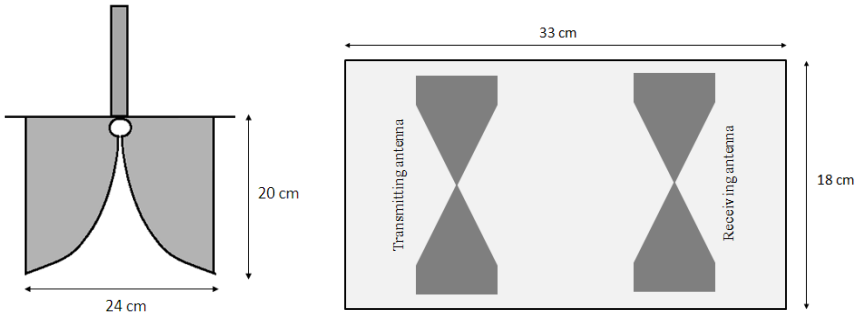

(a) FD-GPR (b) TD-GPR

Figure 6.1. Illustration of the frequency domain 1–3 GHz Vivaldi (a) and time domain GSSI GPR with a centre frequency of 900 MHz (b).

Owing to the nonlinearity of Equation (2.1) and Green's functions, the topography of the objective function in the selected search space is relatively complex. Consequently, in order to avoid local minima, it is a necessity to employ an effective global optimization strategy. The approach that sequentially combines the global multilevel coordinate search (GMCS) algorithm [Huyer and Neumaier, 1999] with the Nelder-Mead simplex algorithm (NMS) was adopted in this study.

6.3 GPR systems and antenna calibration

6.3.1 GPR systems

In this study, two GPR systems were used, working in the frequency (FD-GPR) and time domain (TD-GPR). The FD-GPR system consists of a stepped-frequency continuous-wave vector network analyzer (VNA, ZNB8, Rohde & Schwarz, Munich, Germany) and a homemade single Vivaldi antenna, which simultaneously works as the transmitter and receiver (Figure 6.1a). The antenna is made of aluminium and has an aperture of 24 cm and a height of 20 cm [Bhattacharya et al., 2010; Sarkis and Craeye, 2010]. It was connected to the reflection port of the VNA by a N-type 50 Ω impedance coaxial cable. The measurements were performed in the frequency range 1-3.0 GHz, with a step of 6 MHz. We calibrated the VNA at the connection between the antenna feed point and the coaxial cable using a standard Open-Short-Match calibration kit.

The TD-GPR system is the model SIR-20 from Geophysical Survey Systems, Inc. (GSSI, Salem, Massachusetts, USA) equipped with 900 MHz centre frequency transmitting and receiving bowtie antennas. Figure 6.1b illustrates the antenna geometry with dimensions $33 \times 18 \times 8$ cm. The dipole spacing be-

tween the transmitting and receiving antennas is 15.5 cm and the distance from the dipole to edge of the antenna housing is 7.5 cm. We recorded the GPR data with a time range of 50 ns and 512 samples per scan. For each measurement height, about 1000 traces were collected and averaged. The collected radar data in the time domain were transformed into the frequency domain using the fast Fourier transform. Only data between 0.46 and 1.34 GHz, with the highest signal-to-noise ratio, were considered, resulting in 45 observation frequencies (frequency step of 20 MHz).

For accurate calibration and validation of the antenna model, the measured antenna heights and GPR data should be known with a high level of accuracy. Therefore, in the laboratory, we established a system that remotely controls the whole measurement process from a desktop computer for rapid and accurate data acquisition. For each measurement, a step motor automatically moves the antenna to a specific location given by the operator from the computer. After the antenna reaches its location, the GPR measurement is performed, and the measured data are transferred and stored in the computer. Using this system, we can complete 100 measurements in around 1 hour and a half with measurement errors of the antenna distance lower than 1 mm.

6.3.2 Antenna calibration

In order to apply Equation (2.1) for inverse modeling to estimate the electric properties of a medium, the complex antenna characteristic transfer functions ($T_0(\omega)$, $T_i(\omega)$, $T_s(\omega)$, $\mathbf{R_s}(\omega)$) must be determined. This can be done by inversely solving Equation (2.1) for known layered medium for which the Green's functions $G_{\cdot\cdot}$ and $G^0_{\cdot\cdot}$ can be calculated and $S(\omega)$ can be measured. Such a configuration was used in this study. We carried out 100 GPR measurements corresponding to 100 antenna distances ranging from near- (0 m) to far-fields (0.72 m) over a 3×3 m^2 copper plane working as a PEC.

Both antennas associated with the time and frequency domains were modeled using an equivalent set of source/field points. These source/field point evenly distributed over the antenna aperture for the FD-GPR and along the center line of the transmitting and receiving antennas for the TD-GPR. Bilateral symmetry of the antenna was assumed, which allowed to reduce the number of complex unknowns in the antenna calibration inverse problem. The calibration of the near-field antenna model is a nonlinear inverse complex problem in which the number of transmission and reflection transfer functions rapidly increases with the number of sources/field points. Therefore, an optimization strategy, which is specifically applied for the antenna calibration was suggested by Lambot and André [2013]. In general, the calibration includes two main stages. Firstly, using the far-field measurements, we determine the far-field antenna transmission and reflection transfer functions (single source/field

point) as presented in Lambot et al. [2006a], which are then used as initial guesses for the near-field calibration. Once the initial guesses from the far-field calibration have been determined, a subset of the near-field radar data pertaining to the highest heights is added to the initial far-field subset and the antenna transfer functions are updated using local optimization. This process is repeated until the full radar dataset (100 measurements) is used. We refer to Lambot and André [2013] for more detailed information about this specific optimization procedure.

Figure 6.2 shows the variations of the correlation coefficient (r) and root mean square error (RMS) between the calibrated and measured GPR data versus the number of sources/field points for both FD-GPR and TD-GPR. The figure shows that the agreement between modeled and measured GPR data increases when the number of sources/field points increases. For the frequency domain Vivaldi antenna, the r increases from 0.9298 to 0.9999, while the RMS reduces from 0.1938×10^{-3} down to 0.009×10^{-3} as the number of source/field points varies from 2 to 8 points. For the TD-GPR, these values are 0.951–0.999 and 18.4–2.7. The figure also indicates that, when the number of sources/receivers increases from 2 to 6, the calibration error quickly reduces, and when the number of sources/receivers moves from 6 to 8, it continues reducing but with a much slower speed. For example, with the FD-GPR, the r increases 7% and the RMS decreases 10 times when the number of source/field points increases from 2 to 6, but these values are only 0.06% and 0.5 times when the number of source/field points increases from 6 to 8.

On the other hand, increasing number of source/field points results in a remarkably increasing number of transmission/reflection transfer functions, which causes non-uniqueness and time-consuming problems for the inverse modeling. Figure 6.3 compares the computation time required to complete one forward run using the 2, 4, 6 and 8 sources/field points to characterize the Vivaldi and GSSI antennas. For this example, the medium is modeled by a planar layer above a copper plane and below an air layer with a thickness of 15 cm, a electric permittivity of 7 and an electric conductivity of 0.01 S/m. The antenna height varies between 0 and 10 cm. The computation was performed on a personal computer with an Intel Core 2 Quad (Q9500, 2.83 GHz) processor. The figure shows that for both of the antennas, the computation time becomes significantly longer as the number of source/field points increases due to the fact that more Green's functions are required to calculate. Therefore, in order to keep an optimal number of antenna characteristic transfer functions, we used 6 source/field points to model the antennas in this study.

Figure 6.3 also indicates that, with the same number of source/field points, the computation time for the TD-GPR doubles that for the FD-GPR. It is because for the FD-GPR, the antenna simultaneously works as the transmitter and receiver, and thus, we do not need to evaluate the Green's functions $G_{..}$

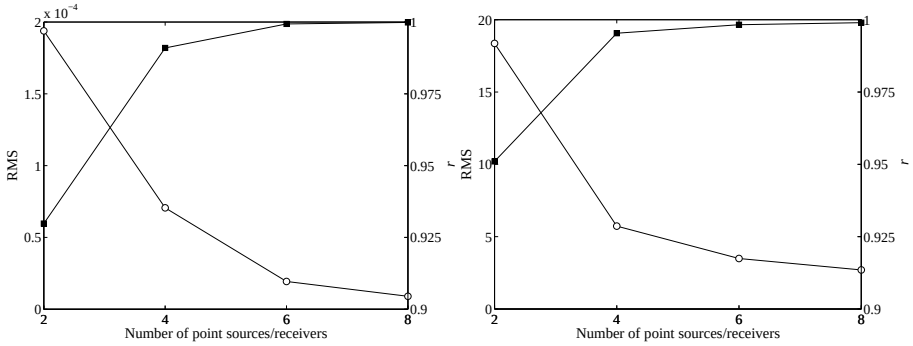

(a) FD-GPR (b) TD-GPR

Figure 6.2. Correlation coefficient and RMS between the modeled and measured GPR data as a function of number of source/field points for the FD- (a) and TD-GPR (b).

($G_{..} = G^0_{..}$), while the TD-GPR has a separate transmitter and receiver, which leads to calculate both series of Green's functions $G_{..}$ and $G^0_{..}$.

Figure 6.4 compares the calibrated and measured GPR data at 100 antenna heights above the copper plane in the time domain for the FD- and TD-GPR systems. The figure shows that for both GPR systems, the calibration closely agrees with the measurements. The relative errors in terms of signal amplitude are lower than 8% for the TD-GPR and 3% for the FD-GPR and their correlation coefficients are 0.9983 and 0.9993, respectively. We can observe, in the time domain, that the main reflections are well reproduced. A part of the internal reflections inside the antenna, which are represented by the horizontal lines in both calibrated and measured data, do not depend on the antenna height. The copper sheet reflections are observed by the curve lines, which indicates that the time for the GPR waves traveling from the antenna to the copper plane and then coming back is positively proportional to the antenna height. The model also properly simulates the multiple reflections between the antenna and the copper plane, appearing after the copper plane reflections. These reflections are particularly visible in the near-field region.

The differences between modeled and measured GPR data (Figure 6.4e, f) mainly appear at the reflections of the copper plane. They may be explained by the measurement errors of the antenna heights. The errors corresponding to the antenna heights at 0 cm are slightly larger than those observed at larger antenna heights. This arises from the much higher sensitivity of the Green's functions with respect to antenna height when this value approaches zero. Therefore, a small error on the measured antenna distance can cause a relatively large error on the Green's functions. The increasing difference between the real antenna and its model representation with decreasing antenna distance is another reason that may partly contribute to the error around 0 cm.

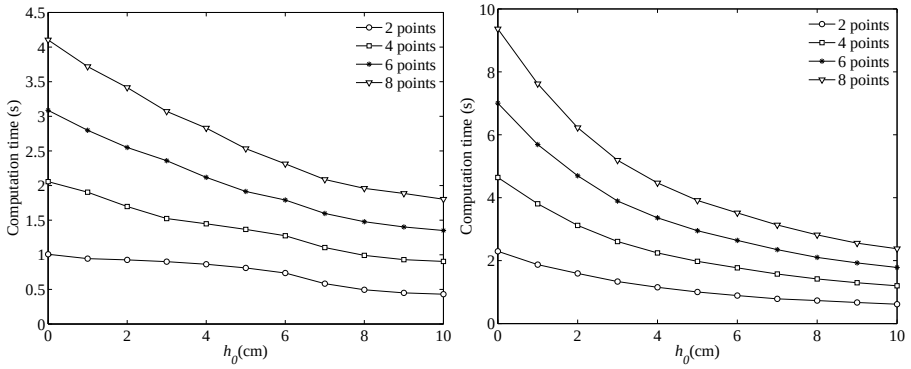

(a) FD-GPR (b) TD-GPR

Figure 6.3. The computation time required to complete one forward run as a function of the antenna height using 2, 4, 6 and 8 sources/field points to characterize the Vivaldi (a) and GSSI antenna (b). The medium is modeled by a planar layer above a copper plane and under an air layer with $\varepsilon_r = 7$, $\sigma = 0.01$ (S/m), $h_1 = 15$ cm. The antenna height ranges from 0 to 10 cm. The computation was performed on a personal computer with an Intel Core 2 Quad (Q9500, 2.83 GHz) processor.

Comparing the performance of the two antennas, we observed that the FD-GPR reproduces the measured GPR data better than the TD-GPR. This may be attributed to the lower dynamic range and larger amplitude/phase drifts for the TD-GPR. For the FD-GPR, the errors corresponding to the internal reflections are negligible as seen in Figure 6.4e, indicating that the transmitting signals are relatively stable during the measurements. However, for the TD-GPR, Figure 6.4f shows that there are still visible errors appearing in the internal reflections at several measurements (e.g., at heights of 28, 38, 42 and 60 cm), implying that the transmitting signals of the TD-GPR are not always the same. The more complex geometry of the GSSI bowtie antenna is another possible reason which may require an other distribution of the source and field points over the antenna aperture.

6.4 Validation

6.4.1 Experimental description

Figure 6.5 illustrates our laboratory experimental setup for model validation using the frequency-domain Vivaldi antenna. The same setup was also used for the GSSI antenna. Both GPR measurements were performed above a sandy soil layer subject to 7 volumetric water contents ranging from 0.0 to 0.32 cm^3/cm^3. The tank was made of wood with a horizontal dimension of 1.5×1.5 m^2 and filled by sand. The thickness of the sand layer was about

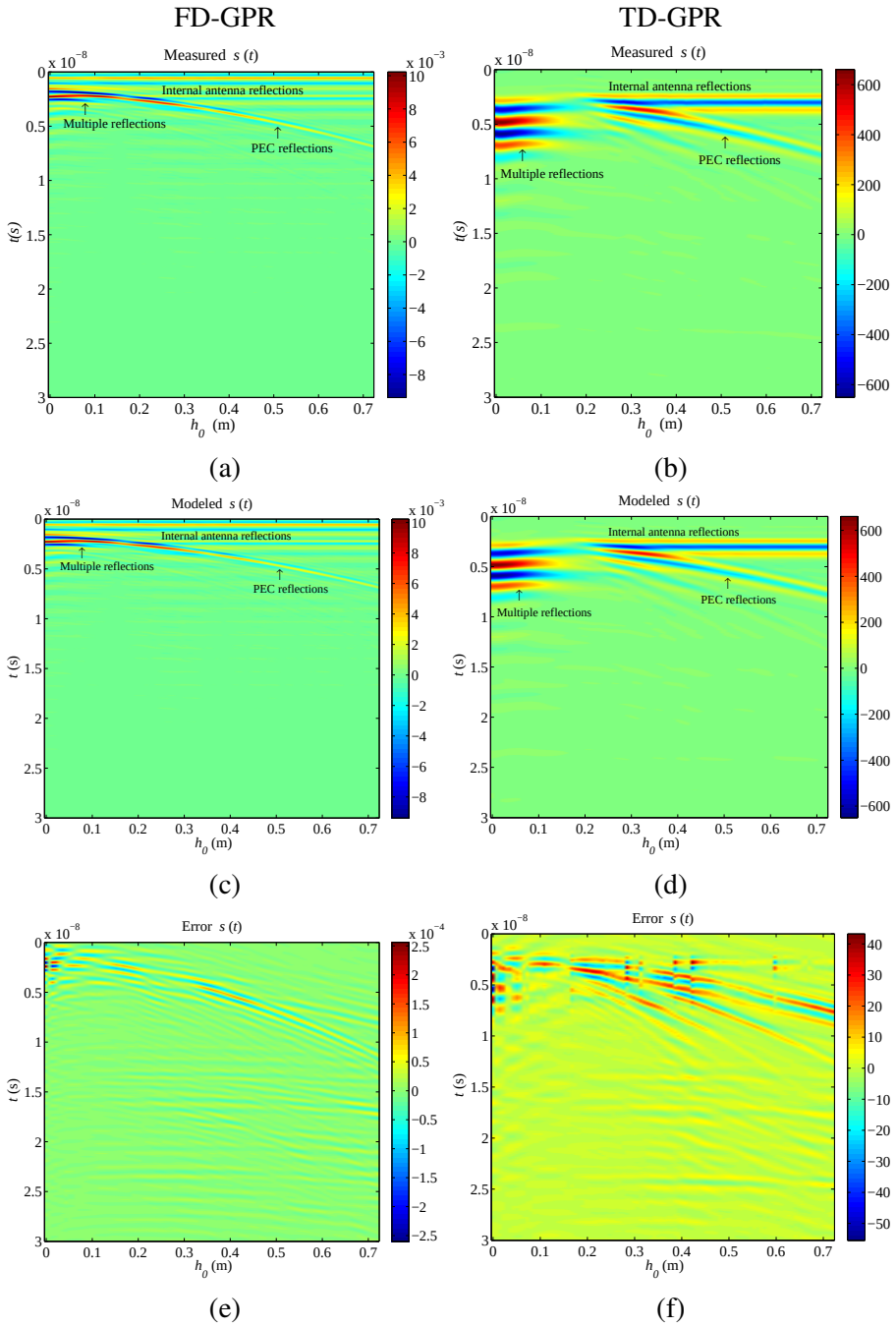

Figure 6.4. Measured (a, b) and modeled (c, d) GPR data expressed in the time domain ($s(t)$) for the antennas at different heights (h_0) over the copper sheet. (e, f) Difference between the measured and modeled data. (a,c,e) Frequency domain Vivaldi GPR. (b,d,f) 900 MHz GSSI time domain GPR.

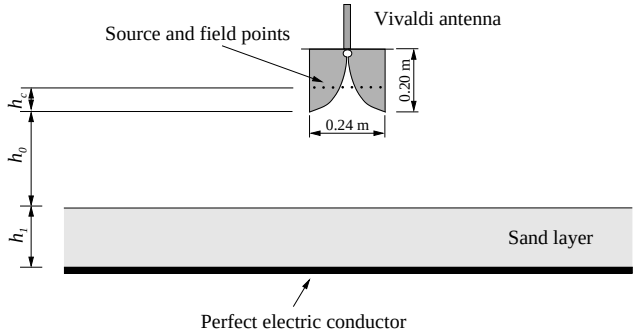

Figure 6.5. Laboratory experimental setup including the sand box made of wood, the Vivaldi antenna, the sand layer subject to different water contents and the copper plane working as a perfect electric conductor.

15 cm. Below the sand layer, a horizontal copper plane worked as a lower boundary to make sure that all underlying materials have no influence on the measured backscattered signal. The antenna was situated at 11 heights from 0 up to 10 cm above the sand surface. For each water content scenario, five sand samples were collected using 250 cm^3-laboratory-made metallic rings with a height of 5 cm and dried in an oven at 105°C for at least 48 hours. Then, the volumetric water content of the samples was estimated and averaged to obtain the measured volumetric water content.

6.4.2 Accuracy of GPR data

Figure 6.6 compares, in both frequency and time domains, the measured and modeled radar data of the WC3 ($\theta = 0.11$ cm^3/cm^3) and WC7 scenarios ($\theta = 0.32$ cm^3/cm^3) with an antenna height of 5 cm. The results were obtained by using the FD- and TD-GPR systems. The figure shows that the full-wave GPR inverse modeling closely reproduces the measured radar signals in both time and frequency domains. In the time domain (right panel), the main antenna reflections are well determined by the inversion. For the FD-GPR (Figures 6.6b and f), the Vivaldi antenna internal reflections appear at the same time and the same amplitudes at around 0–2 ns, regardless of the sand water content. After the internal reflections, we observe the sand surface reflections at 2.5 ns. The surface reflection amplitude of the WC3 is smaller than that of the WC7 scenario, which can be explained by lower permittivity of the WC3 scenario. The copper plane reflection is seen at 4.8 ns for the WC3 and 6.4 ns for the WC7 scenario. The amplitude of the copper reflection for the WC3 is much larger than that for the WC7 amplitude. It is attributed to the fact that due to its higher water content, the wave propagation velocity in the WC7 scenario is smaller and antenna attenuation is larger than in the WC3 scenario, resulting

in longer travel time and smaller amplitude of the copper reflection in the WC7 scenario.

Different from the FD-GPR, the sand surface reflections for the TD-GPR are coupled with the internal reflections at around 2.5–3 ns for both water content scenarios as shown in Figure 6.6d and h. This can be explained by the fact that, the TD-GPR has separated transmitting and receiving antennas. For a small antenna height, the travel time for internal reflection from the transmitter to receiver is not much longer than that from the transmitter to sand surface to receiver. The copper plane reflection appears at around 5.5 ns for the WC3 and 7.3 ns for the WC7 scenario. Similar to the FD-GPR, the amplitude of the copper plane reflection corresponding to the dry sand (WC3) is larger and propagation time is shorter than those of the wet sand (WC7).

Comparing the reflections from the FD- and TD- GPR, we can see that the copper reflection from the TD-GPR is clearer than those from the FD-GPR, especially for the case of the wet sand (WC7) as shown in Figure 6.6f and h. It is because the FD-GPR used a higher frequency range (1–3 GHz) than the TD-GPR (0.46–1.34 GHz), which results in the higher antenna attenuation and thus, less visible copper reflection amplitude.

The figure also shows that the modeled and measured GPR data agree better for the dry than wet sand. For example, in the case of the FD-GPR, there is no visible error in both frequency and time domains for the WC3 scenarios (Figure 6.6a, b). However, for the WC7 scenarios, the errors appear in the frequency domain, which results in the errors of amplitudes at around 2–2.8 ns in the time domain (Figure 6.6e, f). It is because under the impact of the hydraulic gradient, water moves toward the bottom sand layer, which leads to an heterogeneous water content profile with the sand (water content at the bottom is higher than that at the surface layer). For the wetter sand, this effect is stronger and it is technically more difficult to mix the sand sample. Hence, the homogeneous assumption over the sand layer is more violated and the discrepancies between modeled and measured GPR data are larger for wetter sand.

Figure 6.7 plots the modeled and measured GPR misfits versus the antenna height and sand water content. The misfits are quantified by the Normalized Root Mean Square Errors (NRMSE), which is defined as:

$$NRMSE = \frac{1}{\overline{|\mathbf{S}_{11}^{*}(\omega)|}} \sqrt{\frac{\Phi(\mathbf{b})}{n_f}} \tag{6.2}$$

where n_f is the number of stepped operating frequencies, and $\overline{|\mathbf{S}_{11}^{*}(\omega)|}$ is the mean of absolute measured GPR data over the frequency range.

As observed, both GPR systems follow a similar trend in which the NRMSE increases as the antenna approaches the sand surface. For the FD-GPR, when the antenna height is in the range from 1 to 10 cm, the NRMSE is

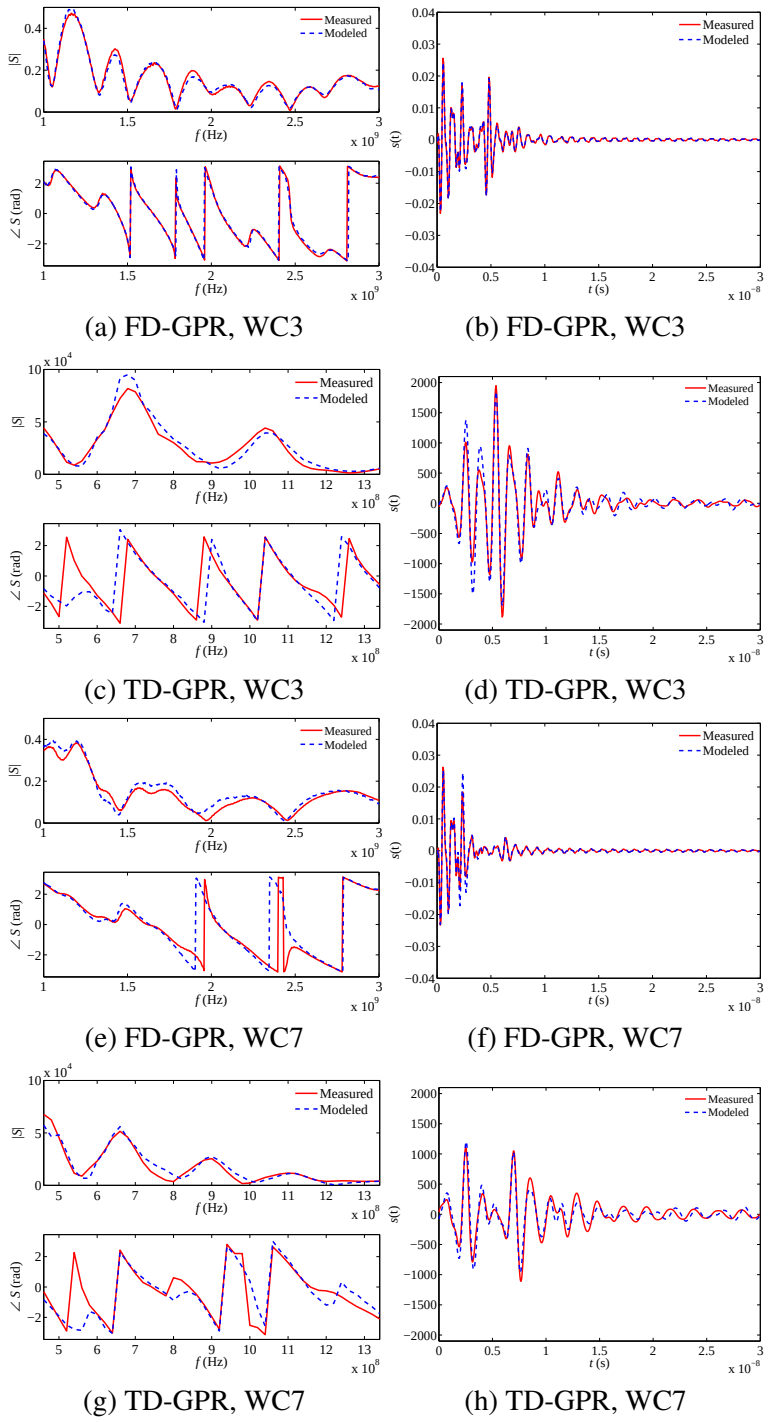

(a) FD-GPR, WC3 (b) FD-GPR, WC3

(c) TD-GPR, WC3 (d) TD-GPR, WC3

(e) FD-GPR, WC7 (f) FD-GPR, WC7

(g) TD-GPR, WC7 (h) TD-GPR, WC7

Figure 6.6. Measured and modeled GPR data in both frequency (left) and time (right) domains for the WC3 (a, b, c, d) and WC7 (e, f, g, h) experiments with an antenna height of 5 cm. The results were obtained by the frequency-domain Vivaldi (a, b, e, f) and time-domain GSSI GPR systems (c, d, g, h).

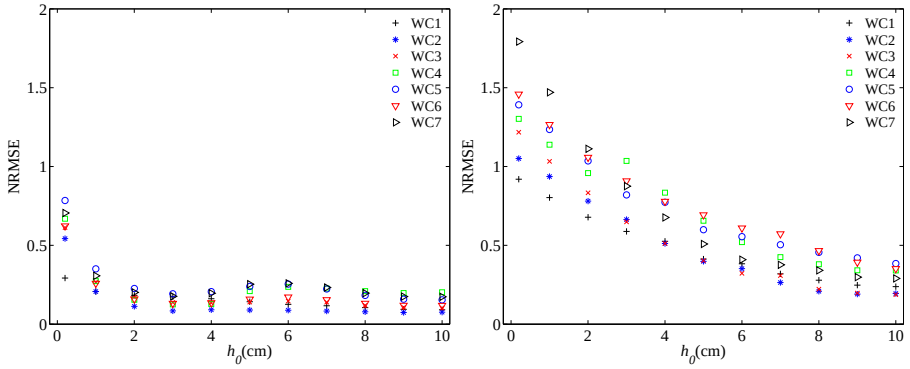

(a) FD-GPR (b) TD-GPR

Figure 6.7. The change of the difference between modeled and measured GPR data of different water content in the frequency domain, estimated by Equation (6.2) corresponding to the (a) FD- and (b) TD-GPR.

relatively small and fluctuates from around 0.1 to 0.3. At these antenna heights, the inverse modeling results well agree with the measurements. However, for a height of 0 cm, except for the WC1 scenario, the NRMSE are larger than 0.5 and up to around 0.78.

For the TD-GPR, the NRMSE gradually increases when the antenna height reduces from 10 down to 0 cm. At an antenna height of 10 cm, the NRMSE varies from 0.24 to 0.38. At a height of 0 cm, these values increase up to 0.92–1.79. It is because when the antenna approaches the medium, the calibrated transmission/reflection transfer functions are less accurate as shown in Figure 6.4. Other factors can also contribute to the misfits are: errors of the inverse modeling, measurement errors of GPR data and antenna height.

With respect to the relationship with the sand water content, Figure 6.7 indicates that, for both GPR systems, the NRMSE is larger for the wetter than drier sand. As explained, when the sand sample is wet, the homogeneity of the sand sample reduces. The reason is caused by the fact that when water content increases, the hydraulic conductivity becomes significant and the initially homogeneous profile rapidly evolves to the water retention curve profile.

6.4.3 Estimation of water content

Figure 6.8 compares the GPR-derived and sampled volumetric water content for the 7 saturation scenarios ranging from dry ($\theta = 0$ cm^3/cm^3) to wet sand ($\theta = 0.32$ cm^3/cm^3). The GPR water content was estimated by both FD- and TD-GPR systems. The GPR water content of each scenario was estimated by averaging the optimized values obtained by inverting GPR data at 11 antenna heights from 0–10 cm. The upper and lower limits of each scenario were

determined by adding and subtracting twice the standard deviation from the average value. The figure shows that the water content values obtained by both GPR systems are in close agreement with the reference sampling ones. The average and maximum errors of the GPR water content for the FD-GPR are 0.012 and 0.045 cm^3/cm^3. These errors are, respectively, 0.016 and 0.034 cm^3/cm^3 for the TD-GPR.

Comparing the water content obtained from two GPR systems, we observe that the FD-GPR generally provides better estimation than the TD one. Except for the WC7 scenario, the water content values estimated from the FD-GPR are more suitable with the sampling ones than those obtained from the TD-GPR. This can be explained by the fact that the calibrated reflection/transmission transfer functions better characterizes the Vivaldi antenna. However, for the wet scenario (WC7), although the two GPR systems underestimate the water content, the TD-GPR provides more accurate estimation. It is because the FD-GPR uses a high frequency range, which makes the antenna signals attenuate significantly, especially in wet conditions, and therefore, its GPR data are insufficient for accurate water content estimation.

The figure also shows that there is not much difference in estimated water content among the measurements at different antenna heights. The standard deviation obtained from 11 antenna height measurements ranges from 0 to 0.005 cm^3/cm^3 for the FD-GPR, and from 0.001 to 0.007 cm^3/cm^3 for the TD-GPR. In general, the standard deviation corresponding to the wet is higher than the dry sand. It is attributed to the fact that the antenna intrudes more deeply when it is nearer the sand surface, while the differences between upper and lower layers increase with increasing water content. Consequently, the difference among water content values obtained from different antenna heights is larger for the wetter sand (water content estimated from the low antenna height measurement tends to be larger than from the high one).

6.5 Soil moisture profile estimation

As stated in the previous section, one of the main factors influencing on the agreement between measured and modeled GPR data as well as the accuracy of water content estimation is the vertical heterogeneity of sand caused by the hydraulic gradient. In this section, we showed this effect using numerical simulations and accounted for it by performing the full-wave GPR inversion with a multi-layered soil profile model instead of 1 homogeneous layer model.

For numerical experiments, we employed the Hydrus-1D [Šimunek et al., 2009], which is a hydrodynamic model simulating the spatiotemporal dynamics of soil moisture profile in the unsaturated zone, to generate numerical soil moisture data. In order to be compatible with the laboratory experiments, we

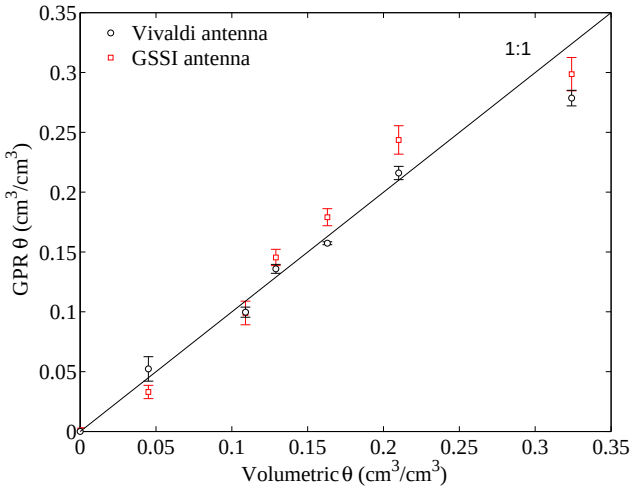

Figure 6.8. Comparison of sampled and GPR-estimated water content values with 7 saturation levels. The GPR water content was estimated by averaging 11 values at antenna heights from 0 to 10 cm. The vertical bar presents twice the standard deviation of the GPR water contents.

considered a synthetic sand column with a thickness of 15 cm and discretized it into 15 equidistant layers. The up and lower boundaries of the simulation domain were fixed at zero fluxes, i.e., no water comes in and out of the sand column. The soil hydraulic parameters for the experiments are taken from Carsel and Parrish [1988] for sandy soil: $\theta_r = 0.045$ cm^3/cm^3, $\theta_s = 0.43$ cm^3/cm^3, $n = 2.68$, $\alpha = 0.145$ cm^{-1}, $K_s = 0.495$ cm/min and $l = 0.5$, in which θ_r and θ_s are, respectively, the residual and saturated soil water content, n and α are the parameters in the van Genuchten retention function [van Genuchten, 1980], K_s is the saturated hydraulic conductivity and l is tortuosity parameter in the conductivity function. Because in our laboratory experiment, it took around 10 minutes to set up the GPR measurements, we also set the simulation period for the numerical experiments at 10 minutes. To illustrate the effect of the hydraulic gradient, the soil moisture condition at the beginning of the simulation period (initial condition) was assumed to be homogenous. We used two scenarios for the initial condition: $\theta(t = 0) = 0.07$ cm^3/cm^3 for the dry sand and $\theta(t = 0) = 0.3$ cm^3/cm^3 for the wet sand.

Figure 6.9 presents the soil moisture profiles at the beginning (t=0) and end of the simulation period (t=10 minutes) for the dry and wet sand scenarios. The figure shows that during the simulation period, while there is only a negligible change in the soil moisture profile for the dry scenario, a considerable change from the initial soil moisture occurs for the wet one. It is because when soil moisture is wet, the gravitational head is significantly larger than the soil matric potential, and therefore, it is much easier for water to move down. By contrast,

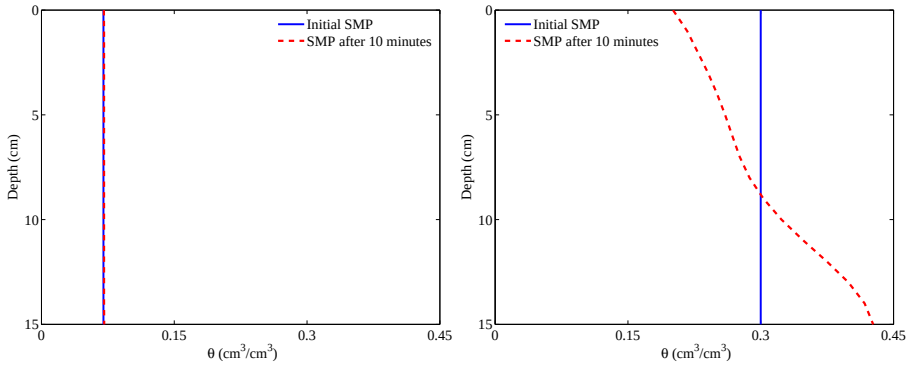

Figure 6.9. Soil moisture profile at the beginning (solid blue line) and end (dashed red line) of the simulation period for the dry (left) and wet (right) scenarios. The initial soil water content profile is constant at 0.07 cm^3/cm^3 for the dry and 0.3 cm^3/cm^3 for the wet scenario.

when sand is dry, the soil matric potential is very high, making it balance with the gravitational one and it is much difficult for water to move downward.

In order to evaluate the effect of the hydraulic gradient on the GPR inversion, we used the forward near-field GPR model (2.1) to produce numerical GPR data for both FD- and TD-GPR from the synthetic soil moisture profiles generated by the Hydrus-1D model. After that, using these data, we performed the full-wave GPR inversion with the 1-layered soil model as presented in section 2 to estimate soil moisture. In addition, for improving the agreement between modeled and measured GPR data, we also performed the inversion with the multi-layered soil profile model, which assumes that the relationship between the soil moisture and soil depth is formulated by the van Genuchten retention curve [van Genuchten, 1980]:

$$\theta = \theta_l + (\theta_u - \theta_l)(1 + |\alpha_s(L - z)|^{n_s})^{-m_s} \tag{6.3}$$

where θ_l and θ_u are, respectively, the lower and upper limits of the soil moisture profile, L denotes the length of the soil column and z is the soil depth, taking positive downward. α_s, n_s, m_s are the parameters controlling the shape of soil moisture profile with $m_s = 1 - \frac{1}{n_s}$. Subscript s implies that parameters α_s, n_s and m_s are not necessarily equal to their counterparts α, n and m of the sand water retention curve. In the electromagnetic model, the soil profile were simulated by 15 dielectric layers with a thickness of 1 cm. This multi-layered soil was situated above a PEC and below an air layer. We assumed that the DC conductivity of water in all soil layers (σ_{DC}) were identical. For this electromagnetic model, the unknown parameter vector in the inverse problem (6.1) was $\mathbf{b} = \mathbf{b}[\theta_l, \theta_u, \alpha_s, n_s, \sigma_{DC}, h_0]$. The spaces for parameter searching were set at $0 < \theta_l < 0.2$ (cm^3/cm^3), $0.2 < \theta_u < 0.45$ (cm^3/cm^3), $0 < \alpha_s < 10$

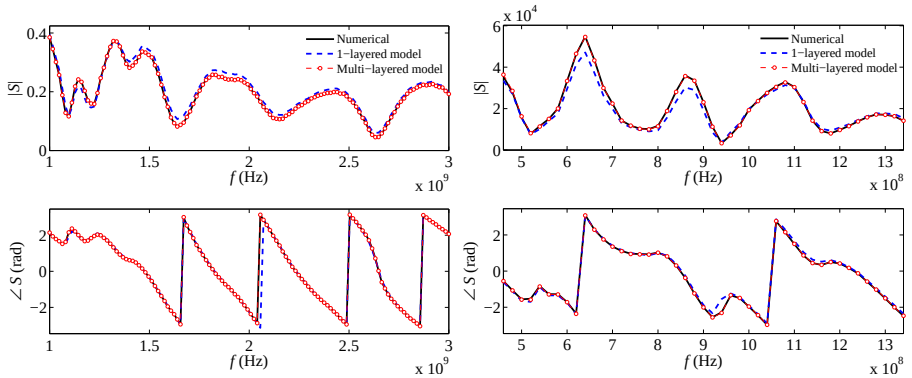

a) FD-GPR b) TD-GPR

Figure 6.10. Modeled and numerical GPR data corresponding to the wet scenario for FD- (a) and TD-GPR system (b). The modeled data were obtained from 1-layered (dashed blue line) and multi-layered (dashed red line) soil model.

(cm^{-1}), $1 < n_s < 30$, $10^{-7} < \sigma_{DC} < 0$ (S/m); $50\% < h_0 < 150\%$ of measured h_0.

Figure 6.10 compares the modeled and numerical GPR data in the frequency domain for the FD- and TD-GPR systems, in which the modeled data were obtained from both 1- and multi-layered soil models for the wet scenario with a synthetic antenna height of 9 cm. We did not compare the results for the dry scenario because there is not much difference among soil moisture at different layers and thus, the GPR inversion with 1-layered model is reasonable. The figure indicates that while there is a perfect agreement between the modeled and numerical GPR data corresponding to the multi-layered soil model, errors are visible for the case of the 1-layered soil model. Consequently, inclusion of the vertical variation of soil moisture in the full-wave GPR inversion can help to reduce the disagreement between the modeled and measured GPR data.

The estimated and synthetic soil moisture for the wet sand scenario is shown in Figure 6.11. For the 1-layered soil model, the soil moisture estimated by both FD- and TD-GPR systems is around 0.3 cm^3/cm^3, which is equal to the initial soil moisture and average value of the soil moisture profile. For the multi-layered soil model, the soil moisture profiles estimated with the FD- and TD-GPR systems and the synthetic one closely agree with each other. Compared to the FD-GPR, the TD-GPR provides a slightly better estimation for the fact that it operates at lower frequencies, which makes the antenna attenuation smaller, and therefore, its data contain more information about soil moisture profile. It is worth noting that although there is no difference between the modeled and numerical GPR data, the estimated and synthetic soil mois-

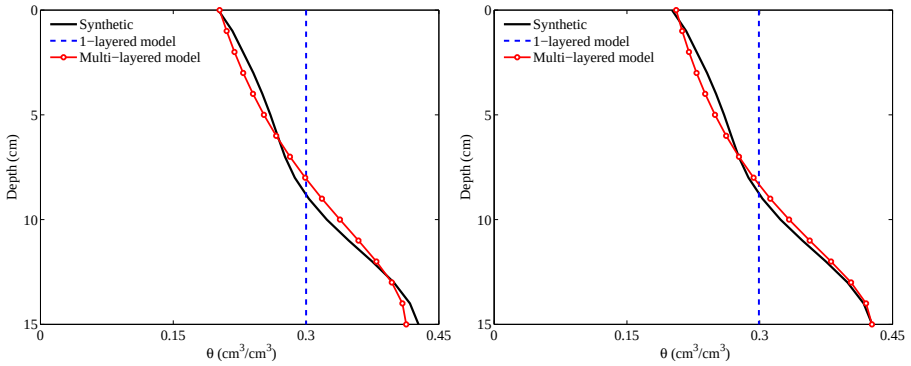

Figure 6.11. Comparison of the modeled and synthetic soil moisture profile corresponding to the wet scenario for the FD- (a) and TD-GPR (b) system. Soil moisture was obtained by the full-wave GPR inversion with the 1-layered (dashed blue line) and multi-layered (circle red line) soil model.

ture profiles are not identical. It is due to the nonuniqueness of the inverse problem caused by the correlation between the soil moisture at different layers in the soil profile.

Finally, we performed the full-wave GPR inversion with the multi-layered soil profile model (6.3) to reconstruct the soil moisture profile for the WC7 scenario in laboratory conditions. We also discretized the sand layer into 15 layers. Figure 6.12a, b, respectively, shows the modeled and measured GPR data with an antenna height of 9 cm for the FD- and TD-GPR systems. For comparison, we also present the GPR data obtained by the inversion with the 1-layered soil model. The figure indicates that for both GPR systems, the agreement between modeled and measured GPR data is significantly improved when the vertical variation of soil moisture profile was accounted for. While there are some clear discrepancies between the modeled and measured GPR data for the 1-layered soil model, we cannot observe any errors for the multi-layered soil profile model.

Figure 6.12c, d presents the soil moisture estimated from the FD- and TD-GPR systems using the 1-layered and multi-layered soil profile models. The figure shows that with the 1-layered soil model, both GPR systems provide a similar soil moisture value at approximately 0.3 cm^3/cm^3. With the multi-layered soil profile model, the soil moisture profile obtained by the two systems exhibits a significant variation. Between depths of 0 and 8 cm, soil moisture rapidly increases from around 0.12 to 0.34 cm^3/cm^3. From 8 cm down to the bottom of the sand column, it remains relatively stable. The vertical variation of soil moisture implies that when the soil becomes wet, the effect of hydraulic gradient is considerable and it is necessary to take into account the vertical

variation of soil moisture by performing the inversion with the multi-layered soil profile model.

6.6 Summary and conclusion

In this chapter, we presented validation results of the full-wave GPR model to estimate the sand water content in near-field conditions using both frequency and time domain GPR systems. The antennas were effectively modeled by a series of infinitesimal source/field points and the transmission/reflection transfer functions. With this model, the fields over the antenna aperture is locally decomposed into several planar fields, which enables us to simultaneously ensure a high accuracy and optimal computation time.

The transmission and reflection transfer functions of the model were determined by a specific optimizing strategy based on various measurements from near- to far-field above a copper plane. The calibration results showed that when the number of source/field points increases from 2 to 8, the modeled and measured GPR data agree better. However, for the sake of computing time and limiting the complexity of the inverse calibration problem, we selected 6 points to characterize both Vivaldi and GSSI antennas. Afterwards, the model was used to predict the water contents of a sand with different saturation levels in laboratory conditions by inverting GPR data. In both time and frequency domains, the model performances in terms of GPR signals was relatively good but reduced when the antenna approached the sand surface. The estimated water content well agreed with the measured ones. The average difference between the GPR and sampling water content was 0.012 cm^3/cm^3 for the FD-GPR, and 0.016 cm^3/cm^3 for the TD-GPR.

When the sand is wetter, the disagreement between the modeled and measured GPR data increased, and the accuracy of the soil moisture estimation reduced. By performing numerical simulations, we found that for the wet sand, the gravitational potential outweighed the soil matric one and therefore, it was easy for water to move down, resulting in the vertical heterogeneity of the sand moisture. As a result, the full-wave GPR inversion with the 1-layered soil model was not adequate to account for this heterogeneity. In order to solve the problem, we used the multi-layered soil model, which formulates the variation of soil moisture with soil depth by the van Genuchten retention curve [van Genuchten, 1980] to simulate the soil moisture profile. Comparing to the 1-layered soil model, the agreement between modeled and numerical (or measured) GPR data and accuracy of the soil moisture estimation obtained by this model were considerably improved.

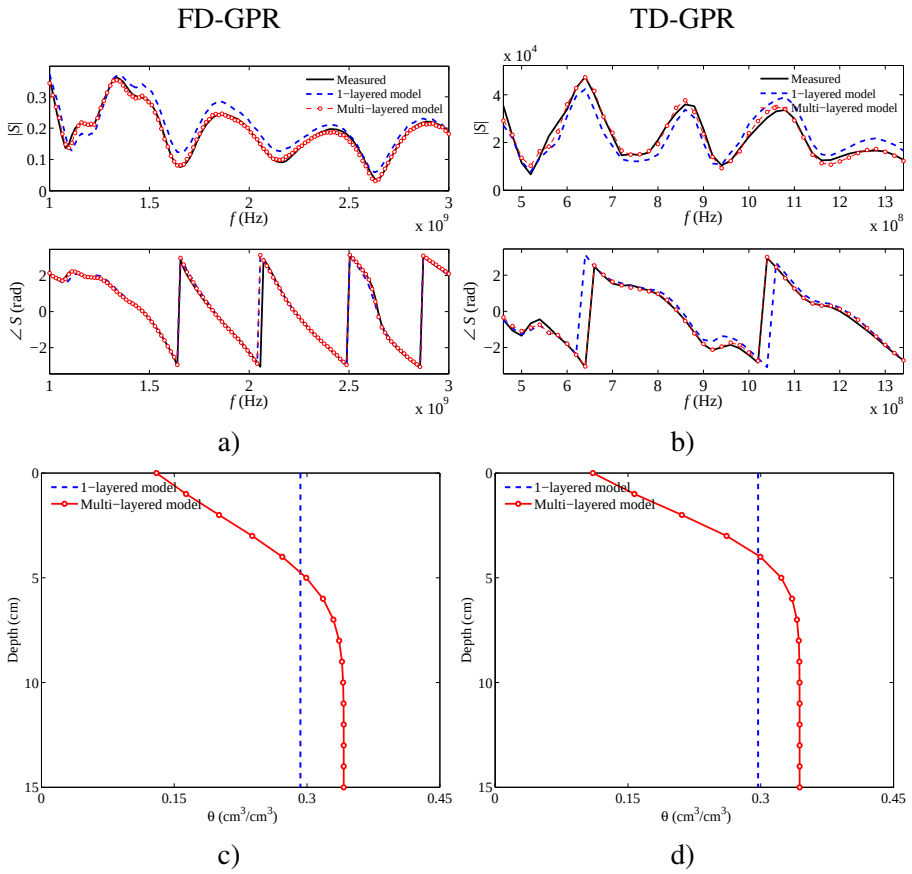

Figure 6.12. Comparison of the modeled and measured GPR data corresponding to the WC7 laboratory scenario with an antenna height of 9 cm for the FD- (a) and TD-GPR (b) systems. The modeled GPR data were obtained from the inversion with 1-layered (dashed blue line) and multi-layered (circle dashed red line) soil model. Soil moisture profile estimated from the FD- (c) and TD-GPR (d) system using 1-layered (dashed blue line) and multi-layered (circle red line) soil model.

Chapter 7

Soil moisture profile reconstruction from ground-penetrating radar data: A maximum likelihood ensemble filter approach*

Abstract In this chapter, we propose a data assimilation framework based on the maximum likelihood ensemble filter algorithm to correct the soil moisture profile prediction using ground-penetrating radar (GPR) data. In this framework, a hydrodynamic model is used to simulate the spatiotemporal dynamics of the soil moisture profile, and a radar electromagnetic model and petrophysical relationships to link the state variable with the observation data, which enables us to directly assimilate the GPR data. Instead of using the surface soil moisture only, the approach allows to use the information of the whole soil moisture profile for the assimilation. We validated our approach through a synthetic study. We constructed a synthetic soil column with a depth of 80 cm and analyzed the effects of the soil type on the data assimilation by considering 3 soil types, namely, loamy sand, silt and clay. The assimilation of GPR data was performed to solve the problem of unknown initial conditions. The numerical soil moisture profiles generated by the Hydrus-1D model were used by the GPR model to produce the "observed" GPR data. The results show that the soil moisture profile obtained by assimilating the GPR data is much better than that of an open-loop forecast. Compared to the loamy sand and silt, the updated soil moisture profile of the clay soil converges to the true state much more slowly. Decreasing the update interval from 60 down to 10 h only slightly improves the effectiveness of the GPR data assimilation for the loamy sand but significantly for the clay soil.

*Adapted from A. P. Tran, M. Vanclooster, and S. Lambot, Improving soil moisture profile reconstruction from ground-penetrating radar data: a maximum likelihood ensemble filter approach, *Hydrology and Earth System Sciences*, 17, 2543-2556, doi:10.5194/hess-17-2543-2013,2013.

7.1 Introduction

Understanding the dynamics of soil moisture at the shallow unsaturated zone is essential for hydrological, meteorological and agricultural research. As a result, development and integration of measurement techniques for quantitative characterization of the shallow unsaturated zone soil moisture is an urgent need.

With recent advancements in electromagnetic theory and computing technology, GPR has become a popular technique to characterize soil moisture with a highly spatial resolution at field scale [Huisman et al., 2003; Robinson et al., 2008b]. Lambot et al. [2004c] developed an advanced method known as full-wave inversion of GPR data, which permits one to use all GPR information for soil moisture estimation. However, for 2-layered or soil moisture profile models, the soil moisture estimation at the lower layers was not adequately accurate due to the ill-posed inverse problem caused by too many unknown parameters and the low sensitivity of GPR data with the electric properties at deeper layers [Lambot et al., 2004b; Minet et al., 2011]. Efforts have been made to increase the accuracy of the soil moisture profile estimation by using the time-lapse GPR data to constrain a soil hydrodynamic model [Kowalsky et al., 2005; Lambot et al., 2006b, 2009; Jadoon et al., 2008, 2012; Looms et al., 2008; Dagenbach et al., 2013]. A joint inversion procedure based on integrated geophysical and hydrodynamic models was demonstrated to optimally estimate the soil unsaturated hydraulic parameters. However, in cases where the soil moisture profile slightly varies with the soil depth, some parameters suffered from relatively large uncertainties due to their low sensitivity to the radar data [Lambot et al., 2006b].

With the development of the data assimilation algorithms, there have been increasingly intensive studies on assimilation of remote-sensed data to improve soil moisture profile prediction [Loew, 2008]. For instance, Hoeben and Troch [2000] and Walker et al. [2001] applied the extended Kalman filter (EKF) to retrieve the soil moisture profile from the near-surface soil moisture measurements. Reichle et al. [2002], Das and Mohanty [2006], De Lannoy et al. [2007a], Huang et al. [2008], Crow et al. [2008] and Draper et al. [2012] assimilated the soil moisture data from remote sensing measurements with the ensemble Kalman filter (EnKF). Application of the variational assimilation methods for updating the soil moisture profile was performed by Reichle et al. [2001] and Sabater et al. [2007]. Montzka et al. [2011] employed the particle filter technique to simultaneously update the soil hydraulic properties and soil moisture profile with the measurements from geophysical and satellite measurements. Most of these studies used only the surface soil moisture, which is obtained by processing the remotely sensed data, to update the whole soil moisture profile. This reduces the improvement of the assimilation due to lack

of information for the assimilation [Pauwels et al., 2007; Das et al., 2008]. In addition, errors caused by the conversion from the remote-sensed data to surface soil moisture also contribute to the smaller effectiveness of the assimilation. There are only few researches that directly use the geophysical data for the assimilation [e.g., Reichle et al., 2002; Huang et al., 2008; Rings et al., 2010]. Reviews on the assimilation of geophysical techniques to soil moisture profile are given in Loew [2008], Reichle [2008] and Vereecken et al. [2008].

In this chapter, we propose a new sequential assimilation procedure to raise the accuracy of the soil moisture profile prediction using time-lapse GPR data. According, whenever GPR measurements are available, they will be assimilated to correct the soil moisture profile estimated by the hydrodynamic model, Hydrus-1D [Šimunek et al., 2009]. The soil moisture profile are linked to GPR data by an observation operator which consists of the GPR model and petrophysical relationships. The assimilation was performed within the maximum likelihood ensemble filter (MLEF) framework developed by Zupanski [2005], for which the problem of the nonlinear observation operator is solved much more effectively than the EnKF techniques. The method estimates the optimal state as the maximum of the probability density function (PDF) instead of the minimum variance like in most of the other ensemble data assimilation methods [Zupanski et al., 2008]. Direct assimilation of GPR data is a prominent advantage of our approach. It avoids solving the time-consuming inverse problem as well as the estimation errors of the soil moisture caused by inversion. In addition, instead of using only surface soil moisture, the approach allows one to use the information of the whole soil moisture profile, which is reflected via the ultra-wideband (UWB) GPR data, for the assimilation. The use of the UWB antenna in this study is also an advantage as it provides more information about a soil moisture profile with better depth resolution in comparison to other classical remote sensing techniques [Lambot et al., 2004b]. Consequently, this approach is expected to provide better estimation than the use of the surface soil moisture only. The assimilation procedure was numerically tested by synthetic simulations to solve the "wrong" initial conditions. The effectiveness of the GPR data assimilation is proved by comparing it with the open-loop prediction where the system propagates from the "wrong" initial conditions without data assimilation [Walker et al., 2001]. The relationship between the assimilation and update interval was also investigated. To the best of our knowledge, this is the first attempt to directly assimilate GPR measurements for updating the soil moisture profile.

7.2 Materials and methods

7.2.1 Data assimilation procedure

Figure 7.1 shows the assimilation procedure that we used to update the state of the soil moisture profile using GPR data, which is outlined below:

1. Specify the initial soil moisture state and initial state ensemble based on the a priori knowledge on the moisture conditions. These values will work as the analysis state and analysis state ensemble at time $t = 0$.

2. Run the Hydrus-1D model to simulate the spatiotemporal dynamics of soil moisture from time t to $t + 1$ and obtain the forecast state and forecast state ensemble at time $t + 1$.

3. Check whether the observation is available. If not, assign the forecast state and its ensemble to the analysis state and ensemble. If yes, apply the MLEF algorithm to estimate the analysis state and analysis state ensemble. The observation operator which includes the petrophysical relationships and electromagnetic model is employed in this step to link the soil moisture state with the GPR observation.

4. Run the Hydrus-1D model for the next time with the initial state being the analysis state and its ensemble obtained from step 3.

This proposed data assimilation scheme consists of 3 components: the hydrodynamic model, the observation operator and the MLEF data assimilation algorithm, which are presented in the following paragraphs.

7.2.2 The hydrodynamic model

In this study, the one-dimensional vertical flow in an homogeneous soil column was simulated by the water flow module of the Hydrus-1D model [Šimunek et al., 2009]. The model numerically solves Richards's equation, which governs the movement of water in the unsaturated zone:

$$C(h)\frac{\partial h}{\partial t} = \frac{\partial}{\partial z}\left[K(\theta)\left(\frac{\partial h}{\partial z} + 1\right)\right], \tag{7.1}$$

where h is the water pressure head, θ is the volumetric water content, t is time, z is the spatial coordinate taken positive upward, and $K(\theta)$ is the unsaturated hydraulic conductivity function. $C(h) = \partial\theta(h)/\partial h$ is the differential

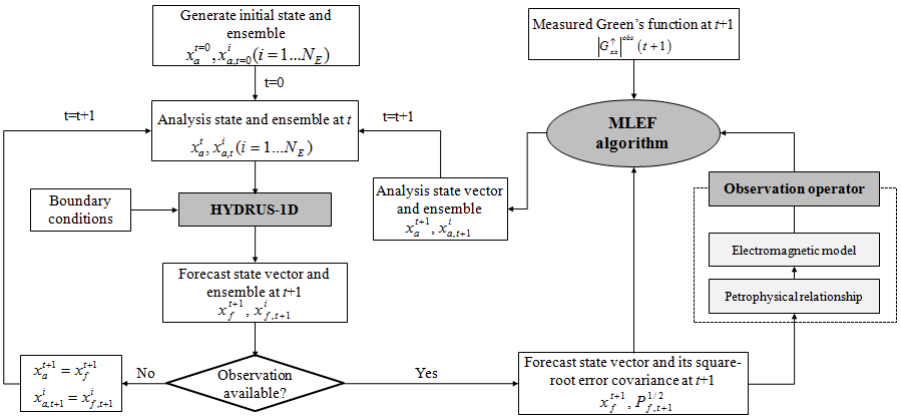

Figure 7.1. Assimilation procedure using GPR data to update the state of the soil moisture profile.

water capacity with $\theta(h)$ being the water retention curve. The unsaturated hydraulic conductivity and water retention curves are described by the Mualem–van Genuchten model [Mualem, 1976; van Genuchten, 1980]:

$$\theta(h) = \begin{cases} \theta_{\mathrm{r}} + \frac{(\theta_{\mathrm{s}} - \theta_{\mathrm{r}})}{[1+|\alpha h|^n]^m} & h < 0 \\ \theta_{\mathrm{s}} & h \geq 0 \end{cases} \tag{7.2}$$

$$K(\theta) = K_{\mathrm{s}} \left(\frac{\theta - \theta_{\mathrm{r}}}{\theta_{\mathrm{s}} - \theta_{\mathrm{r}}} \right)^l \left\{ 1 - \left[1 - \left(\frac{\theta - \theta_{\mathrm{r}}}{\theta_{\mathrm{s}} - \theta_{\mathrm{r}}} \right)^{\frac{1}{m}} \right]^m \right\}^2, \tag{7.3}$$

where

$$m = 1 - 1/n, \;\; n > 1, \tag{7.4}$$

θ_{r} and θ_{s} are, respectively, the residual and saturated water contents, K_{s} is the saturated hydraulic conductivity, α is the inverse of the air-entry value, n is a pore-size distribution index and l is the pore connectivity parameter. In Hydrus model, the numerical solution of Equation (7.1) is obtained by using the standard Galerkin-type linear finite element schemes. The atmospheric boundary with surface layer and free drainage were, respectively, selected for the upper and lower boundary conditions. For the potential evaporation, we used the Penman–Monteith equation [Monteith, 1981].

7.2.3 The observation operator

In this study, we updated the prediction of the soil moisture profile by directly assimilating the GPR data. The radar electromagnetic model [Lambot et al., 2004c] and petrophysical relationships worked as an observation operator to

relate the soil moisture profile with the GPR data. We adopted the GPR measurement system as described in Lambot et al. [2004c]. We simulated radar data for a Vivaldi antenna in the frequency range 1–3 GHz with a frequency step of 6 MHz. The antenna phase center is located at 7.5 cm above the antenna aperture. The frequency dependence of the phase center is accounted for by the transfer functions in the far-field antenna model [Lambot et al., 2004c; Jadoon et al., 2011]. The distance between the antenna aperture and medium was 26.5 cm, for which the far-field assumptions can be satisfied. GPR data are represented by the Green's function $G_{xx}^{\uparrow}(f, b)$ with b being the parameter vector. We refer to Chapter 3 for more the detailed information about the Green's function evaluation.

The vector $b = [\varepsilon_n, \sigma_n, h_n], \quad n = 1, \ldots, N$ contains the layer thickness (h_n), and constitutive parameters governing wave propagation in the medium, namely, electric permittivity (ε_n) and electric conductivity (σ_n). For relating the soil moisture profile with the GPR data, petrophysical relationships are necessary to convert the soil moisture to these constitutive properties. In this study, the relationship between the soil volumetric water content (θ_n) and the electric permittivity was formulated by the model of Ledieu et al. [1986] as

$$\varepsilon = \left(\frac{\theta - b}{a} \right)^2, \tag{7.5}$$

where we fixed $a = 0.1181$ and $b = -0.1841$, which are suitable parameters for a wide variety of soils [Ferré et al., 1996]. The relationship between the soil moisture and electric conductivity was formulated by the model of Rhoades et al. [1976]:

$$\sigma = (c\theta^2 + d\theta)\sigma_{\mathrm{w}} + \sigma_{\mathrm{s}}, \tag{7.6}$$

where σ_{w}=0.075 Sm^{-1} is the electric conductivity of the soil water [Jadoon et al., 2008; Minet et al., 2011], and σ_{s} is the electric conductivity of the dry soil. Table 7.1 presents the σ_{s} and two empirical parameters c and d for the loamy sand, silt and clay soils. Due to the high electric conductivity of the dry soil ($\sigma_{\mathrm{s}} = 4.39 \times 10^{-2}\,\mathrm{S\,m}^{-1}$), the electric conductivity of the clay soil is relatively large, which increases the losses in GPR wave propagation. Consequently, for a given soil moisture profile, we can obtain the electric permittivity and electric conductivity profiles by using Equations (7.5) and (7.6), and afterwards, the GPR data reflected from that profile from Equation (3.6).

For the fact that the assimilation procedure works with real numbers and the phase of the GPR data does not vary, given the fixed antenna height for all measurements, we used the absolute values of the complex GPR data in the frequency domain as the observation data. It is clear that the observation operator relating the Green's function and soil moisture is a complex nonlinear

Table 7.1. Van Genuchten's hydraulic parameters and Rhoades's petrophysical parameters for the loamy sand, silt and clay soils.

Soil type	Loamy sand	Silt	Clay
Hydraulic parameters			
θ_{r} ($\mathrm{cm^3cm^{-3}}$)	0.049	0.050	0.098
θ_{s} ($\mathrm{cm^3cm^{-3}}$)	0.39	0.489	0.459
α ($\mathrm{cm^{-1}}$)	0.0347	0.0066	0.015
n	1.747	1.677	1.253
K_{s} ($\mathrm{cmh^{-1}}$)	4.38	1.82	0.61
l	0.5	0.5	0.5
Petrophysical parameters			
c	1.85	2.10	1.35
d	0.0385	0.2450	-0.0900
σ_{s} ($\mathrm{Sm^{-1}}$)	5.89×10^{-4}	8.99×10^{-4}	4.39×10^{-2}

operator. It is also worth noting that in realistic measurements, the antenna effects are filtered out from the radar data to obtain the Green's function using the far-field antenna model (Equation (1) in Lambot et al., 2004c).

7.2.4 The maximum likelihood ensemble filter

MLEF is an alternative deterministic ensemble filter technique based on control theory [Zupanski et al., 2008]. It is based on a combination of the maximum likelihood and ensemble data assimilation. The MLEF is a posterior maximum likelihood approach, in which the optimal analysis state is obtained as the maximum of the PDF, and determined by minimizing the cost function derived from a multivariate posteriori PDF. The approach share the idea to use the minimization of the cost function to derive the analysis model state with the variational data assimilation. However, as an ensemble-based approach, the minimization is performed in an ensemble-spanned subspace, instead of the full model space like in the variational approach. Since the MLEF uses the maximum likelihood estimation to obtain the analysis model state, it allows one to effectively solve the nonlinearity of both model and observation operator. The following paragraphs present the basic steps of the MLEF algorithm. Detailed explanation can be found in Zupanski [2005] and Zupanski et al. [2008].

Generally, similar to the other assimilation algorithms, the MLEF includes two steps, the forecast and the analysis.

Forecast The forecast step uses the model M (Hydrus-1D) to propagate the system state in time:

$$\mathbf{x}_{t+1}^{\mathrm{f}} = M[\mathbf{x}_t^{\mathrm{a}}] + \boldsymbol{\omega}_t, \tag{7.7}$$

where $\mathbf{x}$ is the $N_{\mathrm{S}} \times 1$ state variable vector with N_{S} being the number of state variables, t and $t+1$ represent the current and next time steps, respectively.

Superscript *f* and a stand for the forecast and analysis. $\boldsymbol{\omega}_t$ is the model error vector, which is Gaussian random variables with zero mean and covariance matrix, $\mathbf{Q}$, assumed to be the same form as the forecast error covariance one, $\mathbf{P}_{\mathrm{f}}$, but with a smaller value:

$$\mathbf{Q} = 5\%\mathbf{P}_{\mathrm{f}}, \tag{7.8}$$

The ith column of the square-root $N_{\mathrm{S}} \times N_{\mathrm{E}}$ forecast error covariance matrix $\mathbf{P}_{\mathrm{f}}^{1/2}$ at time $t+1$ is calculated from the ensemble forecast as seen below:

$$\mathbf{p}_{i,t+1}^{\mathrm{f}} = M[\mathbf{x}_t^{\mathrm{a}} + \mathbf{p}_{i,t}^{\mathrm{a}}] - M[\mathbf{x}_t^{\mathrm{a}}], \quad i = 1, \ldots, N_{\mathrm{E}}, \tag{7.9}$$

where $\mathbf{p}_{i,t}^{\mathrm{a}}$ is the ith column of the square-root, $N_{\mathrm{S}} \times N_{\mathrm{E}}$ analysis error covariance matrix $\mathbf{P}_{\mathrm{a}}^{1/2}$ at time t. N_{E} denotes the number of members of the ensemble.

It is worth noting that at the initial time step, the analysis model state ($\mathbf{x}_{t=0}^{\mathrm{a}}$) and its associated uncertainty ($\mathbf{p}_{i,t=0}^{\mathrm{a}}$) are needed to a priori determine the fact that these values are not available.

Analysis As soon as the observation is available, the analysis step is performed to update the forecast state variable by the maximum likelihood approach. Accordingly, the MLEF seeks the optimal state variable that maximizes the posterior probability distribution, or in other words, minimizing the cost function given by the Gaussian PDFs for the observation and forecast errors:

$$\mathbf{J}(\mathbf{x}) = \frac{1}{2}\left[\mathbf{x} - \mathbf{x}_{\mathrm{f}}\right]^{\mathrm{T}} \mathbf{P}_{\mathrm{f}}^{-1}\left[\mathbf{x} - \mathbf{x}_{\mathrm{f}}\right] + \frac{1}{2}\left[\mathbf{y} - H(\mathbf{x})\right]^{\mathrm{T}} \mathbf{R}^{-1}\left[\mathbf{y} - H(\mathbf{x})\right] \tag{7.10}$$

where the increment vector $\mathbf{x} - \mathbf{x}_{\mathrm{f}}$ can be expressed as a linear combination of the forecast ensemble perturbations $\mathbf{P}_{\mathrm{f}}^{1/2}$:

$$\mathbf{x} - \mathbf{x}_{\mathrm{f}} = w_1\mathbf{p}_1^{\mathrm{f}} + w_2\mathbf{p}_2^{\mathrm{f}} + \cdots + w_{N_{\mathrm{E}}}\mathbf{p}_{N_{\mathrm{E}}}^{\mathrm{f}} = \mathbf{P}_{\mathrm{f}}^{1/2}\mathbf{w}, \tag{7.11}$$

where $\mathbf{w} = (w_1, w_2, \cdots, w_{N_{\mathrm{E}}})^T$ is the weighting coefficient vector, $\mathbf{y}$ denotes the measurement vector (GPR data) and $H(\mathbf{x})$ the observation operator (radar electromagnetic model). $\mathbf{R}$ represents the $N_{\mathrm{O}} \times N_{\mathrm{O}}$ measurement covariance matrix with N_{O} being the length of measurement dataset. Superscript T represents the transpose operator. Our objective is to find the optimal weighting coefficient vector $\mathbf{w}$ that minimizes the cost function (Equation 7.10). In this study, we followed the non-differentiable minimization approach in Zupanski et al. [2008], which estimates the unknown variables by

the generalized nonlinear conjugate-gradient optimization algorithm employing the generalized first derivative, calculated as

$$\nabla_G \mathbf{J}(\mathbf{x}) = \mathbf{P}_{\mathrm{f}}^{-1/2}(\mathbf{x} - \mathbf{x}^{\mathrm{f}}) - (\mathbf{Z}(\mathbf{x}))^T \mathbf{R}^{-1/2}[\mathbf{y} - H(\mathbf{x})] \tag{7.12}$$

in which the ith column of the $N_{\mathrm{O}} \times N_{\mathrm{E}}$ observation perturbation matrix $\mathbf{Z}$, $\mathbf{z}_i$ is calculated as

$$\mathbf{z}_i(\mathbf{x}) = \mathbf{R}^{-1/2}[H(\mathbf{x} + \mathbf{p}_i^{\mathrm{f}}) - H(\mathbf{x})]. \tag{7.13}$$

Since the optimal preconditioning is defined as an inverse square-root Hessian matrix, a changing variable ($\boldsymbol{\xi}$) is introduced using the inverse square-root Hessian matrix as a multiple factor:

$$\mathbf{w} = [\nabla_G^2 \mathbf{J}(\mathbf{x}_{\mathrm{f}})]^{-1/2} \boldsymbol{\xi} \tag{7.14}$$

with the Hessian matrix being calculated $\nabla_G^2 \mathbf{J}(\mathbf{x}_{\mathrm{f}})$ as

$$\nabla_G^2 \mathbf{J}(\mathbf{x}_{\mathrm{f}}) = \mathbf{P}_{\mathrm{f}}^{1/2}[\mathbf{I} + (\mathbf{Z}(\mathbf{x}_{\mathrm{f}}))^T \mathbf{Z}(\mathbf{x}_{\mathrm{f}})], \tag{7.15}$$

where $\mathbf{I}$ is an $N_{\mathrm{E}} \times N_{\mathrm{E}}$ identity matrix and $\mathbf{Z}(\mathbf{x}_{\mathrm{f}})$ is calculated by substituting $\mathbf{x} = \mathbf{x}_{\mathrm{f}}$ into Equation (7.13). Now, the optimization of $\mathbf{w}$ is implemented via the variable $\boldsymbol{\xi}$. If the observation operator is linear and the changing variable (Equation 7.14) is employed, the solution of the optimization problem (Equation 7.10) is obtained in a single step of minimization iteration [Zupanski, 2005].

Once we obtain the analysis state variable at time $t + 1$, the square-root analysis covariance matrix ($\mathbf{P}_{\mathrm{a},t+1}^{1/2}$) is updated by

$$\mathbf{P}_{\mathrm{a},t+1}^{1/2} = \mathbf{P}_{\mathrm{f},t+1}^{1/2} \left[\mathbf{I} + (\mathbf{Z}(\mathbf{x}_{\mathrm{a},t+1}^{\mathrm{opt}}))^T \mathbf{Z}(\mathbf{x}_{\mathrm{a},t+1}^{\mathrm{opt}})\right]^{-T/2}, \tag{7.16}$$

where $\mathbf{x}_{\mathrm{a}}^{\mathrm{opt}}$ represents the optimal analysis state variable. The columns of $\mathbf{P}_{\mathrm{a}}^{1/2}$ are then used in Equations (7.7) and (7.9) for the next analysis cycle.

7.2.5 Numerical simulation

The proposed assimilation procedure was validated by performing numerical simulations, for which the true system was exactly known. We considered a synthetic homogeneous soil column with a depth of 80 cm. This soil column was discretized into 80 equidistant elements. We analyzed the effects of the soil type on the data assimilation by considering 3 soil types: loamy sand, silt and clay. Table 7.1 presents the 6 parameters of the Mualem–van Genuchten's equation to construct the water retention curve and calculate the unsaturated hydraulic conductivity. These parameters were obtained from Schaap et al.

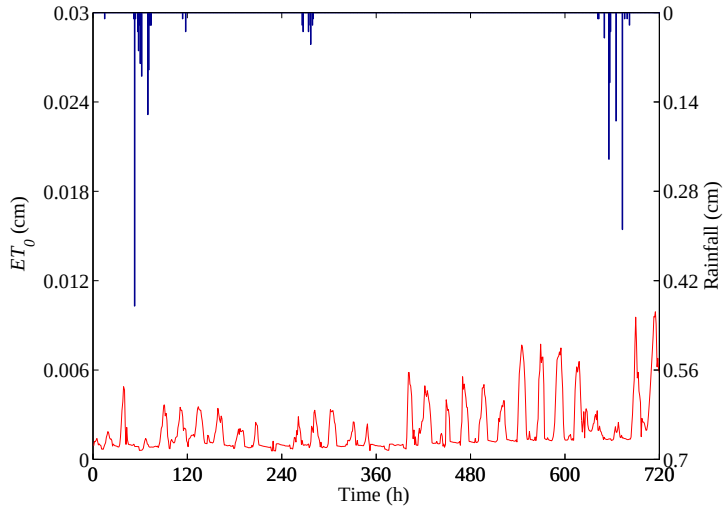

Figure 7.2. Rainfall and potential evaporation time series from 1 April to 30 April 2011 in Louvain-la-Neuve (Belgium).

[2001]. The simulation period was set at 720 h (30 days). For realistic simulations, the hourly rainfall, temperature, humidity and wind speed data were taken from a meteorological station in Louvain-la-Neuve (Belgium) from 1 April to 30 April 2011. Figure 7.2 presents the rainfall and potential evaporation data (ET_0) in this period. The figure shows that there are 3 main rainfall events during the simulation period in which 2 large events occurred at the beginning and end of the period with the maximum rainfall being 0.46 cm. The potential evaporation fluctuates proportionally with the variation of the temperature. It is relatively small from 0 to 400 h but becomes larger from 400 to 720 h due to the increase of the temperature. The minimum and maximum temperature are 2.5 and 26.5 °C, respectively. The average temperature over the period is around 13.8 °C.

In this study, we used the assimilation procedure to solve the problem of the unknown initial conditions. We assumed that the "true" initial profile was constant with $\theta_{t=0}(z) = 0.2$ cm^{3}cm^{-3}, while that of the "forecast" was 0.3 cm^{3}cm^{-3}. From the "true" initial state, the 720 hourly "true" soil moisture profiles were generated using the Hydrus-1D model.

Figure 7.3a, c, e presents the variation of the "true" soil moisture at several depths versus time over the simulation period for the loamy sand, silt and clay soils. In general, there is a good correlation between the forcing data (rainfall and evaporation) and moisture of all types of soil (with time lag). The surface soil moisture ($z = 0$ cm) is the most sensitive to the variation of the rainfall. The peak of the surface soil moisture rapidly appears right after the peak of

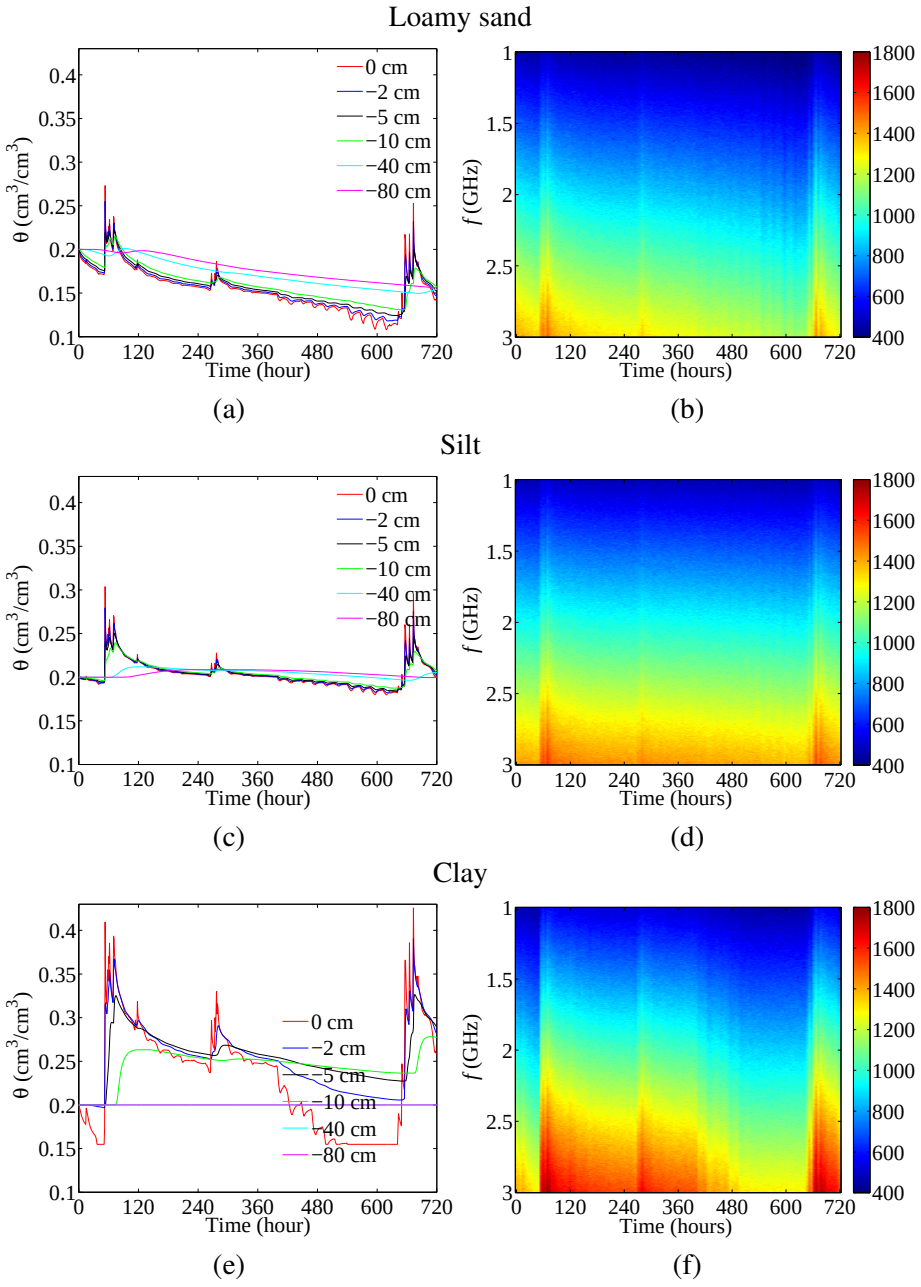

Figure 7.3. (a, c, e) Temporal variation of the "true" soil moisture at several depths of the profile (0, 2, 5, 10, 40 and 80 cm) and (b, d, f) corresponding "observed" frequency-domain absolute Green's functions $|G^{\uparrow}_{xx}(f)|$ over the 720 h simulation period. The results were obtained using the three soil types: (a, b) loamy sand, (c, d) silt and (e, f) clay.

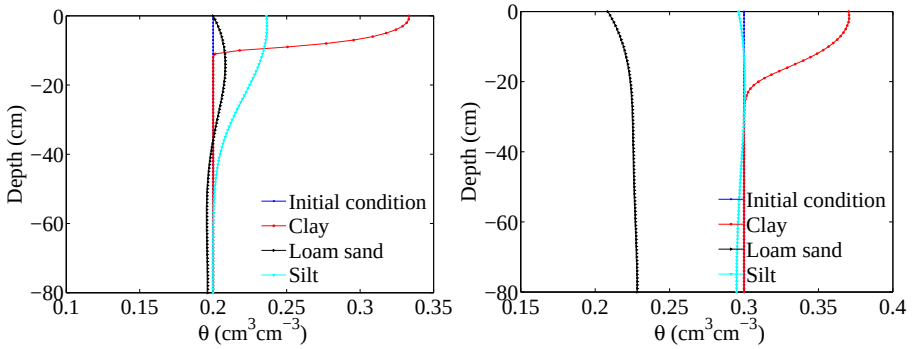

Figure 7.4. Synthetic (a) and forecast (b) soil moisture profiles at initial time (0 h) and at time that the GPR data assimilation begins (80 h) corresponding with the loamy sand, silt and clay soil types.

the rainfall. During the dry period, it sharply reduces due to the evaporation and infiltration processes. When the soil depth increases, the time lag between the rainfall and soil moisture peaks gradually increases. This is explained by the fact that water requires more time to move from the surface to lower soil layers. The soil moisture at the deeper layers also varies more smoothly with time due to the water retention effect of the soil. The effects of the evaporation on the soil moisture is only observed at the near-surface depths ($z = 0$, 2, 5 cm) during the dry period.

The temporal variation of the soil moisture of the three soil types are different. Compared to the silt and clay soils, the loamy sand dries out more quickly, and the differences of the water content among the soil depths are also smaller. This is because this soil type has a low water-holding capacity. By contrast, the clay soil shows its ability to retain water well. Even as the rainfall occurs, the water content at the near-surface layers (from 0 to 10 cm) increases rapidly but it slowly moves down to the lower layers. As a result, the water content at depths 40 and 80 cm is constant at the initial state during the simulation period. For each "true" soil moisture profile, the frequency-domain synthetic GPR data were produced using the forward radar model. In the electromagnetic model, the soil moisture profile was modeled by 80-planar layers with an equal thickness of 1 cm under the air layer and above a lower half space. As for the measurement error covariance, we assumed that only the elements in the main diagonal (i.e., variances) of the observation error covariance matrix $\mathbf{R}$ are different from zero. These elements were calculated corresponding to a constant variance of each element in the soil moisture profile, $\sigma^2 = 0.013^2$. "Observed" GPR data were generated by adding Gaussian random perturbations to the synthetic GPR data. The mean of the perturbations is set to zero

and its standard deviation is equal to the variance components of the observation error covariance matrix.

Figure 7.3b, d, f presents the "observed" frequency-domain absolute values of GPR data (Green's function) corresponding to the three soil types (loamy sand, silt and clay). For each soil type, there are 720 GPR datasets generated from 720 hourly soil moisture profiles. Each dataset has 334 "observed" values of absolute GPR data in a frequency range of 1–3 GHz and a step of 6 MHz. It is worth noting that in realistic practice, in addition to the reflections from the medium (Green's function), the measured GPR data also include the GPR effects. Therefore, the "observed" GPR data in this study correspond to the measured GPR data after filtering the antenna effects. Generally, the figure shows that the absolute value of the Green's function is higher at the higher frequencies, implying that the reflections from the surface layer are stronger than those from the deeper layers. Comparing Fig. 7.3b, d, e with c, d, f, we clearly see that the temporal variation of the GPR data agrees well with that of the soil moisture. The absolute Green's function increases when the soil is wet and vice versa. The 3 peaks of the GPR data occur at approximately the same time as those of the surface soil moisture. This is attributed to the fact that the amplitude of the GPR reflections is stronger as there is a higher contrast in the electric permittivity (and the corresponding soil moisture) between the soil and the air layers. The good correspondence between the GPR and soil moisture data indicates a great potential of GPR to correct the prediction of the soil moisture profile. The figure also indicates that at high frequency (2–3 GHz), the absolute Green's function of the clay is larger than that of the silt and and loamy sand. This can be explained by the higher water content at the upper part of the clay soil moisture profile.

We began to assimilate the GPR data to update the state of the soil moisture profile at a time of 80 h to avoid vertical shape of the soil moisture profile. Figure 7.4a and b, respectively, present the synthetic and forecast soil moisture profiles at initial time (0 h) and at the time that the GPR data assimilation begins (80 h) for the loamy sand, silt and clay soils. Both figures show that the soil moisture profiles corresponding to the three soil types are different due to their different hydraulic parameters, though the initial conditions and forcing data are identical. Under impact of the same amount of rainfall, the discrepancy between the upper and lower parts of the clay soil moisture profile at time step 80 h is much larger than those of the loamy sand and silt soils.

The figure also shows that, compared to the silt and clay soils, after 80 h simulation, the gaps between the "true" and forecast soil moisture profiles of the loamy sand is the smallest. This indicates that the predicted soil moisture profile of the loamy sand soil can converge to the "true" profile without data assimilation if the simulation time is long enough.

In this study, we used an ensemble including 6 members to estimate the

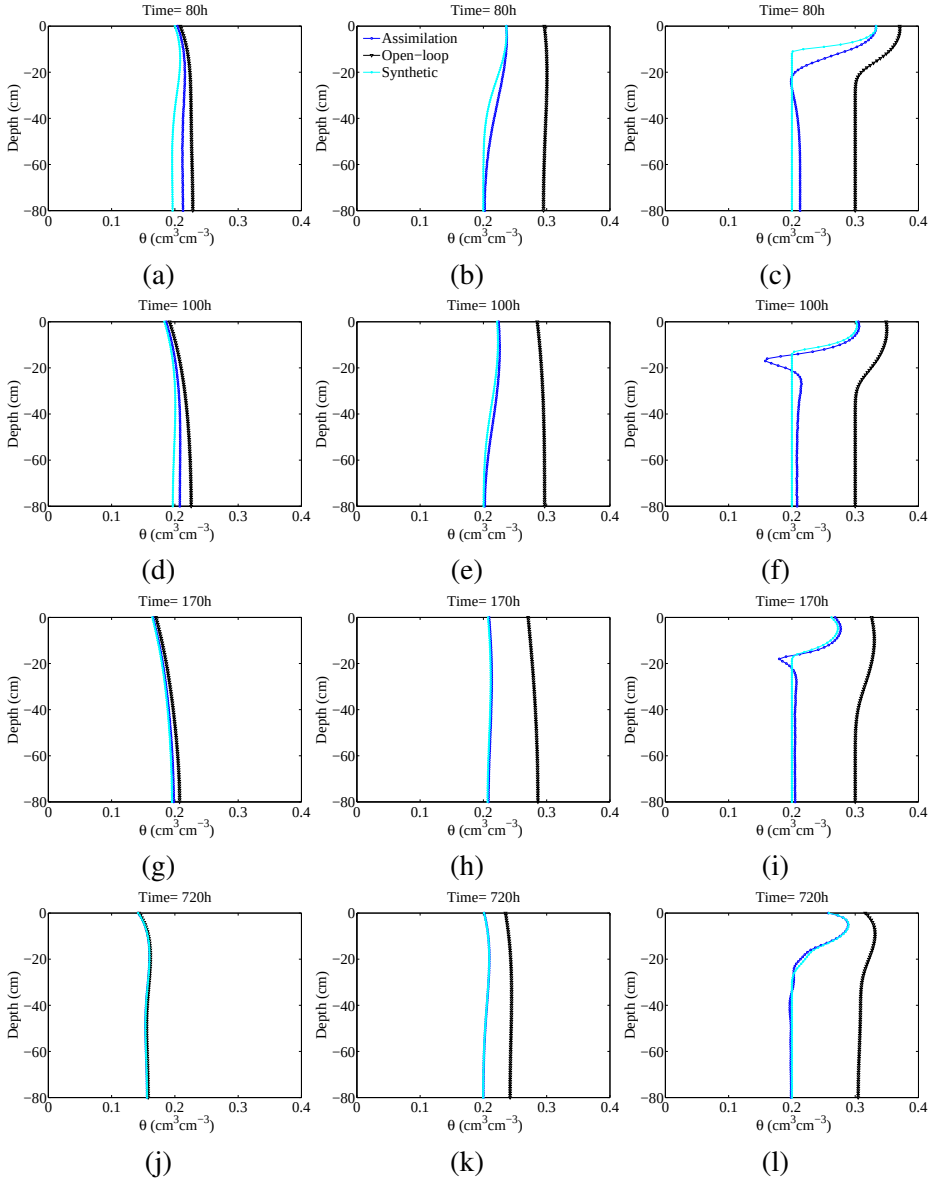

Figure 7.5. Comparison of the open-loop and data assimilation with the synthetic soil moisture profile at times 80, 100, 170, and 720 h. The assimilation was performed every 10 h. The three soil types were accounted for: (a, d, g, j) loamy sand, (b, e, h, k) silt and (c, f, i, l) clay.

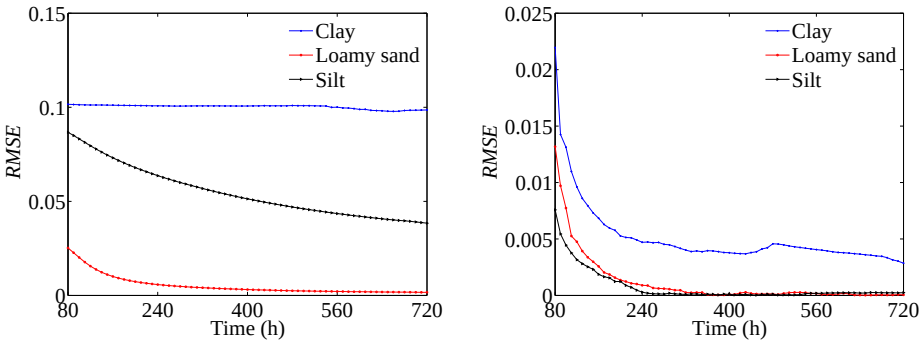

(a) Open-loop (b) Assimilation

Figure 7.6. The RMSE of the open-loop forecast (left) and assimilated (right) soil moisture profiles for clay (blue), loamy sand (red) and silt (black) soils as a function of the simulation time. The update interval is 10 hours.

analysis soil moisture. The initial ensemble was generated from the initial state with the perturbations being assumed as white-noise Gaussian random variables. The standard deviation of the initial perturbations was set to 20 % of the initial state.

To illustrate the effect of the update interval on the assimilation, we performed the data assimilation every 10, 30, and 60 h.

7.3 Results and discussion

7.3.1 Assimilation results

Figure 7.5 compares the "true" and forecast soil moisture profiles of loamy sand, silt and clay at several time steps with an update interval of 10 h. For comparison purpose, in addition to the GPR data assimilation, the results obtained by the open-loop prediction were also presented.

As for the effectiveness of the assimilation, the figure shows that the performance of the GPR assimilation is much better than the open-loop prediction for all soil types. However, this performance is different for loamy sand, silt and clay soils. At time 80 h (1st assimilation cycle), the assimilation significantly improves the forecast soil moisture profile. The soil moisture profiles of the 3 soil types updated by the GPR data assimilation approach the "true" state much more closely than the open-loop profiles. At time 100 h (3th assimilation cycle), while the discrepancies between the assimilated and "true" soil moisture profile are clearly observed for the clay soil, they are very small for the loamy sand and silt soils. With respect to the open-loop prediction, there are still large gaps between the open-loop forecast and "true" soil moisture profile

of the silt and clay soils. Contrastingly, the open-loop moisture profile of the loamy sand rapidly approaches the "true" state, indicating the wrong initial conditions can be effaced for this soil if the simulation time is long enough. Until a time of 170 h (10th assimilation cycle), for the loamy sand and silt soils, the assimilated and "true" soil moisture profiles are approximately identical. For the clay soil, a good agreement between the updated and "true" soil moisture profile is found from the surface to a depth of 16 cm. For the deeper layers, the errors are higher (around 0.5–2 $\times$ 10^{-2} $\mathrm{cm^3cm^{-3}}$). At this time, the differences between the open-loop prediction and "true" state are negligible for the loamy sand, while these differences are still large for the silt and clay soils. At the end of the simulation period (time = 720 h), it is impossible to separate the "true" soil moisture profile of the loamy sand from the assimilated and open-loop ones. A perfect agreement between the updated and "true" soil moisture is also observed for the silt soil. However, the errors of the open-loop prediction for this soil type are relatively large (around 4×10^{-2} $\mathrm{cm^3cm^{-3}}$), though they are smaller than at time 170 h. With respect to the clay soil, while no improvement is observed for the open-loop prediction, the agreement between the estimated soil moisture profile with assimilation and the synthetic one increases with absolute errors lower than 8×10^{-4} $\mathrm{cm^3cm^{-3}}$.

The figure also presents that the upper part of the soil moisture profile is better corrected than its lower counterpart, which is more clearly seen for the clay soil. This can be explained by the fact that the GPR data for the assimilation mostly reflect the variations of the soil moisture at near-soil surface due to the electric and dielectric losses. The correction of the deeper soil moisture profile is mainly based on the hydrodynamic interactions between the upper and lower layers. Consequently, for the soils with a good downward drainage (loamy sand and silt in this study), the variations of the soil moisture at the upper layers quickly influence on the lower layers. This leads to an easy correction of the wrong initial problem. By contrast, the variation of the soil moisture at the upper layers takes much longer time to propagate downward for the clay soil. Additionally, compared to the loamy sand and silt soils, the clay soil has the higher electric conductivity, which causes the larger electric losses and, therefore, reduces the GPR penetrating depth. As a result, it is more difficult to correct the whole soil moisture profile.

The comparison between the "true" and the forecast with and without GPR assimilation was quantitatively evaluated by the root mean square error (RMSE), which is formulated as

$$\mathrm{RMSE} = \sqrt{\frac{1}{N_\mathrm{S}} \sum_{i=1}^{N_\mathrm{S}} (x_i^\mathrm{a} - x_i^\mathrm{true})^2}. \tag{7.17}$$

Figure 7.6 presents the RMSE of the soil moisture profile obtained by the

open-loop forecast and GPR data assimilation as a function of the simulation time for the 3 soil types. The update interval is 10 h. Comparing Fig. 7.6a and b, we observed that, for all soil types, the RMSE of the open-loop prediction is much higher than that of the data assimilation. The smallest difference between the open-loop and GPR assimilation was found for the loamy sand due to its ability to self-converge to the "true" state. The RMSE of the open-loop prediction for this soil type ranges from 1.6×10^{-3} to 1.3×10^{-2} larger than that of the GPR data assimilation. This quantity is 3.8–8 $\times 10^{-2}$ for the silt, and 8–9.7 $\times 10^{-2}$ for the clay soil.

As for the relationship between the RMSE and soil type, the figure shows that the temporal variation of the RMSE both for the open-loop and GPR assimilation relies on the hydraulic parameters of the soil. The rapid change of the water pressure head with the soil moisture helps the RMSE to quickly reduces with the simulation time, i.e., the wrong initial conditions is easy to be corrected. Indeed, for the loamy sand, the RMSE both for the open-loop and GPR assimilation sharply reduces with time and converges to the "true" soil moisture profile (with $\mathrm{RMSE} < 2 \times 10^{-3}$) at time step 610 h (for the open-loop prediction) and 180 h (for the GPR assimilation). For the silt soil, the RMSE for the open-loop prediction steadily decreases from 8.7×10^{-2} to 3.8×10^{-2}, while the GPR data assimilation quickly reduces and is approximately equal to the "true" state at time 160 h. The RMSE for the clay soil remains stable over the simulation period for the case of the open-loop prediction, indicating that the wrong initial conditions cannot be self-corrected in this simulation period. After the first assimilation cycle at time step 80 h, the RMSE reduces suddenly from around 1×10^{-1} to 2.2×10^{-2} and continue to decrease to 5×10^{-3} at time 210 h. From time 210 h to the end of the simulation period, the RMSE reduce slightly from 5 to 3×10^{-3} for the fact that the corrected soil moisture at the upper part of the soil moisture profile has a low effect on its lower part due to the slow downward movement of the wetting front.

7.3.2 Effect of the update interval

The effects of the update interval on the GPR data assimilation is shown in Fig. 7.7, which plots the temporal variation of the RMSE for the GPR assimilation corresponding to update intervals of 10, 30 and 60 h. It is worth noting that, for each soil type, the RMSE of all update intervals at the first assimilation cycle are identical because they started assimilating at the same time step (80 h). The figure shows that the RMSE of the soil moisture profile obtained by GPR data assimilation for all update intervals is relatively small compared to the open-loop prediction, indicating that the wrong initial condition can be effectively corrected by assimilating GPR data even with the update interval up to 2.5 days.

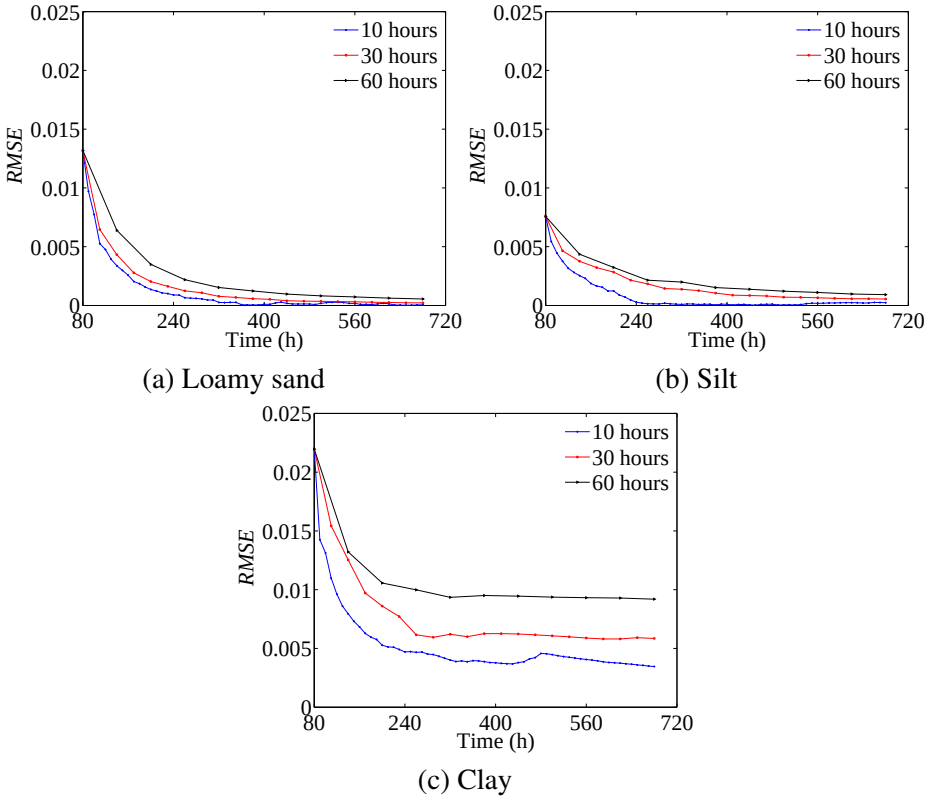

Figure 7.7. The RMSE of the soil moisture profile obtained by the assimilation of GPR data with different update intervals, namely 10, 30 and 60 h. The three soil types were compared, namely, (a) loamy sand, (b) silt and (c) clay.

As for the relationship between the assimilation and update interval, for the three soil types, the figure shows a trend that the RMSE increases with decreasing update interval. However, this dependence is different for different soil types. For the loamy sand and silt soils, the obtained results indicate that for this "wrong" initial condition problem, decreasing update interval does not much improve the effectiveness of the GPR data assimilation. The difference of the RMSE obtained from the update intervals of 10 and 60 h varies from 5×10^{-4} to 3×10^{-3} for loamy sand, and from 7×10^{-4} to 2×10^{-3} for silt soils. The stronger effects of the update interval on the GPR data assimilation is found for the clay soil. The difference of the RMSE between update intervals of 10 and 60 h varies in the range 5–6 $\times 10^{-3}$. These facts can be explained by observing Fig. 7.3. The figure shows that the temporal variation of the surface layers of the clay soil, which are the most sensitive layers with the GPR signal, is very large compared to that observed for the loamy sand and silt soil. As a result, decreasing update interval enables us to more closely follow the soil

moisture dynamics. In addition, as mentioned, for its high drainage ability, the discrepancy between "true" and forecast states of the loamy sand considerably reduces with the simulation time even without data assimilation, whilst this discrepancy levels off for the clay soil. Consequently, while decreasing update interval insignificantly impacts on the effectiveness of the GPR data assimilation for the loamy sand, it better corrects the predicted soil moisture profile for the silt and clay soils.

7.4 Conclusion

In this chapter, we explored the potentials of assimilating UWB GPR data based on the MLEF technique. Resorting to an accurate radar model for wave propagation in planar layered media, the approach directly assimilates the GPR data to update the soil moisture profile. This is different from the common approaches which assimilate the surface soil moisture obtained from remote sensing techniques to update the whole soil moisture profile. Our approach allows us to avoid solving the difficult, time-consuming inverse problem to estimate the soil moisture from GPR data. We validated our approach using synthetic experiments for the 3 typical soil types (loamy sand, silt and clay) in which the initial conditions were assumed to be wrong, as they are usually not known in practice. The obtained results demonstrated that for all soil types, the RMSE of the prediction without the GPR data assimilation is much larger than that with the GPR data assimilation.

The results also reveal that the effectiveness of the GPR data assimilation depends on the hydraulic properties of the soil type. Due to its high drainage capacity, the updated soil moisture profile of the loamy sand quickly converges to "true" state. In contrast, the updated moisture profile of the clay soil takes much longer time to approach the "true" profile, especially at the deep layers.

With respect to the relationship between the assimilation and update interval, the obtained results show that for the wrong initial condition problem, decreasing update interval slightly improves the updated soil moisture profile for the loamy sand and silt soils with the difference of the RMSE between update intervals of 10 and 60 h lower than 3×10^{-3}, while it significantly increases the effectiveness of the GPR data assimilation for the clay soil with the maximum difference of the RMSE among the update intervals of 6×10^{-3}.

The success of the proposed approach appears to be promising for using GPR data to improve the real-time soil moisture profile prediction at the field scale, which is very important in water and agricultural management. However, this study only solved the problem of wrong initial condition. The soil hydraulic parameters were assumed to be exactly known, which does not usually occur in practice. Moreover, the study ignored the frequency dependence

of the electric conductivity and permittivity, which cause errors for the observation operator. In order to reduce these errors, the frequency dependence of the electric properties should be taken into account in realistic applications. These problems will be addressed in next chapter.

Chapter 8

Joint estimation of soil moisture profile and hydraulic parameters by ground-penetrating radar data assimilation *

Abstract In this chapter, we improved the data assimilation scheme in Chapter 7 by combining the Maximum Likelihood Ensemble Filter algorithm and the state augment approach to simultaneously estimate the model state and parameters. The assimilation scheme includes a soil hydrodynamic model to simulate the soil moisture dynamics, a full-wave electromagnetic wave propagation model and petrophysical relationship to link the state variable with the GPR data. The hydraulic parameters are estimated jointly with the soil moisture with the state augmentation technique. The approach allows for the direct assimilation of GPR data, thus maximizing the use of the information. The proposed approach was validated by numerical experiments assuming wrong initial conditions and hydraulic parameters. The synthetic soil moisture profiles were generated by the Hydrus-1D model, which then were used by the electromagnetic model and petrophysical relationship to create "observed" GPR data. The results show that the data assimilation significantly improves the accuracy of the hydrodynamic model prediction. Compared with the surface soil moisture assimilation, the GPR data assimilation better corrects the soil moisture profile and hydraulic parameters. The results also show that the estimated soil moisture profile in the coarse soil converges to the "true" state more rapidly than in the fine one. Of the three unknown parameters of the Mualem-van Genuchten model, the estimation of n is more accurate than that of α and K_s.

* Adapted from A. P. Tran, M. Vanclooster, M. Zupanski, and S. Lambot, Joint Estimation of Soil Moisture Profile and Hydraulic Parameters by Ground-penetrating Radar Data Assimilation with Maximum Likelihood Ensemble Filter, *Water Resources Research*, accepted with minor revision.

8.1 Introduction

During the last decade, many novel measurement techniques have been developed to monitor unsaturated soil moisture dynamics for its importance to hydrological and meteorological studies as well as agriculture and irrigation management [Annan, 2005; Vereecken et al., 2008]. As one of the non-invasive geophysical techniques, GPR has become a powerful tool to quantify the soil moisture at the field scale [Huisman et al., 2003]. Compared to the airborne/spaceborne remote sensing techniques (e.g., passive microwave, radiometers, synthetic aperture radars (SAR), scatterometers), GPR can provide soil moisture data with a much higher spatial resolution (around 0.1–1 m). Its characterization depth is also larger for the fact that GPR works near the soil surface. However, because GPR is more suitable for occasional than continuous measurement, it is impractical to use this technique for highly-temporal soil moisture characterization [Vereecken et al., 2008].

Soil moisture profiles can be estimated by employing a soil hydrodynamic model with given boundary and initial conditions. This approach provides the whole soil moisture profiles with fine spatial and temporal resolutions. However, the accuracy of the soil moisture estimation strongly relies on the knowledge of soil hydraulic parameters [Walker et al., 2001; Lambot et al., 2009], which are often derived from a soil particle size distribution using pedotransfer functions [Schaap et al., 2001; Weynants et al., 2009; Mohammadi and Vanclooster, 2011]. Yet, the natural heterogeneity of soils and the lack of detailed soil property maps cause significant errors for the soil parameterization schemes. In that sense, the integration of geophysical measurements into a hydraulic model could considerably improve the accuracy of the hydraulic model [Robinson et al., 2008a]. Indeed, the vertical distribution of the electric properties of the soil are controlled by both electromagnetic and hydrodynamic laws, which consequently can be used to infer the soil moisture profile. For example, Rucker and Ferré [2004]; Kowalsky et al. [2005]; Looms et al. [2008] integrated time-lapse bore-hole GPR data into a hydrodynamic model in a coupled hydro-geophysical inversion framework. Time-lapse soil moisture images obtained from travel-time tomography analysis of GPR data were inverted to calibrate the soil hydraulic parameters. However, due to the significant assumptions related to electromagnetic wave propagation and using only a part of information (travel-time) contained in GPR data, there were inherent errors in the reconstructed soil moisture images.

Lambot et al. [2004c] developed an analytical antenna model for the off-ground GPR configuration, allowing to rapid data acquisition over large areas by mounting the GPR system on the motorcycle (see Minet et al. [2011]). However, the unknown penetrating depth of GPR, the continuously varying soil moisture with depth and the ill-posed electromagnetic inverse problem

when dealing with a relatively large number of unknowns, often complicates the soil moisture estimation at deep layers with this method. To solve this problem, a joint electromagnetic-hydrodynamic inversion scheme that integrates the GPR model into the hydrodynamic model was developed, permitting to use the full-wave GPR data for the calibration of the soil hydraulic parameters [Lambot et al., 2006b]. The above parameter estimation is known as the batch calibration in which the parameters were assumed to be time-invariant and estimated by using historical time-series data. The disadvantages of this calibration methodology are that it does not account for the errors in input, output and model structure and that it attributes all of these errors to the model parameter uncertainty [Moradkhani et al., 2005b].

Data assimilation is an analysis technique that incorporates observations into a mathematic model of a real system to improve the accuracy of the system state estimation. In its traditional form, the technique assumes that the model parameters are a-priori known and the updating process is applied only for the state variables. However, in practice, the model parameters are usually unknown and difficult to obtain. There is also no guarantee that the model parameters do not change over time. As a result, updating state variables alone is insufficient to produce reliable estimations of the system dynamics. Recent studies have shown that simultaneous updating model parameters and states substantially improved the accuracy of the model estimation [Smith et al., 2013]. For example, Moradkhani et al. [2005b] employed the dual state-parameter estimation approach based on the Ensemble Kalman Filter (EnKF) to correct both parameters and state variables of a hydrologic model. Moradkhani et al. [2005a]; Montzka et al. [2011] estimated the model parameters and state variables using the sampling importance resampling particle filter (SIR-PF). Zupanski and Zupanski [2006] corrected the state variables, bias and model parameters by combining the ensemble data assimilation, state augmentation, and parameter and model bias estimation methods. De Lannoy et al. [2007b] applied different algorithms to correct the state and forecast bias of the Community Land Model simulations using the EnKF with soil moisture observations. Smith et al. [2013] updated the system state and parameters of a morphodynamic model using the three-dimensional variational (3D-Var) data assimilation scheme. Vrugt et al. [2013] developed the particle-DREAM method that combines the strengths of Sequential Monte Carlo sampling and Markov Chain Monte Carlo (MCMC) simulation with the Difference Evolution Adaptive Metropolis (DREAM) algorithm for joint parameter and state estimation.

Using GPR data to correct the wrong initial soil moisture condition in a data assimilation framework was firstly investigated by Tran et al. [2013b]. Instead of surface soil moisture, the approach used information of the whole soil moisture profile, which is reflected via the GPR data, for the assimilation.

This allowed to take the advantage of better penetrating depth of GPR, therefore, provide better soil moisture profile estimation than the use of the surface soil moisture only. Moreover, the approach helped to avoid the ill-posed electromagnetic inversion due to a large number of unknown variables and the continuously varying soil moisture with depth. The dependence of the GPR penetrating depth on the soil moisture was also effectively solved via the observation operator, which links the whole soil moisture profile with GPR data. The obtained results showed that direct assimilation of GPR data enabled to quickly correct the wrong initial condition. However, in this study, the soil hydraulic parameters were assumed to be exactly known.

In this chapter, we explore the possibility of the GPR data assimilation to solve the case that both initial moisture conditions and model parameters are poorly known. To do that, we modify the assimilation framework in Chapter 7 by combining the MLEF algorithm and the state augment approach to simultaneously estimate the model state and parameters. We assumed that three key parameters of the Hydrus-1D model are unknown, namely, n, α and K_s to keep the size of the augmented vector reasonable. The empirical observation operator is also replaced by a more accurate one, which accounts for the different composition of soil mixture and the frequency dependence of soil electric properties (conductivity and permittivity). The approach is validated using synthetic experiments. We compared three scenarios in this study, namely, open-loop prediction (without data assimilation), surface soil moisture assimilation and GPR data assimilation.

8.2 Theory

The general data assimilation scheme is basically similar to what we presented in Chapter 7. The spatiotemporal soil moisture dynamics in the unsaturated zone is simulated by Hydrus-1D model [Šimunek et al., 2009]. The GPR model [Lambot et al., 2004c] and petrophysical relationships are the nonlinear observation operator to link the state variables (soil moisture profile) with observed GPR data and the data assimilation is performed within the MLEF data assimilation algorithm proposed by Zupanski [2005]. In this chapter, we only present the modifications to improve the accuracy of the observation operator and simultaneously estimate soil moisture and soil hydraulic parameters.

8.2.1 The petrophysical relationship

The soil moisture profile and GPR data do not directly link to each other but via the electric properties and wave propagation phenomena. The relationship between these electric properties and the GPR data is formulated by the

electromagnetic model, which was presented in Chapter 3. The relationship between these properties and the soil moisture profile is typically described by petrophysical formulas [Lesmes and Friedman, 2005]. In this chapter, we used a conceptual dielectric mixing model known as the complex refractive index model (CRIM) to relate the soil moisture with the complex permittivity. The model assumes that the soil mixture is composed of three components, namely, air, water and soil matrix. As a result, its complex permittivity (ε_e) is calculated as the combination of the complex permittivity of these three components as below:

$$\sqrt{\varepsilon_e} = \theta\sqrt{\varepsilon_w} + (\phi - \theta)\sqrt{\varepsilon_a} + (1 - \phi)\sqrt{\varepsilon_s} \tag{8.1}$$

in which ϕ and θ are the porosity and volumetric water content of soil, respectively; ε_a, ε_w and ε_s are the permittivities of air, water and soil matrix, respectively. The relative electric permittivity of the air is $\varepsilon_a = 1 + i0$ and that of the soil matrix is $\varepsilon_s = 4.5 + i0.05$ for loamy sand, $\varepsilon_s = 4.5 + i0.1$ for silt and $4.5 + i0.25$ for clay soil [Boyarskii et al., 2002]. The real part of the complex electric permittivity is usually called as relative permittivity (dielectric constant) and represents the total polarisability including non-polar and dipolar polarization of the soil particles. The imaginary part represents the total energy losses (dielectric and ionic losses). It is worth nothing that while the real part of the complex permittivity of the three soil types are approximately similar, the imaginary part of the clay soil is greater than that of loamy sand and silt, implying that the energy losses are larger in the clay soil. The complex permittivity of the free water component is described by the Debye's equation [Debye, 1929]. Compared to the empirical formulas, the CRIM model permits to take into account the dependencies of soil complex permittivity on soil types, soil porosity and frequency, which is expected to reduce the errors of the observation operator. We refer to Chapter 5 for more detailed explanation of this petrophysical relationship.

For a given soil moisture profile, we can obtain the complex electric permittivity by using Equation (8.1), and then, the Green's function which corresponds to that moisture profile using the electromagnetic model of Lambot et al. [2004c]. These two models formulate a complex nonlinear observation operator which transforms the soil moisture profile into the GPR data.

8.2.2 The state augmentation method

We updated the soil hydraulic parameters (n, α and K_s) jointly with the state variables by combing the MLEF method with the state augmentation technique. The state augmentation is a conceptual technique that estimates the model parameter vector $\mathbf{v}$ by appending it to the model state vector $\mathbf{x}$ to con-

stitute an augmented state vector $\mathbf{z}$ as:

$$\mathbf{z} = \begin{bmatrix} \mathbf{x} \\ \mathbf{v} \end{bmatrix} \tag{8.2}$$

in which $\mathbf{z} \in \mathbb{R}^{N_z=N_x+N_v}$ with N_x and N_v being the number of state variables and unknown parameters, respectively. Time evolution of the augmented state vector $\mathbf{z}$ from time t to $t+1$ is described by:

$$\mathbf{z}_{t+1} = \widetilde{M}(\mathbf{z}_t) + \boldsymbol{\omega}_{t+1} \tag{8.3}$$

where vector $\boldsymbol{\omega}_{t+1}$ is a Gaussian random noise, representing the model error. Function $\widetilde{M} : \mathbb{R}^{N_z} \longrightarrow \mathbb{R}^{N_z}$ is defined as:

$$\widetilde{M}(\mathbf{z}_t) = \begin{bmatrix} M(\mathbf{x}_t, \mathbf{v}_t) \\ \mathbf{v}_t \end{bmatrix} \tag{8.4}$$

where M is the mathematical model simulating the system state dynamics, which is the Hydrus-1D model in this study. Equation (8.4) indicates that the model parameters do not change when the hydraulic model is performed from one step to the next step.

The augmented state vector $\mathbf{z}_{t+1}$ at time $t+1$ is related to the observation vector $\mathbf{y}_{t+1} \in \mathbb{R}^{N_o}$ (GPR data) with N_o being number of measurements, by:

$$\mathbf{y}_{t+1} = \widetilde{H}(\mathbf{z}_{t+1}) + \boldsymbol{\varepsilon}_{t+1} \tag{8.5}$$

where $\boldsymbol{\varepsilon}_{t+1} \in \mathbb{R}^{N_o}$ denotes the observation error vector, which accounts for the errors caused by GPR measurements and imperfect observation operator. The augmented observation operator $\tilde{H} : \mathbb{R}^{N_z} \longrightarrow \mathbb{R}^{N_o}$ is defined as:

$$\widetilde{H} = \begin{bmatrix} H(\mathbf{x}_{t+1}) \\ \mathbf{v}_{t+1} \end{bmatrix} = H(\mathbf{x}_{t+1}) \tag{8.6}$$

in which H is the nonaugmented observation operator (electromagnetic model and petrophysical relationship). Equation (8.6) shows that the unknown parameter vector does not influence on the observation operator because there is no available observation relating directly to the parameter component of the augmented state vector. The parameters are estimated by the cross-covariances between the errors of these parameters and those of the state variables, $\mathbf{P}_{f,xv} \subset \mathbf{P}_f$. Consequently, there is no improvement in parameter estimation if the parameter-state error covariance is equal to zero.

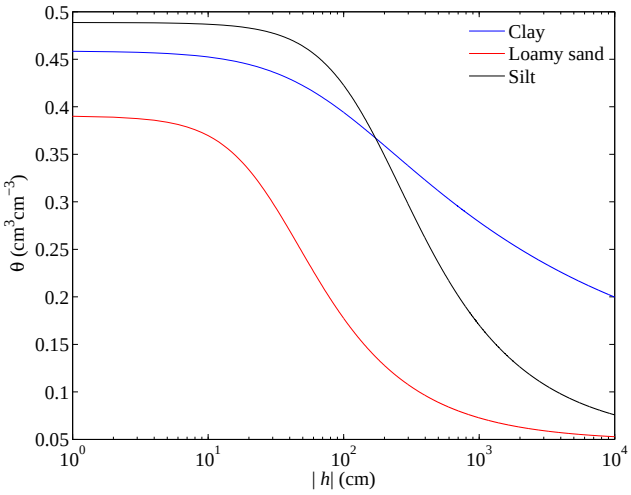

Figure 8.1. Water retention curves for the three soil types: clay, loamy sand and silt.

8.3 Experimental setup

8.3.1 Numerical experiment

The proposed data assimilation procedure was validated by numerical experiments. The data assimilation was performed to estimate the soil moisture and hydraulic parameters of a synthetic homogeneous soil column during a period of 1320 hours (55 days). The soil column with a depth of 80 cm was divided into 80 layers, resulting in a thickness of 1 cm for each layer. The soil porosity that is used by the CRIM model was set to $\phi = 0.4$. For evaluating the performance of the assimilation scheme with different soil types, three typical soils were selected, namely, loamy sand, silt and clay. Figure 8.1 presents the water retention curves of these soils, with the hydraulic parameters were obtained from Schaap et al. [2001]. The figure shows that at the high potential pressure head, the clay soil can hold much more water than the loamy sand and silt soils.

With respect to the upper boundary conditions, we used the hourly rainfall, temperature, humidity and wind speed data in a period ranging from 27 May to 23 July 2011 at a meteorological station in Louvain-la-Neuve (Belgium). We assumed that the "true" initial moisture was $\theta_{t=0}(z) = 0.2$ cm^{3}cm^{-3} for the whole soil profile. From the "true" initial state, 67 synthetic soil moisture profiles with an interval of 20 hours were generated using the Hydrus-1D model. The left panel of Figure 8.2 shows the temporal variation of the rainfall and synthetic soil moisture profiles at soil depths of 0, 10, 40 and 80 cm corresponding to the clay, loamy sand and silt soils. The figure shows that

there is relatively high rainfall over the simulation period. The total amount of rainfall in this period is 19.2 cm, and the maximum rainfall is 1.67 cm/hour. With respect to the temporal variation of the soil moisture, the soil moisture at the surface (z=0 cm) is the most sensitive to the rainfall. Its dynamics closely follows the rainfall variation with the peaks appearing right after the rainfall peaks. When the soil depth increases, the soil moisture exhibits smoother variations and the time-lag between the rainfall and soil moisture increases and the soil moisture peaks decrease. This is especially true for the clay soil. While the soil moisture at the surface layer for this soil changes abruptly, that at the bottom ($z = 80$ cm) still stays at its initial value during the simulation period. This is because a part of water is kept at the upper layers due to the water retention ability in soil matrix. Compared to the loamy sand and silt soils, the clay retains water better, enabling it to store more water at the surface layers and thus, much clearer discrepancy between upper and lower soil moisture is observed.

We assumed that the GPR measurements were performed in the 800-2200 MHz frequency range with a step of 6 MHz, resulting in 234 different frequencies ($N_o = 234$) and the distance between the antenna aperture and the soil surface was set to $h_0 = 34$ cm. In the electromagnetic model, the soil moisture profile was discretized into 80-planar dielectric layers with an equal thickness of 1 cm under an air layer and above a lower half space. With this antenna configuration, for each synthetic soil moisture profile, corresponding synthetic Green's functions were artificially created using the CRIM model (Equation (8.1)) and electromagnetic model (Chapter 3). The "observed" GPR data were generated by adding Gaussian random perturbation with mean of zero and standard deviations of 15 ($\sigma = 15$) to the synthetic Green's function. As for the observation error covariance matrix (**R**), we assumed that there was no mutual correlation between the measurement errors, i.e., the off-diagonal elements of the matrix were equal to zero. The on-diagonal elements were calculated corresponding to a constant variance $\sigma^2 = 15^2$.

The right panel of Figure 8.2 presents 67 time-lapse "observed" GPR datasets for the three soil types. The measurement errors are represented by small oscillations in the figure. The figure shows that there is a positive correlation between the soil moisture and the GPR data. When the soil moisture is large, the GPR signal is strong and vice versa, implying that the GPR data reflect the temporal dynamics of the soil moisture well. The GPR signals at the high frequencies are stronger than those at the low frequencies, which means that the GPR data contain more soil moisture information at the upper than the lower soil layers. The figure also shows that the GPR reflections are much stronger for the clay than the loamy sand and silts, which is caused by the higher soil moisture at the upper layers in this soil.

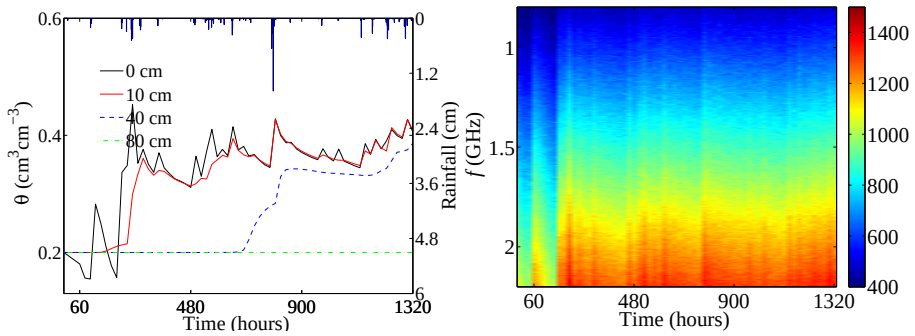

(a) Clay

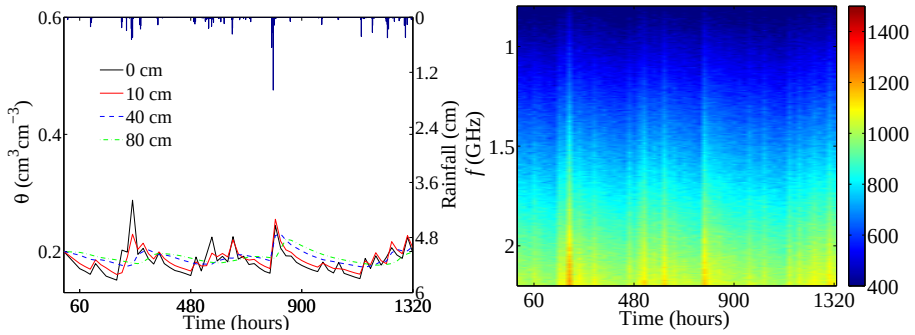

(b) Loamy sand

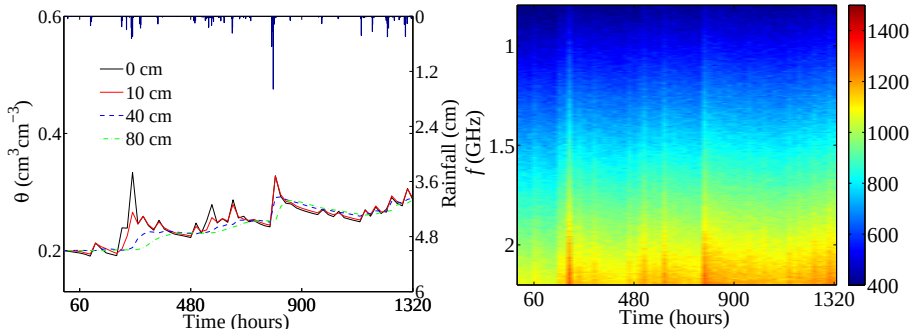

(c) Silt

Figure 8.2. Temporal variation of the synthetic soil moisture at several depths (0, 10, 40 and 80 cm) (left pannel) and GPR data (right pannel) of the clay (a), loamy sand (b) and silt soil (c) over the simulation period. The GPR data are represented by the absolute Green's function in the frequency domain. For reference, rainfall data are also plotted.

8.4 Results and discussion

8.4.1 Soil moisture profile estimation

We began to assimilate the GPR data to simultaneously update the state of the soil moisture profile and hydraulic parameters at time 60-hour. We assumed the "forecast" initial moisture of the whole soil profile was constant at $\theta = 0.3$ cm^3cm^{-3}. The initial values of n, α and K_s parameters are 1.4, 0.02 cm^{-1} and 2.2 $cm.h^{-1}$, respectively. The length of the augmented state vector is 84, which includes 81 soil moisture points and 3 parameters. For retrieving the analysis state, we used an ensemble with 15 members, in which the initial ensemble was randomly generated using a Gaussian distribution with mean equal to the initial states and standard deviation equal to 10% of these values. Three scenarios were compared in this study: the open-loop prediction, GPR data assimilation, and surface soil moisture assimilation. The open-loop prediction only propagates the soil moisture state from the initial and boundary conditions without assimilation. The two remaining scenarios estimate both soil moisture profile and soil hydraulic parameters by assimilating GPR and surface soil moisture data. The difference between these two scenarios are that while the observation operator in the GPR data assimilation is the antenna model and petrophysical relationship, it is a $(N_o \times N_z)$ matrix with the first element equal to one and the others to zero in the surface soil moisture assimilation. We used an updating interval of 20 hours for the data assimilation.

Figure 8.3 compares the moisture profiles obtained by the three scenarios with the synthetic ones for the clay, loamy sand and silt soils at several time (t=60-, 140-, 220-, 1180-hour). The figure shows that the estimated soil moisture profile with the assimilation agrees with the "true" state much better than those with the open-loop prediction. At time $t = 60$-hour (1st assimilation cycle), the soil moisture profiles estimated by the assimilation (with GPR and surface soil moisture) are considerably closer to the synthetic ones than the open-loop. The GPR data assimilation corrects the soil moisture better than the surface soil moisture assimilation. After 5 assimilation cycles, at time $t = 140$-hour, while there is no improvement for the open-loop prediction scenario, the discrepancies between the synthetic and estimated soil moisture profiles gradually reduce for the two data assimilation scenarios. Particularly, the soil moisture profiles obtained by the GPR assimilation are very near the synthesis for the loamy sand and silt soils. At time $t = 220$-hour (9th assimilation cycle), a perfect agreement between the soil moisture profile retrieved by the GPR assimilation and synthetic ones is observed for the loamy sand and silt soils. A very good estimation is also seen for the 10 cm upper layers ($z = 0 - 10$ cm) of the clay soil but below 10 cm, the errors are still visible. For the surface soil moisture assimilation, discrepancies between the

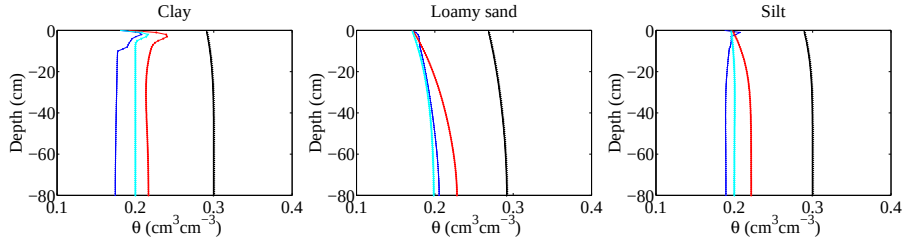

(a) Time = 60-hour (1st data assimilation cycle)

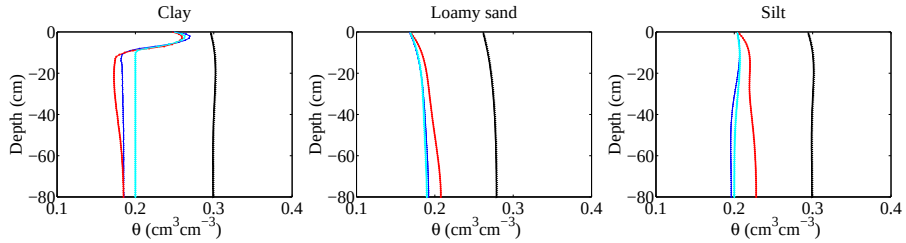

(b) Time = 140-hour (5th data assimilation cycle)

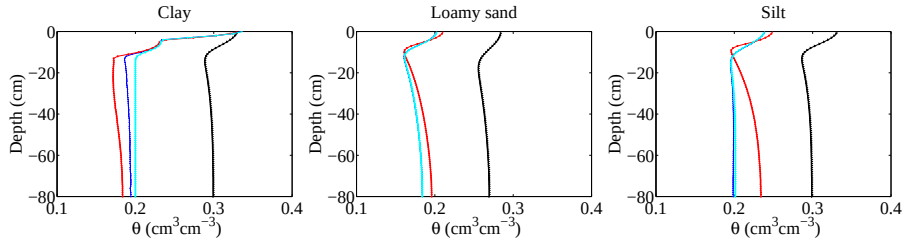

(c) Time = 220-hour (9th data assimilation cycle)

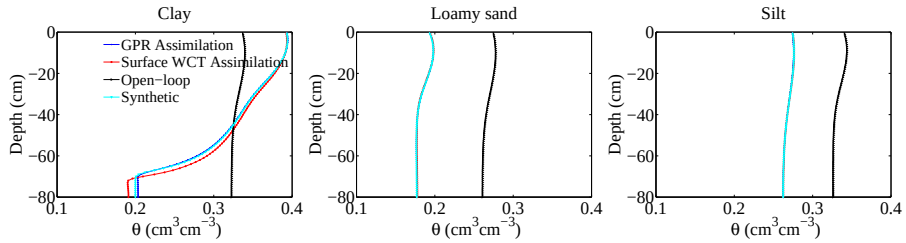

(d) Time = 1180-hour (57th data assimilation cycle)

Figure 8.3. Comparison of synthetic soil moisture profiles (cyan line) and those obtained by the three scenarios: GPR data assimilation (blue line), surface soil moisture assimilation (red line) and open-loop prediction (black line). The comparison is presented at time 60- (a), 140- (b), 220- (c) and 1180-hour (d). Data assimilation was performed with updating interval of 20 hours. The three soil types were accounted for: Clay (left), loamy sand (middle) and silt (right).

estimated and synthetic soil moisture also decrease but are still larger than the GPR assimilation. At time $t = 1180$-hour (57th assimilation cycle), for the GPR assimilation, a very good agreement is observed for all soil types, except for only small errors appearing at the bottom layers ($z = 70 - 80$ cm) of the clay soil. For the surface soil moisture assimilation, no visible errors are observed for the loamy sand and silt soils. For the clay soil, although differences between modeled and synthetic soil moisture profiles significantly reduce, errors are seen at depths from 40 down to 80 cm. The better performance of the assimilation with GPR data than surface soil moisture can be explained by the fact that GPR data contain soil moisture information not only at the surface but also deeper soil layers.

For the two data assimilation scenarios, the figure also shows that the soil moisture at the upper layers is corrected better and more rapidly than the lower ones. Although GPR has soil moisture information beyond the surface layer, it also does not contain information of the whole soil profile due to the attenuation effect. As a result, for both types of data for the assimilation, the correction of soil moisture at the low layers largely relies on the propagation of the corrected soil moisture at the upper layers. The soil moisture at the lower layers can be corrected only after the upper soil moisture is corrected. This is also the reason why the estimation of the soil moisture profile for the coarse soil (loamy sand and silt) is faster than the fine soil (clay). Compared to the loamy sand and silt, the clay soil can hold more water (water content changes more slowly with the pressure head as shown in Figure 8.1). As a result, it is very difficult for water to move downward, which makes the corrections at the upper layers to take a longer time to influence the lower layers. For the GPR data assimilation, the high water retention ability of the clay soil causes too much soil moisture at the upper layers and therefore, prevents the GPR waves from deeper intrusion, reducing the soil moisture information contained in GPR data. In addition, the high apparent conductivity of the clay soil, which increases the attenuation of GPR signal, also contributes to the more shallow characterization depth of the GPR when facing this soil type.

The comparison of the three scenarios are quantitatively evaluated by means of RMS. Figure 8.3 shows the temporal variations of this criterion for each scenario over the simulation period. The figure clearly shows that both assimilation scenarios significantly outperforms the open-loop prediction. For example, the ratios of the RMS of the GPR data assimilation to those of the open-loop for the loamy sand range from 21 to 1200. These values are 9.7–903, and 1.2–4.9 for the silt and clay soils, respectively. Comparing the two assimilation scenarios, we observe that the RMS of the GPR assimilation is smaller than that of the surface soil moisture assimilation. However, this criterion of the two scenarios is very small and approximately equal to each other at 560-hour (26th assimilation cycle) for the loamy sand and at 420-hour (19th

assimilation cycle) for the silt soil. It is because at these times the correction of the surface soil moisture propagated to the bottom layer. For the clay soil, it takes much longer time for the RMS of the two scenarios to be small (at around 1260-hour (61th assimilation cycle)) because the surface soil moisture correction very slowly moves to the bottom layer.

The figure also indicates that for the loamy sand and silt soils, the most effective adjustments of the data assimilation scenarios occur from time 60 to 220-hour with the GPR data and from 60 to 420-hour with the surface soil moisture data. After that, the improvement is relatively small because very good agreements between the estimated and "true" soil moisture profile states were obtained. However, for the clay soil, the correction of the hydrodynamic simulation is very slow. The RMS fluctuates around 0.002–0.03 and 0.003–0.036 over the simulation period for the GPR and surface soil moisture assimilation, respectively.

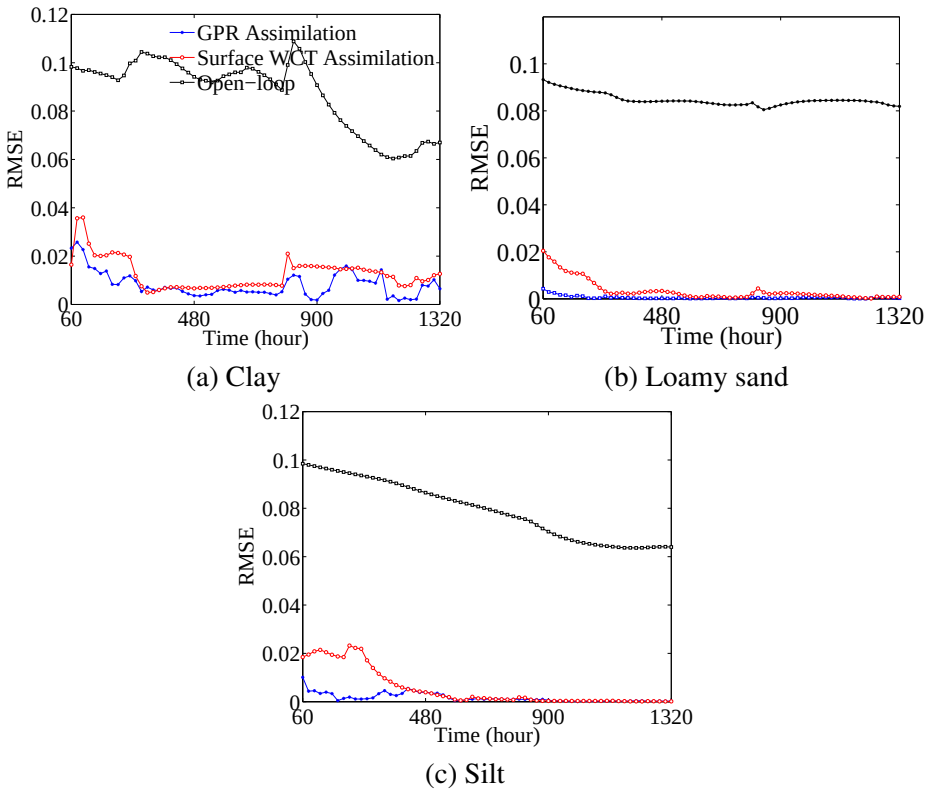

Figure 8.4. The RMS of the Clay (a), loamy sand (b) and silt (c) soils as a function of simulation time. Blue and red lines represent the RMS obtained by the GPR and surface soil moisture assimilation scenarios, respectively; black line denotes the open-loop RMS.

8.4.2 Parameter estimation

Figure 8.5 illustrates the variations of the hydraulic parameters (n, α and K_s) estimated by the GPR and surface soil moisture data assimilation during the simulation period. The "true" and initial values of these parameters are also plotted for comparison. The figure indicates that, with both data types (GPR and surface soil moisture), the estimated hydraulic parameters at the end of the simulation period are nearer the "true" ones than the initial values, implying that the data assimilation is able to correct not only the state variables but also model parameters. Comparing the two data types, the parameter estimation with the GPR data is more accurate than that with the surface soil moisture for all parameters. For example, for the case of the loamy sand, while with the GPR data assimilation, the parameters quickly approach and approximately equal the "true" value at 220-hour, parameter errors are still clearly observed for the surface soil moisture assimilation. This is because the GPR data assimilation has more information to constraint the parameter variation than the surface soil moisture assimilation.

The figure also shows that the parameter n converges to the stable state more quickly and is more accurate than α and K_s. For example, with the GPR data assimilation, from time 220-hour to the end of the simulation period, the maximum relative error of the estimated n for the loamy sand soil is lower than 1%, while the average relative errors of the α and K_s are, respectively, 3.6% and 3.2% in this period. Similar trends are also found for the clay and silt soils. This is attributed to the fact that the soil moisture (and its corresponding GPR data) is more sensitive to n, and less sensitive to α and K_s. The strong cross-correlation between the α and K_s, which leads to the instability of the parameter estimation, is another reason for less accuracy of these two parameters. These reasons lead to a consequence that although a perfect agreement between modeled and synthetic soil moisture profiles is reached, there are still differences between estimated and "true" parameters. We refer to Jadoon et al. [2008]; Lambot et al. [2009] for more detailed analysis on the sensitivity and stability of the soil hydraulic parameters estimation by GPR measurements.

8.5 Conclusion

In this study, a sequential GPR data assimilation was developed to simultaneously update the model state and parameters by combing the hydrodynamic model, GPR electromagnetic model, petrophysical relationship, MLEF technique and state augmentation method. The approach permits to directly assimilate GPR data, which takes advantages of the greater intrusion depth of GPR compared to the remote sensing measurement techniques for a more effective assimilation. The hydrodynamic model, Hydrus-1D, was used to simulate

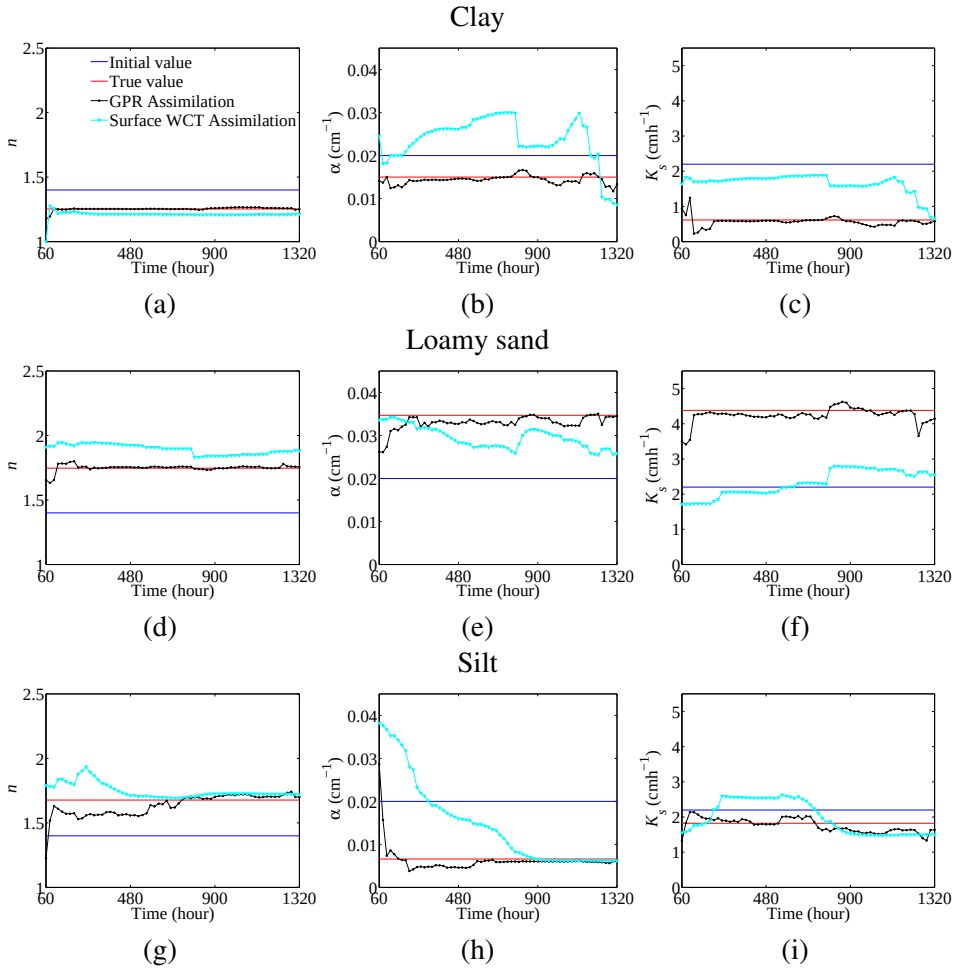

Figure 8.5. Variations over the assimilation period of the hydraulic parameters, namely, n (a, d, g), α (b, e, h) and K_s (c, f, i) (black line). The parameters are obtained by assimilating GPR (black line) and surface soil moisture data (cyan line). For comparison, the initial (blue line) and "true" (red line) values of these parameters are also plotted. The three soil types were accounted for: Clay (a, b, c), Loamy sand (d, e, f) and Silt (g, h, i).

the space–time dynamics of soil moisture in the unsaturated zone, while the GPR model and petrophysical relationship work as the observation operator that links the soil moisture state to the GPR data. The MLEF technique, which effectively solves the problem of nonlinear observation operator, is coupled with the state augmentation method to estimate the soil moisture profile and hydraulic parameters.

We numerically evaluated the assimilation scheme by comparing three scenarios: open-loop, surface soil moisture assimilation and GPR assimilation. The results show that the GPR and surface soil moisture assimilation significantly improves the wrong model parameters and initial conditions. The results also point out that the hydraulic parameters are well estimated, especially with the GPR data assimilation. The estimation of the parameter n is more accurate than that of α and K_s for the fact that the GPR data are more sensitivity to n than the two remaining parameters.

Comparing the performance of the two data types, the GPR data assimilation outperforms the surface soil moisture assimilation in terms of both soil moisture and model parameter estimation. It is because in addition to the surface layer, GPR data contain soil moisture information at the deeper layers. The results also show that for both data types, soil moisture is better corrected for the loamy sand and silt than the clay soil due to the fact that the soil moisture correction at the upper layers propagates more quickly to the deeper layers in the coarse (loamy sand and silt) than the fine soil (clay).

The results obtained by this study shows a promising way to estimate the soil moisture profile and hydraulic parameters from field-scale GPR data. The proposed data assimilation scheme can be also effectively applied for other geophysical techniques (e.g., electromagnetic induction (EMI)). However, this study only considered the GPR measurement error. The other error sources coming from input data (rainfall), model structure and observation operator, which may affect on the data assimilation have not been taken into account yet. These errors should be accounted for in the future research under laboratory or field conditions.

Chapter 9

Conclusion and Perspectives

In this thesis we attempted to increase the accuracy of soil moisture estimation by improving full-wave GPR inversion and petrophysical relationships. For the GPR inversion, we further developed the antenna model introduced by Lambot and André [2013], which characterizes the antenna by a set of source/field points and frequency-dependent transmission/reflection transfer functions. We successfully calibrated and validated the model using both numerical and laboratory experiments. Then, we improved the petrophysical relationship that links the soil electric properties with soil moisture by coupling full-wave GPR inverse modeling, soil dielectric mixing model and Debye's equation to account for the frequency dependence of the electric properties and thereby directly estimate soil moisture.

Another question addressed in this thesis was integrating the GPR model into the hydrodynamic model to characterize the soil hydraulic properties and soil moisture profile in a sequential data assimilation framework. In this framework, the hydrodynamic model was employed to simulate the spatiotemporal dynamics of soil moisture in the unsaturated zone, while the GPR model and petrophysical relationships were used to link the soil moisture profile with GPR data. Instead of using the surface soil moisture only, the approach allows us to use the information of the whole soil moisture profile for the assimilation. The main results obtained in each chapter are summarized in the following paragraphs.

9.1 Conclusion

In Chapter 2, we numerically evaluated the newly-developed full-wave GPR model under a blind test. The synthetic antennas were simulated by a FDTD model (GprMax3D) based on a bowtie GSSI-GPR with a center frequency of 1.5 GHz. For calibration, synthetic GPR data were produced with different antenna heights above an artificial PEC. By matching these synthetic data with our near-field modeled data, the transmission/reflection transfer functions were determined. We then employed the calibrated model to estimate the electric properties of a synthetic medium subject to 8 scenarios of layering, thickness

and electric properties, which represent most of the realistic cases. Very good agreements with the modeled values were obtained, especially for the electric permittivity with relative errors lower than 5%. The success of this numerical test proves that the near-field antenna model can provide a similar result as the FDTD model with a much more effect in term of computing time.

In Chapter 3, we determined the antenna height threshold for the near- and far-field modeling by analyzing the spatial variation of the Green's function over the antenna aperture for different GPR systems (Vivaldi, BBHA 9120-F and 400-MHz GSSI). When the ratio between the antenna height and maximum dimension of the antenna aperture is greater than 1.2, the amplitude of the spatial derivatives of the Green's function approximately equal to zero, and therefore, they are considered to be constant everywhere over the antenna aperture. Consequently, the antenna height threshold is a function of the maximum antenna aperture and set to $h = 1.2D$. The threshold was validated both by using numerical and laboratory experiments with a Vivaldi antenna operating at a frequency range of 1–3 GHz. The numerical results indicated that above the antenna height threshold, the performance of the near- and far-field antenna models is similar, both in magnitude and phase. For laboratory experiments, we compared the inversion results of both models with GPR measurements from 0 to 70 cm above a water layer. The results showed that the near-field GPR model perfectly estimated the antenna height and water thickness at all antenna heights with very small differences between modeled and measured GPR data. The difference between far-field modeled and measured data reduced rapidly as the antenna height increased from 0 to $1.2D$. When the antenna height was larger than $1.2D$, the far-field model data were in very good agreement with the near-field modeled and measured data. We also expanded the problem by investigating the relationship between the antenna height threshold and the number of source/field points that characterizes the antenna. For the Vivaldi antenna, the obtained results showed that when the antenna height was larger than 29 cm, the far-field antenna model should be used. When the antenna height was in the range 2-29 cm, the 4 source/field points were sufficient to model the antenna, and when the antenna height was smaller than 2 cm, we have to use 6 source/field points to characterize the antenna. This study provides a theoretical approach to specify the antenna height threshold above which the far-field model is hold and can be applied for the reconstruction of layered media.

In Chapter 4, we tackled the antenna array modeling problem by proposing an effective strategy to calibrate the antenna array, which then can be used to reproduce the electric properties of a multi-layered medium by the full-wave inverse modeling. The array was considered as a combination of several couples of transmitting-receiving antennas with different offsets in which each couple is modeled by the new near-field antenna model. The proposed cali-

bration strategy was based on the approach that progressively completes the model structure from simple to full array model. Accordingly, the results from the simple antenna model were used as initial guesses for the more complicated one. In addition, the special structure of the antenna array model enables us to couple linear-nonlinear optimization algorithms to considerably reduce the number of unknown parameters for the model calibration. We also proposed a procedure to convert the gain in the time domain to the frequency one and applied this gain to both modeled and measured array data to compensate for the signal attenuation. The results showed that the calibration approach worked well at all antenna offsets with correlation coefficients of the modeled and measured data larger than 0.9979 and root mean square errors less than 2.3×10^{-5}. The success of the model calibration demonstrates a great potential of the full-wave antenna array inverse modeling for accurate quantification of the electric properties of multi-layered media, especially deep layers.

In Chapter 5, we improved the accuracy of soil moisture estimation by coupling the soil dielectric mixing model and the full-wave GPR inversion. This approach allowed to consider the frequency dependence of the electric permittivity and apparent conductivity in GPR inverse modeling. Moreover, with this approach, soil moisture was directly obtained from GPR inversion without the need for a specific relationship nor a priori information about soil porosity. For mixing models, we used two models, namely CRIM and Wang and Schmugge [1980]'s model. While CRIM model considers 3 components in soil mixture (soil particle, water and air), Wang and Schmugge [1980]'s model contains one more component known as bound water in its formula. The approach was applied to the laboratory measurements above a sandy soil layer. The estimated Green's functions were well fitted with those of the measurements, resulting in a very high accuracy of the estimated water content. The average absolute errors obtained by the approach were less than 0.013 cm^3/cm^3 and the correlation coefficients were greater than 0.97. Comparing the two mixing models, the water contents estimated by the CRIM were slightly more accurate than those of the Wang and Schmugge (1980)'s model for the dry sands, but less accurate for the wet sands. The results also pointed out that for the sandy soil, while the electric permittivity was approximately constant, the apparent conductivity significantly increased with increasing frequency. This study provides a new approach to use the soil mixing model for increasing the accuracy of soil moisture estimation.

In Chapter 6, we showed validation results of the full-wave GPR model to estimate the sand water content in near-field conditions using both frequency (Vivaldi) and time domain ((900 MHz GSSI) GPR systems. We used 6 source/field points to simulate both antennas, which was optimal for a reasonable computing time, acceptable complexity of the inverse calibration problem and accurate characterization of the antennas. We employed the CRIM mixing

model to relate the electric properties and correlated electric properties. After calibration, the model was used to estimate the water content of a sand with different saturation levels in laboratory conditions by inverting GPR data. In both time and frequency domains, the model performance in terms of GPR signals was relatively good but reduced when the antenna approached the sand surface. The obtained results showed that the estimated water content well agreed with the measured ones. The average difference between the GPR and sampling water content was 0.012 cm^3/cm^3 for the FD-GPR, and 0.016 cm^3/cm^3 for the TD-GPR, respectively. Comparing the two antennas, the estimation from the FD-GPR was better than the TD-GPR for the dry, but worse for the wet sand because the TD-GPR operates at a lower frequency range. As the sand became wetter, the agreement between the modeled and measured GPR data reduced, and the estimated soil moisture estimation was less accurate. The numerical simulations showed that it is due to the inherently variable hydrostatic pressure resulting in an heterogeneous water content profile (water moved downward). As a result, the full-wave GPR inversion with the 1-layered soil model was not adequate to account for this heterogeneity. The problem was solved by using the multi-layered soil model based on the van Genuchten retention curve [van Genuchten, 1980] to describe the vertical profile. Both numerical and laboratory experiments pointed out that, comparing to the 1-layered soil model, the agreement between modeled and numerical (or measured) GPR data and accuracy of the soil moisture estimation obtained by this model were considerably improved. The successful validation of the near-field GPR model in laboratory conditions indicates a great potential of this model for practical applications, e.g., digital soil mapping and non-destructive testing of materials.

In Chapter 7, we explored the potentials of GPR data assimilation to correct soil moisture profile prediction from an unsaturated hydrodynamic model. Hydrus-1D model [Šimunek et al., 2009] was used to propagate the system state in time and electromagnetic model [Lambot et al., 2004c] and petrophysical relationships to link the state variable with the GPR data. Data assimilation was performed based on the MLEF algorithm [Zupanski, 2005], which more effectively solves the nonlinear observation operator of the GPR model than the Kalman filter method. The approach directly assimilates GPR data to update the soil moisture profile, while the common approaches in remote sensing use only the surface soil moisture to update the whole soil moisture profile. The approach helped us to avoid solving the difficult, time-consuming inverse problem to estimate the soil moisture from GPR data. Direct assimilation of GPR data allowed to take advantages of the greater intrusion depth of GPR data compared to the remote sensing techniques for a more effective assimilation. The approach was validated using synthetic experiments for the 3 typical soil types (loamy sand, silt and clay) in which the initial conditions were assumed to be unknown. The obtained results demonstrated that for all soil types, the

RMSE of the prediction without the GPR data assimilation was much larger than that with the GPR data assimilation. The results also showed that reducing update interval slightly improved the soil moisture profile estimation for the loamy sand and silt soils, but significantly for the clay soil. By combining the hydrological and GPR models in a data assimilation framework, this study provides an interesting way to use time-lapse GPR data for estimation of soil moisture profile with a high spatiotemporal resolution.

In Chapter 8, we expanded the assimilation framework in Chapter 7 to simultaneously estimate both soil moisture profile and hydraulic parameters. The state vector (soil moisture profile) in Chapter 7 was augmented by the parameter vector containing parameters n, α and K_s using the state augmentation technique. As a result, instead of estimating soil moisture profile only like in Chapter 7, the approach could jointly estimate soil moisture and hydraulic parameters. It is different from the batch model calibration approach presented in Lambot et al. [2006b] in the sense that while in the batch model calibration, the model parameters are assumed to be time-invariant and estimated by using the whole time-series data, the proposed data assimilation framework sequentially updates the soil moisture and model parameters whenever the GPR measurement is available. It also allows us to explicitly account for the errors in input, output and model structure, while the batch calibration devotes these errors to the model parameter uncertainties. The results showed that the GPR data assimilation significantly improved the estimation of soil moisture profile and hydraulic parameter estimation. Compared with the surface soil moisture assimilation, the GPR one outperformed. Of the three parameters, the parameter n was better estimated than α and K_s because GPR data are more sensitivity to n than the two remaining parameters. The results also showed that soil moisture was better corrected for the loamy sand and silt than the clay soil for the fact that the soil moisture correction at the upper layers propagates more quickly to the deeper ones in the loamy sand and silt than the clay soil. The approach presented in this chapter allows to simultaneously solve the problems of wrong initial conditions and soil hydraulic parameters, which has a great potential to apply for realistic applications where these data are usually not available.

9.2 Perspectives

The numerical and laboratory evaluation of the new near-field GPR model presented in this thesis showed that the model works well in both near- and far-field conditions. Different from the far-field GPR model, with the near-field one, the antenna is able to operate close or in contact with the medium, thereby increasing information about medium contained in the GPR data. As

a result, the medium electric properties can be better obtained. The model can be effectively applied for many practical applications, e.g., digital soil mapping and nondestructive testing of materials. Especially, for quantitative characterization of soil moisture, the accuracy of soil moisture is more improved when coupling the full-wave inversion of GPR data with the soil dielectric mixing model. However, due to complex interaction between antenna and dielectric layered medium, there are still some discrepancies between measured and modeled GPR data at very near-field region (≤ 1 cm) (see Chapters 2 and 6). Therefore, it is required a more effective measurement strategy for calibration or configuration of antenna characterization to improve the performance of the near-field GPR model in this region. In addition, the validation of the near-field GPR model and soil dielectric mixing model in the thesis was limited to laboratory conditions with a sandy soil. In realistic applications where soil exhibits a large heterogeneity and complicate soil structure and soil type, the problem becomes more difficult. Future research will attempt to account for them in GPR inverse modeling.

The preliminary success of the antenna array modeling and calibration opened a great development avenue for future development of GPR because it allows to simultaneously obtain different datasets in a single measurement. However, problems of optimal number of antenna elements and antenna design for maximizing information content for each specific purpose have not been answered yet. How to integrate all of the antenna array measurements in an efficient data fusion technique to retrieve the best parameters is also still a challenging question.

The GPR data assimilation scheme was successfully applied to simultaneously estimate both model state and parameters with the numerical experiments. This scheme can be applied not only for GPR but also other geophysical techniques. It is a new progress to integrate the geophysical measurements into hydrological model for monitoring soil moisture dynamics. However, this scheme has never been applied for realistic conditions where the errors related to input and output data, observation operator, model structure, and parameters cannot be controlled. The complexity of soil structure, heterogeneity of soil types, interactions with plant roots and vegetation cover make the problem much more complicated. In addition, for more effective applications, the data assimilation with 1-D hydrological model is insufficient. For future research on this topic, 2- or 3-D hydrological model should be accounted for. Moreover, in this thesis, the errors of the hydrological model and the observation operator were assumed to follow the Gaussian distribution with a mean of zero. However, in realistic applications, these errors are usually bias. As a result, the biases of the model and observation operator should be considered as the unknown and estimated during the assimilation process (see [Pauwels et al., 2013]). Another problem with the data assimilation scheme is that although

it well solves the problem of nonlinear observation operator, similar to the Kalman filter approach, the MLEF assimilation scheme still relies on the Gaussian assumption for state variables and model parameters, which do not always satisfy in reality. The up-to-date assimilation techniques allow us to solve the problem by: 1) using nonlinear, monotonous transfer functions to transform the observed states to Gaussian ones [Schöniger et al., 2012], or 2) employing the particle filter assimilation algorithm, which does not require any assumptions about the model dynamics or the density function of state variables and observation [Arulampalam et al., 2002; Andrieu et al., 2010]. Future researches will investigate these techniques for more effective GPR data assimilation.

This thesis does not cover the integration of different geophysical techniques, which helps to constrain the inverse problems to estimate soil moisture. For example, while GPR is more sensitive with the electric permittivity than the electric conductivity, EMI is more sensitive with the latter than former. As a result, joint inversion of data measured by these two techniques potentially helps to avoid the nonuniqueness of inverse problem and thus, enhances the accuracy of both permittivity and conductivity as well as their correlated soil-water variables [Moghadas et al., 2010]. For data assimilation, the priori values of soil hydraulic parameters can be obtained from soil properties (texture, bulk density, and carbon content) by using pedotransfer functions [Vereecken et al., 1989; Schaap et al., 2001]. Soil moisture state can be roughly approximated from the weather conditions. In the data assimilation scheme, they will be initial values, which helps the data assimilation to locate the optimal solutions more quickly and accurately.

The near-field GPR model presented in this research can be also applied for a wide range of environmental and engineering applications. For example, our model provides high resolution information about the pavement layer thickness, concrete moisture for the road, as well as the location and quantity of deteriorated concrete and corrosion induced delaminations, depth of reinforcing steel and thickness or bond of overlays for the bridges. In an underground coal mining operation, our model can be employed to filter unnecessary signals from raw GPR data, thereby making reflections from coal mines become more visible, increasing the opportunity to detect them. The remediation of contaminated sites requires knowledge on the contaminant distribution in the subsurface. The interpretation of the GPR signals based on the near-field GPR model can support to find the contaminated location, which traditionally requires expensive campaign of site investigation, drilling and sampling.

Bibliography

Abudayyeh, O., Yehia, S., Abdel-Qader, I., and Zalt, A. GPR imaging for bridge deck condition assessment. *Bridge Structures*, 4(2), 2008.

Alvarez-Mozos, J., Casali, J., Gonzalez-Audicana, M., and Verhoest, N. E. C. Assessment of the operational applicability of radarsat-1 data for surface soil moisture estimation. *IEEE Transactions on Geoscience and Remote Sensing*, 44(4):913–924, 2006. doi: 10.1109/TGRS.2005.862248.

André, F., Leeuwen, C. V., Saussez, S., Durmen, R. V., Bogaert, P., Moghadas, D., Rességuier, L. D., Delvaux, B., Vereecken, H., and Lambot, S. High-resolution imaging of a vineyard in south of france using ground-penetrating radar, electromagnetic induction and electrical resistivity tomography. *Journal of Applied Geophysics*, 78:113–122, 2012. doi: 10.1016/j.jappgeo.2011.08.002.

Andrieu, C., Doucet, A., and Holenstein, R. Particle markov chain monte carlo methods. *Journal of the Royal Statistical Society: Series B (Statistical Methodology)*, 72(3):269–342, 2010. doi: 10.1111/j.1467-9868.2009.00736.x.

Annan, A. P. GPR–History, Trends, and Future Developments. *Subsurface Sensing Technologies and Applications*, 3(4):253–270, 2002.

Annan, A. P. GPR methods for hydrogeological studies. In Hubbard, Y. R. and S.S., editors, *Hydrogeophysics*, page 532, Springer, New York, 2005.

Annan, A. P., Cosway, S. W., and Redman, J. D. *Water table detection with ground-penetrating radar*, pages 494–496. Society of Exploration Geophysicists, 1991.

Arulampalam, M. S., Maskell, S., Gordon, N., and Clapp, T. A tutorial on particle filters for online nonlinear/non-gaussian bayesian tracking. *IEEE Transactions on Signal Processing*, 50(2):174–188, 2002. doi: 10.1109/78.978374.

Atteia, G. E. and Hussein, K. F. A. Realistic model of dispersive soils using plrc-fdtd with applications to GPR systems. *Progress In Electromagnetics Research B*, 26:335–359, 2010.

Bailey, J. T., Evans, S., and Robin, G. d. Q. Ground-penetrating radar surveys used in archaeological investigations. *Nature*, 204:420–421, 1964.

Bano, M. Effects of the transition zone above a water table on the reflection of GPR waves. *Geophysical Research Letters*, 33(13):5, 2006.

Bartalis, Z., Wagner, W., Naeimi, V., Hasenauer, S., Scipal, K., Bonekamp, H., Figa, J., and Anderson, C. Initial soil moisture retrievals from the metop-a advanced scatterometer (ascat). *Geophysical Research Letters*, 34(20): L20401, 2007. doi: 10.1029/2007GL031088.

Bell, J. P., Dean, T. J., and Hodnett, M. G. Soil moisture measurement by an improved capacitance technique, part ii. field techniques, evaluation and calibration. *Journal of Hydrology*, 93(1–2):79–90, 1987. doi: 10.1016/0022-1694(87)90195-8.

Benedetto, A., Benedetto, F., De Blasiis, M., and Giunta, G. Reliability of signal processing technique for pavement damages detection and classification using ground penetrating radar. *IEEE Sensors Journal*, 5(3):471–480, 2005.

Bhattacharya, A., Sarkis, R., Hislop, G., Lambot, S., and Craeye, C. Modeling of an ultra-wideband antenna array devoted to near-field imaging. In *Antennas and Propagation Conference (LAPC), 2010 Loughborough*, pages 545–548, 2010. doi: 10.1109/LAPC.2010.5666913.

Bogena, H. R., Huisman, J. A., Oberdörster, C., and Vereecken, H. Evaluation of a low-cost soil water content sensor for wireless network applications. *Journal of Hydrology*, 344(1-2):32–42, 2007.

Boyarskii, D. A., Tikhonov, V. V., and Yu., K. N. Model of dielectric constant of bound water in soil for applications of microwave remote sensing. *Progress In Electromagnetics Research*, 35:251–269, 2002. doi: 10.2528/PIER01042403.

Brocca, L., Melone, F., Moramarco, T., Wagner, W., Naeimi, V., Bartalis, Z., and Hasenauer, S. Improving runoff prediction through the assimilation of the ascat soil moisture product. *Hydrology and Earth System Sciences*, 14 (10):1881–1893, 2010. doi: 10.5194/hess-14-1881-2010.

Brown, J., Harper, J., Pfeffer, W., Humphrey, N., and Bradford, J. High-resolution study of layering within the percolation and soaked facies of the greenland ice sheet. *Annals of Glaciology*, 52(59):35–42, 2011. doi: 10.3189/172756411799096286.

Buchner, J., Wollschläger, U., and Roth, K. Inverting surface GPR data using fdtd simulation and automatic detection of reflections to estimate subsurface water content and geometry. *Geophysics*, 77(4):H45–H55, 2012. doi: 10.1190/geo2011-0467.1.

Carsel, R. F. and Parrish, R. S. Developing joint probability distributions of soil water retention characteristics. *Water Resources Research*, 24(5):755–769, 1988. ISSN 1944-7973. doi: 10.1029/WR024i005p00755.

Chen, H. W. and Huang, T. M. F. Finite-difference time-domain simulation of GPR data. *Journal of Applied Geophysics*, 40(1-3):139–163, 1998. 0926-9851 doi: DOI: 10.1016/S0926-9851(98)00019-6.

Chen, Y., Yang, S., He, S., and Nie, Z. Fast analysis of microstrip antennas over a frequency band using an accurate mom matrix interpolation technique. *Progress In Electromagnetics Research*, 109:301–324, 2010.

Chew, W. C. *Waves and Fields in Inhomogeneous Media*. Van Nostrand Reinhold, New York, 1990.

Conyers, L. B. Innovative ground-penetrating radar methods for archaeological mapping. *Archaeological Prospection*, 13(2):139–141, 2006.

Cook, J. Borehole–radar exploration in a coal seam. *GEOPHYSICS*, 42(6): 1254–1257, 1977. doi: 10.1190/1.1440790.

Craeye, C., Tijhuis, A. G., and Schaubert, D. H. An efficient mom formulation for finite-by-infinite arrays of two-dimensional antennas arranged in a three-dimensional structure. *IEEE Transactions on Antennas and Propagation*, 52 (1):271–282, 2004.

Crocco, L., Soldovieri, F., Millington, T., and Cassidy, N. J. Bistatic tomographic GPR imaging for incipient pipeline leakage evaluation. *Progress in Electromagnetics Research*, 101:307–321, 2010.

Crow, W., Kustas, W., and Prueger, J. Monitoring root-zone soil moisture through the assimilation of a thermal remote sensing-based soil moisture proxy into a water balance model. *Remote Sensing of Environment*, 112(4): 1268–1281, 2008.

Dagenbach, A., Buchner, J. S., Klenk, P., and Roth, K. Identifying a parameterisation of the soil water retention curve from on-ground GPR measurements. *Hydrology and Earth System Sciences*, 17(2):611–618, 2013. doi: 10.5194/hess-17-611-2013.

Daily, W., Ramirez, A., LaBrecque, D., and Nitao, J. Electrical resistivity tomography of vadose water movement. *Water Resources Research*, 28(5): 1429–1442, 1992. doi: 10.1029/91WR03087.

Daniels, J. J., Allred, B., Binley, A., Labrecque, D., and Alumbaugh, D. Hydrogeophysical case studies in the vadose zone. In Rubin, Y. and Hubbard, S. S., editors, *Hydrogeophysics*, volume 50, pages 413–440. Springer Netherlands, 2005. 978-1-4020-3102-1.

Das, N. N. and Mohanty, B. P. Root zone soil moisture assessment using remote sensing and vadose zone modeling. *Vadose Zone Journal*, 5(1):296–307, 2006.

Das, N. N., Mohanty, B. P., Cosh, M. H., and Jackson, T. J. Modeling and assimilation of root zone soil moisture using remote sensing observations in walnut gulch watershed during smex04. *Remote Sensing of Environment*, 112(2):415–429, 2008.

David, G. and Renato, I. Measurements of water content distribution in vertical subsurface flow constructed wetlands using a capacitance probe: benefits and limitations. *Desalination*, 243(1–3):182–194, 2009. doi: 10.1016/j.desal.2008.05.012.

Davis, J. L. and Annan, A. P. Ground penetrating radar for high resolution mapping of soil and rock stratigraphy. *Geophysical Prospecting*, 37:531–551, 1989.

Davit, H. *Adaptive vector finite element methods for the Maxwell equations*. PhD thesis, May 2007.

De Lannoy, G. J. M., Houser, P. R., Pauwels, V. R. N., and Verhoest, N. E. C. State and bias estimation for soil moisture profiles by an ensemble kalman filter: Effect of assimilation depth and frequency. *Water Resources Research*, 43(6):W06401, 2007a. doi: 10.1029/2006WR005100.

De Lannoy, G. J. M., Reichle, R. H., Houser, P. R., Pauwels, V. R. N., and Verhoest, N. E. C. Correcting for forecast bias in soil moisture assimilation with the ensemble kalman filter. *Water Resources Research*, 43(9):W09410, 2007b. doi: 10.1029/2006WR005449.

Debye, P. *Polar molecules*. Reinhold, New York, 1929.

Deparis, J. and Garambois, S. On the use of dispersive apvo GPR curves for thin-bed properties estimation: Theory and application to fracture characterization. *Geophysics*, 74(1):J1–J12, 2009.

Dingman, S. L. *Physical Hydrology*. McMillan, New York, USA, 1994.

Dirksen, C. and Dasberg, S. Improved calibration of time domain reflectometry soil water content measurements. *Soil Science Society of America Journal*, 57:660–667, 1993.

Dobson, M. C., Ulaby, F. F., Hallikainen, M. T., and El-Rayes, M. A. Microwave dielectric behavior of wet soil - Part II: Dielectric mixing models. *IEEE Transactions on Geoscience and Remote Sensing*, 23:35–46, 1985.

Doetsch, J., Linde, N., and Binley, A. Structural joint inversion of time-lapse crosshole ert and GPR traveltime data. *Geophysical Research Letters*, 37 (24):L24404, 2010. doi: 10.1029/2010GL045482.

Draper, C. S., Reichle, R. H., De Lannoy, G. J. M., and Liu, Q. Assimilation of passive and active microwave soil moisture retrievals. *Geophysical Research Letter*, 39(4):L04401, 2012. doi: 10.1029/2011GL050655.

Dérobert, X., Iaquinta, J., Klysz, G., and Balayssac, J.-P. Use of capacitive and {GPR} techniques for the non-destructive evaluation of cover concrete. *{NDT} & E International*, 41(1):44–52, 2008. doi: 10.1016/j.ndteint.2007.06.004.

Drusch, M. Initializing numerical weather prediction models with satellite-derived surface soil moisture: Data assimilation experiments with ecmwf's integrated forecast system and the tmi soil moisture data set. *Journal of Geophysical Research: Atmospheres*, 112:D03102, 2007. doi: 10.1029/2006JD007478.

Durand, S. and Slodic, M. Fully discrete finite element method for maxwell's equations with nonlinear conductivity. *IMA Journal of Numerical Analysis*, 31(4):1713–1733, 2011. doi: 10.1093/imanum/drr007.

Ernst, J. R., Maurer, H., Green, A. G., and Holliger, K. Full-waveform inversion of crosshole radar data based on 2-D finite-difference time-domain solutions of Maxwell's equations. *IEEE Transactions on Geoscience and Remote Sensing*, 45(9):2807–2828, 2007.

Evett, S. R. Soil water measurement by neutron thermalization. *Encyclopedia of Water Science*, pages 889–893, 2003.

Famiglietti, J. S., Rudnicki, J. W., and Rodell, M. Variability in surface moisture content along a hillslope transect: Rattlesnake hill, texas. *Journal of Hydrology*, 210(1–4):259–281, 1998. doi: 10.1016/S0022-1694(98)00187-5.

Farnoosh, N., Shoory, A., Moini, R., and Sadeghi, S. H. H. Analysis of thin-wire ground penetrating radar systems for buried target detection, using a hybrid mom-fdtd technique. *NDT & E International*, 41(4):265–272, 2008. doi: 10.1016/j.ndteint.2007.11.001.

Feng, X., Sato, M., Zhang, Y., Liu, C., Shi, F., and Zhao, Y. CMP antenna array GPR and signal-to-clutter ratio improvement. *Geoscience and Remote Sensing Letters, IEEE*, 6(1):23–27, 2009. doi: 10.1109/LGRS.2008.2006634.

Fernández-Pantoja, M., Yarovoy, A., Rubio Bretones, A., and González García, S. Time domain analysis of thin-wire antennas over lossy ground using the reflection-coefficient approximation. *Radio Science*, 44(6):RS6009, 2009.

Ferré, P. A., Rudolph, D. L., and Kachanoski, R. G. Spatial averaging of water content by time domain reflectometry: Implications for twin rod probes with and without dielectric coatings. *Water Resources Research*, 32(2):271–279, 1996.

Francese, R. G., Finzi, E., and Morelli, G. 3-D high-resolution multi-channel radar investigation of a roman village in northern Italy. *Journal of Applied Geophysics*, 67(1):44–51, 2009. doi: 10.1016/j.jappgeo.2008.09.004.

Gader, P. D., Mystkowski, M., and Zhao, Y. Z. Y. Landmine detection with ground penetrating radar using hidden markov models, 2001.

Galagedara, L. W., Parkin, G. W., Redman, J. D., and Endres, A. L. Field studies of the GPR ground wave method for estimating soil water content during irrigation and drainage. *Journal of Hydrology*, 301:182–197, 2005a.

Galagedara, L. W., Redman, J. D., Parkin, G. W., Annan, A. P., and Endres, A. L. Numerical modeling of GPR to determine the direct ground wave sampling depth. *Vadose Zone Journal*, 4:1096–1106, 2005b.

Gentili, G. G. and Spagnolini, U. Electromagnetic inversion in monostatic ground penetrating radar: TEM horn calibration and application. *IEEE Transactions on Geoscience and Remote Sensing*, 38(4):1936–1946, 2000.

Gerhards, H., Wollschlager, U., Yu, Q., Schiwek, P., Pan, X., and Roth, K. Continuous and simultaneous measurement of reflector depth and average soil-water content with multichannel ground-penetrating radar. *Geophysics*, 73(4):J15–J23, 2008. doi: 10.1190/1.2943669.

Ghasemi, F. S. A. and Abrishamian, M. S. A novel method for fdtd numerical GPR imaging of arbitrary shapes based on fourier transform. *NDT & E International*, 40(2):140–146, 2007.

Giannopoulos, A. Modelling ground penetrating radar by gprmax. *Construction and Building Materials*, 19(10):755–762, 2005.

Gonzalez-Ovejero, D. and Craeye, C. Interpolatory macro basis functions analysis of non-periodic arrays. *Antennas and Propagation, IEEE Transactions on*, 59(8):3117–3122, 2011. doi: 10.1109/TAP.2011.2158947.

Gorriti, A. G. *Electric characterization of sands with heterogeneous saturation distribution*. PhD thesis, Delft University of Technology, 2004.

Grandjean, G., Paillou, P., Baghdadi, N., Heggy, E., August, T., and Lasne, Y. Surface and subsurface structural mapping using low frequency radar: A synthesis of the mauritanian and egyptian experiments. *Journal of African Earth Sciences*, 44(2):220–228, 2006.

Grasmueck, M. 3-d ground-penetrating radar applied to fracture imaging in gneiss. *Geophysics*, 61(4):1050–1064, 1996. doi: 10.1190/1.1444026.

Grote, K., Hubbard, S. S., and Rubin, Y. Field-scale estimation of volumetric water content using GPR ground wave techniques. *Water Resources Research*, 39(11):1321, 2003.

Heimovaara, T. J. Frequency domain analysis of time domain reflectometry waveforms, 1, Measurements of the complex dielectric permittivity of soils. *Water Resources Research*, 30(2):189–199, 1994.

Heitman, J. L., Basinger, J. M., Kluitenberg, G. J., Ham, J. M., Frank, J. M., and Barnes, P. L. Field evaluation of the dual-probe heat-pulse method for measuring soil water content. *Vadose Zone Journal*, 2(4):552–560, 2003. doi: 10.2113/2.4.552.

Hilhorst, M. A., Dirksen, C., Kampers, F. W. H., and Feddes, R. A. Dielectric relaxation of bound water versus soil matric pressure. *Geophysics*, 65:311–314, 2001.

Hinkel, K. M., Doolittle, J. A., Bockheim, J. G., Nelson, F. E., Paetzold, R., Kimble, J. M., and Travis, R. Detection of subsurface permafrost features with ground-penetrating radar, barrow, alaska. *Permafrost and Periglacial Processes*, 12(2):179–190, 2001. doi: 10.1002/ppp.369.

Hoeben, R. and Troch, P. A. Assimilation of active microwave observation data for soil moisture profile estimation. *Water Resources Research*, 36(10): 2805–2819, 2000.

Holger, G. *Ground Penetrating Radar as a Quantitative Tool with Applications in Soil Hydrology*. PhD thesis, University of Heidelberg, 2008.

Huang, C., Li, X., Lu, L., and Gu, J. Experiments of one-dimensional soil moisture assimilation system based on ensemble kalman filter. *Remote Sensing of Environment*, 112(3):888–900, 2008.

Huang, Z. B., Demarest, K. R., and Plumb, R. G. An fdtd/mom hybrid technique for modeling complex antennas in the presence of heterogeneous

grounds. *Ieee Transactions on Geoscience and Remote Sensing*, 37(6): 2692–2698, 1999.

Hubbard, S. S. and Rubin, Y. Introduction to hydrogeophysics. In Rubin, Y. and Hubbard, S. S., editors, *Hydrogeophysics*, volume 50 of *Water Science and Technology Library*, pages 3–21. Springer Netherlands, 2005. ISBN 978-1-4020-3101-4. doi: 10.1007/1-4020-3102-5_1.

Hubbard, S. S., Peterson, J., Majer, E., Zawislanski, P., Williams, K., Roberts, J., and Wobber, F. Estimation of permeable pathways and water content using tomographic radar data. *The Leading Edge*, 16(11):1623–1630, 1997. doi: 10.1190/1.1437539.

Huisman, J. A., Sperl, C., Bouten, W., and Verstraten, J. M. Soil water content measurements at different scales: accuracy of time domain reflectometry and ground penetrating radar. *Journal of Hydrology*, 245:48–58, 2001.

Huisman, J. A., Hubbard, S. S., Redman, J. D., and Annan, A. P. Measuring soil water content with ground penetrating radar: A review. *Vadose Zone Journal*, 2:476–491, 2003.

Hupet, F. and Vanclooster, M. Intraseasonal dynamics of soil moisture variability within a small agricultural maize cropped field. *Journal of Hydrology*, 261(1-4):86–101, 2002.

Huyer, W. and Neumaier, A. Global optimization by multilevel coordinate search. *Journal of Global Optimization*, 14(4):331–355, 1999.

Jackson, T. J. Iii. measuring surface soil moisture using passive microwave remote sensing. *Hydrological Processes*, 7(2):139–152, 1993. doi: 10.1002/hyp.3360070205.

Jadoon, K. Z., Lambot, S., Slob, E. C., and Vereecken, H. Uniqueness and stability analysis of hydrogeophysical inversion for time-lapse proximal ground penetrating radar. *Water Resources Research*, 44, 2008.

Jadoon, K. Z., Lambot, S., Slob, E. C., and Vereecken, H. Analysis of horn antenna transfer functions and phase-center position for modeling off-ground GPR. *IEEE Transactions on Geoscience and Remote Sensing*, 49(5):1649–1662, 2011. doi: 10.1109/TGRS.2010.2089691.

Jadoon, K. Z., Wëihermuller, L., Scharnagl, B., Kowalsky, M. B., Bechtold, M., Hubbard, S. S., Vereecken, H., and Lambot, S. Estimation of soil hydraulic parameters in the field by integrated hydrogeophysical inversion of time-lapse ground-penetrating radar data. *Vadose Zone Journal*, 11(4), 2012. doi: 10.2136/vzj2011.0177.

Jol, H. M. *Ground penetrating radar theory and applications*. Elsevier Science, Amsterdam, The Netherlands, 2009.

Kerkez, B., Glaser, S., Bales, R., and Meadows, M. Design and performance of a wireless sensor network for catchment-scale snow and soil moisture measurements. *Water Resources Research*, 48(9):W09515, 2012. doi: 10.1029/2011WR011214.

Kerr, Y. H. Soil moisture from space: Where are we? *Hydrogeology Journal*, 15(1):117–120, 2007. doi: 10.1007/s10040-006-0095-3.

Klein, L. A. and Swift, C. T. An improved model for the dielectric constant of sea water at microwave frequencies. *IEEE Transactions on Antennas and Propagation*, AP-25(1):104–111, 1977.

Kool, J. B. and Parker, J. C. Analysis of the Inverse Problem for Transient Unsaturated Flow. *Water Resources Research*, 24:817–830, 1988.

Kornelsen, K. C. and Coulibaly, P. Advances in soil moisture retrieval from synthetic aperture radar and hydrological applications. *Journal of Hydrology*, 476(0):460–489, 2013. doi: 10.1016/j.jhydrol.2012.10.044.

Kowalsky, M. B., Finsterle, S., Peterson, J., Hubbard, S. S., Rubin, Y., Majer, E., Ward, A., and Gee, G. Estimation of field-scale soil hydraulic and dielectric parameters through joint inversion of GPR and hydrological data. *Water Resources Research*, 41:W11425, 2005.

Lambot, S. and André, F. Full-wave modeling of near-field radar data for planar layered media reconstruction. *IEEE Transactions on Geoscience and Remote Sensing*, 2013. doi: 10.1109/TGRS.2013.2259243.

Lambot, S., Javaux, M., Hupet, F., and Vanclooster, M. A global multilevel coordinate search procedure for estimating the unsaturated soil hydraulic properties. *Water Resources Research*, 38(11):1224, 2002.

Lambot, S., Hupet, F., Javaux, M., and Vanclooster, M. Laboratory evaluation of a hydrodynamic inverse modeling method based on water content data. *Water Resources Research*, 40(3):W03506, 2004a.

Lambot, S., Rhebergen, J., van den Bosch, I., Slob, E. C., and Vanclooster, M. Measuring the soil water content profile of a sandy soil with an off-ground monostatic ground penetrating radar. *Vadose Zone Journal*, 3(4): 1063–1071, 2004b.

Lambot, S., Slob, E. C., van den Bosch, I., Stockbroeckx, B., and Vanclooster, M. Modeling of ground-penetrating radar for accurate characterization of

subsurface electric properties. *IEEE Transactions on Geoscience and Remote Sensing*, 42:2555–2568, 2004c.

Lambot, S., van den Bosch, I., Stockbroeckx, B., Druyts, P., Vanclooster, M., and Slob, E. C. Frequency dependence of the soil electromagnetic properties derived from ground-penetrating radar signal inversion. *Subsurface Sensing Technologies and Applications*, 6:73–87, 2005.

Lambot, S., Antoine, M., Vanclooster, M., and Slob, E. C. Effect of soil roughness on the inversion of off-ground monostatic GPR signal for noninvasive quantification of soil properties. *Water Resources Research*, 42:W03403, 2006a.

Lambot, S., Slob, E. C., Vanclooster, M., and Vereecken, H. Closed loop GPR data inversion for soil hydraulic and electric property determination. *Geophysical Research Letters*, 33:L21405, 2006b.

Lambot, S., Slob, E. C., and Vereecken, H. Fast evaluation of zero-offset Green's function for layered media with application to ground-penetrating radar. *Geophysical Research Letters*, 34:L21405, 2007.

Lambot, S., Slob, E. C., Rhebergen, J., Lopera, O., Jadoon, K. Z., and Vereecken, H. Remote Estimation of the Hydraulic Properties of a Sand Using Full-Waveform Integrated Hydrogeophysical Inversion of Time-Lapse, Off-Ground GPR Data. *Vadose Zone Journal*, 8(3):743–754, 2009.

Lane, J. A. and Saxton, J. A. Dielectric dispersion in pure polar liquids at very high radio frequencies. iii. the effect of electrolytes in solution. *Proceedings of the Royal Society of London. Series A, Mathematical and Physical Sciences*, 214(1119):531–545, 1952.

Ledieu, J., De Ridder, P., De Clercq, P., and Dautrebande, S. A method of measuring soil moisture by time domain reflectometry. *Journal of Hydrology*, 88:319–328, 1986.

Lesmes, D. P. and Friedman, S. P. Relationships between the electrical and hydrogeological properties of rocks and soils. In Rubin, Y. and S., H. S. S., editors, *Hydrogeophysics*, pages 87–128. Springer, Dordrecht, The Netherlands, 2005.

Linford, N., Linford, P., Martin, L., and Payne, A. Stepped frequency ground-penetrating radar survey with a multi-element array antenna: Results from field application on archaeological sites. *Archaeological Prospection*, 17(3): 187–198, 2010. doi: 10.1002/arp.382.

Loew, A. Preface: Remote sensing data assimilation special issue. *Remote Sensing of Environment*, 112(4):1257, 2008. doi: 10.1016/j.rse.2007.07.003.

Looms, M. C., Jensen, K. H., Binley, A., and Nielsen, L. Monitoring unsaturated flow and transport using cross-borehole geophysical methods. *Vadose Zone Journal*, 7(1):227–237, 2008.

Looyenga, H. Dielectric constants of heterogeneous mixtures. *Physica*, 31(3):401–406, 1965.

Lopera, O., Milisavljevic, N., and Lambot, S. Clutter reduction in GPR measurements for detecting shallow buried landmines: a Colombian case study. *Near Surface Geophysics*, 5(1):57–64, 2007a.

Lopera, O., Slob, E. C., Milisavljevic, N., and Lambot, S. Filtering soil surface and antenna effects from GPR data to enhance landmine detection. *IEEE Transactions on Geoscience and Remote Sensing*, 45(3):707–717, 2007b.

Mahfouf, J. F. Assimilation of satellite-derived soil moisture from ascat in a limited-area nwp model. *Quarterly Journal of the Royal Meteorological Society*, 136(648):784–798, 2010. doi: 10.1002/qj.602.

Mahmoudzadeh, M. R., Francés, A. P., Lubczynski, M., and Lambot, S. Using ground penetrating radar to investigate the water table depth in weathered granites-sardon case study, Spain. *Journal of Applied Geophysics*, 79:17 – 26, 2012. doi: 10.1016/j.jappgeo.2011.12.009.

Merz, B. and Bardossy, A. Effect of spatial variability on the rainfall runoff process in a small loess catchment. *Journal of Hydrology*, 212:304–317, 1998.

Michalski, K. A. and Mosig, J. R. Multilayered media Green's functions in integral equation formulations. *IEEE Transactions on Antennas and Propagation*, 45(3):508–519, 1997.

Michot, D., Benderitter, Y., Dorigny, A., Nicoullaud, B., King, D., and Tabbagh, A. Spatial and temporal monitoring of soil water content with an irrigated corn crop cover using surface electrical resistivity tomography. *Water Resources Research*, 39(5):1138, 2003. doi: 10.1029/2002WR001581.

Minet, J., Laloy, E., Lambot, S., and Vanclooster, M. Effect of GPR-derived within-field soil moisture variability on the runoff response using a distributed hydrologic model. *Hydrology and Earth System Sciences Discussions*, 7(6):8947–8986, 2010a. doi: 10.5194/hessd-7-8947-2010.

Minet, J., Lambot, S., Slob, E. C., and Vanclooster, M. Soil surface water content estimation by full-waveform GPR signal inversion in the presence of thin layers. *IEEE Transactions on Geoscience and Remote Sensing*, 48: 1138 – 1150, 2010b. doi: 10.1109/TGRS.2009.2031907.

Minet, J., Wahyudi, A., Bogaert, P., Vanclooster, M., and Lambot, S. Mapping shallow soil moisture profiles at the field scale using full-waveform inversion of ground penetrating radar data. *Geoderma*, 161:225–237, 2011.

Moghadas, D., André, F., Slob, E. C., Vereecken, H., and Lambot, S. Joint full-waveform analysis of off-ground zero-offset ground penetrating radar and electromagnetic induction synthetic data for estimating soil electrical properties. *Geophysical Journal International*, 182(3):1267–1278, 2010. doi: 10.1111/j.1365-246X.2010.04706.x.

Mohammadi, M. H. and Vanclooster, M. Predicting the soil moisture characteristic curve from particle size distribution with a simple conceptual model. *Vadose Zone Journal*, 10(2):594–602, 2011. doi: 10.2136/vzj2010.0080.

Monteith, J. L. Evaporation and surface temperature. *Quarterly Journal of the Royal Meteorological Society*, 107(451):1–27, 1981.

Montzka, C., Moradkhani, H., Weihermüller, L., Franssen, H.-J. H., Canty, M., and Vereecken, H. Hydraulic parameter estimation by remotely-sensed top soil moisture observations with the particle filter. *Journal of Hydrology*, 399:410–421, 2011.

Moradkhani, H., Hsu, K.-L., Gupta, H., and Sorooshian, S. Uncertainty assessment of hydrologic model states and parameters: Sequential data assimilation using the particle filter. *Water Resources Research*, 41(5):W05012, 2005a. doi: 10.1029/2004WR003604.

Moradkhani, H., Sorooshian, S., Gupta, H. V., and Houser, P. R. Dual state–parameter estimation of hydrological models using ensemble kalman filter. *Advances in Water Resources*, 28(2):135–147, 2005b.

Mualem, Y. A new model for predicting the hydraulic conductivity of unsaturated porous media. *Water Resources Research*, 12:513–522, 1976.

Nadakuduti, J., Genda, C., and Zoughi, R. Semiempirical electromagnetic modeling of crack detection and sizing in cement-based materials using near-field microwave methods. *IEEE Transactions on Instrumentation and Measurement*, 55(2):588–597, 2006.

Neal, A. Ground-penetrating radar and its use in sedimentology: principles, problems and progress. *Earth-Science Reviews*, 66:261–330, 2004. doi: http://dx.doi.org/10.1016/j.earscirev.2004.01.004.

Nelder, J. A. and Mead, R. A simplex method for function minimization. *The Computer Journal*, 7(4):308–313, 1965. doi: 10.1093/comjnl/7.4.308.

Nied, M., Hundecha, Y., and Merz, B. Flood-initiating catchment conditions: a spatio-temporal analysis of large-scale soil moisture patterns in the elbe river basin. *Hydrology and Earth System Sciences*, 17(4):1401–1414, 2013. doi: 10.5194/hess-17-1401-2013.

Nigel, J. C. Evaluating lnapl contamination using GPR signal attenuation analysis and dielectric property measurements: Practical implications for hydrological studies. *Journal of Contaminant Hydrology*, 94(1–2):49–75, 2007. doi: 10.1016/j.jconhyd.2007.05.002.

Olhoeft, G. R. Thawing of permafrost along the trans-alaska pipeline. In *Proceedings of the Symposium on Permafrost Geophysics: Ottawa, Canada, Nuclear Regulatory Commission Technical Memo*, pages 103–109, 1980.

Owsley, D. W. Techniques for locating burials, with emphasis on the probe. *Journal of Forensic Sciences*, 40:735–740, 1995.

Paltineanu, I. C. and Starr, J. L. Real-time soil water dynamics using multisensor capacitance probes: Laboratory calibration. *Soil Science Society of America Journal*, 61(6):1576–1585, 1997.

Pan, X., Wollschlager, U., Gerhards, H., and Roth, K. Optimization of multi-channel ground-penetrating radar for quantifying field-scale soil water dynamics. *Journal of Applied Geophysics*, 82(0):101–109, 2012. doi: 10.1016/j.jappgeo.2012.02.007.

Papadopoulos, N., Sarris, A., Yi, M., and Kim, J. Urban archaeological investigations using surface 3D ground penetrating radar and electrical resistivity tomography methods. *Exploration Geophysics*, 40(1):56–68, 2009.

Patriarca, C., Lambot, S., Mahmoudzadeh, M. R., Minet, J., and Slob, E. C. Reconstruction of sub-wavelength fractures and physical properties of masonry media using full-waveform inversion of proximal penetrating radar. *Journal of Applied Geophysics*, 74(1):26–37, 2011. doi: http://dx.doi.org/10.1016/j.jappgeo.2011.03.001.

Pauwels, V. R. N., Verhoest, N. E. C., De Lannoy, G. J. M., Guissard, V., Lucau, C., and Defourny, P. Optimization of a coupled hydrology-crop growth

model through the assimilation of observed soil moisture and leaf area index values using an ensemble kalman filter. *Water Resources Research*, 43(4): W04421, 2007.

Pauwels, V. R. N., De Lannoy, G. J. M., Hendricks Franssen, H.-J., and Vereecken, H. Simultaneous estimation of model state variables and observation and forecast biases using a two-stage hybrid kalman filter. *Hydrology and Earth System Sciences*, 17(9):3499–3521, 2013. doi: 10.5194/hess-17-3499-2013.

Pedro, C. D., Wellington, R., Elnatan, C. F., and D., J. A. S. A high sensitivity single-probe heat pulse soil moisture sensor based on a single npn junction transistor. *Computers and Electronics in Agriculture*, 96:139–147, 2013. doi: 10.1016/j.compag.2013.05.003.

Pettinelli, E., Di Matteo, A., Mattei, E., Crocco, L., Soldovieri, F., Redman, J. D., and Annan, A. P. GPR response from buried pipes: measurement on field site and tomographic reconstructions. *IEEE Transactions on Geoscience and Remote Sensing*, 47(8):2639–2645, 2009.

Redman, J. D., Davis, J. L., Galagedara, L. W., and Parkin, G. W. Field studies of GPR air launched surface reflectivity measurements of soil water content. In Koppenjan, S. and Hua, L., editors, *Proceedings of the Ninth International Conference on Ground Penetrating Radar*, pages SPIE 4758:156–161, Santa Barbara, California, USA, 2002.

Reichle, R. H. Data assimilation methods in the earth sciences. *Advances in Water Resources*, 31(11):1411–1418, 2008. doi: 10.1016/j.advwatres.2008.01.001.

Reichle, R. H., Entekhabi, D., and McLaughlin, D. B. Downscaling of radio brightness measurements for soil moisture estimation: A four-dimensional variational data assimilation approach. *Water Resources Research*, 37(9): 2353–2364, 2001.

Reichle, R. H., McLaughlin, D. B., and Entekhabi, D. Hydrologic data assimilation with the ensemble kalman filter. *Monthly Weather Review*, 130(1): 103–114, 2002.

Rhoades, J. D., Raats, P. A. C., and Prather, R. J. Effects of liquid-phase electrical conductivity, water content, and surface conductivity on bulk soil electrical conductivity. *Soil Science Society of America Journal*, 40:651–655, 1976.

Rings, J., Huisman, J. A., and Vereecken, H. Coupled hydrogeophysical parameter estimation using a sequential bayesian approach. *Hydrology and Earth System Sciences*, 14(3):545–556, 2010. doi: 10.5194/hess-14-545-2010.

Robinson, D. A., Jones, S. B., Wraith, J. M., Or, D., and Friedman, S. P. A review of advances in dielectric and electrical conductivity measurement in soils using time domain reflectometry. *Vadose Zone Journal*, 2:444–475, 2003.

Robinson, D. A., Abdu, H., Lebron, I., and Jones, S. B. Imaging of hill-slope soil moisture wetting patterns in a semi-arid oak savanna catchment using time-lapse electromagnetic induction. *Journal of Hydrology*, 416–417(0): 39–49, 2012. doi: 10.1016/j.jhydrol.2011.11.034.

Robinson, D. A., Binley, A., Crook, N., Day-Lewis, F. D., Ferre, T. P. A., Grauch, V. J. S., Knight, R., Knoll, M., Lakshmi, V., Miller, R., Nyquist, J., Pellerin, L., Singha, K., and Slater, L. Advancing process-based watershed hydrological research using near-surface geophysics: a vision for, and review of, electrical and magnetic geophysical methods. *Hydrological Processes*, 22(18):3604–3635, 2008a.

Robinson, D. A., Campbell, C. S., Hopmans, J. W., Hornbuckle, B., Jones, S. B., Knight, R., Ogden, F., Selker, J., and Wendroth, O. Soil moisture measurement for ecological and hydrological watershed-scale observatories: A review. *Vadose Zone Journal*, 7(1):358–389, 2008b.

Rodríguez-Pérez, J. R., Plant, R. E., Lambert, J.-J., and Smart, D. R. Using apparent soil electrical conductivity (eca) to characterize vineyard soils of high clay content. *Precision Agriculture*, 12(6):775–794, 2011. ISSN 1385-2256. doi: 10.1007/s11119-011-9220-y.

Rodriguez-Iturbe, I. Ecohydrology: A hydrologic perspective of climate-soil-vegetation dynamies. *Water Resources Research*, 36(1):3–9, 2000. doi: 10.1029/1999WR900210.

Roth, K., Schulin, R., Fluhler, H., and Attinger, W. Calibration of time domain reflectometry for water-content measurement using a composite dielectric approach. *Water Resources Research*, 26(10):2267–2273, 1990.

Rubin, Y. and Hubbard, S. S. *Hydrogeophysics*, volume 50. Springer, The Netherlands, 2005.

Rucker, D. F. and Ferré, T. P. A. Parameter estimation for soil hydraulic properties using zero-offset borehole radar: Analytical method. *Soil Science Society of America Journal*, 68(5):1560–1567, 2004.

Rucker, D. F. and Ferre, T. P. A. Automated water content reconstruction of zero-offset borehole ground penetrating radar data using simulated annealing. *Journal of Hydrology*, 309(1-4):1–16, 2005.

Saarenketo, T. Electrical properties of water in clay and silty soils. *Journal of Applied Geophysics*, 40(1-3):73–88, 1998.

Sabater, J. M., Lionel, J., Jean-Christophe, C., François, B., and Patricia, D. R. From near-surface to root-zone soil moisture using different assimilation techniques. *Journal of Hydrometeorology*, 8(2):194–206, 2007.

Saintenoy, A., Schneider, S., and Tucholka, P. Evaluating ground penetrating radar use for water infiltration monitoring. *Vadose Zone Journal*, 7(1):208–214, 2008.

Sarkis, R. and Craeye, C. Circular array of wideband 3d vivaldi antennas. In *URSI International Symposium on Electromagnetic Theory (EMTS)*, pages 792–794, 2010. doi: 10.1109/URSI-EMTS.2010.5637231.

Sato, M., Hamada, Y., Feng, X., Kong, F. N., Zeng, Z., and Fang, G. GPR using an array antenna for landmine detection. *Near Surface Geophysics*, 2 (1):7–13, 2004. doi: 10.3997/1873-0604.2003011.

Schaap, M. G., Leij, F. J., and van Genuchten, M. T. rosetta: a computer program for estimating soil hydraulic parameters with hierarchical pedotransfer functions. *Journal of Hydrology*, 251(3–4):163–176, 2001.

Schmugge, T. Applications of passive microwave observations of surface soil moisture. *Journal of Hydrology*, 212–213(0):188–197, 1998. doi: 10.1016/S0022-1694(98)00209-1.

Schöniger, A., Nowak, W., and Hendricks Franssen, H.-J. Parameter estimation by ensemble kalman filters with transformed data: Approach and application to hydraulic tomography. *Water Resources Research*, 48(4):W04502, 2012. doi: 10.1029/2011WR010462.

Scott, M., Duke, J., J. C., Davidson, N., Washer, G., and Weyers, R. Automated characterization of bridge deck distress using pattern recognition analysis of ground penetrating radar data. *Materials Evaluation*, 58(11): 1305–13091309, 2000.

Seneviratne, S. I., Corti, T., Davin, E. L., Hirschi, M., Jaeger, E. B., Lehner, I., Orlowsky, B., and Teuling, A. J. Investigating soil moisture–climate interactions in a changing climate: A review. *Earth-Science Reviews*, 99(3–4): 125–161, 2010. doi: 10.1016/j.earscirev.2010.02.004.

Serbin, G. and Or, D. Ground-penetrating radar measurement of soil water content dynamics using a suspended horn antenna. *IEEE Transactions on Geoscience and Remote Sensing*, 42:1695–1705, 2004.

Shutko, A. M. and Reutov, E. M. Mixture formulas applied in estimation of dielectric and radiative characteristics of soils and grounds at microwave-frequencies. *Ieee Transactions on Geoscience and Remote Sensing*, 20(1): 29–32, 1982.

Simmons, G. The surface electrical properties experiment. Technical report, 1972.

Simunek, J. and Hopmans, J. Parameter optimization and nonlinear fitting. In *Methods of Soil Analysis: Part 4. Physical Methods*, pages 139–157. Soil Science Society of America, Inc, Soil Science Society of America Book Series, 2002.

Slater, L. and Comas, X. The contribution of ground penetrating radar to water resource research. In Harry, M., editor, *Ground penetrating radar: theory and applications*, pages 203–246. Elsevier Science, Amsterdam, The Netherlands, 2009.

Slob, E. C. and Fokkema, J. Coupling effects of two electric dipoles on an interface. *Radio Science*, 37(5):1073, 2002. doi: 10.1029/2001RS2529.

Slob, E. C., Sato, M., and Olhoeft, G. Surface and borehole ground-penetrating-radar developments. *Geophysics*, 75(5):75A103–75A120, 2010. doi: 10.1190/1.3480619.

Smith, P. J., Thornhill, G. D., Dance, S. L., Lawless, A. S., Mason, D. C., and Nichols, N. K. Data assimilation for state and parameter estimation: application to morphodynamic modelling. *Quarterly Journal of the Royal Meteorological Society*, 139:314–327, 2013. doi: 10.1002/qj.1944.

Soldovieri, F., Lopera, O., and Lambot, S. Combination of advanced inversion techniques for an accurate target localization via GPR for demining applications. *IEEE Transactions on Geoscience and Remote Sensing*, 49(1): 451–461, 2011.

Spagnolini, U. and Rampa, V. Multitarget detection/tracking for monostatic ground penetrating radar: application to pavement profiling. *IEEE Transactions on Geoscience and Remote Sensing*, 37(1):383–394394, 1999.

Steelman, C. M. and Endres, A. L. Assessing vertical soil moisture dynamics using multi-frequency GPR common-midpoint soundings. *Journal of Hydrology*, 436-437(0):51–66, 2012.

Stogryn, A. The brightness temperature of a vertically structured medium. *Radio Science*, 5(12):1397–1406, 1970.

Sudduth, K. A., Kitchen, N. R., Bollero, G. A., Bullock, D. G., and Wiebold, W. J. Comparison of electromagnetic induction and direct sensing of soil electrical conductivity. *Agron. J.*, 95(3):472–482, 2003.

Tomizawa, Y., Arai, I., and Gotoh, S. Development of an array antenna landmine detection radar system. In Furuta, K. and Ishikawa, J., editors, *Anti-personnel Landmine Detection for Humanitarian Demining*, pages 45–62. Springer London, 2009. doi: 10.1007/978-1-84882-346-4_4.

Topp, G. C., Davis, J. L., and Annan, A. P. Electromagnetic Determination of Soil Water Content: Measurements in Coaxial Transmission Lines. *Water Resources Research*, 16:574–582, 1980.

Topp, G. C., Davis, J. L., and Annan, A. P. The Early Development of TDR for Soil Measurements. *Vadose Zone Journal*, 2:492–499, 2003.

Tran, A. P., Ardekani, M. R. M., and Lambot, S. Coupling of dielectric mixing models with full-wave ground-penetrating radar signal inversion for sandy-soil-moisture estimation. *Geophysics*, 77(3):H33–H44, 2012.

Tran, A. P., André, F., Craeye, C., and Lambot, S. Near-field or far-field full-wave ground penetrating radar modeling as a function of the antenna height above a planar layered medium. *Progress in Electromagnetics Research B*, 141:415–430, 2013a.

Tran, A. P., Vanclooster, M., and Lambot, S. Improving soil moisture profile prediction from ground-penetrating radar data: a maximum likelihood ensemble filter approach. *Hydrology and Earth System Sciences*, 17:2543–2556, 2013b. doi: 10.5194/hess-17-2543-2013.

Tran, A., Warren, C., André, F., Giannopoulos, A., and Lambot, S. Numerical evaluation of a full-wave antenna model for near-field applications. *Near Surface Geophysics*, 11(2):155–165, 2013c.

Trinks, I., Gustafsson, J., Emilsson, J., Gustafsson, C., Johansson, B., and Nissen, J. Efficient, large-scale archaeological prospection using a true 3D GPR array system. *ArchéoSciences*, (33):367–370, 2009.

Tronicke, J., Holliger, K., Barrash, W., and Knoll, M. Multivariate analysis of cross-hole georadar velocity and attenuation tomograms for aquifer zonation. *Water Resources Research*, 40(1):W01519, 2004. ISSN 1944-7973. doi: 10.1029/2003WR002031.

Valente, A., Morais, R., Tuli, A., Hopmans, J., and Kluitenberg, G. Multifunctional probe for small-scale simultaneous measurements of soil thermal properties, water content, and electrical conductivity. *Sensors and Actuators A: Physical*, 132(1):70–77, 2006. doi: 10.1016/j.sna.2006.05.010.

van Genuchten, M. T. A closed-form equation for predicting the hydraulic conductivity of unsaturated soils. *Soil Science Society of America Journal*, 44:892–898, 1980.

Vaughan, C. J. Ground-penetrating radar surveys used in archaeological investigations. *Geophysics*, 51(3):595–604, 1986.

Vereecken, H., Maes, J., Feyen, J., and Darius, P. Estimating the soil-moisture retention characteristic from texture, bulk-density, and carbon content. *Soil Science*, 148(6):389–403, 1989.

Vereecken, H., Huisman, J. A., Bogena, H., Vanderborght, J., Vrugt, J. A., and Hopmans, J. W. On the value of soil moisture measurements in vadose zone hydrology: A review. *Water Resources Research*, 44, 2008.

Verhoest, N. E. C., Lievens, H., Wagner, W., Alvarez-Mozos, J., Moran, M. S., and Mattia, F. On the soil roughness parameterization problem in soil moisture retrieval of bare surfaces from synthetic aperture radar. *Sensors*, 8(7): 4213–4248, 2008.

Vrugt, J. A., ter Braak, C. J. F., Diks, C. G., and Schoups, G. Hydrologic data assimilation using particle markov chain monte carlo simulation: Theory, concepts and applications. *Advances in Water Resources*, 51(0):457–478, 2013. doi: 10.1016/j.advwatres.2012.04.002.

Šimunek, J., Šejna, M., H. Saito, M. S., and van Genuchten, M. T. *The HYDRUS-1D Software Package for Simulating the One-Dimensional Movement of Water, Heat, and Multiple Solutes in Variably-Saturated Media*, volume Version 4.08. University of California, Riverside, Riverside,California, 2009.

Wagner, N., Emmerich, K., Bonitz, F., and Kupfer, K. Experimental investigations on the frequency- and temperature-dependent dielectric material properties of soil. *IEEE Transactions on Geoscience and Remote Sensing*, 49(7):2518–2530, 2011. doi: 10.1109/TGRS.2011.2108303.

Wagner, W., Bloschl, G., Pampaloni, P., Calvet, J. C., Bizzarri, B., Wigneron, J. P., and Kerr, Y. Operational readiness of microwave remote sensing of soil moisture for hydrologic applications. *Nordic Hydrology*, 38(1):1–20, 2007.

Walker, J. P., Willgoose, G. R., and Kalma, J. D. One-dimensional soil moisture profile retrieval by assimilation of near-surface measurements: A simplified soil moisture model and field application. *Journal of Hydrometeorology*, 2(4):356–373, 2001.

Walker, J. P., Houser, P. R., and Willgoose, G. R. Active microwave remote sensing for soil moisture measurement: a field evaluation using ers-2. *Hydrological Processes*, 18(11):1975–1997, 2004. ISSN 1099–1085. doi: 10.1002/hyp.1343.

Wang, J. R. and Schmugge, T. J. An empirical-model for the complex dielectric permittivity of soils as a function of water-content. *Ieee Transactions on Geoscience and Remote Sensing*, 18(4):288–295, 1980.

Warren, C. and Giannopoulos, A. Creating finite-difference time-domain models of commercial ground-penetrating radar antennas using taguchi's optimization method. *Geophysics*, 76(2):G37–G47, 2011. doi: 10.1190/1.3548506.

Weihermüller, L., Huisman, J. A., Lambot, S., Herbst, M., and Vereecken, H. Mapping the spatial variation of soil water content at the field scale with different ground penetrating radar techniques. *Journal of Hydrology*, 340: 205–216, 2007.

West, L. J., Handley, K., Huang, Y., and Pokar, M. Radar frequency dielectric dispersion in sandstone: Implications for determination of moisture and clay content. *Water Resources Research*, 39(2):1026, 2003.

Westermann, S., Wollschläger, U., and Boike, J. Monitoring of active layer dynamics at a permafrost site on svalbard using multi-channel ground-penetrating radar. *The Cryosphere*, 4(4):475–487, 2010. doi: 10.5194/tc-4-475-2010.

Western, A. W., Grayson, R. B., and Blöschl, G. Scaling of soil moisture: A hydrologic perspective. *Annual Review of Earth and Planetary Sciences*, 30:149–180, 2000. doi: 10.1146/annurev.earth.30.091201.140434.

Weynants, M., Vereecken, H., and Javaux, M. Revisiting vereecken pedotransfer functions: Introducing a closed-form hydraulic model. *Vadose Zone Journal*, 8(1):86–95, 2009. doi: 10.2136/vzj2008.0062.

Windsor, C., Capineri, L., Falorni, P., Matucci, S., and Borgioli, G. The estimation of buried pipe diameters using ground penetrating radar. *Insight*, 47 (7):394–399, 2005.

Woodhead, I. M., Buchan, G. D., Christie, J. H., and Irie, K. A general dielectric model for time domain reflectometry. *Soil Science Society of America Journal*, 86:207–216, 2003.

Yarovoy, A. G., Savelyev, T. G., Aubry, P. J., and Ligthart, L. P. Array-based GPR for shallow subsurface imaging. In *Advanced Ground Penetrating Radar, 2007 4th International Workshop on*, pages 12–15, 2007a. doi: 10.1109/AGPR.2007.386516.

Yarovoy, A. G., Savelyev, T. G., Aubry, P. J., Lys, P. E., and Ligthart, L. P. UWB array-based sensor for near-field imaging. *IEEE Transactions on Microwave Theory and Techniques*, 55(6):1288–1295, 2007b. doi: 10.1109/TMTT.2007.896791.

Zupanski, D. and Zupanski, M. Model error estimation employing an ensemble data assimilation approach. *Monthly Weather Review*, 134(5):1337–1354, 2006.

Zupanski, M. Maximum likelihood ensemble filter: theoretical aspects. *Monthly Weather Review*, 133(6):1710–1726, 2005.

Zupanski, M., Navon, I. M., and Zupanski, D. The maximum likelihood ensemble filter as a non-differentiable minimization algorithm. *Quarterly Journal of the Royal Meteorological Society*, 134(633):1039–1050, 2008.

List of Publications

A. Journal articles

1. A. P. Tran, M. R. M. Ardekani, and S. Lambot. Coupling of dielectric mixing models with full-wave ground-penetrating radar signal inversion for sandy-soil-moisture estimation. *Geophysics*, 77(3):H33–H44, 2012.

2. A. P. Tran, F. André, C. Craeye, and S. Lambot. Near-field or far-field full-wave ground penetrating radar modeling as a function of the antenna height above a planar layered medium. *Progress in Electromagnetics Research B*, 141:415–430, 2013a.

3. A. P. Tran, F. André, and S. Lambot. Validation of near-field ground-penetrating radar modeling using full-wave inversion for soil moisture estimation. *IEEE Transaction on Geoscience and Remote Sensing*, 52(11), 2014b. doi10.1109/TGRS.2013.2289952.

4. A. P. Tran, A. D. Coster, and S. Lambot. Near-field intrinsic modeling of antenna array. *Geophysical Research Letters*, To be submitted in December 2013, 2013c.

5. A. P. Tran, M. Vanclooster, and S. Lambot. Improving soil moisture profile prediction from ground-penetrating radar data: a maximum likelihood ensemble filter approach. *Hydrology and Earth System Sciences*, 17:2543–2556, 2013d. doi10.5194/hess-17-2543-2013.

6. A. P. Tran, M. Vanclooster, M. Zupanski, and S. Lambot. Joint estimation of soil moisture profile and hydraulic parameters by ground-penetrating radar data assimilation with maximum likelihood ensemble filter. *Water Resources Research*, Accepted with minor revision, 2014e. 2013WR014583.

7. A.P. Tran, C. Warren, F. André, A. Giannopoulos, and S. Lambot. Numerical evaluation of a full-wave antenna model for near-field applications. *Near Surface Geophysics*, 11(2):155–165, 2013f.

8. S.-S. Yoon, A. P. Tran, and D.-H. Bae. Quantitative comparison of the spatial distribution of radar and gauge rainfall data. *Journal of Hydrometeorology*, 13 (6):1939–1953.

B. Conference articles

1. A.P. Tran, C. Warren, F. André, and S. Lambot. Numerical evaluation of a full-wave antenna model for near-field applications. In *International Workshop on Advanced Ground Penetrating Radar (IWAGPR), 2011 6th*, pages 1–4, 2011. doi10.1109/IWAGPR.2011.5963849.

2. A. P. Tran, F. Wiaux, and S. Lambot. Soil moisture estimation using full-wave inversion of near- and far-field ground-penetrating radar data: A comparative evaluation. In *14th International Conference on Ground Penetrating Radar*, pages 296–300, 2012b. doi10.1109/ICGPR.2012.6254877.

International Conferences

A. Presentations

1. A. P. Tran and S. Lambot. Temporal and spacial characterization of soil moisture by near-field gpr data. *PhD Student Day (ENVITAM2012)*, Gembloux, Belgium, 2012.

2. A. P. Tran, A. M. R. Mahmoudzadeh, and S. Lambot. Frequency dependence of soil permittivity and conductivity estimated by ground-penetrating radar full-waveform inversion. *European Geoscience Union, (EGU2011)*, Vienna, Austria, 2011.

3. A. P. Tran, F. Wiaux, and S. Lambot. Soil moisture estimation using full-wave inversion of near- and far-field ground-penetrating radar data: A comparative evaluation. *14th International Conference on Ground Penetrating Radar (GPR2012)*, Shanghai, China, 2012.

4. A. P. Tran, F. André, and S. Lambot. Soil moisture characterization using a new full-wave, near-field antenna model: From laboratory to field applications, *International Conference on Novel Methods for Subsurface Characterization and Monitoring: From Theory to Practice (NovCare2013)*, Leipzig, Germany, 2013.

5. A. P. Tran, M. Vanclooster, and S. Lambot. Assimilation of ground-penetrating radar data to update vertical soil moisture profile. *European Geoscience Union, (EGU2013)*, Vienna, Austria, 2013.

6. A.P. Tran, C. Warren, F. André, and S. Lambot. Numerical evaluation of a full-wave antenna model for near-field applications. *6th International Workshop onAdvanced Ground Penetrating Radar (IWAGPR2011)*, Aachen, Germany, 2011.

B. Contributions as co-author

1. F. André, A. P. Tran, N. Mourmeaux, and S. Lambot. Integrated modeling of near-field ground-penetrating radar and electromagnetic induction data for reconstructing multilayered media. *14th International Conference on Ground Penetrating Radar (GPR2012)*, Shanghai, China, 2012.

2. F. André, A. P. Tran, N. Mourmeaux, and S. Lambot. Intrinsic modeling of near-field ground penetrating radar and electromagnetic induction antennas for layered medium characterization. *European Geoscience Union (EGU2013)*, Vienna, Austria, 2013.

3. F. André, A. P. Tran, N. Mourmeaux, A. M. R. Mahmoudzadeh, P. Bogaert, and S. Lambot. Integrated modeling of near-field ground-penetrating radar and electromagnetic induction data for digital soil mapping. *3rd Global Workshop Proximal Soil Sensing*, Postdam, Germany, 2013.

4. S. Lambot, A. P. Tran, and F. André. On the importance of modeling antenna-material coupling for quantitative characterization using GPR. *18th European*

Meeting of Environmental and Engineering Geophysics of the Near Surface Geoscience Division of EAGE - Workshop "New Developments on GPR theory and applications", Paris, France, 2012.

5. S. Lambot, A. P. Tran, and F. André. Near-field modeling of radar antennas for wave propagation in layered media: When models represent reality. *14th International Conference on Ground Penetrating Radar (GPR2012)*, Shanghai, China, 2012.

6. S. Lambot, A. P. Tran, and F. André. A closed form full-wave radar model for near-field layered media reconstruction. *XIX Riunione Nazionale di Elettromagnetismo*, Roma, Italy, 2012.

7. S. Lambot, A. P. Tran, and F. André. Far-field and near-field modeling of ground-penetrating radar for digital soil mapping. *16th International Water Technology Conference*, Istanbul, Turkey, 2012.

8. S. Lambot, A. P. Tran, and F. André. Intrinsic modeling of radar antennas: From far-field to near-field conditions. *7th International Workshop onAdvanced Ground Penetrating Radar (IWAGPR2013)*, Nantes, France, 2013.

9. A. M. R. Mahmoudzadeh, A. P. Tran, J. Minet, M. Vanclooster, and S. Lambot. Ground-penetrating radar for temporal soil moisture variability analysis along a land slope. *European Geoscience Union (EGU2012)*, Vienna, Austria, 2012.

10. L. Mertens, A. P. Tran, and S. Lambot Towards physically-based filtering of the soil surface, antenna and coupling effects from near-field gpr data for improved subsurface imaging. *7th International Workshop on Advanced Ground Penetrating Radar (IWAGPR2013)*, Nantes, France, 2013.

11. N. Mourmeaux, F. André, A. P. Tran, and S. Lambot. Modeling of near-field ground-penetrating radar for digital soil mapping. *PhD Student Day (ENVITAM2012)*, Gembloux, Belgium, 2012.

12. N. Mourmeaux, A. P. Tran, F. André, and S. Lambot. Near-field ground-penetrating radar modeling for characterization of a reference water layer at low frequencies. *Near Surface Geoscience*, Bochum, Germany, 2013.

About the author



Anh Phuong Tran was born in Nam Dinh, Vietnam, on November 17, 1983. In 2005, he obtained a bachelor degree in Hydrology at the Faculty of Hydrology, Meteorology and Oceanography, Vietnam National University-University of Science (VNU-HUS, Vietnam). From 2005 to 2008, he worked as a hydrological researcher at the Center for Hydrology and Water Resources, Vietnam Institute of Hydrology, Meteorology and Environment. In 2008, he moved to Seoul, South Korea to pursue the Master program in GIS & Water Resources at the Department of Civil and Environmental Engineering, Sejong University. Supervised by Professor Deg-Hyo Bae, his master thesis demonstrated on coupling of hydrologic model and radar data for flood and inundation prediction. The weather radar and gauging rainfall data were merged together to considerably improve the quality of rainfall input using the conditional kriging method. After that, these gauging-radar combined rainfall data were used as the input for the 2-D hydrologic model for flood and inundation prediction.

In 2010, after completing the master program with greatest distinction, he obtained a four years PhD grant at the Université catholique de Louvain (UCL, Belgium). His PhD research was carried out at the Environmental Science, Earth and Life Science Institute (UCL) under supervision of Professor Sébastien Lambot. His PhD project aims at calibrating and validating the new near-field antenna model and assimilating ground penetrating radar data for hydrogeophysical characterization of soil, which not only provides valuable information for agricultural, engineering and environmental studies but also is applied for the nondestructive testing of materials. Given the interdisciplinary nature of his research, collaboration was established with the Electrical Engineering Group of UCL and Institute for Infrastructure and Environment at the University of Edinburgh within the framework of antenna modeling and the Cooperative Institute for Research in the Atmosphere at the Colorado State University for the data assimilation issue.